Engineering nanocatalysts using mixed metals for hydrodesulfurization of fuel oil

S. MAJODINA

2021

Engineering nanocatalysts using mixed metals for hydrodesulfurization of fuel oil

By

Siphumelele Majodina

Submitted in fulfilment/partial fulfilment of the requirements for the degree of Students qualification to be awarded at the Nelson Mandela University

December 2021

Supervisor: Dr Adeniyi S. Ogunlaja

Co-supervisor: Prof Zenixole R. Tshentu

DECLARATION

I, *Siphumelele Majodina 217553532*, hereby declare that the treatise/ dissertation/ thesis for Students qualification to be awarded is my own work and that it has not previously been submitted for assessment or completion of any postgraduate to another University or for another qualification.

 .....

Siphumelele Majodina

Official use:

In accordance with Rule G5.11.4, I hereby declare that the above-mentioned treatise/ dissertation/ thesis is my own work and that it has not previously been submitted for assessment to another University or for another qualification. However, material from publications by the student may be embodied in a treatise/dissertation/ thesis.

ABSTRACT

Crude oil is a complex blend containing thousands of hydrocarbons, non-hydrocarbon compounds and heavy metals. These hydrocarbons are mixed with variable quantities of sulfur-, nitrogen-, and oxygen-containing compounds. The combustion of fuel containing organosulfur compounds results in the emission of sulfur oxides (SO_x) into the atmosphere. These toxic gases escape into the atmosphere resulting in air pollution, which is a large contributor to global warming. Air pollution also causes pulmonary diseases, allergies and may even lead to human death. It can also cause harm to other living organisms such as animals and food crops. Thus, mandating the reduction of sulfur in organosulfur compounds in fuel to <10 ppmS by the environmental protection agency. Several studies have been conducted to remove sulfur from fuels, most of which have focused on removing refractory sulfur compounds due to the difficulty in removing sulfur in these compounds. However, the currently employed hydrodesulfurization (HDS) catalysts suffer in producing fuels complying with the future standards of fuels quality. Generally, HDS catalysts are made up of metallic components, Co (Ni) and Mo (W), on porous supports, the catalytic activity of these catalysts strongly depends on the amount of NiWS (CoMoS) phases in it and to the extent in which these phases are exposed on the catalyst support surfaces and this is engineered using chelating agents and size of catalysts. To this end, nanosized materials (nanocatalysts) are considered most suitable, as reported active phases of HDS catalysts are exposed, hence improving the hydrodesulfurization of sulfur-containing compounds in fuels. Nanocatalysts results in nanoparticles and when impregnated on a support will results in high surface area, and enhances electronic property, which increases the activity of the catalyst allowing the most refractory sulfur to be removed. The addition of chelating agents such as EDTA, acetic acid, and citric acid further improves the activity of the catalysts by producing more active phases on the catalyst. In this research project, nanocatalysts will be synthesised using mixed metals with and without chelating agents and tested for HDS activity and selectivity towards sulfur using refractory organosulfur compounds in fuels under industrial HDS conditions. This work was divided into two sections, and this dissertation summarizes the research outcomes of each phase.

The first section examines the effect of chelating ligands, namely, ethylenediaminetetraacetic acid (EDTA), citric acid (CA), and acetic acid (AA), on CoMo HDS activity and the sulfidation mechanism. In this study, chelating ligands seem to have a beneficial effect on HDS activity. Detailed mechanistic aspects of interactions between chelating ligands and metallic species (Co-chelating ligands) were also studied. Characterization by SC-XRD revealed that the presence of the chelating ligand result in the formation of complex with cobalt, and the effect of this complex was shown by TG-DSC analysis. This showed that the presence of chelating ligand leads a to delay of cobalt sulfidation as the complex decomposes at higher temperatures, which was the main cause of improving HDS activity. It was also shown that chelating ligands play a role in dispersion of metal oxides and sulfided metal oxides (TEM and XPS). XPS results showed low MoS_2 phase for $CoMo/Al_2O_3$ (45%), while $CoMo\text{-}EDTA/Al_2O_3$ (63%) catalyst resulted in high MoS_2 phases. From all the catalysts, $CoMo\text{-}CA/Al_2O_3$ (98%) gave the highest

catalytic activity, and the increase in activity could be attributed to the formation of octahedral molybdenum oxides as they are easily reducible during sulfidation and result in more dispersed active phases and weak metal-support interaction.

The second section examines the effect of a promoter (Rh) and different chelating ligands (EDTA, AA, and CA) on the catalyst RhMo supported with alumina. In this phase, rhodium was used as promoter, the following trend for catalytic activity was observed: $RhMo/Al_2O_3$ (88%) > $RhMo\text{-}AA/Al_2O_3$ (73%) > $RhMo\text{-}CA/Al_2O_3$ (72%) > $RhMo\text{-}EDTA/Al_2O_3$ (68%). This could be that the addition of chelating ligand complexed both metallic species retarding sulfidation of both metals, hence lowering the HDS activity. Studies show that it is possible for the citric acid to complex with both promoter and an active metal (Mo), and this might result in the formation of molybdenum dimers, trimers and tetramers which are difficult to sulfide. XPS analysis showed that unchelated catalyst have more MoS_2 phases of 63%, hence higher dispersion than the chelated catalyst, this could be the reason for high activity in $RhMo/Al_2O_3$ (88%) catalyst.

ACKNOWLEDGEMENT

I would like to express my gratitude to everyone who supported me throughout my Master's programme. I wish to thank my supervisors, Dr Ogunlaja and Prof Tshentu for their guidance, encouragement, valuable input, and support throughout this work. To Dr Ogunlaja, I am grateful for the push and always being available whenever I need help, for being patient and making this dream come true. My gratitude goes to Prof Tshentu, for the opportunity you have given me for taking me as your student during honours programme, for giving me this project, and your support throughout.

I want to express my gratitude to my fellow colleagues; Tendai Dembaremba for always making time when I need help and challenging me to learn more, Nazi, Zizipho, Nompilo, Mzuu, Siyabonga Shoba, Dr Moleko-Boyce, Dr JMV and everyone for their support and help. I want to thank Thulie for her support throughout my journey, and Shane for the support and words of encouragement.

A special and heartfelt thanks to my mother (Nomzwebango Mandlovu), thank you for believing in me before I did, for the support and love and amazing parent till the end, to my brother Msindisi for always checking up on me and making me laugh. Mcebisi, Loyiso, Asingisile, Nosiyolise, Tubie, Luu, Manibi, Olwethu I am grateful for their support and motivation.

I would like to thank Nelson Mandela University, Sasol, and NRF for their financial support through my studies.

Thanks to Rhodes, UJ, and iThemba labs for helping with analysis.

Lastly, I want to thank God for being with me throughout this work, for giving me strength to carry on and hope. For the opportunity and blessings and placing such wonderful people in my life. Without Him I would not be here to begin with.

DEDICATION

This thesis is dedicated to:

My mother, siblings who have always been with me and encouraged me. All I have accomplished was possible due to their love and support. This is also dedicated to me for not giving up when things were tough.

Table of content

List of Figures

List of tables

List of Abbreviations

AA	Acetic acid
BET	Brunauer-Emmett-Teller
BT	Benzothiophene
BP	Biphenyl
CA	Citric acid
CHB	Cyclohexyl benzene
Co	Cobalt
CoO	Cobalt oxide
DBT	Dibenzothiophene
DDS	Direct desulfurization
DMDBT	Dimethyl dibenzothiophene
DFT	Density functional theory
EDX	Energy dispersion X-ray
FTIR	Fourier transform infrared.
GC	Gas chromatograph
HDS	Hydrodesulfurization
HYD	Hydrogenation
H_2S	Hydrogen sulfide
ICP	Inductively coupled plasma.
Mo	Molybdenum
MoO_3	Molybdenum trioxide
MPa	Mega pascal
nm	Nanometer
S	Sulfur
SO_x	Sulfur oxides
SEM	Scanning electron microscopy
TH-DBT	Tetrahydrodibenzothiophene

TEM	Transmission electron microscopy
UV-DRS	Ultra-violet diffuse reflection spectroscopy
XRD	X-ray diffraction
XRF	X-ray fluorescence
XPS	X-ray photoelectron spectroscopy

Chapter One

Introduction and Literature review

Chapter one focuses on the background of the study which includes the detrimental effects of organosulfur compounds in petroleum and their environmental issues. This chapter also covers hydrotreating process, common hydrotreating catalysts and its components and hydrodesulfurization process in general. A review on improvement of intrinsic activity of HDS catalyst can be improved is discussed.

1.1. Introduction

Fossil fuels are the main source of energy worldwide; Crude oil is one of the main sources of fuels and it occurs naturally and contains several organic components such as diesel, gasoline, jet fuels, kerosene etc., they serve as the major source of energy in the world (Saleh, 2015). It is a mixture of hydrocarbons and contains several impurities such as nitrogen, oxygen, metals and sulfur (Théodet, 2010). By far, the most common impurities are the organic sulfur compounds. According to the Energy efficient potential in South Africa, (2015) Oil is used mainly in transport sectors, and it also used as a primary energy source and about 35% was used. **Table 1.1** shows the total final consumption by fuel in 2012.

Table 1.1: The total final consumption by fuel (OECD/IEA, 2015).

Total final consumption	**Percentage (%)**
Oil	35
Coal	24
electricity	24
Gas	2
Traditional biomass	13
Morden biomass	3

Due to an increasing amount of population, more transportation is in need; hence, more fuel will be in demand. As a result, more fuel will be refined; this will lead to an increase in air pollution since during the refinery of fuel harmful gases escape to the atmosphere. All fossil fuels contain a variety of organic and inorganic sulfur compounds, and sulfur is the third most abundant element in crude oil.

Combustion of sulfur containing compounds in fossil fuels emits sulfur oxides in the atmosphere, which can cause adverse effects on the health, environment, and economy. Sulfur containing compounds exist in different forms as shown in **Figure 1.1**. The most complex organosulfur compounds are the compounds with aromatic rings and are also known as the refractory sulfur compounds (Steiner, 2002).

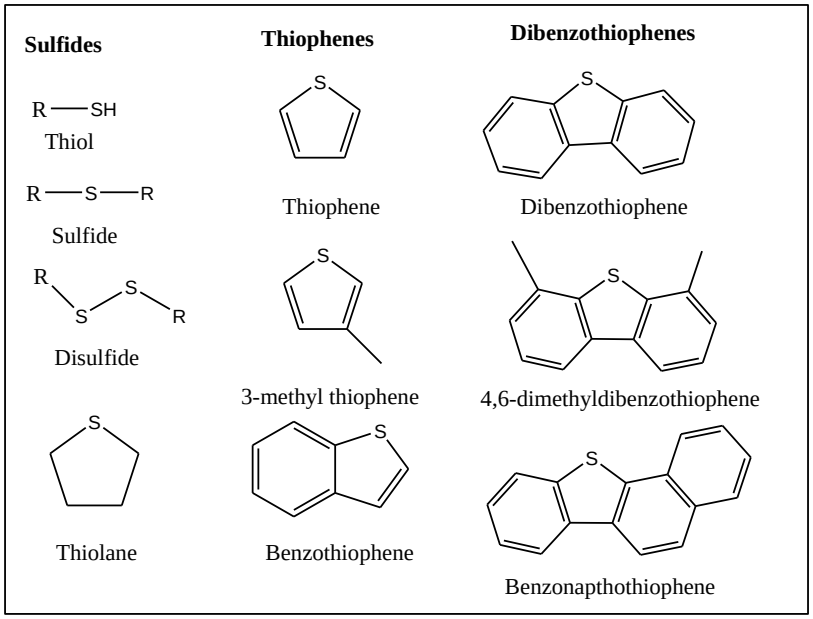

Figure 1.1: Some of the sulfur containing derivatives present in petroleum (Ahmad, 2013)

1.1.1 Detrimental effects of sulfur compounds in petroleum

Sulfur containing compounds are corrosive in nature, when they are present in abundance in crude oil; they poison refining catalyst thus, leading to reduction of the catalyst efficiency (Corro, 2002). Sulfur containing compounds are foul-smelling and toxic, therefore handling and processing of petroleum products with odour creates health problems. They cause corrosion by directly reacting to the metal surface causing damages in storage tanks, pipes, and equipment's, reducing their durability and high repair maintenance costs (Ahmad, 2013). Sulfur as SO_x contributes to atmospheric pollution (Torres-Nieto & Garcia, 2007). During combustion of fuels, sulfur contents are oxidized and released as SO_2 which gets photo-catalytically oxidized to sulfur trioxide (SO_3) in the atmosphere and under humid conditions; SO_3 reacts with water vapours present in the fuel gases to form sulfuric acid (H_2SO_4) causing acid rain (Saleh, 2015). The following reaction shows how acid rain is formed:

$$2SO_2 + 2O_2 \rightarrow 2SO_3 \quad (1)$$

$$SO_3 + H_2O \rightarrow H_2SO_4 \text{ (Acid rain)} \quad (2)$$

Acid rain is one of the major environmental problems; it adversely affects the biota and its surroundings, it primarily affects soil by washing away the nutrients needed by the plants to grow (Saleh, 2015). Acid

rain also damages forest trees, leads to cold weather and drought; it runs off drains into lakes, streams, and marshes where it disturbs the aquatic life (**Fig. 1.2**).

Figure 1.2: Impact caused by acid rain.

Another major disadvantage of sulfur compounds in petroleum is that they deactivate base metals and precious metal catalysts used in refining petroleum (Kent *et al*., 2010). During refining process, these sulfur compounds selectively adsorb over the surface or active sites of the metal present in the catalysts, thereby reducing their activity. The loss of activity occurs after the formation of metal sulfides when organosulfur compounds contact the surface of one of the metals found in the catalyst. Due to nuisance caused by sulfur compounds in the form of health effect, environmental pollutant and hurdling in the refining processes, the environmental regulators in South Africa have mandated stringent legislation with the aim of reducing sulfur levels to an ultra-low level to < 10 ppmS by 2017 (this was receded) as shown in **Figure 1.3** (Babich & Moulijn, 2003; Song & Ma, 2003).

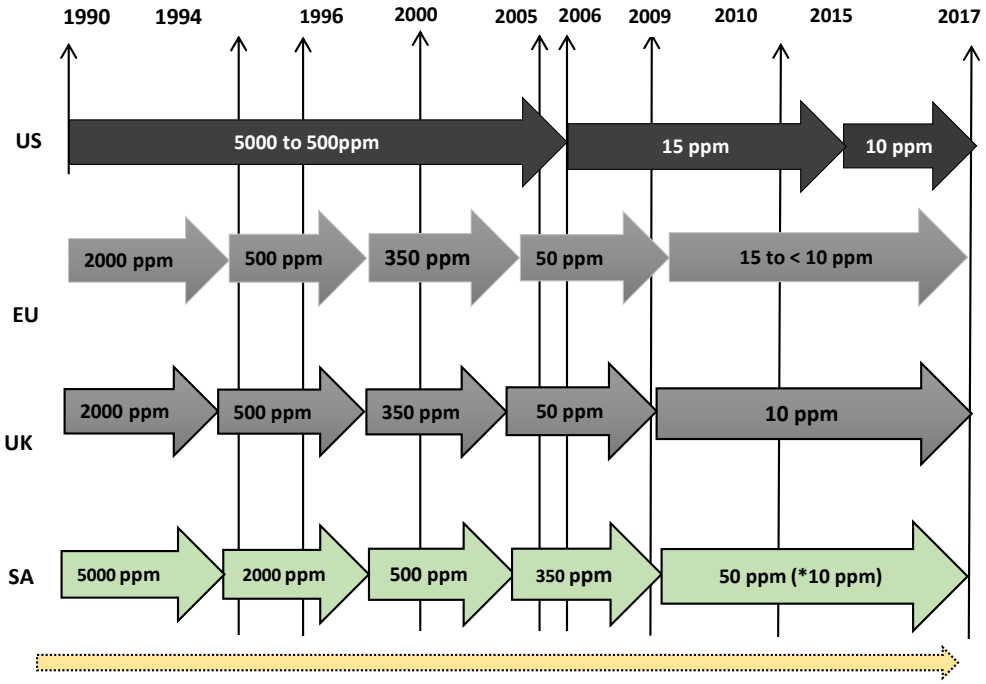

Figure 1.3: Trends in diesel sulfur fuel specifications for United State (US), United Kingdom (UK), Europe Union (EU) and South Africa (SA) over the years. *The SA target of 10 ppm meant to come into effect in 2017 was receded (Barbara *et al*., 2011; Song *et al*., 2003; Saleh, 2015).

Due to different reactivity of sulfur containing compound, the rates of sulfur removal differ in several orders of magnitude. Generally, thiols and disulfides are highly reactive as compared to thiophenes, the sulfur can be removed under mild conditions, similarly the saturated cyclic sulfur compounds and aromatic system in which sulfur is present in six-membered are also highly reactive. The activity of organosulfur compounds (5 membered ring structure) decreases in the following order: thiophenes > benzothiophenes > dibenzothiophenes (**Figure 1.4**) (Whitehurst *et al.*, 1998). Similarly, 4,6-dimethyldibenzothiophene (4,6-DMDBT) and 4- methyldibenzothiophene (4-MDBT) are less reactive than any other compounds mentioned earlier, but the 4,6–DMDBT is less reactive than 4-MDBT. However, the trend reverses for highly condensed ring structure (four or more), the activity tends to increase as the ring structure increases in size. The reason for this behaviour is that there are several different chemical pathways through which sulfur can be removed from a molecule and the preferred pathway changes for different compound structures. **Figure 1.4** gives a presentation of the reactivity of different sulfur based compounds. Alkyl substituents in dibenzothiophene (DBT) compounds greatly increase the difficulty of hydrodesulfurization, due to steric hindrance caused by the methyl-substituents at 4,6- position and is mainly said to be the reason behind the refractory nature of this compound.

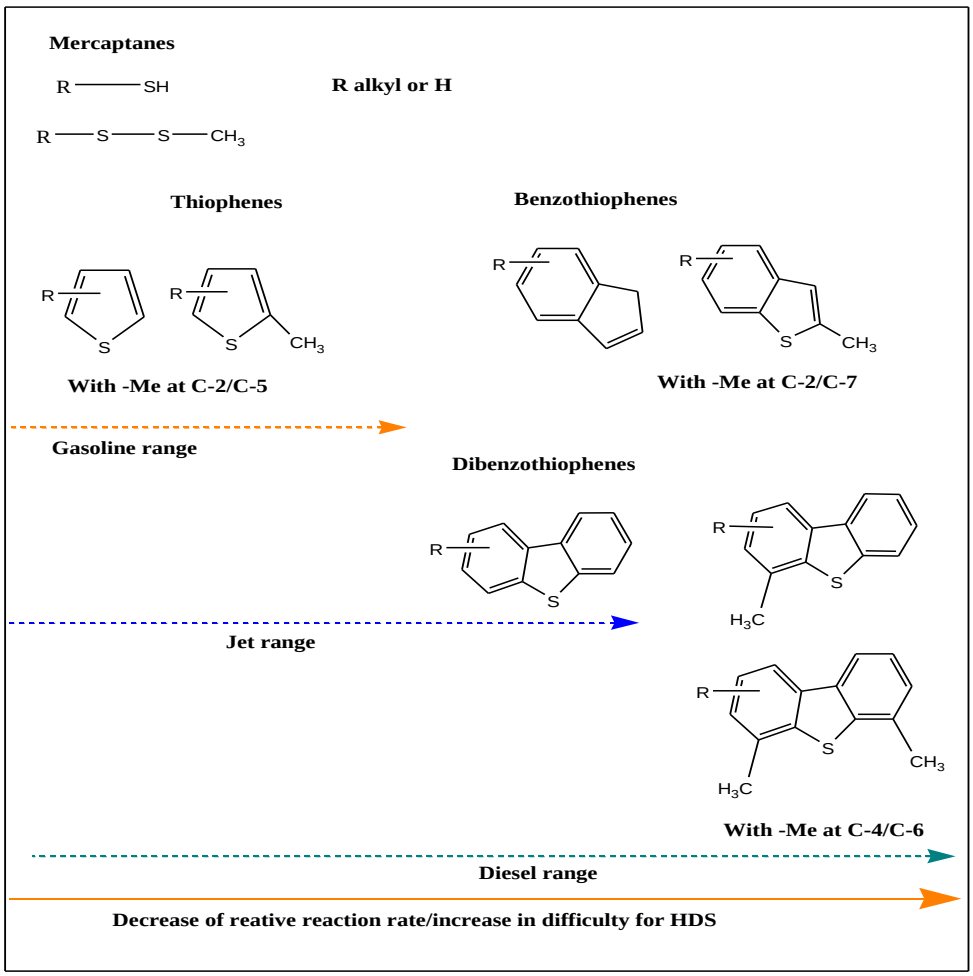

Figure 1.4: Relationship between the type and size of sulfur compound in different fractions of distillate and their relative reactivity. In the range of diesel, molecules such as dibenzothiophenes and alkyldibenzothiophenes predominate, which present low reactivity for HDS (Whitehurst *et al.*, 1998).

1.1.2 Research problem

Fuel is a complex mixture; it consists of organic compounds and other impurities such as sulfur. These sulfur containing compounds are corrosive in nature, and during combustion of fuels, sulfur containing compounds (SO_x) are released to the atmosphere. The presence of SO_2 gets liberated into the atmosphere leading to serious environmental pollution problems such as acid rain. Acid rain is one of the major environmental problems, it adversely affects the biota and its surroundings (Saleh, 2015, Ahmad, 2013). Sulfur compounds deactivate metal catalysts used and reduce their activity. In order to stop this serious environmental deterioration, worldwide environmental authority has been implemented in order to limit the amount of sulfur compounds in petroleum. The environmental regulations have mandated stringent legislation with the aim of reducing sulfur levels to an ultra-low level between 5-10 ppmS.

Hydrodesulfurization which is the current process used in eliminating sulfur compounds, suffers from reducing the refractory organosulfur compounds such as dibenzothiophene (DBT) and the alkylated

substituted dibenzothiophene (4- and/or 6- positions) and this is because of the nature of the employed catalyst. Noble metal catalysts, such as Pd or Pt, have gained increasing attention due to their high hydrogenation activity (Stanislaus & Cooper, 1994). However, these catalysts are sensitive towards poisoning by sulfur compounds. Furthermore, there has been enormous amount of research, focusing on the designing active phase of hydrotreating catalysts, however, the various catalysts have been a matter of great debate and many questions remain, to be answered.

A complicating factor is the large number of variables in preparation, pre-treatment, and activity measurement conditions. Differences in these conditions can (partially) explain the contradictory results found in literature. As a consequence, it is sometimes very difficult to compare results from different studies reported. Therefore, the main subject of this dissertation is to compare the characterization and HDS activities of synthesized chelated catalysts and is therefore one of the subjects of this dissertation.

The major disadvantage of sulfur compounds present in fuel is that they deactivate the base metals and precious metal catalysts used during refinery process (Kent *et al*., 2010). During this process, sulfur species are selectively adsorbed over the surface or active sites of metals present in the catalysts, thereby causing inactivation or reducing of their activity.

Ultra-deep HDS is needed to reach the sulfur content limit (Braggio *et al*., 2018); (Salazar, Schmidt, & Lauritsen, 2019). Therefore, highly active catalysts seem to be the critical factor to deal with the bulk sulfur compounds and remove them selectively from refractory alkyl-substituted DBT (4,6-DMDBT). Sulfur removal from sterically hindered compounds present a strong inhibition effect of polyaromatics. To overcome this problem, the HDS unit needs to increase working parameters such as pressure and temperature, however, this carries along another series of problems. Coke deposition and gradual segregation of active phases may be observed in a long time if the working catalyst loses stability.

The nature of the support plays a key role in the morphology, dispersion, and in the catalytic activity of the catalyst (Chen & Goodman, 2006); (Venezia, Parola, & Liotta, 2017). A high edge dispersion is important since it increases the amount of the promoter (Co) that can be accommodated at the edges forming the active Co-Mo-S structure (Chen & Goodman, 2006). However, the support interaction also has important implications for the intrinsic activity of the active sites. There are two types of phases present Type I and Type II (active). The existence of these two different structures is related to the interaction between the metal and the support (alumina OH groups) during the preparation. Type I is a phase where there is a strong interaction between the metal and support, and studies have shown that this linkage can be broken by high temperature during sulfidation, but this leads to decrease of MoS_2 dispersion. Sulfidation is a complex reaction, and strong metal-support interaction can cause poor reducibility of the metal species, which makes sulfidation of the catalyst difficult leading to poor activity (Medici & Prins, 1996).

1.2 Literature review

Refining process can be used to eliminate several harmful contents in fuels such as sulfur. Before finding ways to reduce sulfur contents, various parameters need to be taken into consideration such as identifying the nature and the type of sulfur compounds present in crude oil or petroleum and their distribution in distillate fractions, to know various problems associated with organosulfur compounds, to understand the technological background of different desulfurization techniques and identify their limitations. Among these other techniques, studies show that hydrotreating is a significant part of refineries around the world, and hydroprocessing catalysts constitutes about one third of the catalysts sold around the world. Hydrodesulfurization is so far the only process employed for desulfurization in the refineries.

Transition Metal Sulfide (TMS) catalysts are the cornerstone of hydroprocessing industry, because of their innate stability of their catalytically active phases. HDS catalysts consist of two or more metals, the promoter, and the active metal. The most common hydrotreating catalysts contain the active metal as Molybdenum (Mo) or Tungsten (W), a promoter metal most commonly Nickel (Ni) or Cobalt (Co). The ɣ-Al_2O_3 is by far the most universally used support owing to excellent physical and chemical properties suitable to hydrotreating and associated reactions. The most used HDS catalysts are CoMo and NiMo. In a typical CoMo or NiMo catalyst, Co (Ni) acts as promoter while Mo acts as the main active component of the catalyst activity. The promoter increases the electron density of the active metal, resulting in an increasing number of electrons in the highest occupied molecular orbital. These electrons are donated from the promoter to the active metal, weakening as metal-sulfur bond, hence increasing HDS activity (Harris & Chianelli, 1986; Chianelli *et al*., 2002). It is also believed that the promoter can lower the oxidation state of the active metal (Mo) through electron transfer. For each series of catalysts, the activity was found to be directly proportional to the amount of a promoter (-Co, -Ni) present in the form of Co-Mo-S (Tøpsoe, 1982).

1.2.1 Hydrodesulfurization (HDS) process and reaction mechanism

1.2.1.1 HDS process

Hydrodesulfurization (HDS) is the most used method for removing sulfur from organosulfur compounds that are present in fuels. This process is important industrially since sulfur compounds are poisonous in precious metal–based catalysts (Saleh, 2015). HDS is an important catalytic process where sulfur atom in organosulfur compounds are converted to hydrocarbons and hydrogen sulfide (H_2S) which can be easily separated from the fuel. This process takes place in the presence of sulfided metal-based catalyst such as Co/Mo/Al_2O_3 or Ni/Mo/Al_2O_3. **Figure 1.5** shows a general schematic of how this process occurs:

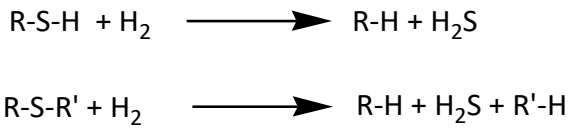

Figure 1.5: General hydrodesulfurization process (Babich & Moulijn, 2003).

In the process the feed is treated with hydrogen gas (H_2) in a specially designed reactor at high temperatures (300-400˚C) and pressures (>200 atm) (Javidli & De Klerk, 2012). The temperature is increased by heat exchange with the reactor effluent and continued being raised by a furnace to obtain the required temperature (Mochida & Motoki, 2004). The feed gets hydro-processed in the presence of the catalyst in the reactor while hydrogen gas is flowing in a specific pressure. After separation, formed products are passed through a cooler to the separator (Saleh, 2015). Gases such as H_2S and H_2 separate from the liquid product in the separator, while high-pressure gas H_2 gets recycled to the HDS reactor and low-pressure rich in H_2S and is passed to amine treated to remove H_2S gas. The obtained liquid product is further fractionated into the desired product according to their boiling points.

1.2.1.2 HDS reaction mechanism

The ease of removal of sulfur atom from a petroleum stream depends greatly on the structure of the organosulfur compound being treated. Generally, acyclic sulfur compounds such as thiols and disulfides are highly reactive and can be removed under very mild conditions, it is also easy to remove sulfur atom in saturated cyclic sulfur compounds due to their high reactivity. However, compounds which are incorporated into a 5 membered ring (thiophene) are less reactive and the reactivity decreases as the ring structure becomes increasingly condensed (e.g., 1>2>3 rings) (Whitehurt *et al*., 1998). For highly condensed ring structures (4 or more rings), the reactivity trend reverses, and reactivity tends to increase as the ring structure increases in size. The reason for this behaviour is that there are several different chemical pathways through which sulfur atom can be removed from organosulfur molecule and the preferred pathway changes for different sulfur compounds. The alkyl substituents in DBT compounds greatly increases the difficulty of HDS, this is due to the steric hindrance caused by the methyl substituents at 4,6-position which is the main reason behind the refractory nature of this compound. Once organosulfur compound and H_2 have been chemisorbed on the catalytic surface, they interact with each other to complete desulfurization.

There are two types of desulfurization pathways, these are Direct Desulfurization (DDS) and Hydrogenation (HYD) pathway. Direct desulfurization pathway involves the removal of sulfur without hydrogenation. Sulfur atom is removed from the structure and replaced by hydrogen (Mochido & Choi, 2006), while hydrogenation pathway involves hydrogenation (partial and total hydrogenation) of the

organic compound prior to the sulfur removal. At least one aromatic ring adjacent to the sulfur containing ring is hydrogenated before sulfur atom is removed and replaced by hydrogen (**Figure 1.6**).

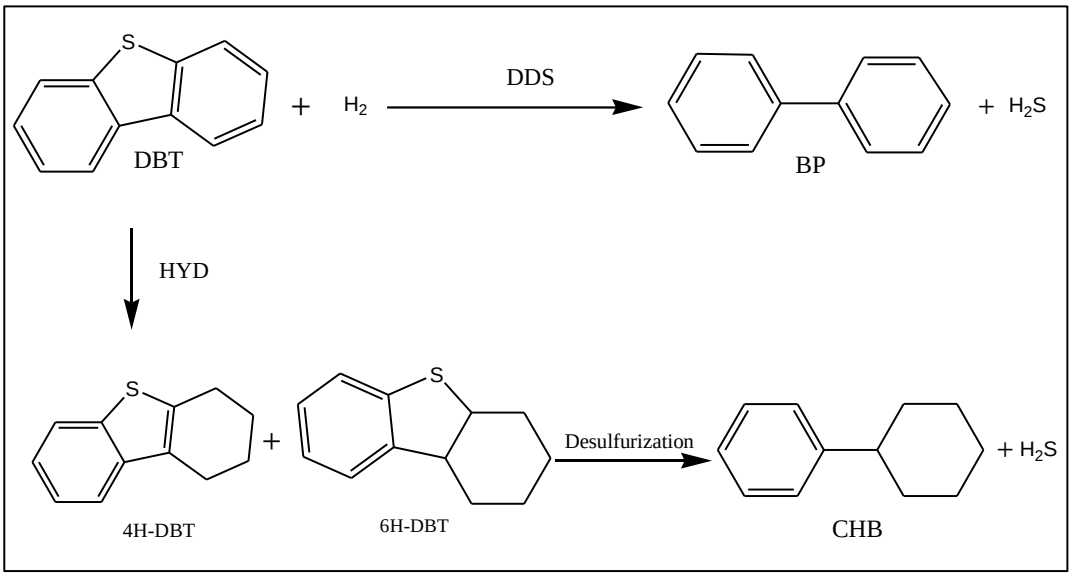

Figure 1.6: Reaction pathways for HDS of DBT. (Mochida & Chio, 2014).

For most refractory sulfur compounds at least one aromatic ring adjacent to the sulfur containing ring is hydrogenated before sulfur atom is removed and replaced by H_2 in HYD pathway. Both pathways proceed in parallel; however, the nature of the catalyst and the nature of the substrate steers the preference of either pathway (Saleh, 2015; Xiang *et al*., 2011).

Different organosulfur compounds prefer different pathways, as the ring of the structure increases the direct pathway becomes more difficult. For dibenzothiophene (DBT), DDS results in the formation of biphenyl (BP) through hydrogenolysis. In HYD pathway, aromatic rings are first hydrogenated and this is followed by the cleavage of C-S bond. During HYD one of the phenyl rings is hydrogenated forming tetrahydodibenzothiophene (4H-DBT) and hexahydrodibenzothiophene (6H-DBT), followed by C-S cleavage by hydrogenolysis (Alibouri *et al*., 2009). According to Shafi and Hutching (Shafi & Hutching, 2000) hydrogenation followed by desulfurization is the most likely route to reach low sulfur compound (Shafi & Hutching, 2000) for the refractory sulfur compounds as shown in **Figure 1.6**. This is due to the steric hindrance of the methyl groups, which hinder the interaction of sulfur atom with the active site of the catalyst and therefore hydrogenation of the aromatic ring prior to removal of sulfur is generally thought to decrease this steric hindrance. Hence, facilitates HDS reaction by making the sulfur removal easier (Chianelli *et al*., 2006). It has been proposed that the different active sites found in the catalysts are responsible for both routes (Xiang *et al*., 2011).

1.2.1.3 Chemistry and reactivity trends of metals and metal sulfides

HDS catalysts are metal based; therefore, the focus is to understand the activity trend of various Transition Metal Sulfides (TMS) across the periodic table. Study of periodic trends have focused more on the electronic structure of the sulfides. This has resulted in different points of view concerning the origin of these trends, which are discussed in this chapter (Tøpsoe *et al*., 1996). Experiments conducted for benzothiophene (BT) and dibenzothiophene (DBT) indicated that HDS activity is related to the position of the metal in the periodic table (Pecoraro & Chianelli, 1981). Second and third row of the periodic table for DBT in a medium-pressure autoclave model reaction gave a so-called volcano plot as shown in **Figure 1.7**.

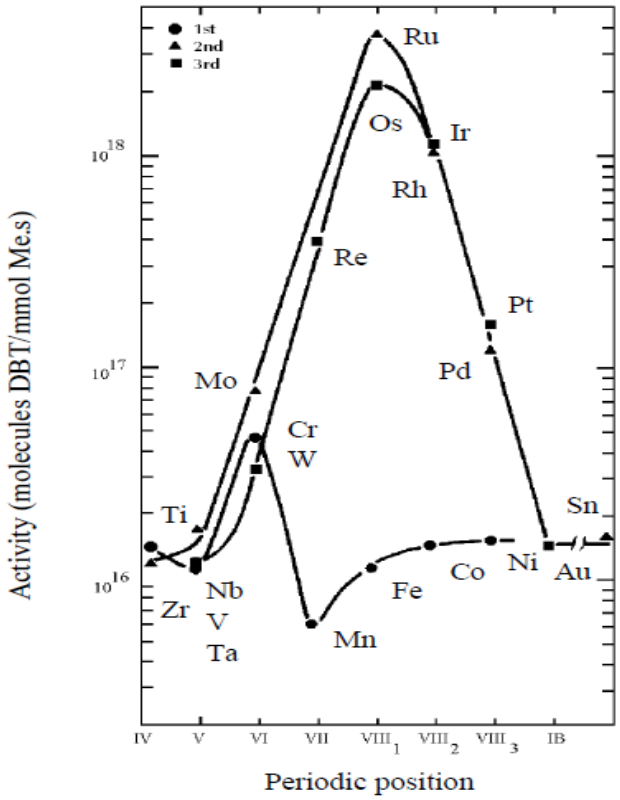

Figure 1.7: Periodic trends for the HDS of dibenzothiophene in an autoclave reactor using bulk transition metal sulfides (Pecoraro & Chianelli, 1981).

The volcano plot shown in **Figure 1.7** shows that the second and the third row of the metals in the periodic table are more active than the first row. The maximum activity was obtained at the sulfides of Ruthenium (Ru), Osmium (Os), Rhodium (Rh) and Iridium (Ir) in the second and third row transition metals, respectively. The first row appeared to be relatively inactive with a distinct minimum at MnS. These trends were explained in terms of the strength of the metal-sulfur bond. The two different models used in assessing the M-S bond strength, Topsoe *et al*., 1993 suggested that HDS activity increases with decreasing metal-sulfur bond energy (Topsoe *et al*. 1993; Pecoraro & Chianelli, 1981). According to Pecoraro & Chianelli, (1981) these trends must be of an electronic nature. The volcano plot can be

explained in terms of Sabatier's principle; according to Sabatier's principle for the catalyst to be active, it should form a sufficiently stable intermediate with the reacting molecules. The highest activity for desulfurization is linked to transition metal with the lowest sulfur bond energy; therefore, the transition metal sulfides with the lowest metal-sulfur bond energy will have the largest number of sulfur vacancies hence highest activity. Further studies were conducted using thiophene; obtained results concluded that the number of sulfur vacancies does not control the reaction rate, but the strength of the transition metal sulfides - thiophene interaction. This was further supported by effective medium theory results conducted by (Moses *et al*., 2014), that the highest activity was found for the transition metal sulfides with the lowest metal-sulfur bond energy. These results were supported by plotting the activity of the TMS as a function of heat of formation per mol of metal-sulfur bond as shown in **Figure 1.8**.

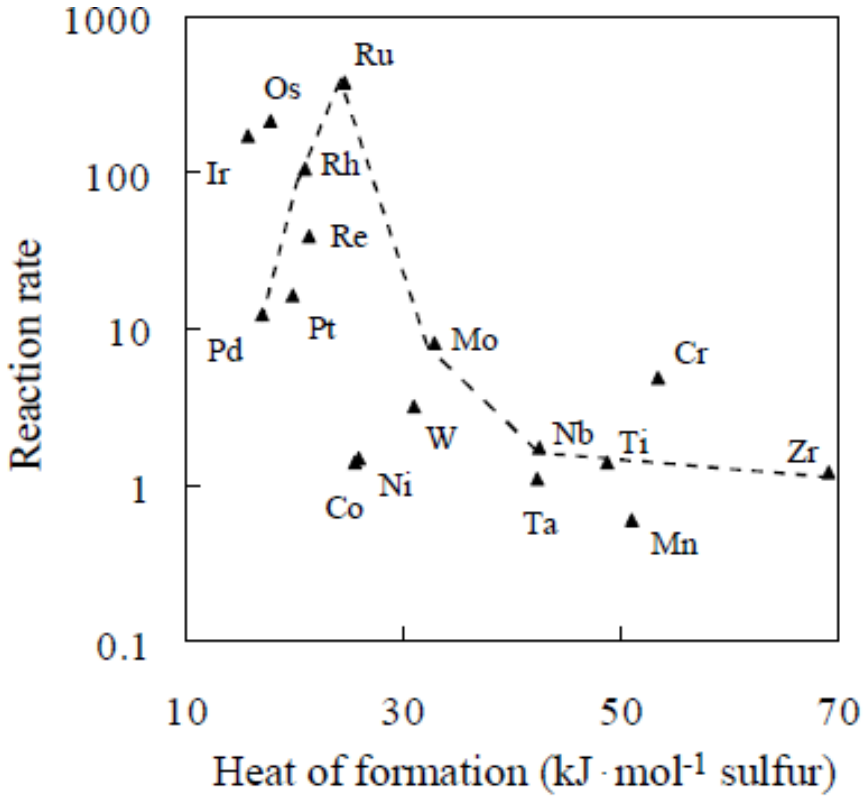

Figure 1.8: HDS activity as a function of the heat of formation of TMS on mol^{-1} of sulfur basis (Tøpsoe *et al*., 2007) periodic trend for 4d TMS.

Three effects were looked at: the electronic effect of a transition metal in a sulfur environment, geometric effect of a structure for a given transition metal sulfide, and chemical effect of local active site configuration. For the second and third row of the periodic table it was observed that the most active catalysts have intermediate values of the heat of formation (30-55 kcal/mol). This suggests that Mo-S bond strength at the surface of the catalyst support must not be too strong or too weak to obtain the maximum desulfurization rate (Topsoe *et al*., 2007).

The M-S bond strength was also assessed by ab initio method, and from the results, it was concluded that there is a relationship between maximum HDS activity and the optimum M-S bond strength

(Pecoraro & Chianelli, 1981). It was discovered that used models are linked to this idea that since catalysis takes place on Coordinatively Unsaturated Sites (CUS), the HDS activity is directly related to the number of vacancies available on the surface and the activity is also determined by the M-S bond energy (Tøpsoe *et al*., 2007).

b) The CoMoS model

The active phase of the catalyst is achieved when the promoter i.e., Co atom is located on the edges and corners of MoS_2 slabs to form CoMoS active phases (Kabsgaard *et al*., 2010). The monolayer model Co (Ni)-Mo-S phase model was proposed to explain the role of the promoter and its location in the catalyst (Tøpsoe, 2007). Several models have been proposed to explain the morphology of MoS_2 catalysts and the role of Co- or Ni promoters in HDS catalysis. The Rim-Edge model was developed by (Daage & Chianelli, 1994) to derive a correlation between the structure and selectivity of MoS_2 catalysts for hydrogenation and hydrogenolysis reaction. They proposed MoS_2 to be crystallites, arranged in layers and are anisotropic in nature (Helveg *et al*., 2000). These crystallites are imagined as a stack of discs, the top and the bottom layer represent the edge sites while the sites forming the edges of the interior layers are rim sites and were found to be active, and the activity of the catalyst emanates from MoS_2. Fully sulfur-saturated Mo edges of MoS_2 sites with metallic character on the brim sites help in adsorption of sulfur-containing compounds (Moses *et al*., 2007). Rim is responsible for both hydrogenation and direct HDS, which creates the ability for adsorption of refractory organosulfur compounds, while the edge site is responsible for hydrogenation only (Topsoe *et al*., 1996), and the catalytic active sites are shown in **Figure 1.9**.

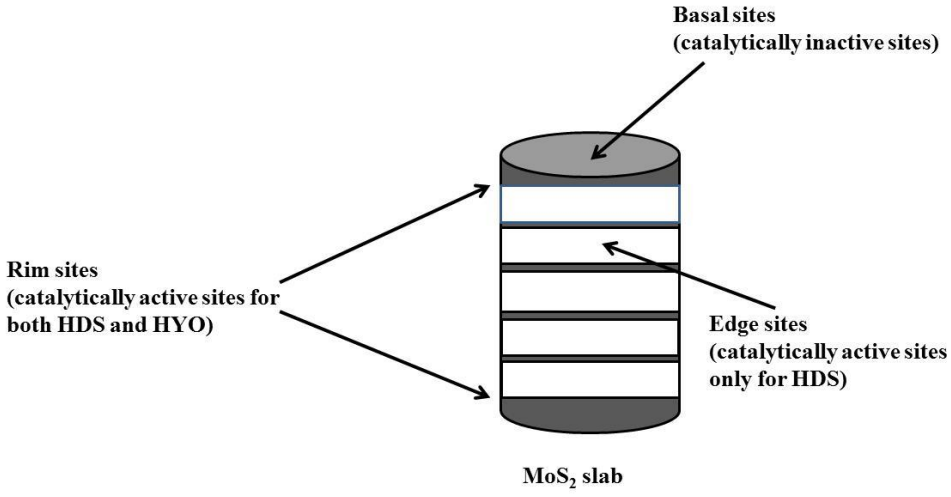

Figure 1.9: Representation of catalytically active sites on MoS_2-based HDS catalyst showing rim-edge for MoS_2 monolayer (Fan *et al*., 2007).

The most accepted model for the active phase was proposed by Tøpsoe *et al*, (1996). Suggested the formation of a new sulfided phase when the promoter (Co or Ni) is incorporated to an active metal

sulfide (Mo or W), denoted CoMoS phase and are responsible for the removal of sulfur (Tøpsoe *et al*., 1996). A study by Han et al. suggested that the existence of two types of structures as Type I and Type II are due to the interaction of the support and the catalyst (Han *et al*., 2016). Type I is associated with a single layer MoS_2 structures and result in incomplete sulfidation of MoO_4 to MoS_2 crystallites. This phase has strong links to the support (Mo-O-Al), hence lowers the activity (Lui *et al*., 2017). Theoretical studies confirmed that the presence of oxygen linkages increase the energy required forming sulfur vacancies. Type II phase has multilayer structure with weak interaction or interacts weakly by van der Waals forces, which gets fully sulfided resulting in greater HDS activity (Lui *et al*., 2017).

Isoda *et al*., (1996) carried out a comparative study on the HDS of 4,6-DMDBT over alumina-supported commercial CoMo and NiMo catalysts. These studies were conducted at a temperature of 270°C, and a H_2 pressure of 3.0 MPa. Under identical experimental conditions, the conversion of 4,6- DMDBT over the NiMo catalyst was 68%, whereas that over the CoMo catalyst was only 49%. (Reinhoudt *et al*., 1999) Conducted a comparative study on alumina based CoMo, NiMo, and NiW catalysts. The Co and Mo contents of the CoMo/ɣ-Al_2O_3 catalyst were 3.0 and 9.5 wt.%, respectively. The NiMo/ɣ-Al_2O_3 catalyst contained 1.4 wt.% of Ni and 7.9 wt.% of Mo. The Ni and W contents of the NiW/ɣ-Al_2O_3 catalyst were 3.0 and 9.5 wt.%, respectively. The HDS experiments were conducted using 4-E (4-ethyl), 6-M (6- methyl) DBT in hexadecane at 390°C and a total pressure of 6.0 MPa. The NiW-based material was found to be more active than the CoMo or NiMo catalyst presumably due to its greater hydrogenation (HYD) capability. The higher activity of the NiW/Al_2O_3 catalyst as compared to that of the CoMo/Al_2O_3 or NiMo/Al_2O_3 catalyst has similarly been reported by (Robinson *et al*., 1999).

In another study conducted by (Lecrenay *et al*., 1998), reported that the CoMoS-based alumina catalyst showed a higher activity for the transalkylation of isopropylbenzene than that of a NiMoS-based alumina catalyst. Each catalyst contained 3 wt. % of promoter metal (Ni or Co) and 10 wt. % of molybdenum oxides. The NiMoS based catalyst was also more active than the CoMoS based one for the hydrogenation of naphthalene. The pseudo-first-order rate constant for the HDS of 4,6- DMDBT (in decane) at 270˚C over the NiMo-based alumina catalyst was approximately double that of the CoMo-based alumina catalyst. This indicated that the HYD property of the NiMo-based material had more influence than the cracking property of the CoMo based catalyst for the HDS of 4,6-DMDBT.

Theoretical studies, particularly those based on DFT calculations have greatly contributed to the understanding of physical/chemical properties of material based on MoS_2 and their relationship with the experimentally observed properties. (Šarić *et al*., 2018) modelled the adsorption of sulfur containing molecules on the S-edge, M-edge, corner edge and basal plane of CoMoS using DFT. They obtained adsorption configurations and energies pointed to a preference towards physisorption at the S-edge and chemisorption in vacancies at the M-edge and corner. Smaller molecules such as thiols were found to prefer vacancies when adsorbing, while larger, sterically hindered molecules such as 4,6-DMDBT prefer physisorption on the brim of the edges or basal plane through van der Waal interactions. They

found that HYD leads to preference towards adsorption at vacancies for thiophene and DBT while for 4,6-DMDBT HYD leads to preferential adsorption on the S-edge brim, and concluded that this might be the reason why 4,6-DMDBT does not get desulfurized directly but follow HYD.

1.2.2 Role of support in hydrotreating reaction

The primary use of the support is for dispersing the active phase of the catalyst and stabilize the MoS_2 based HDS catalyst. It plays a crucial role in affecting the catalytic activity such as influencing the morphology of the active phase, and in modifying the electronic properties and participate in bifunctional reactions with acid sites. A good support consists of; high surface area, optimum pore diameter (5-15 nm), acidity and moderate metal-support interaction. Different support materials show different activity because they consist of their distinct textural, structural properties and the extent of interaction with the active metal. A lot of studies have been conducted on variety of supports such as TiO_2, ZrO_2, silica-alumina, mixed oxides etc. (Carati *et al*., 2003; Duchet *et al*., 1991; Grzechowiak *et al*., 2001). It was discovered that TiO_2 and ZrO_2 show high activity, but their low surface area is a limitation (Caero *et al*., 2003). ZrO_2 small pore size makes it difficult to disperse active phases (Michaud *et al*., 1998), small pore also prevents diffusion of large bulky molecules onto the active sites which leads to pore blockage and a decrease in the catalytic activity. Alumina support (γ-Al_2O_3) is the most used support for HDS catalysts in industries (Xia *et al*., 2003), this is due to its thermal, affordability and chemical stability. A support morphology is crucial in determining the physicochemical properties which influence the catalytic behaviour of the catalyst. The acidity of the alumina support is one of the most important features which control the dispersion of CoMo phases also affect the metal-support interaction Chen *et al*., (2013).

The Bronsted acidity found in the support and helps in isomerization of sterically hindered organosulfur compounds (alkyl DBTs) by overcoming the steric hindrances, thus enhancing HDS activity Breysse *et al*., (2003a). Breysse *et al*, (2008) also showed that the acidity character of the support enhances the catalytic properties of sulfide phase, and an increase in hydrotreating activity is linked to the electron deficient nature of S^{2-} particles in acidic environment. The support needs not to be too acidic or too basic, since too much of either might lead to poor metal-support interactions thus poor Mo dispersion (Valwncia & Klimova, 2011). The basic site of the support also plays a role, it results in better dispersion of MoO_4 and leads to the formation of low coke. Therefore, optimum metal-support interactions are desired to obtain proper sulfidation and dispersion of active species and to generate more type II active phases. The chemical nature of the support material dictates the nature of the active phase.

1.2.3 Role of chelating ligands on HDS reactions

The catalytic activity mostly depends on the structure and the formation of active molybdenum sulfide phases, which influences the activity of the catalyst. The active phase of the catalyst is achieved when the promoter i.e., Co atom is located on the edges and corner of MoS_2 slabs to form CoMoS phases (Kibsgaard *et al*., 2010). Research has shown that during the activation of the catalyst, Mo starts to sulfide at 175 ºC (Coulier *et al*., 2001; Kishan *et al*., 2000), while the promoter starts to sulfide earlier e.g., Co or Ni (50-150 ºC). The promoter will sulfide and form sulfided phases (CoS or NiS) and will interact with the support before Mo starts to sulfide. As a result, chances of the promoter to be located at the corner and edges of MoS_2 will be less, hence leading to the formation of less CoMoS active phases.

The use of organic additives (Chelating agents) influences the sulfidation process and the activity of the catalyst. Chelating ligands are molecules that have two or more donor atoms available to bind a metal cation to form a complex (Sun *et al*., 2003). There are different types of chelating ligands used in catalytic processes to enhance the activity of the catalyst such as: citric acid (CA), ethylene diamine tetraacetic acid (EDTA), glycol, nitriloacetic acid (NTA) etc. Additions of organic additives in the catalysts are used to further improve the performance of the hydrotreating catalysts (Rana *et al*., 2007). According to (De Leon *et al*., 2010; Han *et al*., 2016; Rashidi *et al*., 2013) the nature of the additives imposes changes on the catalyst such as thermal stability, modulate the metal-support interaction, improve the dispersion of metal sulfides, acidity and could generate coordinatively unsaturated (CUS) sites in the catalyst. Such vacancies are thought to be created upon reaction of hydrogen with a surface sulphide group, which leads to the formation of H_2S and an empty coordinated site, this provides the driving force upon extrusion of sulfur from organosulfur compound. CUS are electron deficient they interact with electron donor compounds and adsorb organosulfur compounds which bond to the unsaturated Mo ions creating a metal-sulfur bond and become more active in both pathways. They increase acidity of the support, which exhibits electronic properties of MoS_2 and enhance the hydrogenation activity (Han *et al*., 2017) and favours acid-catalysed reactions such as dealkylation (cracking) and isomerization of alkyl-substituted DBTs thus enhancing the activity and acidity. Isomerization results in more reactive isomers, it also decreases the interaction of the promoter and the support which leads to the formation of multi-layered MoS_2 slabs, resulting in type II phases and these leads to the formation of polymolybdates which are easily sulfided. This agrees with the results obtained by Cattaneo *et al.*, (2000), where the study confirmed this by conducting analysis extended X-ray absorption fine structure (EXAFS) for $CoMo/Al_2O_3$ with and without chelating agents.

It has been reported that the most visible effects of additives occur during sulfidation process. Addition of additives to the catalyst allow the degree of promotion by retarding the sulfidation of the promoter metal (Co), thus inhibiting the formation of inactive phases (Co_9S_8). The use of chelating ligands on

catalysts such as CoMo for hydrotreating has shown positive effect on the activity (Stanislaus *et al*., 2000; Cattaneo *et al*., 1999; Rana *et al*., 2007). According to literature chelating ligands start to decompose above 200 ºC, which leaves the promoter as ions, thus the chances of released promoter ions to move to the edges and corners of already formed MoS_2 slabs are high and result in the formation of more CoMoS active phases (Sundaramurthy *et al*., 2005). Therefore, by delaying the sulfiding temperature of the promoter at a temperature where the active metal is already sulfided allows the formation of more type II CoMoS active phases, which increases the activity.

The effect of chelating agents on HDS activity depends on the quantity and the type of ligand used. EDTA is one of the most used chelating agents in enhancing HDS catalyst, the presence of EDTA helps in the formation of more octahedral MoO_3 (polymolybdates) phases that are easily reducible, which will increase metal dispersion and is favourable during sulfidation of both CoO and MoO_3 as they will start sulfiding at similar temperatures (Badoga *et al*., 2012a) thus resulting in the formation of Type II phases. In the presence of chelating agent, the small amounts of Co oxides are obtained; this is because most of the Co presents complexes with chelating agent (EDTA). Hence does not participate in helping with the dispersion of MoO_3, resulting in the formation of large MoO_3 crystallites. Larger MoO_3 crystallite leads to poor metal dispersion, resulting in reduced metal-support interactions (Badoga *et al*., 2012; Badoga *et al*., 2014). Although EDTA causes poor metal oxide dispersion in oxide state of the catalyst, the metal dispersion improves significantly during sulfidation and this is confirmed by HRTEM and CO chemisorption. At sulfiding temperature above 150 ºC MoO_3 starts to sulfide, these large crystallites break and migrate inside the pores of the support leading to better dispersion as EDTA-Co complex is still stable. At a sulfidation temperature of (200- 220°C) EDTA-Co complex breaks down and release Co ions which help to further improve the dispersion of Mo (Sundarumurthy *et al*., 2005; Dugulan *et al*., 2004).

Citric acid is another chelating agent used in HDS catalysts, its presence improves the dispersion of Mo oxide by forming Mo citrate complexes on the support surface and forms polymolybdate phases and increases the dispersion of the metals, resulting in more type II phases. The addition of CA also increases the degree of promotion by retarding sulfidation of Co, thus inhibiting the formation of Co_9S_8 crystallites. Suarez-Toriello *et al* showed that CA could induce the isolation of impregnated metal species avoiding excessive metal-support interactions and can delay the promoter reduction to high temperatures. Zhang *et al*., (2016) showed that the addition of CA can transform MoO_4^{2-} or β-$CoMoO_4$ species into polymolybdate species and recovers Co^{2+} ions from sub-superficial $CoAl_2O_4$ spinel and therefore induces the formation of more CoMoS sites.

A comparative study was carried out on HDS with catalysts synthesized on SBA-15 support with and without EDTA as a chelating ligand. All the catalysts were synthesized by wet impregnation procedure and dried at 110°C for 5 h. The resulting catalysts were NiMo/SBA-15 (with 12.5 wt.% Mo and 2.5 wt.% Ni) on the catalyst. The catalytic study was conducted at the temperature of 370 ˚C and 8.8 MPa

pressure in bitumen-derived coke light gas oil (KLGO). Sulfided catalysts were designated by CAT 0 (NiMo/SBA-15), CAT 1 (NiMo/SBA-15, EDTA/Ni molar ratio 1), and CAT 2 (NiMo/SBA-15, EDTA/Ni molar ratio 2). For comparison purposes $NiMo/Al_2O_3$ catalysts was also synthesized using wet impregnation method. The conversion of these catalysts is reported in **Table 1.2**. Badoga, (2015) observed that NiMo/SBA-15 (EDTA) catalysts have greater HDS catalytic activity compared to catalysts without EDTA. The sulfur conversion followed the order: CAT2 > CAT1 > CAT 0 > $NiMo/\gamma$-Al_2O_3. The higher activity of CAT 2 catalyst is due to the presence of more EDTA, which forms a complex with almost all Ni present, and it also delays the Ni sulfidation temperature which results in the formation of more dispersed type II NiMoS active phases, hence increases HDS activity (Badoga, 2015).

Table 1.2: HDS activities of $NiMo/\gamma$-Al_2O_3 and CAT 0 to 2 catalysts with KLGO at 370°C (catalyst = 5 cm^3, P = 8.8 MPa)

Catalysts	**% Sulfur conversion**
$NiMo/\gamma$-Al_2O_3	68
CAT 0: EDTA/Ni molar ratio 0	70
CAT 1: EDTA/Ni molar ratio 1	75
CAT 2: EDTA/Ni molar ratio 2	82

From the conversion obtained in **Table 1.2**, it is evident that the beneficial effect of EDTA on hydrotreating activity is because of delay in promoter (Ni)-sulfidation temperature, allowing more molybdenum to be sulfided, and this also reported by (Sundaramurthy *et al*., 2005).

Similarly, Nikulshin *et al*., (2014) conducted a study of different $CoMo/Al_2O_3$ catalysts with and without chelating ligand. The catalysts were synthesized with Co/Mo ratio of (0.16, 0.20, 0.30-0.32), and the four catalysts were impregnated with different chelating ligands (NTA, EDTA, CA and TA). The catalytic tests were conducted on solution containing DBT and 4,6-DMDBT at 240°C and 340°C and total pressure of 3.5 MPa. Studies showed that the addition of chelating agents resulted in more active phase resulting in higher activity; the catalyst containing CA exhibited the highest HDS conversion while the catalyst with no chelating agent resulted in low conversion (**Table 1.3**).

Table 1.3: Investigation of different catalysts in HDS activity.

Catalysts	Co/Mo ratio	Content in the catalysts (wt.%)		Conversion (%)	
		Mo	Co	DBT	4,6-DMDBT
Co_2Mo_{10}/Al_2O_3	0.20	10.0	1.2	19.1	10.1
Co_3[NTA]-Co_2Mo_{10}/Al_2O_3	0.32	10.0	3.2	20.7	23.4
Co_3[EDTA]-$Co2Mo_{10}/Al_2O_3$	0.30	10.1	3.0	22.2	26.6
Co_3[TA]-Co_2Mo_{10}/Al_2O_3	0.30	10.1	3.0	33.3	49.0
Co_3[CA]-Co_3Mo_{10}/Al_2O_3	0.30	10.1	3.0	35.3	51.5

Nitrilotriacetic acid (NTA), Ethylenediaminetetraacetic acid (EDTA), Citric acid (CA) and Tartaric acid (TA)

In another study conducted by Pena *et al.*, (2014), three CoMo/SBA-15 catalysts were prepared by impregnation in the molar ratio Co: EDTA = 1:1 and Co: CA = 1:2. The catalysts were denoted CoMo(x) or CoMo(x)(y) where x = MO_3 wt.% and y = E (EDTA) or C (CA) at the pH = 9 and dried at room temperature for 12 h then dried at 100˚C for 4 h. The catalytic test was conducted on solution containing BDT at 300°C and 7.3 MPa pressure. **Table 1.4** shows different catalysts that were used to investigate the highest activity towards the removal of sulfur in the DBT

Table 1.4: Catalysts with and without chelating agents and their overall conversions towards DBT.

Catalysts	Chelating agent	MoO_3 (wt.%)	CoO_3 (wt.%)	DBT conversion (%)	
				4 h	8 h
CoMo6	-	6	1.5	15.5	37.4
CoMo12	-	12	3	25.2	53.2
CoMo6E	EDTA	6	1.5	33.9	61.9
CoMo12E	EDTA	12	3	38.4	76.5
CoMo18E	EDTA	18	4.5	47.6	91.6
CoMo6C	CA (Citric Acid)	6	1.5	22.2	42.8
CoMo12C	CA	12	3	30.5	61.5
CoMo18C	CA	18	4.5	35.2	77.4

As it can be seen in **Table 1.4** that catalysts with chelating agents exhibit higher conversion (higher catalytic activity) than the ones without chelating agents. The higher activity decreases in the following order: CoMo(x)E > CoMo(x)C > CoMo(x). The effect of the chelating agent depends on the type and quantity of chelating agent used (Cattaneo *et al*., 2000).

The work of Medic & Prins, (1996) focussed on $NiMo/SiO_2$ catalysts using complexing agents. These authors showed that both Ni and Mo could complex to NTA (Medic & Prins, 1996). They concluded

that the MoS_2 dispersion was independent of the presence of NTA and that NTA mainly had a dramatic influence on the sulfidation of Ni. The role of NTA and similar complexing agents is to prevent the sulfidation of Ni at low temperature, and thus increase the formation of the NiMoS phase leading to higher HDS activity (Medici & Prins, 1996). De Jong *et al*., (1996) concluded more precisely that NTA retards the sulfidation of Co to such an extent that the order of sulfidation of Co and Mo changes. As a result, the sulfidation of Co is retarded to temperatures where MoS_2 is already formed (De Jong *et al*., 1996). Shimizu *et al*., (1998) & Ohta *et al*., (1999) extended the use of complexing agents to other complexing agents, e.g., cyclohexane diamine tetra-acetic acid (CyDTA), and other catalysts, e.g., NiW. They concluded that by using complexing agents the dibenzothiophene HDS activity of $CoMo/Al_2O_3$ and NiW/Al_2O_3 increases in the order NTA < EDTA < CyDTA (Shimizu *et al*., 1998); (Ohta *et al*., 1999). It was also found that the complexing agents had little effect on the activity of $NiMo/Al_2O_3$ (Shimizu *et al*., 1998); (Ohta *et al*., 1999). The authors concluded that complexing agents interact strongly with Co (or Ni), thereby preventing Co (or Ni) from interacting with Mo (or W) or Al_2O_3 (Ohta *et al*., 1999).

Furthermore, it was concluded that pre-formation of a MoS_2-like structure was necessary to induce the promoting effect (Ohta *et al*., 1999). However, these authors could not explain the small effect of complexing agents on $NiMo/A_{l2}O_3$. These numbers, which represent the stability of the metal-agents complex, are only slightly higher for Ni than for Co. Hence, one would expect similar effects of these complexing agents on Co- and Ni-promoted catalysts. Reports by Cattaneo *et al*., (1999) & Cattaneo *et al*., (2000) confirmed this, by showing that EDTA, which retards the sulfidation of Ni to somewhat higher temperatures than NTA, leads to a higher activity than NTA for $NiMo/SiO_2$ catalysts. They found also that using ethylene diamine (ED) as complexing agent results in highly active catalysts (Cattaneo *et al*., 1999; Catttaneo *et al*., 200). However, the Ni-ED complexes were found to be highly unstable, which resulted in sulfidation of Ni at very low temperature, which seems in contradiction with all results described above (Cattaneo *et al*., 1999; Cattaneo *et al*., 2000). Medici & Prins, (1996) showed that chelating agents, like NTA, prefer complexation with Ni^{2+} and MoO_4^{2-} does only form complexes when all Ni-ions are complexed to NTA. The same accounts for EDTA. This shows that the addition of additives leads to higher HDS activity, by promoting electronic properties of the catalysts. Nanosized materials further provides unique electronic and chemical properties that were not observed in bulk catalysts, hence will further improve the catalytic activity even further. It is well known that the critical challenge in producing fuels of ultra-low sulfur is the complete removal of refractory sulfur-containing compounds with steric hindrance such as alkyl derivatives for DBT. Nanoparticles exhibit novel properties which are different from the bulk material's properties. It develops unique electronic and chemical properties that are not observed in bulk form of the material. In recent years, the advancements in nanoscience and nanotechnology have brought a revolution in the field of catalysis. The key objective of nanocatalysis research is to produce 100 % selectivity, extreme high activity, low energy

consumption, and long lifetime. This can be achieved by controlling the size, shape, special distribution, surface composition and electronic structure, and thermal and chemical stability (Oro and Clever, 2008; Bayram *et al*., 2010).

Nanomaterial produces ultra-small bimetallic clusters on the support (Singh, Kunzuru, & Sivakumar, 2016), and this can be concluded that the higher activity of nanoclusters on the support maybe due to the better dispersion or smaller particle size compared to the non-nanocatalyst. The smaller crystal size results to a greater number of CUS sites, these anion vacancies or CUS sites are responsible for HDS catalytic activities, hence nanoparticles on alumina supported catalysts showed higher activities (Murali *et al*., 2003). Nanomaterials also have properties that are useful for enhancing reactivity, durability, and surface-to-volume ratio (Law *et al*., 2004; Gao & Goodman, 2012), which plays a role in the reactivity of solid catalyst. According to Singh *et al*. 2016 they increase the probability of formation of surface defect such as kinks, corners having under coordinated surface sites which contributes to increasing catalytic activity and they are easily reducible and sulfidable. Therefore, smaller active metal particles are expected to be catalytically more reactive due to their high surface area and can be created at an environment milder than in the industrial conditions.

1.3 Knowledge gaps

From the above, it can be concluded that there are still many unresolved questions and a lot of contradictions concerning the use and role of complexing agents. One of the concerns is the exact role of the complexing agent on HDS catalyst activity. Secondly, the effects of complexing agents on catalyst dispersion have not been reported.

Furthermore, the electronic properties of chelating ligands coordinated to catalyst sites Mo and promoters such as Co, Rh, is not clear from experimental and theoretical viewpoint due to limited literature. The combined effects of support Al_2O_3, and chelating ligands (citric acid (CA), EDTA and acetic acid (AA) on the activity of CoMo and RhMo hydrotreating catalyst have not been studied in detail. Therefore, the study seeks to address these gaps.

1.4 Hypothesis

1. Addition of chelating ligands will enhance the following: the active metal dispersion, the formation of more octahedral MoO_3, the amount of type II Co (Rh)-Mo-S phases and give optimum metal support interactions.

2. The use of Co (Rh) as a promoter will lead into more metal dispersion, will also lead to more interaction with the chelating ligands which will affect metal-support interactions resulting in further enhancement of type II Co (Rh)-Mo-S phases. Additionally, chelating ligands will boost HDS activities.

3. Chelating ligands such as EDTA, AA and CA will help in multiple stacking of MoS_2 active phase, resulting in enhanced hydrogenation reactions. This will improve HDS activities and optimize metal support interaction.

1.5 Research questions

1. Will the chelated catalysts influence catalytic activity?

2. Which of the chelated catalysts will yield the highest activity?

3. Will the theoretical study on the electronic properties of the catalysts help in explaining different HDS activity obtained by the catalysts?

1.6 Aim and objectives of the research

The study is aimed at synthesizing and characterizing well-defined chelated Co-Mo and Rh-Mo nanocatalysts that have an exceptionally high site-specific activity for hydrogenative desulfurization of model fuels. The specific objectives were to:

(i) synthesize various unsupported and supported (with alumina) nanocatalysts containing varying composition of mixed precious - base metal and chelating ligands;

(ii) characterize the active phases of various catalysts (Oxides and Sulfided using FTIR and UV-Vis) spectroscopies, TGA-DSC, BET, PXRD and SC-XRD, ICP-OES, EDX, XPS, SEM and TEM;

(iii) study the influence of chelating agents (CA, AA and EDTA) on HDS of dibenzothiophene (DBT);

(iv) conduct theoretical study on the electronic properties of the single crystal catalyst obtained using Density Functional Theory (DFT) calculations;

(v) test the most active catalyst in a simulated model fuel.

1.7 Structure of the dissertation

In this dissertation, various catalysts were synthesized, characterized, and tested for the hydrotreating of model fuel in a Parr reactor under industrial hydrotreating conditions. The results from various characterization techniques were analysed and explained to correlate the corresponding catalytic activities. To accomplish the research objectives, the work was divided into four phases. This thesis is comprised of 6 chapters which describes the research outcomes for each phase.

Chapter 1 focuses on the effect of the presence of organosulfur in fuel oil and the effect it has on the environment. It further gives a review that deals with interpretations put forward in literature with regarding to the periodic HDS activity trends of the various transition metal sulfide (TMS). The focus is on the metal-sulfur bond energy, different HDS mechanism are also discussed in this chapter and HDS mechanisms. This chapter also discusses the role played by chelating ligands on HDS catalysts and how it affects the HDS activity.

Chapter 2 discusses the instruments used for characterization in this project. The principles and applications of the important characterization technique used in this work are explained briefly. The method of preparation and catalytic applications used is briefly discussed.

Chapter 3 discusses CoMo related catalysts, and the effect caused by the addition of chelating ligands on the catalysts. Addition of chelating ligands were seen to have beneficial effect on hydrotreating activity, especially CA. It was shown that both EDTA, AA and CA play a major role in redispersion of active phases during sulfidation and favors the formation of octahedral molybdenum oxides.

The examined the effect of metal (Rh) with and without chelating ligands are discussed in **Chapter 4.** In this chapter during catalysts synthesis rhodium is used as a promoter and the research outcomes and discussion of this phase are presented.

Chapter 5 summarizes the findings (conclusion) of the entire research project and provides recommendation for future work.

Chapter Two

Experimental

2.1 Materials and Chemicals

All chemicals used were obtained from Sigma-Aldrich. Cobalt(II) nitrate hexahydrate (98%), ammonium heptamolybdate (99%), rhodium(II) chloride (98%), ethylenediaminetetraacetic acid (EDTA), citric acid monohydrate (99.5%), acetic acid (99%), heptane, benzothiophene (98%), dibenzothiophene (98%), 4,6-dimethyldibenzothiophene (97%), Gamma alumina support (γ-Al_2O_3).

2.1.1 Synthesis of EDTA, CA and AA chelated catalysts

(i) Synthesis of Alumina support catalysts

For uncalcined catalyst: $Co(NO_3)_2.6H_2O$ (1.00 mMol) or $RhCl_3$ (1.00 mMol) and $(NH_4)_6Mo_7O_{24}.4H_2O$ (2.00 mMol) was added in 30 mL deionized water with (Co (Rh)/Co (Rh) + Mo) 0.33 molar ratio. The pH was adjusted to pH = 9 and the solution was added to the γ-alumina support (1 g), and the resulting mixture was transferred into a Teflon-lined stainless-steel autoclave, and then hydrothermally treated at 453 K for 4 h. The product was filtered and washed using deionized water and dried at 393 K for 12 h and calcined at 773 K for 4 h.

(ii) Synthesis of Chelated alumina support catalysts

For chelated catalysts: 1 g of Calcined alumina support (773 K) was impregnated (wet impregnation method) with a solution of $Co(NO_3)_2.6H_2O$ (1.00 mMol) or $RhCl_3$ (1.00 mMol), $(NH_4)_6Mo_7O_{24}.4H_2O$ (2.00 mMol), EDTA (1. 00 mMol), CA (2.00 mMol), and AA (2.00 mMol). The following molar ratios were used; Co: EDTA 1:1, Co: CA 1:2, and Co: AA 1:2 (Peña *et al*., 2014). The starting materials were added in 20 mL deionized water with (Co/Co +Mo) with the molar ratio of 0.33 (Chen *et al*., 2019; Castillo-Villalón *et al*., 2015). The pH was adjusted with ammonia solution to pH = 9, and the resulting solution was impregnated on the alumina (γ-Al_2O_3) support (1 g) for 4 h and dried at room temperature and then at 393 K overnight.

(iii) Catalyst sulfidation and hydrodesulfurization measurements

Before hydrodesulfurization the oxide catalyst was sulfided using 5 wt.% of CS_2 in 100 mL heptane, and the reaction was carried on in 4 MPa H_2 and 573 K for 4 h. The hydrotreating of model fuel was performed in a Parr reactor operating at typical industrial conditions. The model fuel consisted of 374 ppmS in dibenzothiophene (DBT). The details of the reactor set up are mentioned in Section 2.2.10.

Prior to catalytic test, the catalysts (2 g) were sulfided using 100 mL heptane solution-containing 10 wt.% of CS_2 under hydrogen pressure of 4.0 MPa with the temperature of 573 K and maintained 4 h to

ensure complete sulfidation. The sulfided catalysts (in original size) were recovered by filtration and dried. After sulfiding, HDS studies of the catalysts were performed in 100 mL of heptane containing (0.22 g) DBT under H_2 pressure of 4.0 MP with 573 K and maintained for 6 h. The samples (DBT product) were collected for further analysis. The conversion of DBT and selectivity was determined using GC-MS. GC conditions for determination and quantification of oxidation products were carried out by using a ZB-5MSi capillary column (30 m x 0.25 mm x 0.25 μm). Helium was used as carrier gas at a flow rate of 1.63 mL min^{-1} with an average velocity of 30.16 cm. sec^{-1} and a pressure of 63.73 KPa. The analysis run was started with an oven temperature of 313 K ramping to 573 K @ 15°C min^{-1}.

The hydrotreating reaction setup is shown in **Figure 2.1**. DBT model fuel together with the catalyst was added on the Parr reactor and sealed. The setup consists of a mass flow controller was used to regulate the hydrogen flow. Before the reaction take place, the sample liquid was purged three times and the H_2 was set to a desired amount to reach the maximum pressure required. The Parr reactor has tubes connected to it, where water is passed through the reactor to cool the magnet of the reactor. The reactor was heated to the desired temperature and speed.

Figure 2.1: Hydrotreating reaction experiment setup for Parr reactor.

2.2. Instrumentation

A range of characterization techniques were employed to gain understanding of the physicochemical and chemisorption characteristics of the prepared catalysts, and correlate these to the observed behaviour of the catalyst during catalytic activity evaluations. The characterization techniques are outlined in this chapter.

2.2.1. N_2 adsorption–desorption isotherms

The total surface area of the catalysts at which reactants will be exposed is measured by physical adsorption, namely physisorption (Vasquez, 2007; Anderson and Pratt 1985). It is used to measure the surface area due to its reversibility, as it exhibits low heats of adsorption that prevents structural changes of the surface (Lowell *et al*. 2004). The method used to quantify the surface area was Brunauer Emmett and Teller (BET) which is an extension of Langmuir's studies of absorption. Langmuir described the type I isotherm as an absorption limited to a monolayer. This type is presented in **Figure 2.2**, which resembles a concave curve at low P/Po and reaches a maximum when approaches a value of 1 (Lowell *et al*. 2004).

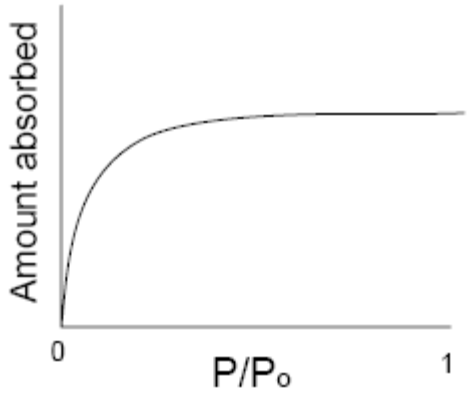

Figure 2.2: Type I isotherm (Vasquez, 2007).

The BET method allows the study of multilayer absorption using the following equation (Vasquez, 2007; Anderson and Pratt, 1985):

$$n^s = \frac{n_m^s + C\ p}{(p_o - p)[1 + (C-1)]\,{}^{p}/_{p_o}}$$

where n^s is the amount of gas absorbed at equilibrium pressure p, with a partial pressure of the absorbate po, $n^m{}_s$ is the total amount of absorbate in the monolayer, while C represents a constant that depends on the adsorbate heat of adsorption. The BET equation can be written as:

$$\frac{p}{n^s(p_o - p)} = \frac{(C-1)}{n_m^s C p_o} + \frac{1}{n_m^s C}$$

To use this equation low p_o values must be used so that it forms a straight line when,

$$\frac{p}{n^s(p_o - p)}$$

is plotted against p/p_o. Therefore, it is possible to obtain the surface area of the material measured by the quantification of the adsorbate on the monolayer with a known area per molecule.

The BET surface area, pore volume, and pore size distribution of the samples were measured with a Micrometrics ASAP 2000 instrument using low temperature N_2 adsorption-desorption isotherms. Prior to analysis, the samples were degassed in vacuum at 80°C. The surface area was computed from these isotherms using multi-point Brunauer-Emmett-Teller (BET) method based on the adsorption data in the partial pressure P/P_0 range from 0.01 to 0.2. The mesoporous volume was calculated from the amount of nitrogen adsorbed at $P/P_0 = 0.95$, assuming that the adsorption on the external surface was negligible compared with adsorption in pores. The pore diameter and pore volume were determined using the BJH method. In all cases, correlation coefficients above 0.999 were obtained.

2.2.2. X-ray diffraction (XRD) analysis

X-rays are created by a fast deceleration of any electrical charged particles such as high kinetic energy electrons. Electrons are produced in different ways; by utilizing an x-ray tube where electrons are produced, creating a high voltage between two electrodes. The electrons are then driven to the anode or target, where the sample is located (Cullity and Stock, 2001). Copper was used as the anode. X-rays are created with the impact of the electrons on the sample, and the x-ray scattered are measured and analysed. The material and crystal shape are determined by the position, intensity, and the shape of the peak shown (Krawitz, 2001). **Figure 2.3** shows how the x-ray diffraction diffracts is analysed. The diffraction angle and interplanar spacing are represented by θ and d', respectively while A, B, A' and B' represent the wavelength. The peak recorded at the angle 2θ, and its intensity is unique of each material (Krawitz, 2001).

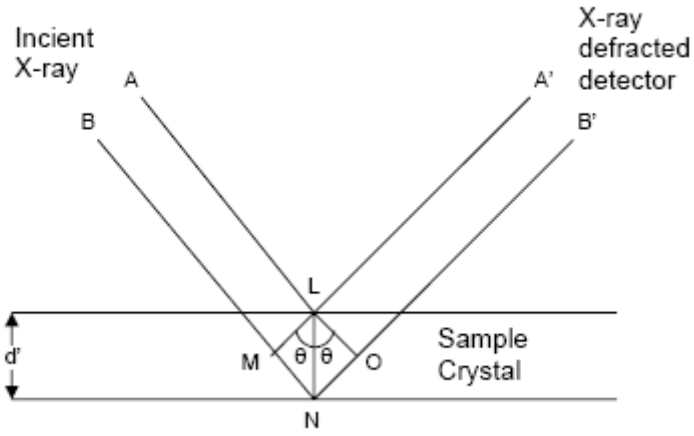

Figure 2.3: X-ray Diffraction (Krawitz, 2001).

X-ray diffraction (XRD) was conducted for crystalline identification, the measurements were performed on a Burker UXS D8 Focus X-ray Diffractometer with a Cu source of X-ray. The measuring wavelength was 0.1506 nm, while the survey measurement was scanned from 10-70 degrees with 0.02-degree increment at the scanning speed of 1 sec/step. The textural properties of the catalysts were measure by adsorption of nitrogen at 77 K using a Micrometrics ASAP 2000 instrument. The samples were degassed at 200 ˚C before the analysis.

The Powder-XRD studies were mainly carried out to identify various phases present in the catalyst samples. This is done by comparing the observed X-ray diffraction patterns with the standard JCPDS (Joint Committee on Powder Diffraction Standards) data files and various phases can be identified. The phenomenon of diffraction comes from the interaction of X-rays with the periodic structures of polycrystalline materials. In conducting this technique, a fixed wavelength is chosen for the incident radiation and Braggs peaks are then measured by observing the intensity of the scattered radiation as a function of scattering angle 2θ. Bragg's equation (eqn1) is used to calculate the d-spacing from the values of the patterns observed.

$$n\lambda = 2dsin\theta \ldots\ldots\ldots\ldots 1$$

Diffraction studies provide information related to the structure, its allotropic transformation, transformations, transition to different phases and purity of the substance. The average particle sizes of the crystals were determined using Scherrer's equation2:

$$T = \frac{K\lambda}{\beta Cos\theta} \ldots\ldots\ldots\ldots\ldots 2$$

where:

T = Average particle size λ = X-ray wavelength

K = Shape factor (0.9) β = Line broadening at half the maximum.

θ = Bragg's angle

For XRD analysis measurements were performed using a multi-purpose X-ray diffractometer D8-Advance from Bruker operated in a continuous scan in locked coupled mode with Cu-K_α radiation. The samples were mounted in the center of the sample holder on a glass slide and levelled up to the correct height. The measurements run within a range in 2ϑ defined by the user with a typical step size of 0.034° in 2ϑ. A position sensitive detector, Lyn-Eye, was used to record diffraction data at a typical speed of 0.5 sec/step which is equivalent to an effective time of 92 sec/step for a scintillation counter. The wide-angle scan was made from 2θ = 5-80˚.

2.2.3. Inductive coupled plasma-optical emission spectroscopic analysis (ICP-OES)

A Perkin Elmer SCIEX Elan-6100 ICP-OES AS-90 with auto sampler was used to determine the concentration of cobalt, molybdenum, and rhodium solutions. ICP-OES consists of a plasma source which generates mono charged ions. The following procedure was used to quantify estimated elements of the sample. A sample (0.1 g) was dissolved in 5 ml concentrated nitric acid at a temperature of 80 ˚C for 3 days. After cooling, samples were further dissolved in 100 mL of Millipore water to make 5% of nitric acid solution by volume and to ensure the final dissolution of the metals. The final solution was filtered with 0.55 µm filter and analyzed.

2.2.4. Fourier transform infrared spectroscopy (FT-IR)

The FT-IR spectroscopy shines a beam containing many frequencies of light at once and measures how much of the beam is being absorbed by the sample. This instrument is used for identifying different types of chemical bonds present in a molecule by producing an infrared absorption spectrum that is like a molecular fingerprint. By interpreting the infrared absorption spectrum, the chemical bonds in a molecule can be determined. FT-IR spectrometers can be used for metal, organic synthesis. The spectra of IR for organic compounds have two areas, viz: the functional group region within 4000 - 1500 cm^{-1} and the fingerprinting region within 1500 - 400 cm^{-1} (Oyagi 2012; Ingle & Crouch, 1988; Malifetsane, 2015) while the functional groups for metals are obtained within a region of 500-1000 cm^{-1}.

FTIR spectrometer components consist of a source, interferometer, sample compartment, detector, amplifier, A/D converter, and a computer. During analysis, the source generates radiation which passes the sample through the interferometer and reaches the detector. Then the signal is amplified and converted to digital signal by the amplifier. The signal is then transferred to a computer in which Fourier transform is carried out. The main advantage of Infrared absorption spectroscopy is that it is capable to

analyse all gas, liquid, and solid form samples. Other several advantages of FTIR include the accuracy of wavenumber is high, and the error is within the range of ± 0.01 cm^{-1}. The scan time of all frequencies is short (approximately 1 s). The resolution is extremely high (0.1 ~ 0.005 cm^{-1}). The interference from stray light is reduced. Because of such advantages, FTIR Spectrometers have replaced dispersive IR spectrometers (Ingle & Crouch, 1988).

FT-IR indicates a fingerprint of a sample with absorption peaks which corresponds to the vibration frequencies between the bonds of the atoms. Each material is a unique combination of atoms, no two compounds produce the exact same IR. Hence, using this technique one can conduct qualitative analysis of different materials. This method can be used to measure solid, liquid, or gaseous samples that are in the beam of infrared light.

2.2.5. Ultraviolet-visible for Ultraviolet-Visible (UV-Vis) Spectroscopy

UV-Vis studies were done using Shimadzu UV-3100. Ultraviolet-visible (UV-Vis) spectroscopic analysis is normally carried out in solutions, but it also possible to study solids and gases. The wavelength of the electromagnetic spectrum covered by the UV-Vis region is 200 - 800 cm^{-1}. The energy associated with this region is in the form of electronic transitions from ground state to excited high energy state. The concentration of compounds that absorb light in the ultraviolet to the visible range is determined using the Beer-Lambert law. The Beer-Lambert law states that the absorbance of a solution is directly proportional to the concentration of the absorbing species in the solution and the path length (Oyagi, 2012).

Malifetsane, 2015 stated that the absorption of UV-Vis radiation corresponds to the excitation of the outer electrons, which are either bonding forming sigma (σ) or pi (π) bonds, or non - bonding lone pair electrons (n). Absorption of UV-Vis radiation in molecules is restricted to certain functional groups containing valence electrons of low excitation energy. There are four possible types of transitions (π–π*, n–π*, σ–σ*, and n–σ*), and they can be ordered as follows: σ–σ* (sigma to sigma star transition) > n–σ* (n to sigma star transition)> π–π* (pi to pi star transition) > n–π* (n to pi star transition), (Oyagi, 2012; Malifetsane, 2015). The possible electronic transitions involving σ, π and n electrons are shown in **Figure 2.4** (Malifatsane, 2015).

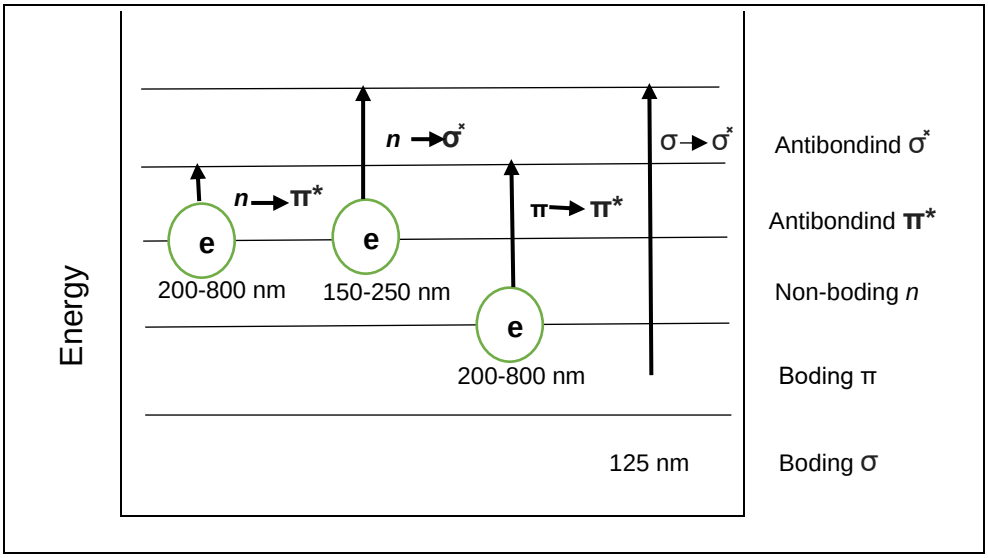

Figure 2.4: Electronic transitions present in UV-Vis at different wavelengths (Malifatse, 2015).

The Ultraviolet-Visible (UV-Vis) spectra for $CoMo/Al_2O_3$, $CoMo\text{-}x/Al_2O_3$ (where x = EDTA, CA, AA) and $RhMo/Al_2O_3$, $RhMo\text{-}x/Al_2O_3$ (where x = EDTA, AA, CA) were recorded on a Shimadzu UV-3100 and the samples were collected. The solid was put in a Quartz cuvette and ran at a wavelength range of 200-800 nm. The Ultraviolet-Visible (UV-Vis) spectra for $CoMo/Al_2O_3$, $CoMo\text{-}x/Al_2O_3$ (where x = EDTA, CA, AA), $RhMo/Al_2O_3$, $RhMo\text{-}x/Al_2O_3$ (where x = EDTA, AA, CA) and $RhV/Al_2O_3$and $RhV\text{-}x/Al_2O_3$ (where x = EDTA, CA, AA) were recorded on a Shimadzu UV-3100. The solid was put in a Quartz glass holder and ran at a wavelength range of 200-800 nm.

1. The instrument was switched on and left to initialize for about 10 minutes.
2. Baseline correction was done using empty glass for every analysis as the blank and the instrument was set to run between the wavelengths of 200 to 800 nm.
3. Glasses were cleaned with acetone.
4. The procedure was repeated for all samples.

2.2.6. Energy dispersive X-ray spectroscopy

EDX is used for the qualitative and quantitative elemental analysis of solid samples, with each elemental analysis having a unique electron configuration. Hence, the energy and the intensity of the X-rays emitted will be dependent on the composition of the solid sample. The equipment is attached to the SEM allow for elemental information to be gathered about the sample being investigated. The technique is non-destructive and has a sensitivity of > 0.1 % for each element heavier than carbon. In EDX the sample is coated with gold, a beam of electron interacts with a solid surface by means of ionization and ejects an inner shell electron. The resultant vacancy is filled by an outer electron, which release its energy either via an Auger electron or emitting an X-ray. This produces characteristic lines in the X-

ray spectrum corresponding to the electron transitions involved. Therefore, since these lines are specific to a given element, the composition of the material can be deduced. TESCAN Vegas TS 5136LM SEM will be used for the analysis at 20 kV.

2.2.7. X-ray photoelectron spectroscopy

X-ray photoelectron spectroscopy (XPS) measurements were performed with a Kratos Axis Ultra X-ray Photoelectron Spectrometer equipped with a monochromatic Al K_α source (1486.6 eV). The base pressure of the system was below 3×10^{-7} Pa. XPS experiments were recorded with 75 W power source using hybrid-slot spectral acquisition mode and an angular acceptance angle of +/-20°. XPS data analysis was performed with Kratos version 2 program. To determine atomic composition of the material's surface composition XPS is used. Upon exposure to X-ray photons, a surface emits photoelectrons and obtained binding energies can be compared to known values to identify the elements of interest and their bonding.

2.2.8. Thermogravimetric Analysis- differential scanning calorimetry (TGA-DSC)

This technique is used to determine the thermal stability of a sample, it measures the amount of rate of change in the weight of the material of interest as a function of temperature in a controlled environment. The determination of thermal stability requires monitoring of the weight loss that occurs during heating at different temperatures. The TGA-DSC used to analyze samples for this research (Perkin Elmer Thermo-gravimetric Analyzer (TGA 4000)). Samples were analyzed in the temperature range from 40-900˚C, at a heating rate of 15 ˚C/ min and gas flow rate of 20 mL/min.

2.2.9. Scanning electron microscopy (SEM)

SEM is generally used for morphological characterization of the catalyst particles such as particle size, shape, surface structure and porosity. Images obtained by SEM are produced from secondary electron beam. The samples should not be transparent to electron transmission. Electrically scattered secondary electrons are emitted caused by the electron impact which creates a volume of primary excitation. These secondary electrons have low energy which will be near the surface and can be emitted outward in all directions. An electron detector system is used to collect both types of emitted electrons and produce a signal proportional to their intensity. The samples are mounted on a silver sample holder with the help of tan adhesive to make the sample surfaces conductively. 20 kV accelerating voltage with different magnification is used to record SEM images.

To investigate the surface morphology and shape of the catalyst SEM was used. The samples were placed in a sample holder covered with a carbon tape to hold the sample. This study was conducted under TESCAN Vegas TS 5136LM SEM and it was operated at 20 kV at 20 mm working distance. The SEM images were taken at magnifications; 10, 20, 50 and 100 µm.

2.2.10. Transmission electron microscopy (TEM)

TEM is a microscopic system which transmits a beam of electrons through a sample to form an image. The electrons behave as a light source with much lower wavelengths making it possible to obtain resolutions a thousand times better than using light microscopes. As the beam is being transmitted through the sample, the electrons interact with a sample (suspended on a grid) to form an image. And imaging devices such as a fluorescent screen, the layer of photographic film or sensors like charge-coupled devices (CCD) are used to focus and magnify these images. CCD is a device for the movement of electrical charge, usually from within the device to an area where the charge can be manipulated (Skoog *et al*. 1992, Oyagi, 2012). TEM helps in investigating the morphology and dispersion of the materials. It provides direct images of the catalyst's structure, enabling accurate particle size distributions to be determined, it also provides information about the deposition of the supported particles. A small amount of each sample was ultrasonically suspended in ethanol and a small drop of the suspension was transferred onto a SPI-copper grid and allowed to dry prior to analysis under the microscope (Dlamini, 2018).

TEM was used to determine the morphology, particle size and dispersion of all catalysts. A small amount of each sample was ultrasonically suspended in methanol and a small drop of the suspension was transferred onto a SPI-carbon copper grid and allowed to dry prior to analysis under the microscope.

2.2.11 Single crystal X-ray diffraction (SC-XRD)

Single crystals of unsupported CoMo-AA and CoMo-EDTA was prepared by taking the mixture solution used during impregnation, the solution was filtered to obtain a clear solution. Suitable crystals of CoMo-AA and CoMo-EDTA suitable for SC-XRD were obtained through slow evaporation of the solution. SC-XRD data of CoMo-AA and CoMo-EDTA were collected at 200 K on a Bruker APEX II CCD diffractometer with graphite monochromated MoKα radiation using APEX2 data collection software and SAINT (Bruker, 2010) for cell refinement and data reduction. The structures were solved by dual-space methods applying SHELXT-2018/2 (Sheldrick, 2015) and refined by least-squares procedures using the numerical method implemented in SADABS (Bruker, 2010). All non-hydrogen atoms were refined anisotropically, and the carbon-bound hydrogen atoms were added in idealized geometrical positions in a riding model. The crystal structure diagrams were drawn with ORTEP-3 for

windows (Farrugia, 2012). Nitrogen bound hydrogen atoms were located on the difference Fourier map and allowed to refine freely when possible. The hydrogen atoms of the water molecules were also located on the difference Fourier map and refined with bond length and angle restraints.

2.2.12 DFT calculations

The molecular structure of Co-AA and Co-EDTA as obtained from single crystal data were optimized by the DFT method using B3LYP functional combined with LANL2DZ/6-311G++(2d,2p) basis sets, respectively. For non-metallic atoms (O, N, C, H) and metal atom (Co, Mo) basis sets 6-311G++(2d,2p), and LanL2DZ were used (Becke, 1993). Calculations were carried out using Gaussian 16 (Frisch et al. 2016). Optimization, and quantum molecular descriptors were given full consideration. Optimized molecules were obtained with Chemcraft visualization program. Quantum molecular descriptors such as ionization potential (*I*), electron affinity (A), chemical potential (μ), electronegativity (χ), global hardness (η), global softness (S) and global electrophilicity (ω) values were calculated using the frontier molecular orbital properties (HOMO and LUMO energy values) by using the following equations (Saravanan & Balachandran, 2014; Polizer & Abu-Awwad, 1998):

Ionization potential (I) = $-E_{HOMO}$ (1)

Electron affinity (A) = $-E_{LUMO}$ (2)

Absolute electronegativity (χ) is related to average value of HOMO and LUMO energies defined by Mulliken (Mulliken, 1934).

Electronegativity $x = \frac{I+A}{2}$ (3)

The softness (*S*) is reciprocal of the hardness (η) (Hoffmann, 1988)

Global hardness, $\eta = \frac{I-A}{2}$ (4)

Global softness, $S = \frac{1}{\eta}$ (5)

Parr *et al*., 1999 defined global electrophilicity index (ω) (Parr *et al*., 1999)

Electrophilicity index $\omega = \frac{\mu^2}{2\eta}$ (6)

where μ is the chemical potential takes the average value of ionization potential (*I*) and electron affinity (*A*) (Padmanabhan *et al*., 2007).

Chemical potential $\mu = -(\frac{I+A}{2})$ (7)

Chapter Three

Hydrotreating of DBT using mesoporous alumina supported CoMo catalyst chelated with EDTA, CA and AA

3.1 Introduction

It is well established that the combustion of fossil fuels causes emission of harmful gases and compounds into the atmosphere that produce long-term disease in living organisms and cause greenhouse effect. The causes of the most concern for pollution in our environment are the emissions of SO_x and CO_2 particulate matter. SO_x gases reduce the efficiency of plant units and sever corrosion of the reactors (Saleh, 2016; Ahmad, 2013). In order to alleviate their impact, stringent environmental regulations have been introduced in many developed countries to reduce sulfur and aromatic contents in the transportation of fuels with the aim of lowering harmful exhaust emissions and enhancing air quality. The relatively low sulfur (< 10 ppmS) concentrations that needs to be achieved in transportation fuels to necessitate the ultra-deep treatment of the fuel feed stream. This is a highly demanding and energy intensive process because the global market for fuel is steadily increasing whilst the quality of the feed streams available is markedly declining; alternative raw materials may need to be processed to meet the ever-increasing additional demand of ultraclean fuel required for transportation (Okamoto, 2014; Stanislau *et al.*, 2010). Therefore, developing advanced hydrotreatment catalysts is of paramount importance not only to reduce some environmental pollution but to also upgrade the process of low-grade feedstock.

Catalytic hydrotreating is the most common mature technology by petroleum refineries to reduce the sulfur levels in fuel. Catalyst used in hydrotreating consists of at least two elements from the group VI and VIII of the periodic table such as W or Mo as the active metal and Ni or Co as the promoter. Transition metal sulfide (TMS) are the cornerstone of hydroprocessing industry due to their innate stability and their catalytic active phases (Sareen & Bhattacharya, 2016). Co(Ni)Mo/Al_2O_3 catalysts are the most widely used catalysts in conventional HDS. Choices of the active metal and promoter are based on the catalytic reactions used for. Studies has shown that Mo based catalysts promoted with Co works best for HDS, while Ni as a promoter favours HDN (Sadhartha, 2011). For the catalyst to be activate it must undergo sulfidation, where oxide metals get converted in sulfide phases and the most desired phase to be formed is MoS_2 which favours the formation of the active phase Type II CoMoS. The CoMoS structure has been recognized as the active structure in the CoMo/Al_2O_3 catalysts firstly proven by Topsoe *et al*., 1981. Alumina (Al_2O_3) support has been widely used for HDS catalyst due to its desirable mechanical and textural properties, low cost and well dispersion of active metals (Badogga, 2012; Xai *et al*., 2013). However, it shows strong interaction with the active metals (Mo, Co). The OH group

present on the surface of this support strongly interacts with molybdenum oxide which leads to the formation of tetrahedral co-ordination of molybdenum species with Mo oxide monolayer (Qu, 2003). Formed monolayers get strongly bounded tetrahedral molybdenum oxides and this shows resistance towards Mo reduction or sulfidation as compared to Mo reduction when its octahedrally coordinated (Badogga, 2015). This leads to incomplete sulfidation, resulting in less formation of the active MoS_2, and this affects the catalytic activity (Badogga *et al*., 2015). Studies have shown that the addition of chelating ligands to the impregnation solution during the preparation of the HDS catalyst have significant improvement in the catalytic activity (Stanislaus, 2006). The use of chelating agents leads to weak metal-support interactions forming large MoO_3 crystallites, which are easy to sulfide (Bui *et al*., 2019). This is because the chelating agent interacts with the support *via* OH group. In addition, the presence of chelating agents helps in the formation of Mo oxide in octahedral structures, which are easily reducible (Smegal *et al*., 2013; Klimova, 2014). The use of chelating agent favors the formation of stable complex with Co or Ni and during sulfidation at above 200°C, the chelating agent start to decompose, leaving Co (Ni) as cations, hence allowing them to move to the edges and the corners of the already formed MoS_2 slabs forming more active phases (Type II CoMoS) (Sundaramurthy *et al*., 2005; Dugulan *et al*., 2004). Through the formation of Mo and/or Co complexes with the chelating agents, the improved HDS catalytic activity has been ascribed to (i) lower formation of cobalt aluminate and (ii) modification of the sulfidation of Co and Mo (Blanchard *et al*., 2016). Therefore, the formation of Co-chelating ligand complex results in the delay of sulfidation of the promoter to higher temperatures where Mo has already started to sulfide, resulting in an increase in catalytic activity.

The synthesis, characterization, and catalytic performance of alumina-supported Co-Mo citrate in the ultra-deep HDS reaction of straight-run gas oil were examined Klimova *et al*., (2010). The oxidic catalyst metal precursors consist of Mo^{6+} citrate anions with Co^{2+} cations coordinated to the carboxyl groups and terminal oxygen atoms deposited on alumina, and a maximum HDS activity was obtained in the catalyst thermally treated at 220°C. Citric acid (CA) as a chelating agent was used to synthesize the SBA-15-supported NiMo sulfide catalysts which were evaluated in the HDS reaction of DBT and 4,6-DMDBT. Similar study was performed by Zhang *et al*., (2016) using CA to modify CoMo/γ-Al_2O_3 calcined catalysts their results revealed that the sulfidation degree of the MoO_x species and the activity of the CoMo catalysts linearly increased with the CA applied (Zhang *et al*., 2016; de Leon *et al*., 2019, Klimova *et al*., 2013. These authors also proposed that the MoO_4^{2-} or β-$CoMoO_4$ species can be successfully transformed into polymolybdate species. The addition of CA can also help to recover Co^{2+} ions from the sub-superficial $CoAl_2O_4$ spinels and, therefore, induce the formation of more CoMoS sites (Klimova *et al*., 2013).

Van Haandel *et al*., (2017) emphasized a more beneficial role of CA than EDTA for the activity of CoMo/Al_2O_3 catalysts and they attributed it to weaker interaction of Co with the alumina support, allowing its sulfidation at low temperature. The results showed that CA also favor the formation of

more polymerized polymolybdates interacting weakly with the support and therefore leading to an easier Mo sulfidation. The associated low temperature regions for Co and Mo sulfidation were the main parameter affecting all the final catalytic activity (Bui *et al*., 2019; Van Haandel *et al*., 2017).

In literature there are some contradictions regarding the role played by chelating ligands on the HDS activity. Therefore, the aim of the current work study is to determine the effect of different chelating ligands on active phase dispersion and morphology and relate it to catalytic activity. In this work catalysts with and without chelating agent (EDTA, AA, CA) are synthesized in alumina support, which were evaluated in the HDS reactions of dibenzothiophene (DBT). The addition of chelating agents was used to improve the activity of the catalysts. The catalysts were characterized using BET, ICP, XRD, UV-Vis, FT-IR, SEM, EDX, XPS, TEM, and TG-DSC. All these characterization techniques provided information about the structural composition and morphology, appearance and arrangements of the constituents and the elemental composition.

The crystal structures of Co-AA and Co-EDTA obtained during the synthesis of CoMo-AA and CoMo-EDTA were analysed by single-crystal X-ray diffraction. Detailed bulk compositions and thermal stability were confirmed by means of infrared (IR) spectroscopy and thermogravimetry analyses, respectively. Theoretical studies *via* density functional theory (DFT), provided insight into the electronic properties of the various chelated catalysts.

This chapter discusses the synthesis and characterization of chelated and unchelated $CoMo/Al_2O_3$ based catalysts. The as-synthesized catalysts were evaluated in the hydrodesulfurization of dibenzothiophene and model fuel in a Parr reactor under industrial conditions. HDS catalysts were characterized using BET, ICP, XRF, XRD, UV-Vis, FT-IR, SEM, EDS, XPS, TEM, SC-XRD (unsupported catalyst) and TGA-DSC. The (Co/Co+Mo) molar ratio of 0.33 was maintained for each catalyst, EDTA: Co (1:1) molar ratio, and Co:CA (AA) (1:2) molar ratio was used. An increase in HDS activity was observed due to the incorporation of chelating agents. SC-XRD studied the oxide state of CoMo complexed with AA and EDTA, the analysis showed that chelating agents led to Co-chelating agent complex. The complexation was further confirmed by TGA-DSC. This led to the formation of more Type II CoMoS during sulfidation due to the delay of Co sulfidation (Badoga, 2012). The work may lay the groundwork for directing the future design of efficient HDS catalysts.

3.2. Results and discussion

3.2.1 Rationale for complexation

The use of the chelating ligand in $CoMoO_4$ catalyst is to promote complexation with the promoter (cobalt): and many ligands decompose at a temperature above 200 °C. This allows the active metal (molybdenum) to sulfide forming MoS_2. The decomposition of cobalt-chelating agent complex leaves

the promoter ion to move to the edges and corners of already formed MoS_2 slabs, resulting in the formation of more Co-Mo-S active phase (Type II) (Sundaramurthy *et al*., 2005). Therefore, the addition of chelating agent leads to ligand-promoter complex formation and delays the sulfidation of the promoter to high temperature while molybdenum oxide already starts to sulfide leading to a more active sulfided phase. Molybdenum acts as an active site, hence bonds with oxides forming an inactive phase of the catalyst and to activate the catalyst, the molybdenum oxide (MoO_3) is hydrodesulfurized to form MoS_2 which is the active phase of the catalyst. **(Figure 3.1)** shows the shapes of the crystals of CoMo-AA (stick-like) and CoMo-EDTA (rhombic shaped). It is worth mentioning that the chelating ligand complexed with a promoter (Co). Generally, the asymmetric unit comprises of two crystallographically independent Co (II) ion designated as Co (1) and Mo (V or VII) ion. TGA-DSC studies of unsupported catalysts (CoMo-AA and CoMo-EDTA) were employed to further show chelation within supported catalysts (see Section 3.5.11), DFT studies were also conducted to study the effect of chelating agents (AA, EDTA) on Co.

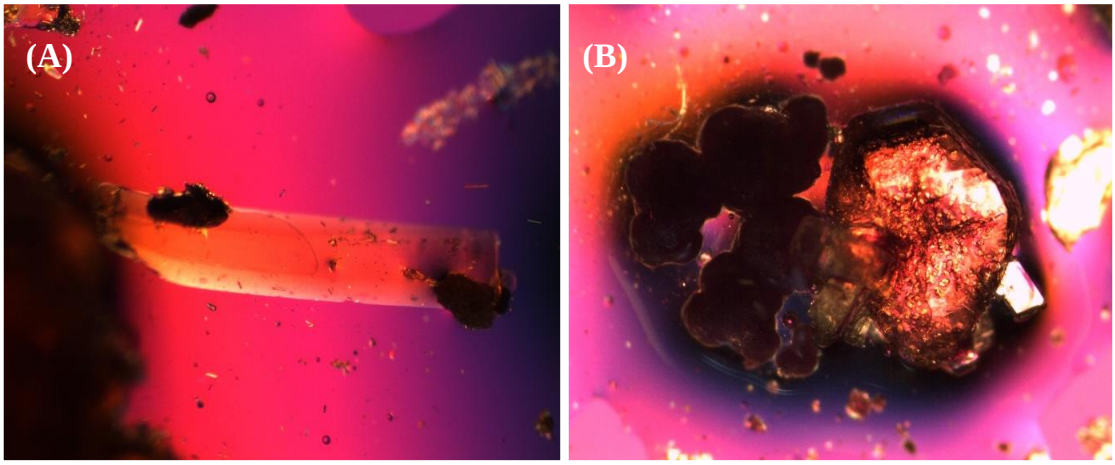

Figure 3.1: Images of crystals of (A) CoMo-AA and (B) CoMo-EDTA.

3.2.2 SC-XRD analysis of CoMo-EDTA and CoMo-AA

CoMo-EDTA: The crystal structure of CoMo-EDTA is presented in **Figure 3.2**. It crystallizes in the orthorhombic space group with Pmn21 (No.31). Data collection parameters are presented in **Table 3.1**. The octahedral coordination spheres of each Mo was completed by four bridging oxides to other Mo metal ions, and two bridging oxides; Mo (1) was connected to O(8) and O(23) bridging with O(9), O(10), O(11) and O(27). Mo (2) was coordinated with O(12) and O(13) forming a bridge with O(11), O(14), O(19) and O(27). Mo(3) coordinated with O(16) and O(17) while bridging with O(11), O(14), O(15) and O(18), respectively. Lastly Mo(4) bridged with all oxygen; O(10), O(11), $O(11^a)$, O(15), O(19) and $O(19^a)$ as presented in **Table 3.2**. The presence of water molecules in each end completed the distorted octahedral coordination sphere. In Mo(1-4)–O(8, 23, 13, 12, 16 & 17) the bond distances are in the range 1.709–1.723 Å and was significantly lower than that of Mo(1-4)–O(9, 10, 11, 14, 15, 17, 19 & 27) in the range of 1.934–2.502 Å. This might be due to the bridging character of the oxides

or higher charge density compared to water molecules (Banerjee *et al*., 2011). The presence of water molecules in each end of molybdenum part of the crystal completed the distorted octahedral coordination sphere. The degree of distortion shown in **Table 3.3** are reflected in the *cisoid* for molybdenum; for Mo(1) [72.26(10) –104.00(16)^{o}], Mo(2) [69.71(7)–105.83(11)^{o}], Mo(3) [71.82(10)–105.15(16)^{o}] and Mo(4) [77.15(12)–171.77(9)]. While the *transoid* angles for molybdenum; M(1) [155.26(15) –162.98(14)^{o}], Mo(2) [146.36(14)–175.54(11)^{o}], Mo(3) [154.17(15)–163.42(14)^{o}] and Mo(4) [143.39(16) –171.77(9)^{o}], this deviated from linearity and this was likely due to the bridging features and steric requirement in the connection of the two units.

Co is coordinated with EDTA in a hepta coordinated–(N_2O_5) environment. The coordination environment of Co(1) was formed by seven donors: five [O(1 &1^{a}), O(5)] donor atoms, and two amine nitrogen's [N(1) and N(2)]. The presence of water molecule led to distortion, and the coordination of the donors led to an asymmetric dimer shown in **Table 3.1**. The Co(1)–O bond distances where the oxygen is connected with sodium ions was slightly different than that coordinated with acetate ion donors; Co(1)–O(1 &1^{a}) = 2.142(4) Å, Co(1)–O(5) = 2.277(4) was slightly higher than that of Co(1)–O(3 & 3^{a}) = 2.106(5) Å, and the coordination of Co(1)–N(1) = 2.280(5) Å and Co(1)–N(2) = 2.275(6) has longer bond lengths than the average oxygen donors (Banerjee *et al*., 2011). This might be due to different steric effect and electron density around N and Co atoms (Banergee *et al*., 2011). **Table 3.3** shows bond angles between the metal and donors; The degree of distortion in Co complex are reflected in the *cisoid* [74.50(15) –79.77(12) Å] and *transoid* angles [116.70(13) –148.02(4) Å] (Maji *et al*., 2017). Both Mo and Co complexes are connected by water molecule, where Co was connected *via* intramolecular H bond while Mo was connected *via* oxygen of water lattice and Mo was also connected *via* oxygen of acetate ion from Co ion, respectively (Banerjee *et al*., 2011). Hydrogen bond geometry for complex Co-AA crystal is shown in **Table 3.4**.

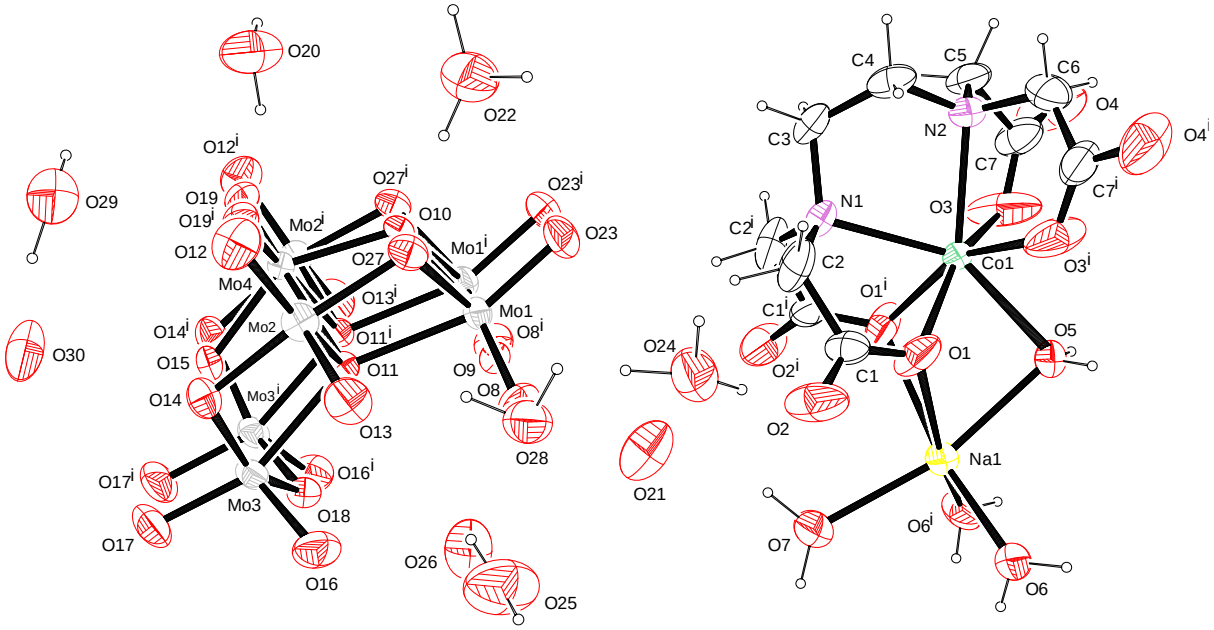

Figure 3.2: ORTEP diagram of CoMo-EDTA with ellipsoids drawn at 50% probability level. Symmetry elements: (i) 1-x, +y, +z. Selected symmetry generated disorder of the EDTA ligand omitted for clarity.

Table 3.1: Crystal data and details of structure determination.

Compound	**CoMo-EDTA**	**CoMo-AA**	**CoMo Complex**
Empirical formula	Mo_7O_{27}, $C_{10}H_{20}CoN_2O_{12}$, $12(H_2O)$, $3(O)$	$C_4H_{14}CoO_8$	$2(CoH_4Mo_8O_{31})$, $2(CO)$, $16(O)$, $2(H_2O)$
Formula weight	1761.97	296	3085.05
Temperature (K)	296	296	296
Wavelength (Å)	0.71073	0.71073	0.71073
Crystal system	Orthorhombic	Monoclinic	Triclinic
Space group	Pmn21 (No.31)	P21/c	P-1(No.2)
D (cal) [g/cm^3]	2.300	1.715	2
Volume (Å^3)	2544.0(3)	482.29(3)	1800.06(13)
Z	2	2	1
Unit cell dimensions			
a (Å)	16.3617(13)	4.8029(2)	10.2722(4)
b (Å)	9.6950(7)	11.9147(5)	13.9640(6)
c (Å)	16.0376(12)	8.4514(3)	14.2545(6)
α (°), β (°), ɣ (°)	90, 94.274(2), 90	90, 94.274(2), 90	62.870(2), 87.074(2), 81.630(2)
F(000)	1716	258	1448
Crystal size (mm)	0.32 x 0.39 x 0.55	0.21x0.30x0.37	0.05 x 0.22 x 0.23
θ range for data collection (°)	1.8, 28.3	3.0, 28.3	1.7, 28.4
Database *h*/*k*/*l*	-21,21/-12,12/-21,21	-6,6/-15,15/-10,10	-13, 13/-16, 18/0,19
Tot uniq., Data, R (int)	49019, 6542, 0.021	8923, 1200, 0.024	48962, 8964, 0.052
Observed Data [I > 2.0 σ(I)]	6265	1080	7945
Refinement			
Nref, Npar	6542, 369	1200, 79	8962, 98
Final indices [R, wR2, S]	0.0179, 0.0474, 1.10	0.0178, 0.0496, 1.05	0.0335, 0.0832, 1.06
Largest peak and hole (eÅ^{-3})	-0.48, 0.62	-0.21, 0.25	1.13, 1.40

Table 3.2: Selected bond distances (Å) in the crystal structure of CoMo-EDTA.

Atoms	**Distance**	**Atoms**	**Distance**
Mo(1)–O(8)	1.712(3)	Co(1)–N(2)	2.275(5)
Mo(1)–O(9)	1.934(2)	Co(1)–O(1[a])	2.142(4)
Mo(1)–O(10)	2.249(3)	Co(1)–O(3[a])	2.106(5)
Mo(1)–O(11)	2.157(3)	Na(1)–O(1)	2.487(4)
Mo(1)–O(23)	1.712(3)	Na(1)–O(5)	2.346(5)
Mo(1)–O(27)	1.981(3)	Na(1)–O(6)	2.345(4)
Mo(2)–O(11)	2.171(2)	Na(1)–O(7)	2.334(5)
Mo(2)–O(12)	1.709(3)	Na(1)–O(1[a])	2.487(4)
Mo(2)–O(13)	1.728(3)	Na(1)–O(6[a])	2.345(4)
Mo(2)–O(14)	1.920(3)	O(1)–C(1)	1.233(6)
Mo(2)–O(27)	1.914(3)	O(2)–C(1)	1.238(7)
Mo(2)–O(19[b])	2.502(2)	O(3)–C(7)	1.224(8)
Mo(3)–O(11)	2.148(3)	O(4)–C(7)	1.237(9)
Mo(3)–O(14)	1.978(3)	N(1)–C(2)	1.453(6)
Mo(3)–O(15)	2.275(3)	N(1)–C(3)	1.497(9)
Mo(3)–O(16)	1.707(4)	N(1)–C(2[a])	1.453(6)
Mo(3)–O(17)	1.713(3)	N(1)–C(3[a])	1.497(9)
Mo(3)–O(18)	1.931(2)	N(2)–C(4)	1.466(9)
Mo(4)–O(10)	1.906(3)	N(2)–C(5)	1.459(12)
Mo(4)–O(11)	2.254(2)	N(2)–C(6)	1.448(13)
Mo(4)–O(15)	1.885(3)	N(2)–C(4[a])	1.466(9)
Mo(4)–O(19)	1.739(2)	N(2)–C(5[a])	1.459(12)
Mo(4)–O(11[b])	2.254(2)	N(2)–C(6[a])	1.448(13)
Mo(4)–O(19[b])	1.739(2)	O(5)–H(5)	0.8400
Co(1)–O(1)	2.142(4)	O(5)–H(5[a])	0.8400
Co(1–O(3)	2.106(5)	O(6)–H(6B)	0.8000
Co(1)–O(5)	2.277(4)	O(6)–H(6A)	0.8800
Co(1)–N(1)	2.280(5)	O(7)–H(7A)	0.9600

Table 3.3: Selected bond angles (°) in crystal structure of CoMo-EDTA

Atoms	**Angle**	**Atoms**	**Angle**
O(3[a])–Co(1)–O(5)	79.54(13)	O(14)–Mo(2)–O(19[b])	80.29(12)
N(1)–Co(1)–N(2)	77.15(17)	O(19b)–Mo(2)–O(27)	79.92(12)
O(1[a])–Co(1)–N(1)	76.18(13)	O(11)–Mo(3)–O(14)	73.03(11)
O(3a)– Co(1)–N(1)	116.70(13)	O(11)–Mo(3)–O(15)	71.82(10)
O(1[a])–Co(1)–N(2)	130.30(11)	O(11)–Mo(3)–O(16)	94.26(12)
O(3a)–Co(1)–N(2)	74.50(15)	O(11)–Mo(3)–O(17)	157.58(14)
O(1 [a])–Co(1)–O(3[a])	155.15(15)	O(11)–Mo(3)–O(18)	87.74(15)
O(1)–Co1–O(3[i])	81.26(19)	O(14)–Mo(3)–O(15)	84.08(12)
O(3)–Co(1)–O(5)	79.54(13)	O(14)–Mo(3)–O(16)	100.76(15)
O(3)–Co(1)–N(1)	116.70(13)	O(14)–Mo(3)–O(17)	92.09(15)
O(3)–Co(1)–N(2)	74.50(15)	O(14)–Mo(3)–O(18)	154.17(15)
O(1[a])–Co(1)–O(3)	81.26(19)	O(15)–Mo(3)–O(16)	163.42(14)
O(3)–Co(1)–O(3[a])	108.2(2)	O(15)–Mo(3)–O(17)	90.39(15)
O(5)–Co(1)–N(1)	148.02(14)	O(15)–Mo(3)–O(18)	73.42(12)
O(5) –Co(1) –N(2)	134.83(17)	O(16)–Mo(3)–O(17)	105.15(16)
O(1) –Co(1) –O(5)	79.77(12)	O(16)–Mo(3)–O(18)	97.66(15)
O(1) –Co(1) –N(1)	76.18(13)	O(17)–Mo(3)–O(18)	100.43(18)
O(1) –Co(1) –O(3)	155.15(15)	O(10)–Mo(4)–O(11)	76.82(11)
O(1) –Co(1) –O(5)	79.77(12)	O(10)–Mo(4)–O(15)	143.39(16)
O(1) –Co(1) –N(2)	130.30(11)	O(10)–Mo(4)–O(19)	100.66(12)
O(1) –Co(1) –O(1[a])	81.66(15)	O(10)–Mo(4)–O(11[b])	76.82(11)
O(8) –Mo(1) –O(9)	97.45(14)	O(10)–Mo(4)–O(19[b])	100.66(12)
O(8) –Mo(1) –O(10)	162.98(14)	O(11)–Mo(4)–O(15)	77.15(12)
O(8) –Mo(1) –O(11)	93.25(12)	O(11)–M(4)–O(19)	171.77(9)
O(8) –Mo(1) –O(23)	104.00(16)	O(11)–Mo(4)–O(11[b])	88.36(7)

Table 3.3: Continued

Atoms	Angle	Atoms	Angle
O(8) –Mo(1) –O(27)	99.82(14)	O(11)–Mo(4)–O(19^{b})	83.43(9)
O(9) –Mo(1) –O(10)	73.80(12)	O(15)–Mo(4)–O(19)	101.44(13)
O(9) –Mo(1) –O(11)	88.33(15)	O(11^{b})–Mo(4)–O(15)	77.15(12)
O(9) –Mo(1) –O(23)	100.15(18)	O(15)–Mo(4)–O(19^{b})	101.44(13)
O(9) –Mo(1) –O(27)	155.26(15)	O(11^{b})–Mo(4)–O(19)	83.43(9)
O(10) –Mo(1) –O(11)	72.26(10)	O(19)–Mo(4)–O(19^{b})	104.78(10)
O(10) –Mo(1) –O(23)	92.06(15)	O(11^{b})–Mo(4)–O(19^{b})	171.77(9)
O(10) –Mo(1) –O(27)	84.78(12)	O(12) –Mo(2) –O(19^{a})	79.51(11)
O(11) –Mo(1) –O(23)	159.49(14)	O(15) –Mo(4) –O(19)	101.44(13)
O(11) –Mo(1) –O(27)	73.18(10)	O(11^{b}) –Mo(4) –O(15)	77.15(12)
O(23) –Mo(1) –O(27)	92.72(15)	O(15) –Mo(4) –O(19^{b})	101.44(13)
O(11) –Mo(2) –O(12)	149.22(11)	O(11^{b}) –Mo(4) –O(19)	83.43(9)
O(11) –Mo(2) –O(13)	105.83(11)	O(19) –Mo(4) –O(19^{b})	104.78(10)
O(11) –Mo(2) –O(14)	73.59(13)	O(11^{b}) –Mo(4) –O(19^{b})	171.77(9)
O(11) –Mo(2) –O(27)	74.13(13)		
O(11) –Mo(2) –O(19^{b})	69.71(7)		
O(12) –Mo(2) –O(13)	104.95(13)		
O(12) –Mo(2) –O(14)	101.33(18)		
O(12) –Mo(2) –O(27)	101.47(18)		
O(13) –Mo(2) –O(14)	98.76(18)		
O(13) –Mo(2) –O(27)	98.87(18)		
O(13) –Mo(2) –O(19^{b})	175.54(11)		
O(14) –Mo(2) –O(27)	146.36(14)		

Table 3.4: Hydrogen bond geometry for complexes 1-4 in crystal packing.

Atoms	D-H... Å	H…A/Å	D…A/Å	D-H... A/°	Symmetry code
O(7)-H(7A)-O(21)	0.9600	2.0800	2.988 (9)	161.00	-
O(20)-H(20A)-O(19)	0.9700	1.9600	2.897 (5)	163.00	1-x, y, z
O(22)-H(22A)-O(27)	0.9500	1.8500	2.798 (6)	173.00	-
O(22)-H(22B)-O(2)	1.0100	1.8600	2.871 (6)	177.00	-x, -1+y, z
O(24)-H(24A)-O(2)	1.0400	1.7300	2.764 (6)	174.00	-
O(24)-H(24B)-O(8)	1.0300	1.9800	2.939 (5)	153.00	-
O(25)-H(25A)-O(1)	0.9600	2.0300	2.902 (6)	149.00	½-x,2-y, ½ +z
O(25)-H(25B)-O(8)	0.8200	2.3900	2.877 (7)	119.00	-
O(28)-H(28B)-O(13)	0.9400	1.9200	2.783 (5)	152.00	-
O(29)-H(29A)-O(30)	1.0000	2.3200	3.189 (11)	144.00	-

CoMo-AA: The hexacoordinated mononuclear compound in **Figure 3.3A** was obtained as a pink crystalline product, by refluxing cobalt (II) acetate and hexaammonium molybdate with hydrazine in deionized water and acetic acid (chelating medium). CoMo-AA crystallizes in the monoclinic space group with P21/c. Data collection parameters are presented in **Table 3.1**. The asymmetric unit comprises of one crystallographically independent Co(II) ions complex with acetic acid and water molecules, designated as Co(1) presenting distorted octahedral geometry. The coordination environment of Co(1) was formed by six donors: the equatorial plane constructed by four [O(3), O(3^i), O(4) and O(4^i)] donors atoms from water molecules while the axial position were occupied by the remaining two donor atoms originate from acetate ions [O(1) and O(1^i)], respectively (Banerjee *et al*., 2011). Selected bond lengths and angles pertaining to the coordination are tabulated in **Tables 3.6** and **Table 3.5**. The Co(1)-O bond distance of Co with the water molecules was slightly different with that of acetate ion donors; for Co(1)-O(1&1^i) = 2.0962(8) Å was slightly higher than that of Co(1)-O(3&3^i) = 2.0892(10) Å and, Co(1)- (4&4^i) = 2.1195(9) Å (Banerjee *et al*., 2011). This might be due to the rigidity of acetate ions or higher charge density compared to water molecules (Banerjee *et al*., 2011).

The degrees of distortion of the coordination spheres are reflected in the *cisoid* [89.34(4)-90.57(4) °] and the *transoid* angles (Maji et al., 2017) shown in **Table 3.6**. The sum (360.00°) of the equatorial angles [O(3)-Co(1)-O(4) 89.34(4)° , O(3^i)-Co(1)-O(4) 90.66(4)° , O(3^i)-Co(1)-O(4^i) 89.34(4)° , O(3)-Co(1)-O(4^i) 90.66(4)° was equivalent to 360.00°, this reflected that the equatorial oxygen's were in the same plane with the metal center (Maji *et al*., 2017). The complex structure was stabilized by intramolecular H-bonds occurring between the H atoms of the four coordinated water molecules O(3), O(3^i) and O(4), O(4^i) with oxygen's O(1,2) and O(1^i, 2^i) from the acetate ion, respectively (Banerjee *et al*., 2011). Hydrogen bond geometry for complex Co-AA crystal is shown in **Table 3.7**. Additional

crystal, ($CoH_4Mo_8O_{31}$) labelled as MoO was isolated within the sample of CoMo-AA complex (**Fig.3.3 B**). Crystal data and details of the structure is presented in **Table 3.1**. The structure consists of octamolybdate units link together to form a chain in one dimension. Both Mo and Co are coordinated to oxygen atoms with Mo-O distances in the range of 1.767(4)-2.185(4) Å, 1.727(5)-2.173(5) Å, and Co-O distances are in the range of 2.138(4)-2.427(4) Å, 2.042(5)-2.097(5) Å. The bond angles for O-Mo-O are between 68.49(16)°-177.7(2)°, and the bond angles for O-Co-O are between 85.92(19)°-171.3(2)°. The isolated "MoO" confirmed that AA coordinate with Co. The structure contains large-chained voids with disordered water molecules. Furthermore, the crystal turned out to be twinned causing poor data quality and the hydrogen atoms for most of the water molecules could not be located on the difference map.

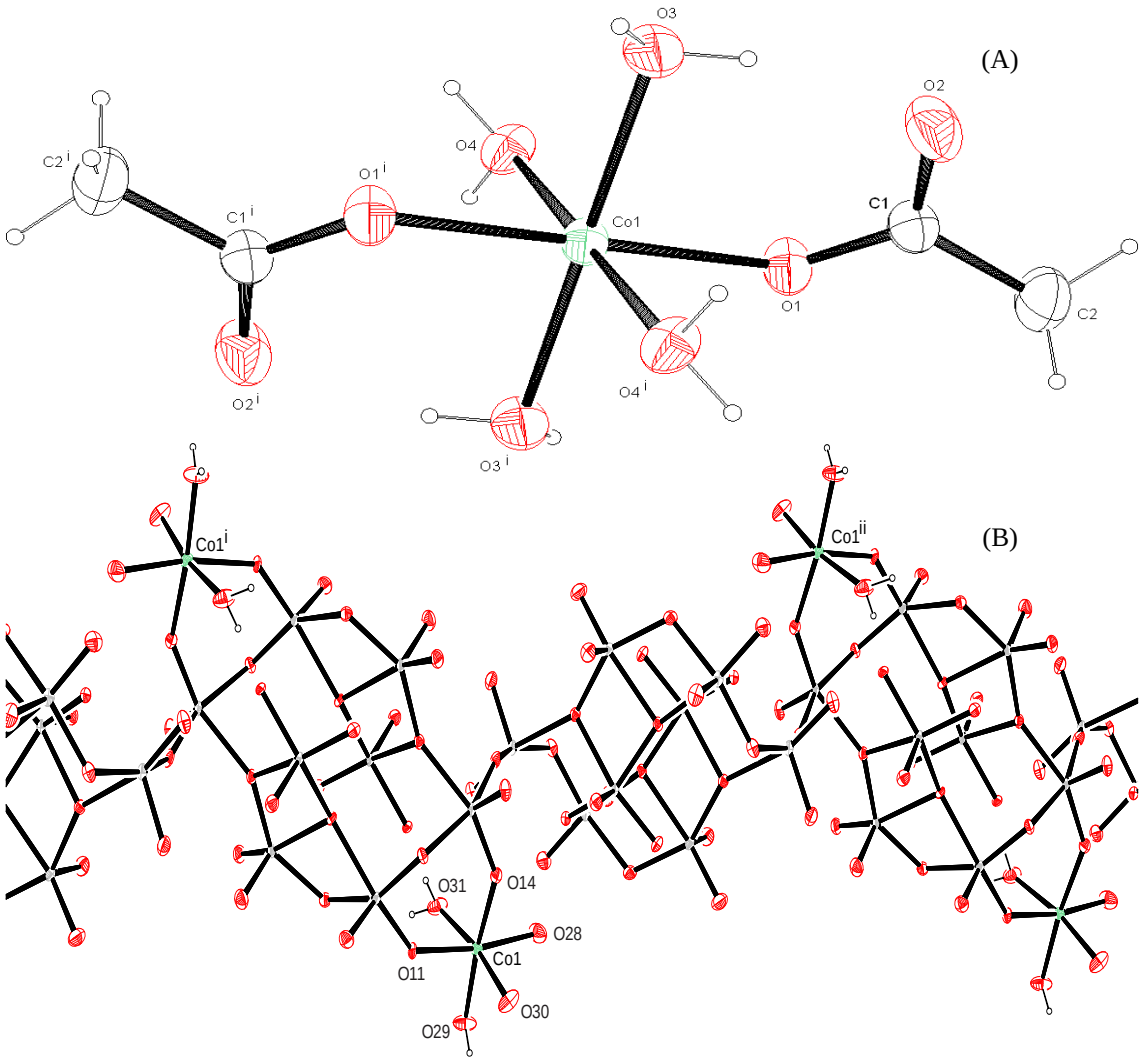

Figure 3.3: (A) ORTEP diagram of CoMo-AA showing the complexation of Co with AA with ellipsoids drawn at 50% probability level. Symmetry elements: (i) 1-x, 1-y, 1-z. (B) OTPER diagram of isolated CoMo complex with ellipsoid drawn 50% probability level. Symmetry elements: 1-x, 1-y, 1-z.

Table 3.5: Selected bond distances (Å).

Atoms	Distance	Atoms	Distance
Co(1)–O(1)	2.0962(8)	O(3)–H(3A)	0.829(10)
Co(1)–O(3)	2.0892(10)	O(3)–H(3B)	0.831(10)
Co(1)–O(4)	2.1195(9)	O(4)–H(4A)	0.840(17)
Co(1)–O(1^{i})	2.0962(8)	O(4)–H(4B)	0.833(15)
Co(1)–O(3^{i})	2.0892(10)	C(1)–C(2)	1.4987(19)
Co(1)–O(4^{i})	2.1195(9)	C(2)–H(2A)	0.9600
O(1)–C(1)	1.2732(15)	C(2)–H(2B)	0.9600
O(2)–C(1)	1.2488(15)	C(2)–H(2C)	0.9600

Table 3.6: Selected bond angles (°).

Atoms	Angle	Atoms	Angle
O(1)–Co(1)–O(3)	90.57(4)	O(3)–Co(1)–O(3^{i})	180.00
O(1)–Co(1)–O(4)	90.18(3)	O(3)–Co(1)–O(4^{i})	90.66(4)
O(1)–Co(1)–O(1^{i})	180.00	O(1^{i})–Co(1)–O(4)	89.82(3)
O(1)–Co(1)–O(3^{i})	89.43(4)	O(3^{i})–Co(1)–O(4)	90.66(4)
O(1)–Co(1)–O(4^{i})	89.82(3)	O(4)–Co(1)–O(4^{i})	180.00
O(3)–Co(1)–O(4)	89.34(4)	O(1^{i})–Co(1)–O(3^{i})	90.57(4)
O(1^{i})–Co(1)–O(3)	89.43(4)	O(1^{i})–Co(1)–O(4^{i})	90.18(3)
O(3^{i})–Co1–O(4^{i})	89.34(4)		

Table 3.7: Hydrogen bond geometry for complex Co-AA crystal.

Atoms	D-H…..Å	H….A/Å	D….A/Å	D-H…A/º	Symmetry code
O(3)-H(3A)-O(4)	0.829(10)	2.086(13)	2.8378(13)	150.7(15)	1+x,y,z
O(3)-H(3B)-O(2)	0.831(10)	1.845(13)	2.6360(14)	159(2)	-
O(4)-H(4A)-O(2)	0.840(17)	1.847(16)	2.7103(13)	173.7(18)	1-x,-1/2+y,3/2-z
O(4)-H(4B)-O(1)	0.833(15)	1.925(15)	2.7243(12)	160.6(15)	1+x,y,z
C(2)-H(2A)-O(3)	0.9600	2.5500	3.4672(19)	160.00	1-x,1/2+y,3/2-z

3.2.3 Theoretical studies: Chemical descriptors of CoMo-EDTA and CoMo-AA

Frontier molecular orbitals which help in predicting the reactivity, and stability of compounds by predicting their electrical transport properties was calculated from the highest occupied molecular orbital (HOMO) and lowest unoccupied molecular orbital (LUMO) energy values of geometrically optimized CoMo-EDTA and CoMo-AA complexes. HOMO has the ability to donate electrons, while LUMO withdraws electrons. It is well known that electron correlation is important for the transition metal complexes and the motion of the electrons are governed by their instantaneous positions not the average position of the other electrons (Kanchi *et al*., 2016). The optimized CoMo-EDTA and CoMo-AA complexes as visualised using Chemcraft program is presented in (**Figure 3.4**) and **(Figure 3.5**), respectively. The HOMO and LUMO of geometrically optimized CoMo-EDTA indicated that HOMO and LUMO energies are not pure but a mixture of Co, O, C and N (**Figure 3.6**), with CoMo-AA complex, HOMO was also not pure but a mixture especially on Co, C and O atoms from the chelating agent, while LUMO energies originated from cobalt ion of CoMo-AA (**Figure 3.7**). CoMo-EDTA presented HOMO orbital energy of -6.111 eV, while the orbital energy for LUMO was -2.280 eV with the HOMO-LUMO gap of 3.831eV. With CoMo-AA complex, the HOMO orbital energy was -11.736 eV and LUMO was -8.851eV, while the HOMO-LUMO gap of 2.885 eV. According to obtained HOMO-LUMO energy band gap CoMo-EDTA < CoMo-AA. This was in agreement with the band gap data reported in (Section 3.5.1). Due to lack of single crystals for CoMo-CA and CoMo the DFT study was limited to CoMo-EDTA and CoMo-AA.

The chemical reactivity varies with the structure of molecules. The lowest value of the potential ionization (I = 6.111 eV) from CoMo-EDTA confirms a better electron donor and the largest value of the affinity (A = 8.851 eV) from CoMo-AA suggests a better electron acceptor (**Table 3.8**). Chemical hardness (softness) value of CoMo-AA (η = 1.443 eV, S = 0.693 eV) was (lesser, greater) than the value obtained for CoMo-EDTA (η = 1.916 eV, S = 0.523 eV) confirming its reactive nature. CoMo-AA possessed higher electronegativity value (χ = 10.294 eV) than CoMo-EDTA so; it was the best electron acceptor. The value of ω for CoMo-AA (ω = 76.421 eV) indicated that it was the stronger electrophile than CoMo-EDTA. It is worth noting that these properties tend to be dampened under high temperatures employed for HDS study. CoMo-EDTA complex gave the highest energy gap which indicates that the complex was highly stable and low reactive. Therefore, it is expected that of all chelated catalysts, CoMo-EDTA/Al_2O_3 exhibit lower activity.

Table 3.8: **Quantum chemical descriptors of Co-EDTA and Co-AA complex**.

Parameter	**CoMo-EDTA**	**CoMo-AA**
E_{HOMO} (eV)	-6.111	-11.736
E_{LUMO} (eV)	-2.280	-8.851
ΔE_{gap} (eV)	3.831	2.885
I (eV)	6.111	11.736
A (eV)	2.280	8.851
μ (eV)	-4.196	-10.294
χ (eV)	4.196	10.294
η (eV)	1.916	1.443
S (eV)	0.523	0.693
ω (eV)	16.859	76.421

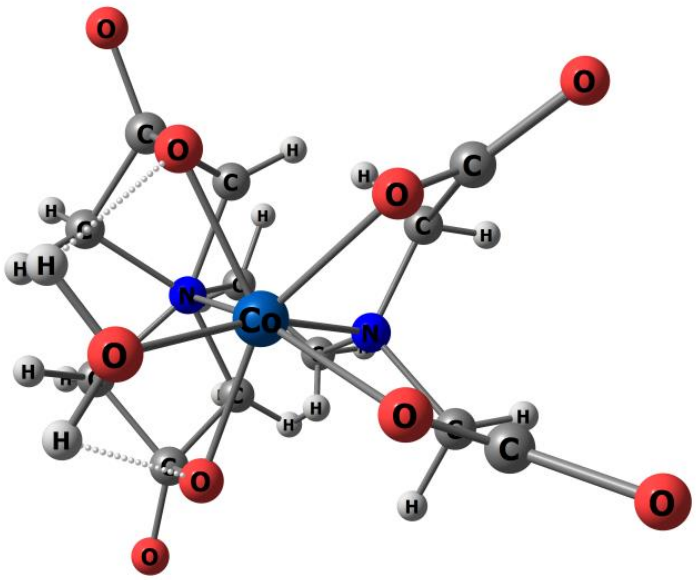

Figure 3.4: Optimized structure of CoMo-EDTA complex at B3LYP/LanL2DZ.

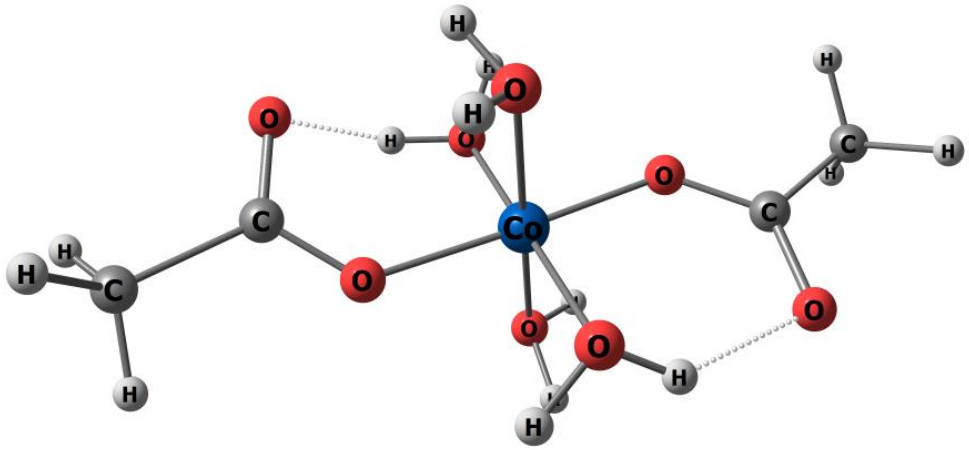

Figure 3.5: Optimized structure of CoMo-AA complex at B3LYP/LanL2DZ.

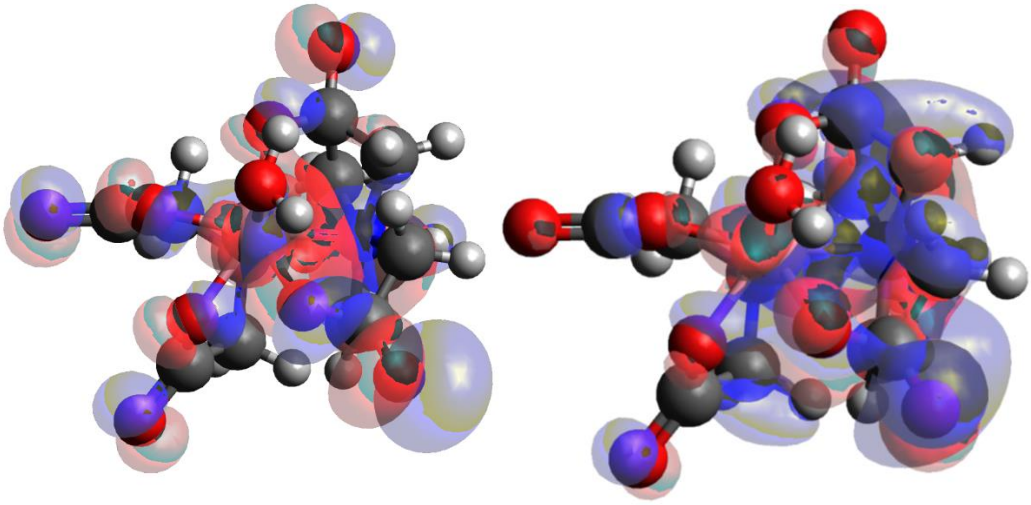

Figure 3.6: Frontier orbitals showing (A) HOMO and (B) LUMO positions of CoMo-EDTA complex (CoMo-EDTA).

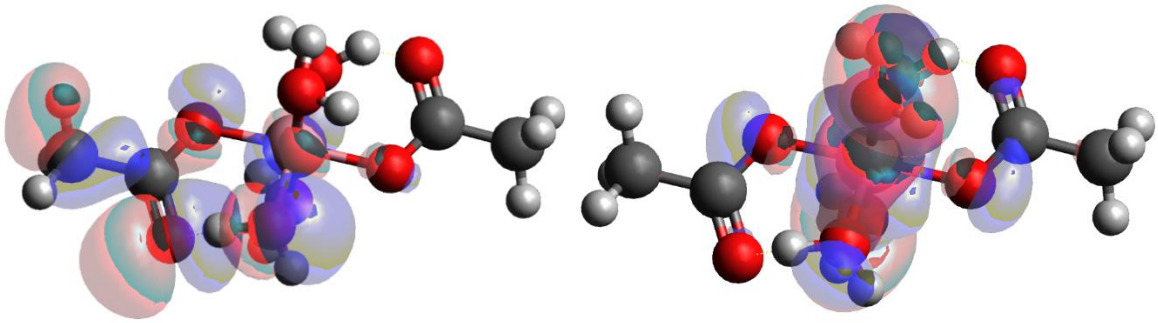

Figure 3.7: Frontier orbitals showing (A) HOMO and (B) LUMO positions of CoMo-AA complex (CoMo-AA).

3.5.1 UV Vis Spectroscopy

The UV-Vis absorption curves showing various coordination environments of Co^{2+} and Mo^{6+} ions in the oxide precursors for $CoMo/Al_2O_3$, $CoMo\text{-}EDTA/Al_2O_3$ and $CoMo\text{-}CA/Al_2O_3$ is presented in **Figure 3.8-3.11**, respectively**.**

$CoMo/Al_2O_3$: A shoulder observed at 320-350 nm was assigned to O^{2-} -Mo^{6+} ligand-to-metal charge transfer transition of Mo^{6+} ions having octahedral coordination (Lee *et al*., 1996; Huirache-Acuña et al., 2015) (**Figure 3.8**). The intense band at 340 nm indicates a more dispersed octahedral Co species (Castillo-Villanon, 2015). The band around 500-550 nm corresponds to d-d transitions of Co^{2+} ions in an octahedral environment of Co-Mo complex (Huirache-Acuna, 2015; Bergwerff *et al*., 2008; Vatutina *et al*., 2019; van der Water *et al*., 2006; Chen *et al*., 2017; Bui *et al*.,2019; Vakros *et al*., 2004; Vatutina *et al*., 2019). This indicated that Co^{2+} interacts with Al_2O_3 (Bui *et al*., 2019). The band at 750 nm was assigned to Co_3O_4 (Vakros *et al*., 2010).

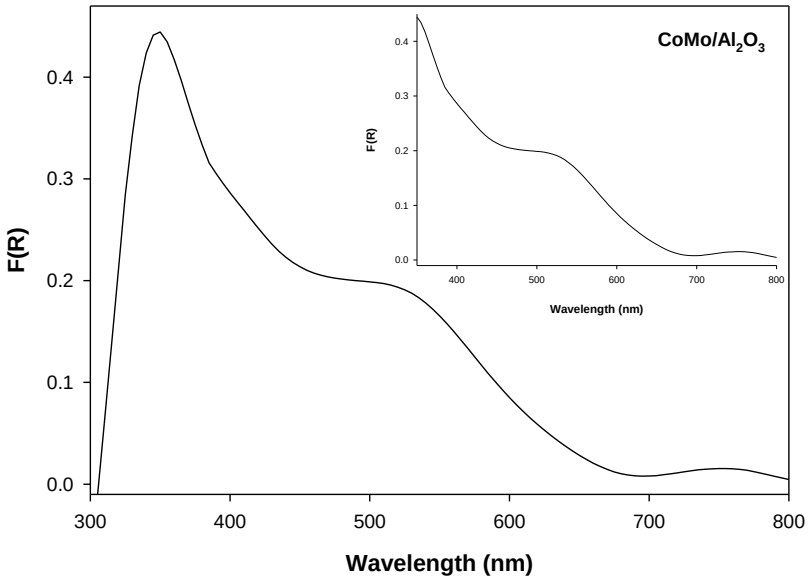

Figure 3.8: UV-Vis spectrum of synthesized $CoMo/Al_2O_3$ catalyst (Inset: visible region 400-700 nm showing the d-d transition).

$CoMo\text{-}EDTA/Al_2O_3$: The UV-Vis spectrum of uncalcined $CoMo\text{-}EDTA/Al_2O_3$ catalyst is presented in **Figure 3.9**. A band at 220-250 nm was attributed to change in transition from O^{2-}-Mo^{6+} ligand-to-metal charge transfer band in octahedral coordination and a formation of less polymerized molybdate species (Bui *et al*., 2019; Weber, 1994). The addition of EDTA lead to a shift of d-d band to a lower wavelength of 545 nm, which indicate a weaker interaction of the Co species with the Al_2O_3 support, resulting in a complexation of Co and a reduction in the agglomeration of Mo species (Rinaldi e*t al*., 2009). At a region of 480-600 nm, there is a triplet characteristic for Co species assigned to cobalt-oxygen species ($CoAl_2O_3$-like): $^4T_{1g}$ (F) ground state ($^4T_{1g}$ (F) to $^4T_{2g}$ (F) and $^4T_{1g}$ (F) to $^4T_{1g}$ (P) of high spin octahedral

Co^{2+} complexes higher states, respectively (Obeso-Estrella *et al*., 2018; Zhang et al., 2019; Cabello *et al*., 2002). The other band between 640 nm is due to the interaction of Co^{2+} with Al_2O_3 forming $CoAl_2O_4$ phase known as cobalt aluminate (Bui *et al*., 2019). A shoulder at 750 nm was observed and was assigned to Co_3O_4 (Vakros *et al*., 2010).

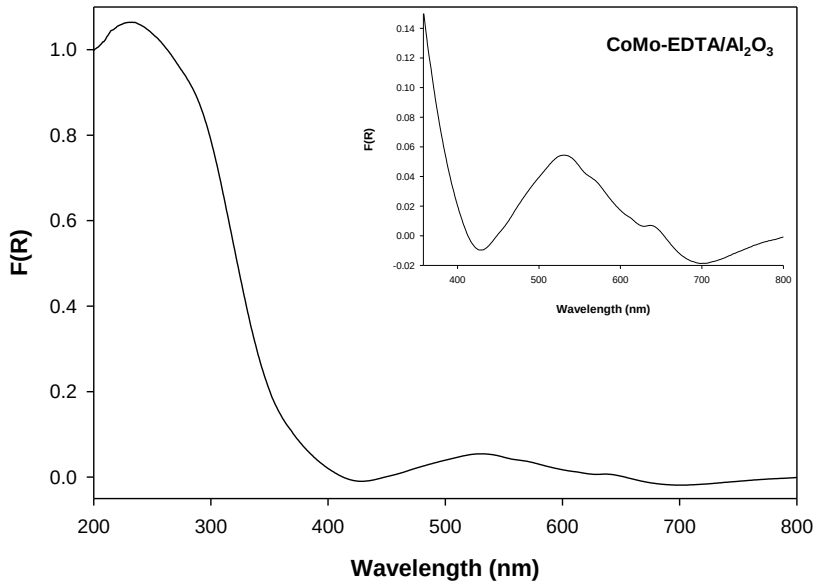

Figure 3.9: UV-Vis spectra for CoMo-EDTA/Al_2O_3 catalyst (Inset: visible region 400-700 nm showing the d-d transition).

CoMo-AA/Al_2O_3: The intense absorption band about 200-280 nm, could be assigned to the ligand-metal charge transfer transitions $O^{2-}\rightarrow Mo^{6+}$ (**Figure 3.10**). The LMCT band centered around 220-280 nm indicates the presence of isolated individual tetrahedral coordinated Mo sites and low-polymerized octahedrally coordinated Mo^{6+} oxide species (Méndez *et al.*, 2017). In the addition to the LMCT bands due to Mo appearing in the UV-region, the visible spectra of this catalyst exhibit a band in the 500-680 nm region, which is associated with Co species and its intensity is an indication of more dispersed O_h Co species. A low intensity shoulder at 400 nm region also confirms the octahedral coordination of Co oxide attributed to their d-d electronic transitions. A broad peak observed at 640 nm was due to the interaction of Co^{2+} with Al_2O_3 support forming $CoAl_2O_4$ phase known as cobalt aluminate (Bui *et al*., 2019). A shift of the band to lower wavelength is an indication of weak interactions of Co species with the support.

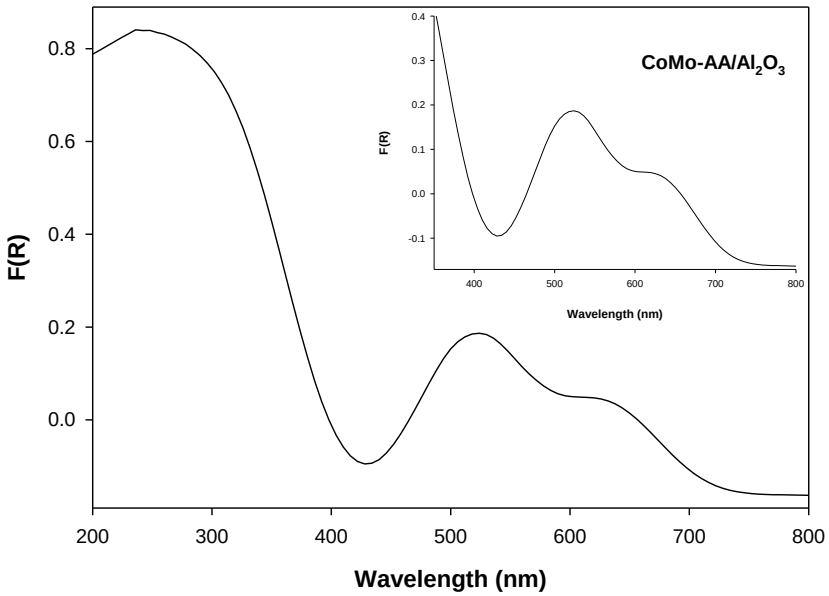

Figure 3.10: UV-Vis spectra for CoMo-AA/Al_2O_3 catalyst (Inset: visible region 400-700 nm showing the d-d transition).

CoMo-CA/Al_2O_3: **Figure 3.11** displays an absorption band at 258-350 nm which is associated to ligand metal-metal charge transfer (LMCT) which involve isolated transition metal sites from $O^{2-} \rightarrow Mo^{6+}$ ions having an octahedral coordination (Lee *et al*., 1996). It can be clearly seen that the proportion of Mo species in octahedral coordination for CoMo-CA/Al_2O_3 is higher than that of CoMo-EDTA/Al_2O_3, due to the relatively larger band area of octahedral Mo species for CoMo-CA/Al_2O_3 at 320-400 nm region. At a region of 480-600 nm, there was a triplet characteristic for Co species, and they were assigned to cobalt-oxygen species ($CoAl_2O_3$-like): $^4T_{1g}$ (F) to $^4T_{2g}$ (F) and $^4T_{1g}$ (F) to $^4T_{1g}$ (P) of high spin octahedral Co^{2+} complexes (Obeso-Estrella *et al*., 2018) higher states, respectively (Zhang *et al*., 2019; Cabello *et al*., 2002). A band in the 500-720 nm regions was associated with Co species. The formation of the triplet is an indication of tetrahedron distortion (Elkabouss *et al*., 2004), likely due to the presence of water molecules in the catalyst and can also be assigned to Co-Al_2O_4 (Zhang *et al*., 2016). The intensity of peaks at 545, 585 and 630 nm in the spectra of the catalysts depends on the chelating agent. The significant decrease in the intensity indicates an increase in cobalt in the octahedral coordination and the formation of the $[Mo_4O_{11}(C_6H_5O_7)2]^{4-}$ complex. The addition of citric acid modifies the interaction between Co and the Al_2O_3 surface, and thus resultant Co-CA complexes are well dispersed on the surface. The observed shift also indicates that the successive impregnation gives rise to smaller supported particles in the catalyst and indicates a decrease in agglomeration of Mo species (Zhang *et al*., 2016; Bui *et al*., 2019). The band at 640 nm indicate that CA is a strong stronger ligand than H_2O, which may lead to the formation of Co (II)-CA complex (Wu *et al*., 2014). A shoulder at 750 nm is observed which was assigned to Co_3O_4 (Vakros *et al*., 2010), and can be attributed to the $^4T_{1g}$ (F) $\rightarrow$ $^4T_{2g}$ (F) and $^4T_{1g}$ (F) $\rightarrow$$^4T_{1g}$ (P) transitions of octahedrally coordinated Co^{2+} ions (Kazakov *et al*., 2019; Wu *et al*., 2014).

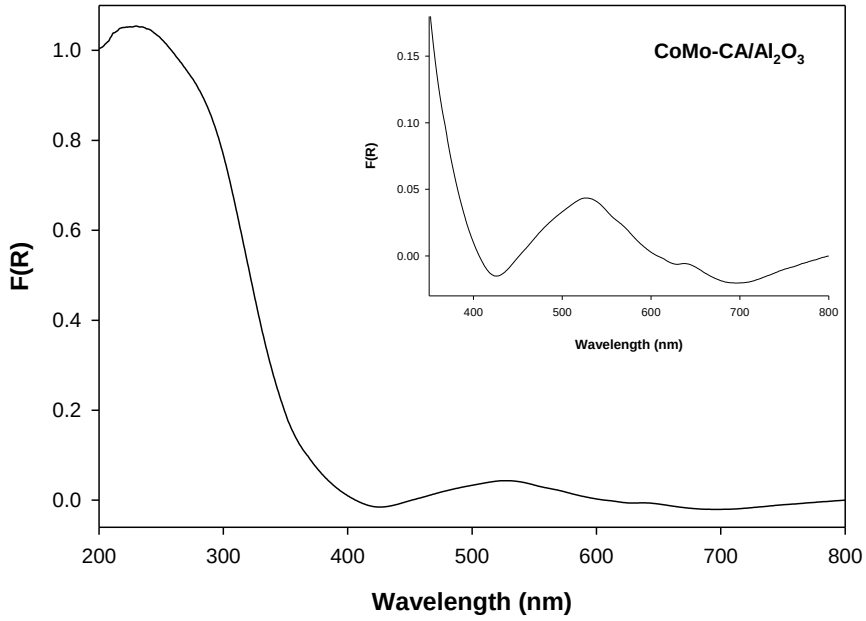

Figure 3.11: UV-Vis spectra for CoMo-CA/Al_2O_3 catalyst (Inset: visible region 400-700 nm showing the d-d transition).

3.5.1.1. Band Gaps of CoMo catalysts

The UV-vis allows the evaluation of the dispersion molybdenum oxides on the support, this is because the electronic edge (E_g) of the ligand-to-metal CT transitions in oxometallates species correlates with the number of neighbouring Mo centers (N_{Mo}) in that species (Tian *et al*., 2010); (Weber, 1995). The correlation between edge energy and the number of the nearest neighbours of MoO_x is calculated by using the formula (N_{Mo} = 16-3.8E_g) presented by Tian *et al*., (2010). CoMo/Al_2O_3 catalyst has the highest number of next nearest neighbours of 3.86, suggesting a MoO_3-like surface composition. While CoMo-EDTA/Al_2O_3 (~2.61), CoMo-AA/Al_2O_3 (~1.34), and CoMo-CA/Al_2O_3 (~1.31) catalysts had the lowest N_{Mo}. Their low N_{Mo} values indicate that chelated catalysts contained a mixture of molybdate species on the support such as $[MoO_4]^{2-}$ and $[Mo_7O_{24}]^{6-}$. The absorption band energy (E_g) is used to compare the dispersion of Mo species for the oxidic catalysts (Zhang *et al*., 2019). Band gaps for CoMo/Al_2O_3, CoMo-EDTA/Al_2O_3, CoMo-AA/Al_2O_3, and CoMo-CA/Al_2O_3 are shown in (**Figures 3.12-3.15**). **Figure 3.12-Figure 3.15** show the E_g values for CoMo catalysts as ~3.195 eV, ~3.859 eV, ~3.525 eV, and ~3.867 eV. The increase in E_g value from unchelated to chelated catalysts confirm that Mo particles are gradually decreasing, hence more dispersed Mo species will be obtained as the particles decrease, leading in the formation of more MoS_2 (Castillo Villaloń al., 2015; Shan *et al*., 2015). The band gap energies are summarized in **Table 3.9**, and the least square regression was employed for the determination of Kubelka-Munk parameters. Assuming indirect and direct allowed electron transitions ($\eta = 2$).

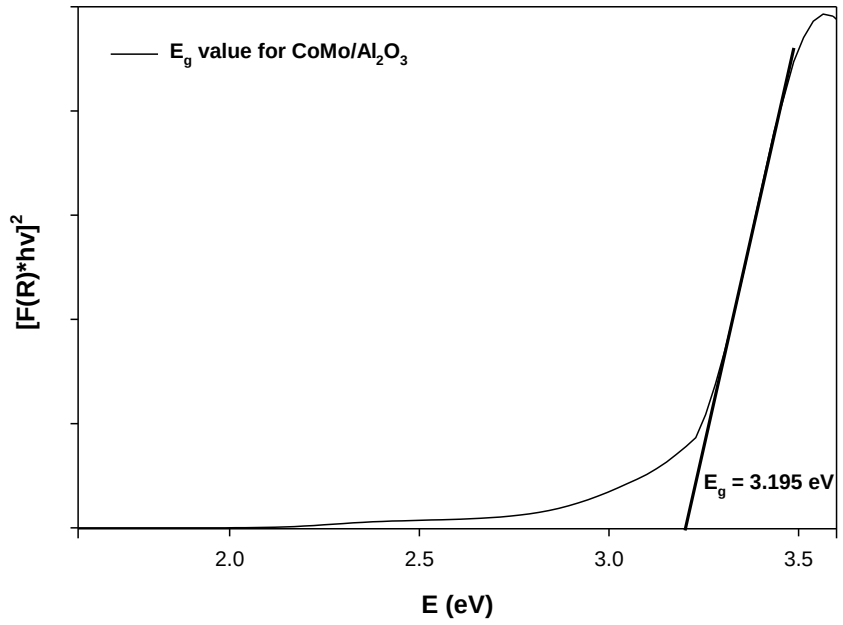

Figure 3.12: The E_g value for $CoMo/Al_2O_3$ obtained from a UV-Vis spectrum.

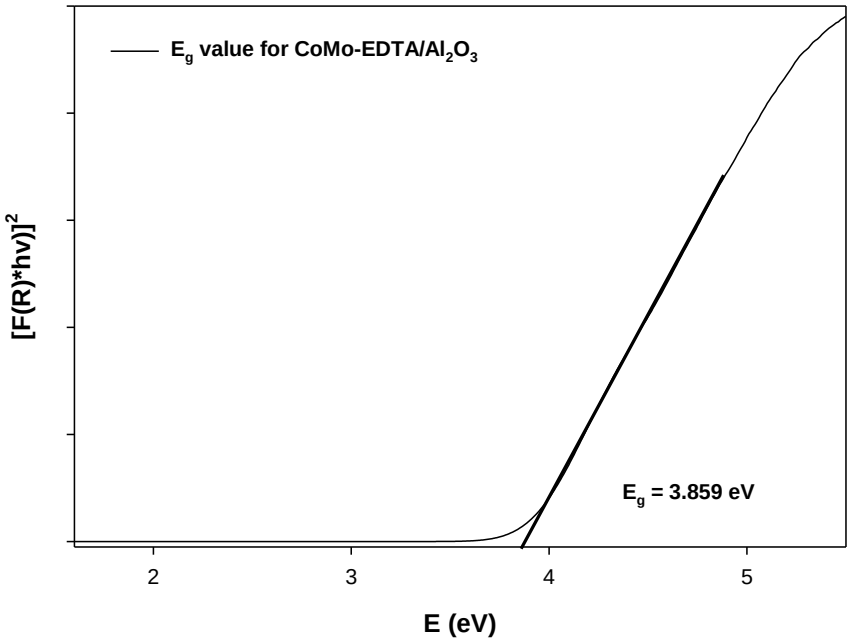

Figure 3.13: The E_g value for $CoMo\text{-}EDTA/Al_2O_3$ obtained from a UV-Vis spectrum.

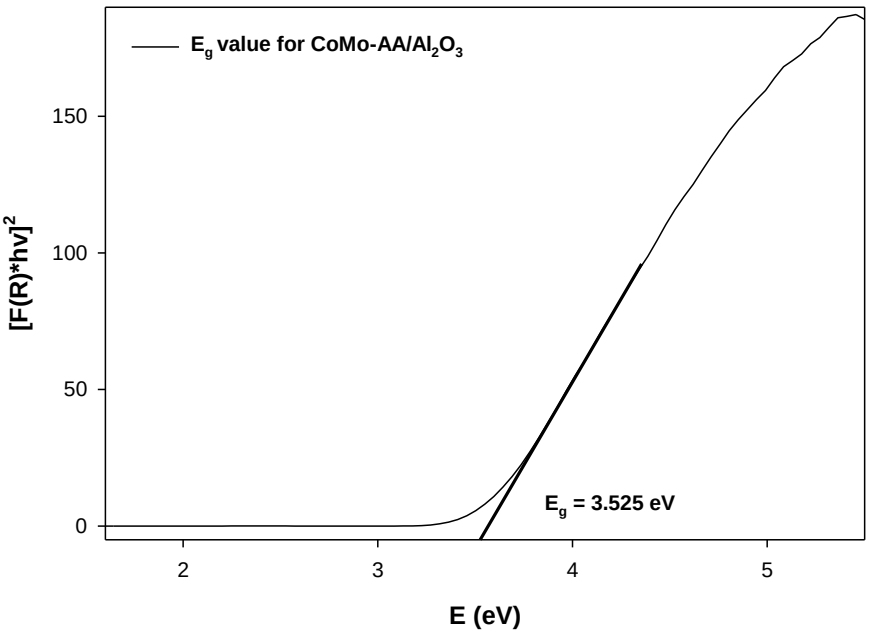

Figure 3.14: The E_g value for CoMo-AA/Al_2O_3 obtained from a UV-Vis spectrum.

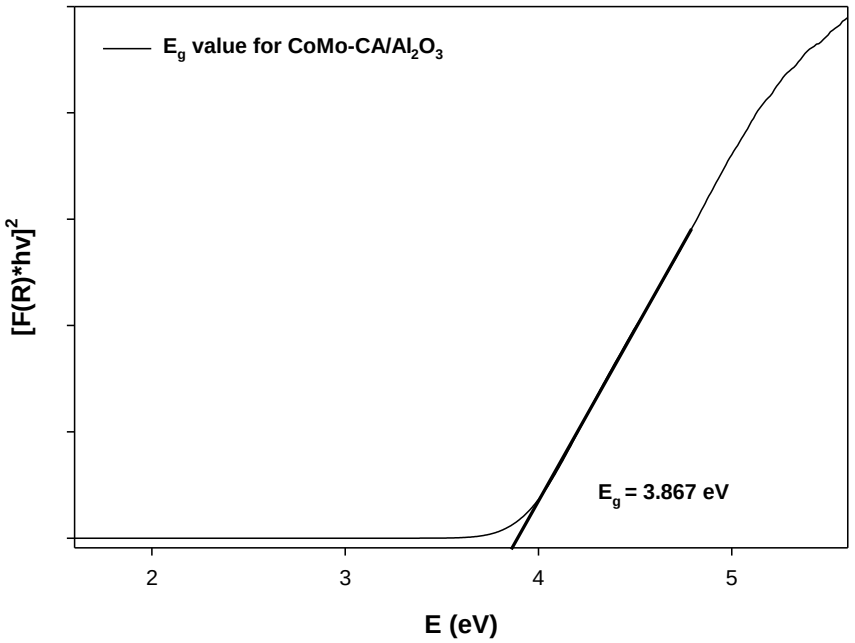

Figure 3.15: The E_g value for CoMo-CA/Al_2O_3 obtained from a UV-Vis spectrum.

The plot of the number of molybdenum next nearest neighbours and E_g values are estimated from the UV-DRS absorption edge energy for CoMo catalysts are shown in **Figure 3.16**. The UV-Vis allowed to evaluate the dispersion of the supported molybdenum oxides. A linear inverse correlation was found between the E_g value and the number of bridging Mo-O-Mo covalent bonds around the central Mo^{6+} cation ($N_{Mo\text{-}O\text{-}Mo}$). The application of this allowed for the determination of the molecular structures of MoO_x species present in supported MoO_x catalysts (Tian *et al*., 2010). The correlation between the edge

energy and number of bridging Mo-O-Mo covalent bonds around the central Mo^{6+} cation was calculated in the formula ($N_{Mo\text{-}O\text{-}Mo} = 11.8\text{-}26E_g$) shown by Tian *et al*., (2010). With increasing E_g number, the $N_{Mo\text{-}O\text{-}Mo}$ decreases. $CoMo/Al_2O_3$ catalyst had the highest $N_{Mo\text{-}O\text{-}Mo}$ (~3.493) while for the chelated $CoMo\text{-}AA/Al_2O_3$, $CoMo\text{-}EDTA/Al_2O_3$ and $CoMo\text{-}CA/Al_2O_3$, these values are ~, 2.635, ~1.767, and ~1.746, respectively, According to the results obtained in **Table 3.9**, $CoMo/Al_2O_3$ consists of $[Mo_7O_{24}]^{6-}$ clusters and traces of $[Mo_8O_{26}]^{4-}$ clusters, $CoMo\text{-}AA/Al_2O_3$ resulted in $[Mo_7O_{24}]^{6-}$ clusters and traces of isolated $[MoO_4]^{-2}$, while $CoMo\text{-}EDTA/Al_2O_3$ and $CoMo\text{-}CA/Al_2O_3$ resulted in alternating MoO_4/MoO_6 and Mo_2O_7 dimers (Tian *et al*., 2010). It is important to clarify MoO_x structures as they are related to the catalytic activity of the HDS catalysts. Mo is considered as an active ingredient of the catalyst, and it is present as a mixture of MoO_4/MoO_6 and polymolybdate clusters, and the former being the main species (Cattaneo *et al*., 1999) on the catalyst. These structure helps in understanding the factors that influence the formation of the active sites on the support during sulfidation, and this study was conducted using EXAFS, UV-Vis, and Raman spectroscopy (Cattaneo *et al*., 1999; Tian *et al*., 2010). The smaller the molybdates are easier to sulfide because no Mo-O-Mo bridging bonds must be cleaved (Cattaneo *et al*., 2001), therefore, in this study we would expect more active phases for $CoMo\text{-}CA/Al_2O_3$ and or $CoMo\text{-}EDTA/Al_2O_3$ as they possess less complex Mo structures.

Table 3.9: Band gap energy and the average number of bridging Mo-O-Mo covalent bonds around the central Mo^{6+} cation ($N_{Mo\text{-}O\text{-}Mo}$) as estimated from the UV-Vis E_g for the oxide CoMo catalysts.

Catalyst	**E_g values**	**$N_{Mo\text{-}O\text{-}Mo}$**
$CoMo/Al_2O_3$	3.195	3.493
$CoMo\text{-}AA/Al_2O_3$	3.525	2.635
$CoMo\text{-}EDTA/Al_2O_3$	3.859	1.767
$CoMo\text{-}CA/Al_2O_3$	3.867	1.746

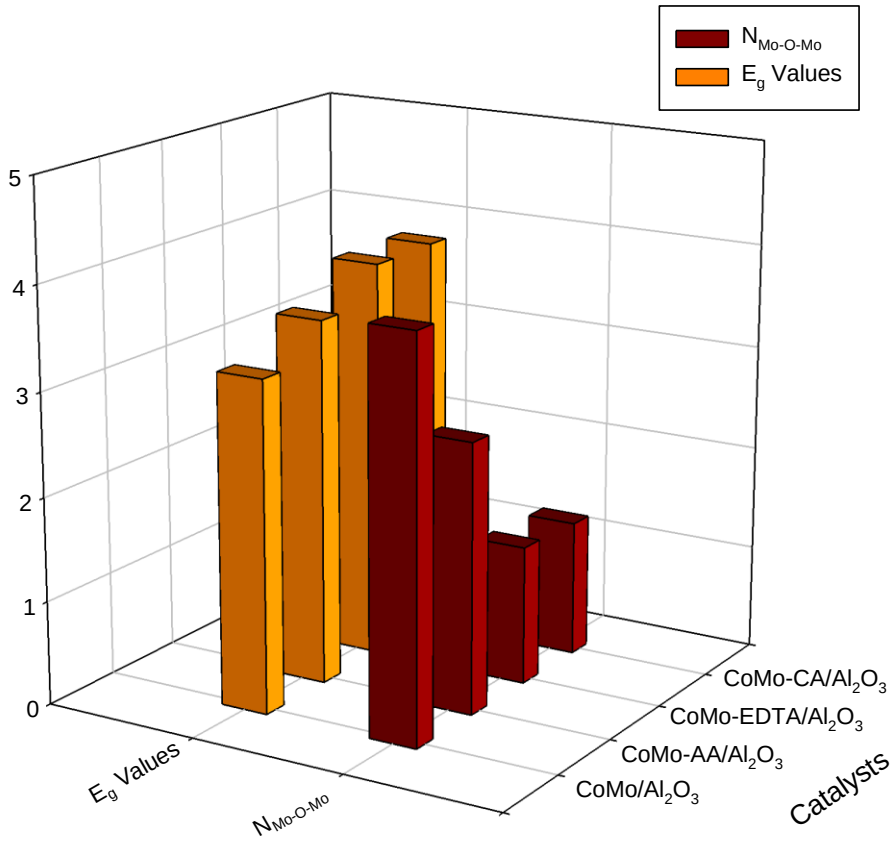

Figure 3.16: The number of molybdenum next nearest neighbours as estimated from the UV-Vis absorption edge energy ($N_{Mo\text{-}O\text{-}Mo} = (11.8\text{-}2.6E_g)$).

3.5.2 Fourier transform infrared spectroscopy (FT-IR)

The FT-IR spectra of synthesized $CoMo/Al_2O_3$, $CoMo\text{-}AA/Al_2O_3$, $CoMo\text{-}EDTA/Al_2O_3$ and $CoMo\text{-}CA/Al_2O_3$ are presented in **Figure 3.17**. The band at 798 and 753 cm^{-1} was attributed to the Mo-O-Mo vibration. The Mo=O stretching vibration is located at 932 cm^{-1}. For the chelated catalysts at 1588 cm^{-1}, the absorption band is could be assigned to $-COO^-$ stretch preserved after impregnation. The band at 14037 cm^{-1} was attributed to the hydrogen bonded $-COO^-$ vibrations due to the presence of water. The band at 1385 cm^{-1} is due to the interaction between $-COO^-$ and -OH groups on the support (Escober, 2017). The weak peak found at 1073 cm^{-1} was associated to the C-O bond from the carboxylic groups present in the citrate (Carrier *et al.*, 2003). The vibration band at 978 cm_{-1} was assigned to Mo-N band for $CoMo\text{-}EDTA/Al_2O_3$ catalyst. The band found in the 430-450 cm^{-1} and 510 cm^{-1} regions are assigned to the O-Mo-O terminal stretching (Cabello *et al.*, 2002; Vatutina *et al.*, 2019). The vibration band at 786 cm^{-1} was associated to Mo-O-Mo bridge stretching and can also be assigned to vibrations of $Co\text{-}O_6$ band and water liberations. (Cabello *et al.*, 2002). While at 521 cm^{-1} and 612, 628, 622 cm^{-1} is attributed to Mo-O-Mo band.

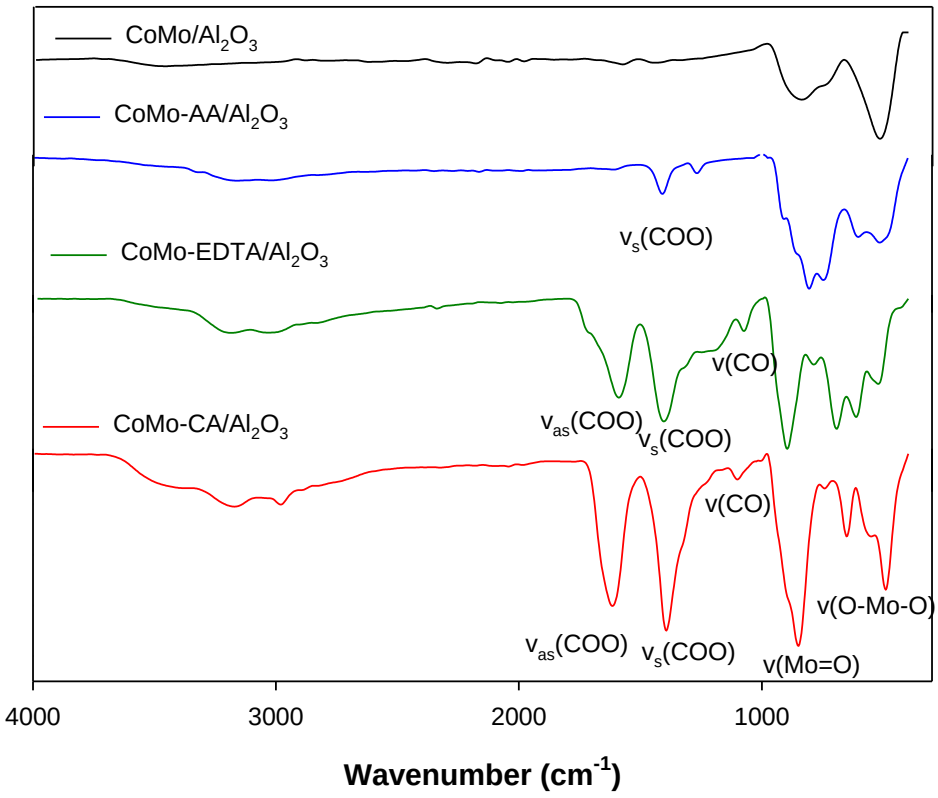

Figure 3.17: FT-IR spectra of $CoMo/Al_2O_3$, $CoMo\text{-}AA/Al_2O_3$, $CoMo\text{-}EDTA/Al_2O_3$ and $CoMo\text{-}CA/Al_2O_3$ catalyst.

3.5.3 N_2 Adsorption-desorption isotherms for supported catalysts

The textural characteristics of catalysts were determined by BET and BJH method. BET surface areas of the samples, total pore volume and average particle size of alumina supported catalysts are reported in **Table 3.10**. N_2 Adsorption-desorption isotherms of $CoMo/Al_2O_3$ catalysts, with and without chelating agents are given in **Figure 3.18**. Results shows that the structure does not change after the addition of chelating agents, this signifies that the alumina support is stable (Badoga, 2012). The obtained results upon addition of chelating ligand leads to slightly different textural characteristic. The pore size significantly affects the stacking of active phase leading to clearly different active sites for the catalyst. The larger pore sized catalysts will provide the accessibility of reaction to corner sites, contributing more direct desulfurization reaction, they also enhance the diffusion rate of reaction species (Zhang, *et al*., 2017); (Rashidi *et al*., 2013). The smaller pore size promotes the accessibility of refractory sulfur containing compounds to the edge sites and more hydrogenation reaction occurs (Zhang, *et al*., 2017), and they also supply the reacting sites.

The surface area and average pore size of $CoMo/Al_2O_3$ was found to be 16.6255 m^2/g and 33.6520 (Å) as shown in **Table 3.10**. Upon modification from the addition of chelating agent, the following results

were obtained; CoMo-AA/Al_2O_3 has the surface area of (19.6998 m^2/g) and average pore size (44.0845 Å), CoMo-EDTA/Al_2O_3, has the surface area of (22.8460 m^2/g) with the pore size of (40.9353), while CoMo-CA/Al_2O_3 has a surface area of (24.2398 m^2/g) and the average pore size of (44.7037 Å). All the chelated catalysts had higher surface area the unchelated catalyst because in the addition of the chelating ligand molecules interact more with the metal components, resulting in better metal dispersion on the support. The surface areas of the catalysts are in the following order; CoMo-CA/Al_2O_3 > CoMo-EDTA/Al_2O_3 > CoMo-AA/Al_2O_3 > CoMo/Al_2O_3. It can be observed that of all catalysts CoMo-CA/Al_2O_3 had the highest surface are and this was due to high interaction of CA with the metals, lessoning the number of pores that were blocked.

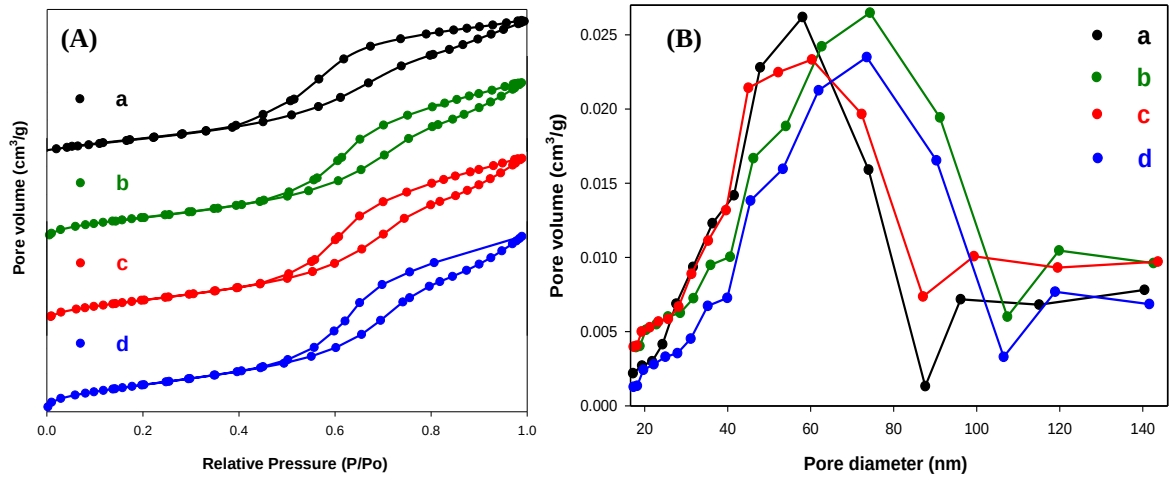

Figure 3.18: (A) N_2 adsorption-desorption isotherms and (B) pore size distribution patterns of series CoMo synthesized catalysts. (a) CoMo/Al_2O_3, (b) CoMo-AA/Al_2O_3, (c) CoMo-EDTA/Al_2O_3, (d) CoMo-CA/Al_2O_3.

Table 3.10: Textural properties of Al_2O_3 and CoMo catalysts.

Sample	**BET surface area**	**Average pore size**	**ICP-OES**	
	(m^2 g^{-1})	**(Å)**	**Co Metal (wt.%)**	**Mo Metal (wt.%)**
CoMo/Al_2O_3	16.6255	33.6520	0.3035	1.5950
CoMo-EDTA/Al_2O_3	22.8460	40.9353	0.0613	1.8475
CoMo-AA/Al_2O_3	19.6998	44.0845	1.0891	1.3954
CoMo-CA/Al_2O_3	24.2398	44.7037	0.2631	0.7511

Generally, the surface area and average pore sizes are close (**Table 3.10**). The results obtained in **Figure 3.18A** indicates that all isotherms are type IV in line with the classification by IUPAC, and this suggests a mesoporous material (Wang *et al*., 2018); (Shan *et al*., 2016). Their hysteresis loops are in the range of relative pressure (P/Po) = 0.6 -0.9 and are type H_2 (Zhang *et al*., 2017), indicating the presence of mesoporous structure. The BJH pore-size distribution plots for CoMo/Al_2O_3, CoMo-AA/Al_2O_3, CoMo-EDTA/Al_2O_3 and CoMo-CA/Al_2O_3 are illustrated in **Figure 3.18B.** The material series displayed a mesopore distribution between 0.6-0.65 nm, upon addition of chelating agent the shape of the isotherm does not change thus indicating the preservation of pore shapes (Nadeina *et al*., 2019). ICP-OES analysis was performed to provide information on the amount of metal composition of each catalyst. For the CoMo catalysts, the Mo content is in the range of 1.8-0.8 wt.% and the Co content was in the range of 1.1-0.06 wt.% as shown in **Table 3.10**.

3.5.4 XPS analysis

XPS analysis is a useful method of obtaining the surface chemistry of various Mo, Co, and S components in multiple oxidation states, as well as obtaining the phases present on the catalysts, which affect the catalytic activity and deactivation through defective sulfidation, metal-support interactions, coke deposition, and reoxidation (Radishi *et al*., 2003). The binding energies (BE's) of Mo 3d, Co 2p, C 1s, S 2p, Al 2p and Al 2s (sulfided samples) were determined by fitting the measured spectra. The Mo 3d and Co 2p spectra were deconvoluted using Origin software. These deconvolutions based on the peak areas relative to each chemical species present on the surface of the solid, allows for the estimation of Mo atoms forming the MoS_2 slabs (Mo sulfidation degree) and Co atoms forming CoMoS phase which is responsible for the activity of the catalyst.

XPS analysis was performed to investigate the chemical species present on the surface of the sulfided CoMo/Al_2O_3 and CoMo-EDTA/Al_2O_3 catalysts, shown in **Figure 3.19** and **Figure 3.20**. The survey scan spectrum shown in **Figure 3.19(a**) and **Figure 3.20(a)** demonstrated the presence of the key elements, Co 2p, Mo 3d, S 2p, O 1s, C 1s, Al 1p and Al 1s, respectively. The binding energies caused by peak splitting due to different oxidation states are between 775-805 eV and 224-238 eV are ascribed to Co 2p and Mo 3d spectra (**Table 3.11**) (Zhang *et al*., 2017). A peak at the binding energy of O 1s at 530 eV is observed for both catalysts, due to the presence of oxygen-containing groups on the alumina support. Binding energy of sulfur (S 2p) in the range of 160.8-166.9 eV is characterised for bridging ligands S^{2-}/S_2^{2-} type in MoS_2 surrounding (Li *et al*., 2014; Grumelli *et al*., 2007) and oxysulfide entities present. The binding energies at 117 and 72 eV corresponds to Al 2s and Al 2p, respectively, which is evident of the presence of alumina support (Wang *et al*., 2017; Lui *et al*., 2019). All the distributions of these elements present in CoMo/Al_2O_3 and CoMo-EDTA/Al_2O_3 catalysts are shown in **Table 3.11**.

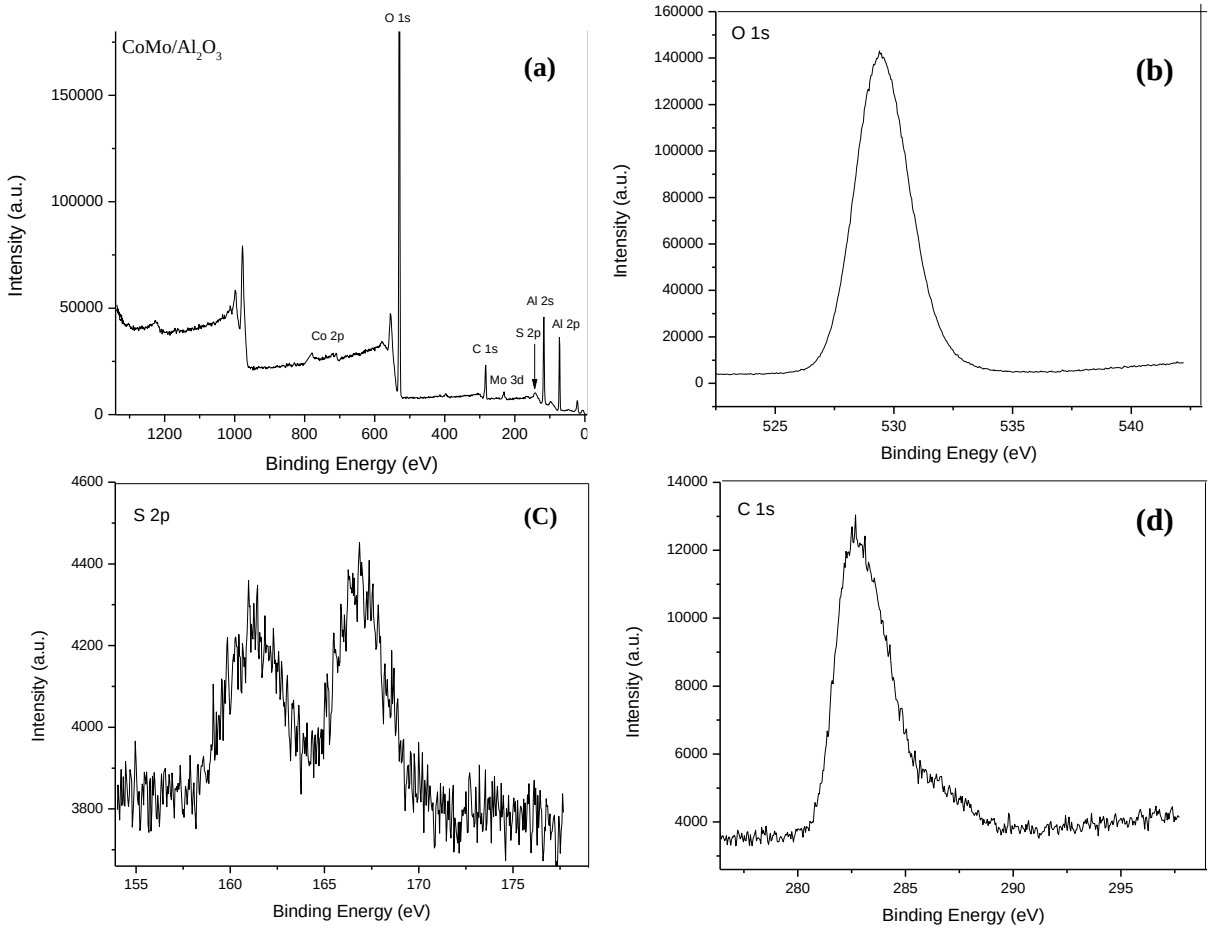
CoMo/Al2O3
(a)
O 1s
Co 2p
C 1s
Mo 3d
S 2p
Al 2s
Al 2p
Intensity (a.u.)
Binding Energy (eV)
O 1s
(b)
Intensity (a.u.)
Binding Enegy (eV)
S 2p
(C)
Intensity (a.u.)
Binding Energy (eV)
C 1s
(d)
Intensity (a.u.)
Binding Energy (eV)

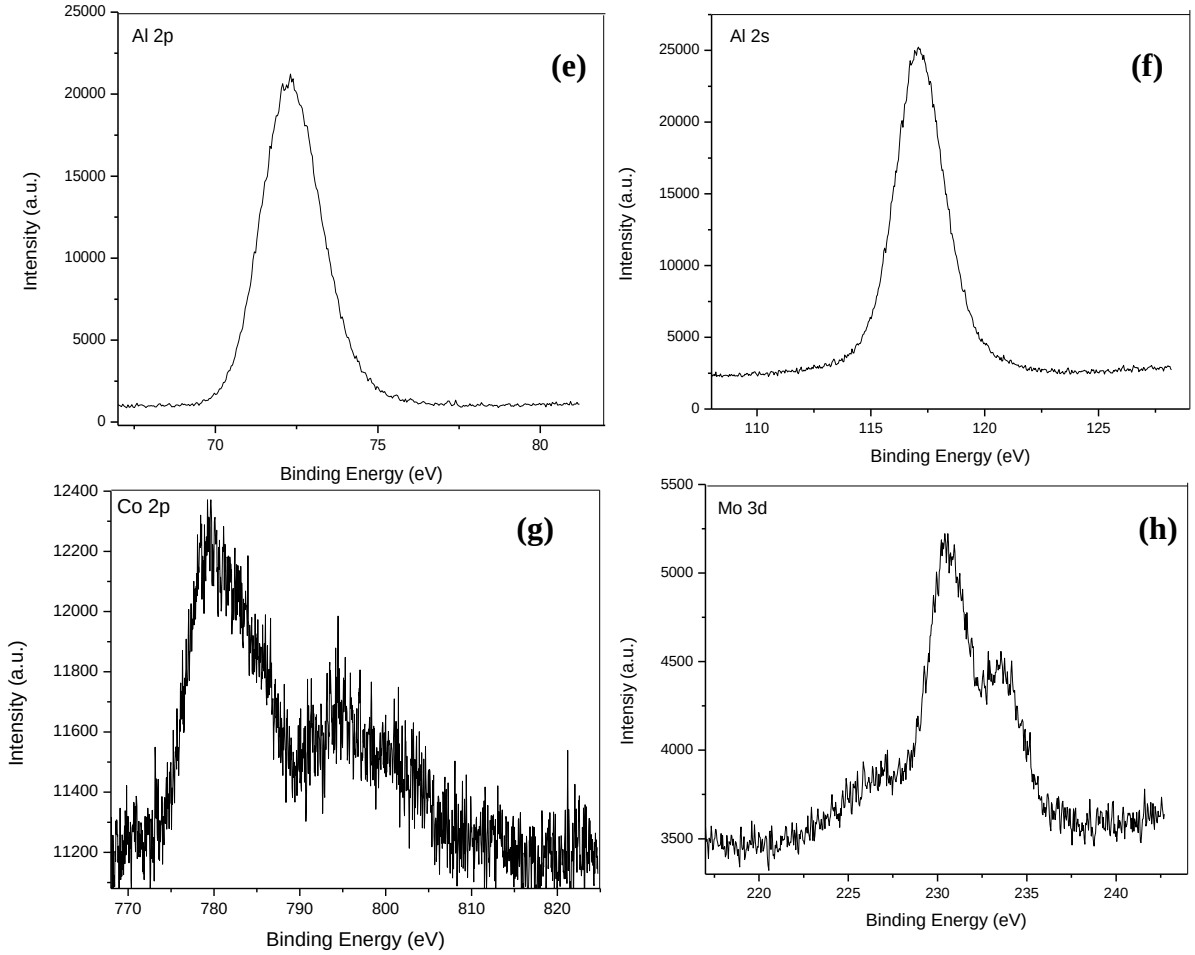

Figure 3.19: XPS spectra for (a) $CoMo/Al_2O_3$ survey spectrum with different elemental contributions, (b) O 1s, (c) S 2p, (d) C 1s, (e) Al 2p, (f) Al 2s, (g) Co 2p, (h) Mo 3d.

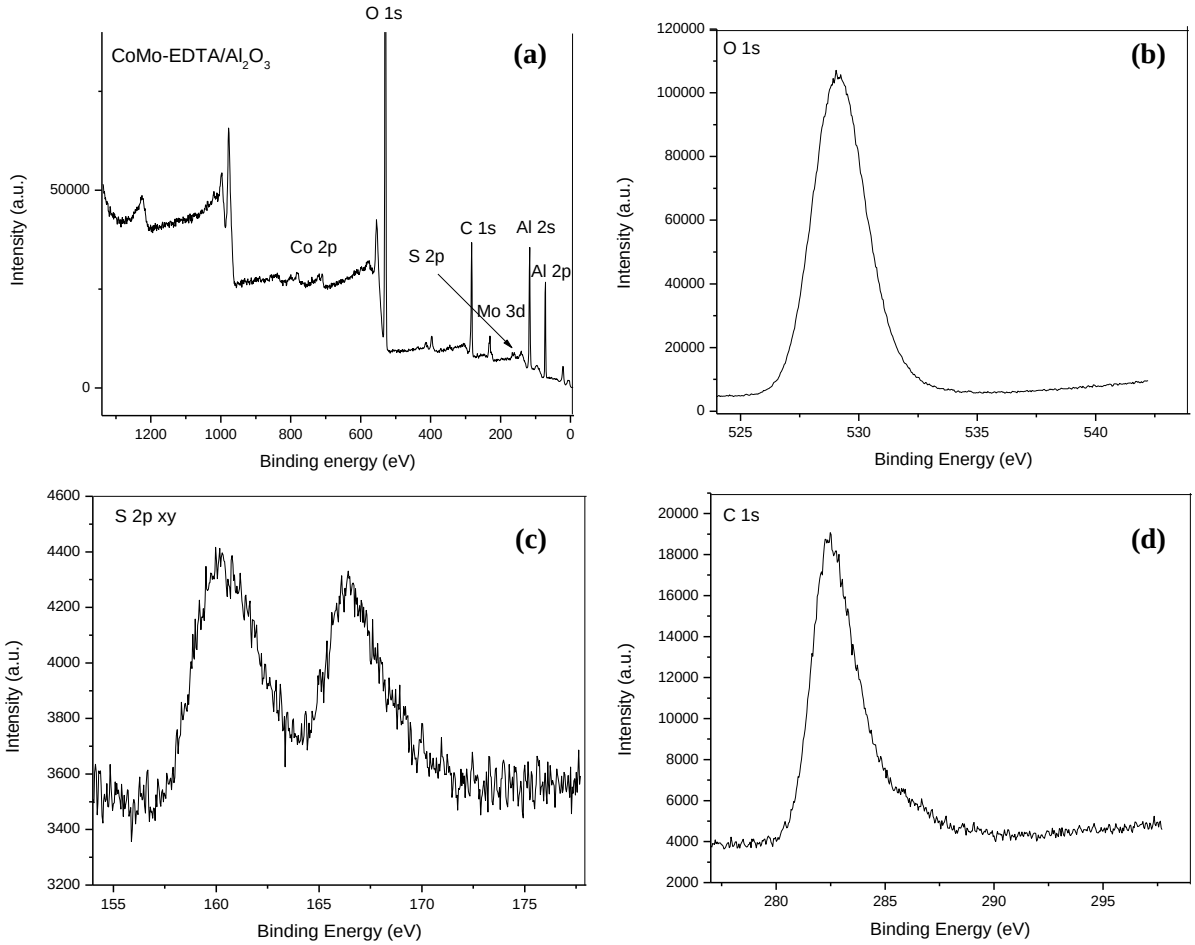
O 1s
CoMo-EDTA/Al2O3
(a)
Intensity (a.u.)
50000
0
Co 2p
S 2p
C 1s
Al 2s
Al 2p
Mo 3d
1200
1000
800
600
400
200
0
Binding energy (eV)
O 1s
(b)
120000
100000
80000
60000
40000
20000
0
525
530
535
540
Binding Energy (eV)
S 2p xy
(c)
4600
4400
4200
4000
3800
3600
3400
3200
155
160
165
170
175
Binding Energy (eV)
C 1s
(d)
20000
18000
16000
14000
12000
10000
8000
6000
4000
2000
280
285
290
295
Binding Energy (eV)

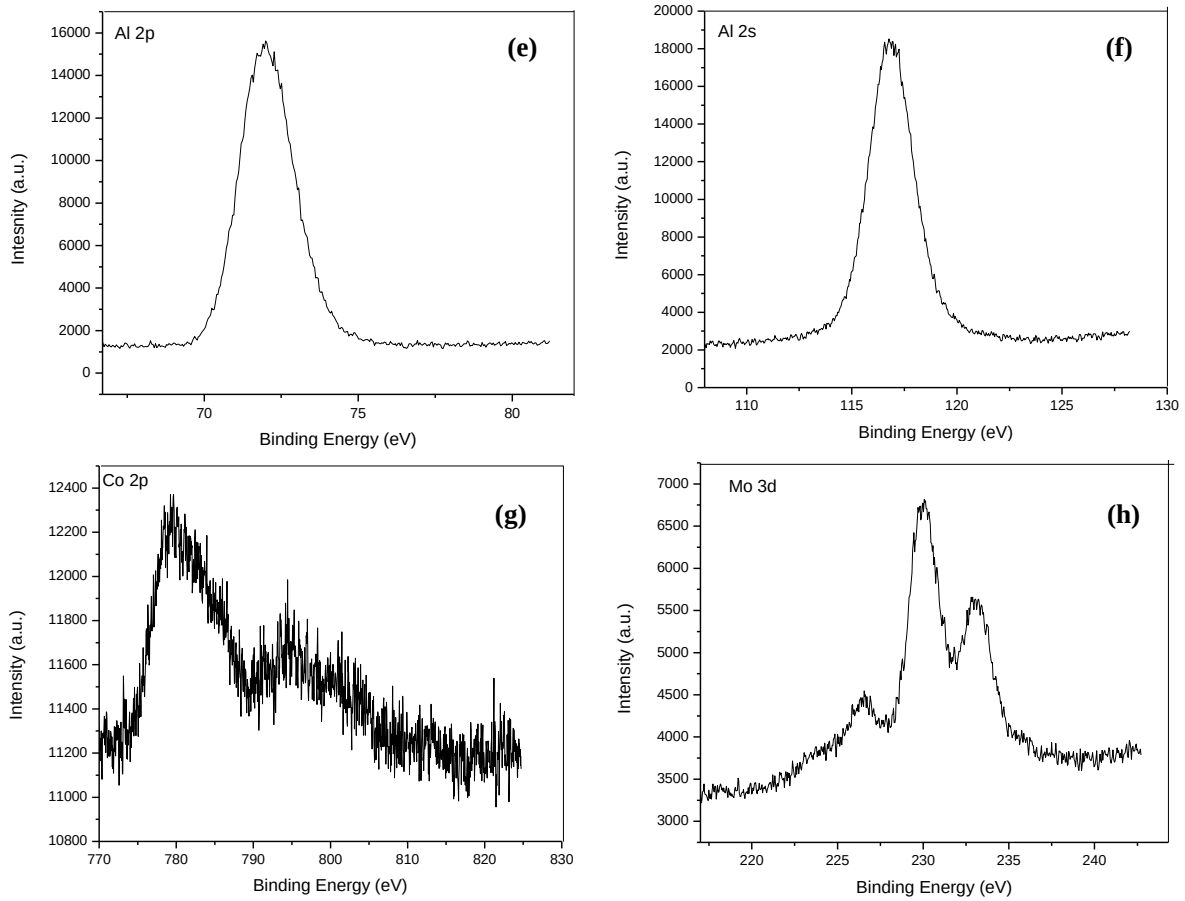

Figure 3.20: XPS spectra for (a) CoMo-EDTA/Al_2O_3 survey spectrum with different elemental contributions, (b) O 1s, (c) S 2p, (d) C 1s, (e) Al 2p, (f) Al 2s, (g) Co 2p, (h) Mo 3d.

Table 3.11: Binding energies determined in XPS experiments for CoMo/Al_2O_3 and CoMo-EDTA/Al_2O_3.

Elements (eV)	**CoMo/Al_2O_3**	**CoMo-EDTA/Al_2O_3**
C 1s	282.2	282.5
O 1s	529.5	529.0
Mo 3d	230.2; 233.5; 226.7	226.0; 230.1; 233.4
Co 2p	780.5; 795.0	778.9; 793.1
S 2p	160.8; 166.7	159.5; 166.8
Al 2p	72.2	72.1
Al 2s	117.1	116.4

To investigate different phases within the catalysts; Mo 3d, Co 2p and S 2p spectra are carefully deconvoluted and presented in **Figure 3.21**. A deconvolution was used to fit the individual peaks present in the catalyst's surface. XPS analysis is one of a useful method in obtaining multiple oxidation states, gaining insight into dispersion of active phases, as well as obtaining different phases for the catalysts, which affects the catalytic activity, support-metal interactions and reoxidation (Radishi *et al*. 2013). The measurements were carried out for $CoMo/Al_2O_3$, $CoMo\text{-}EDTA/Al_2O_3$ catalysts. The deconvolutions were performed to quantify and evaluate Mo 3d as MoS_2 (Mo^{4+} $3d_{5/2}$, $3d_{3/2}$), MoO_xS_y (Mo^{5+} $3d_{5/2}$, $3d_{3/2}$), MoO_x (Mo^{6+} $3d_{5/2}$, $3d_{3/2}$), and sulfide (S^{2-}, S_2^{2-}) and sulfate (SO_x) contributions to estimate the percentage of catalyst activity (Rashidi *et al*., 2013). Co 2p core-level spectra are also decomposed into three contributions, corresponding to Co $2p_{3/2}$ and Co $3p_{1/2}$, evaluated as Co_9S_8, CoMoS, and Co^{2+} in oxidic environment (CoO_x and $CoAl_2O_4$) phases, respectively (Zhang *et al*., 2019).

For Mo^{4+} sulfide ($3d_{5/2}$ BE = 228.8-229.1; $3d_{3/2}$ BE = 232.0-232.1 eV), Mo^{5+} oxysulfide ($3_{d/5}$ BE = 229.6-230.5 eV; $3d_{2/3}$ BE = 232.9-233.4 eV), and Mo^{6+} oxide ($3d_{5/2}$ BE = 232.0-233.0 eV; $3d_{3/2}$ BE = 235.3-236.0 eV) (Frizi *et al*., 2008; Gandubert *et al*., 2007; Nadeina *et al*., 2018; Ninh *et al*., 2011; Nikulshin *et al*., 2016). According to data available in the literature (Gandubert *et al*., 2010; Dupin *et al*., 2001), the deconvolution of the Co 2p XPS for CoO_x (Co^{2+}) is observed between (780.8-793.1 eV), for Co_9S_8 at (777.6-793.2 eV), and for CoMoS between (778.3-793.9 eV) (**Figure 3.21a** & **Figure 3.21c**) (Budukva *et al*., 2019). The contribution of the S 2s peak to the total of the Mo 3d spectrum with energy range of (BE = 225.9-226.3 eV) was identified in **Figure 3.21b** and **Figure 21d** (Beccat *et al*., 1995). Two doublets corresponding to the S $2p_{3/2}$, S $2p_{1/2}$ and SO_4^{2-} are observed. The first one with S $2p_{3/2}$ peak at 162.5 eV can be assigned to S^{2-}, while the second one with the binding energy of 162.1 eV can be attributed to polysulfide (S_2^{2-}) (**Figure 3.21e**). The S $2p_{3/2}$ and S $2p_{1/2}$ for $CoMo\text{-}EDTA/Al_2O_3$ showed characteristic peaks at 162.1 eV, 162.7 eV, and the characteristic peaks of SO_4^{2-} were also observed at 163.2 and 167.1 eV (**Figure 3.21f**) (Contreras *et al*., 2016). Both Mo 3d spectra include the S 2s peaks at 226.0 and 226.1 eV, respectively (Huang *et al*., 2018).

The addition of chelating agent resulted in a shift of Mo $3d_{5/2}$ and Mo $3d_{3/2}$ peak to lower BE **(Table 3.12**) and is indicative of weak metal-support interaction, leading to better dispersion of active phase, hence increase catalytic activity (Muhammad *et al*., 2019). The shift was also noticed in Co $2p_{3/2}$ and Co $2p_{1/2}$ bonding energies for the chelated catalyst (**Table 3.13**). XPS show that the most abundant species is MoS_2 which could not be identified by the XRD analysis due to dispersion. To quantify the relative percentage of Mo^{4+}, Mo^{5+}, and Mo^{6+} species in the total Mo component, the following formula was used:

$$[Mo^{4+}](\%) = \frac{A_{Mo^{4+}}}{A_{Mo^{4+}} + A_{Mo^{5+}} + A_{Mo^{6+}}} \times 100\% \qquad (3.1)$$

In equation (3.1), [Mo^{4+}] represents the sulfidation degree of the samples, A_{Mo}^{4+}, A_{Mo}^{5+}, A_{Mo}^{6+} are the areas of the peaks which assigned to Mo^{4+}, Mo^{5+}, and Mo^{6+} species, respectively (Wang *et al*., 2017; Chen *et al*., 2017).

The percentage of Co_9S_8, CoMoS, and Co^{2+} in the total Co species were calculated by the equation:

$$[CoMoS](\%) = \frac{A_{CoMoS}}{A_{CoMoS}+A_{C_9S_8}+A_{Co^{2+}}} \quad (3.2)$$

where [CoMoS] is the sulfidation degree of the samples investigated, and A_{CoMoS}, A_{Co9S8}, and A_{Co}^{2+} are the areas of the peaks assigned to CoMoS, Co_9S_8, and Co^{2+} species (Wang *et al*., 2017; Chen *et al*., 2017).

The percentage increase of Mo^{4+} in CoMo-EDTA/Al_2O_3 (**Table 3.14**) was due to the addition of chelating agent and was explained by the weakened metal-support interaction and β-$CoMoO_4$ formation (Zhang *et al*., 2019). Weak metal-support interaction favoured the Mo sulfidation forming more MoS_2 active phase which can provide the edge planes to accommodate the Co species as a promoter (Zhang *et al*., 2019). The presence of the chelating agent led to a gradual decrease of MoO_xS_y and MoO_x species (Huang *et al*., 2018). The CoMo/Al_2O_3 resulted in lower percentage of Mo^{4+} and CoMoS, which indicates partial sulfidation, and this agrees with TEM analysis as this catalyst resulted in longer slab length, which could result to lower Co decoration of the MoS_2, forming fewer CoMoS phase (Lui *et al*., 2018). The use of EDTA played a role in Co phases, it resulted in a higher percentage for CoMoS phase, by allowing Co and Mo species to interact easily, and this can be related to a faster sulfidation of molybdenum while Co is complexed with EDTA to a point where more MoS_2 phases have formed, leading to a better availability of Co decorating MoS_2 layers, hereby enhancing HDS activity (Bui *et al*., 2019). The formation of Co-EDTA complex also prevents the formation of $CoAl_2O_4$ which results in the formation of inactive phase (Co_9S_8) (Vatutina *et al*., 2019).

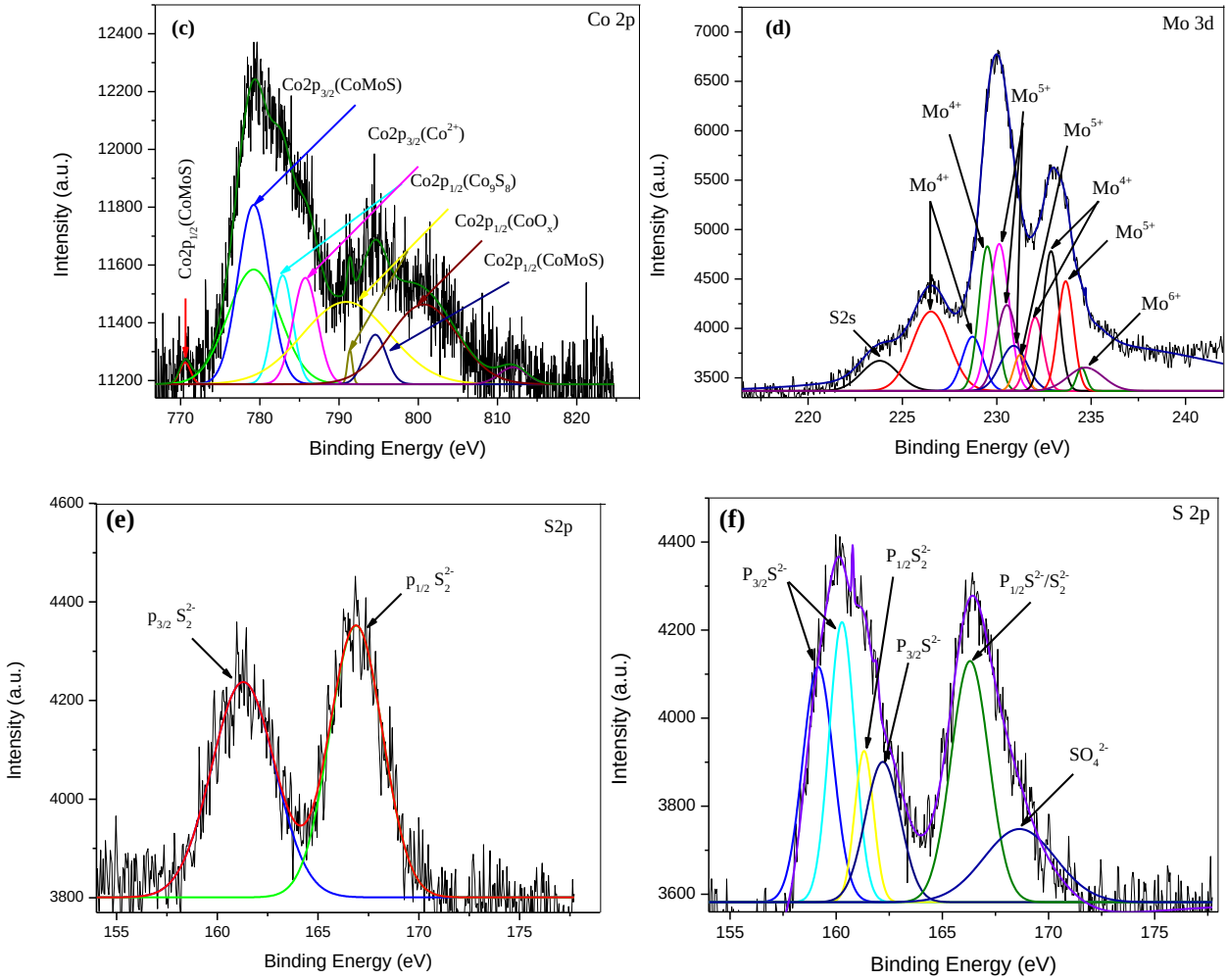

Figure 3.21: XPS deconvolution of $CoMo/Al_2O_3$ and $CoMo\text{-}EDTA/Al_2O_3$ catalysts. Where (a) Co 2p for $CoMo/Al_2O_3$, (b) Mo 3d for $CoMo/Al_2O_3$, (c)Co 2p for $CoMo\text{-}EDTA/Al_2O_3$, (d) Mo 3d for $CoMo\text{-}EDTA/Al_2O_3$, (e) S 2p for $CoMo/Al_2O_3$, (f) S 2p for $CoMo\text{-}EDTA/Al_2O_3$.

Table 3.12: XPS parameters of the different distributions (BE) of Mo 3d obtained for unchelated and chelated $CoMo/Al_2O_3$ catalysts.

Catalysts	BE (eV) Mo $3d_{5/2}$			BE (eV) Mo $3d_{3/2}$		
	Mo^{4+}	Mo^{5+}	Mo^{6+}	Mo^{4+}	Mo^{5+}	Mo^{6+}
$CoMo/Al_2O_3$	229.1	230.5	232.5	232.1	233.9	236.7
$CoMo\text{-}EDTA/Al_2O_3$	229.2	230.0	232.0	232.0	233.6	234.5

Table 3.13: XPS parameters of the different contributions of Co 2p obtained for unchelated and chelated $CoMo/Al_2O_3$ catalysts.

Catalysts	BE (eV) Co $2p_{3/2}$			BE (eV) Co $2p_{1/2}$		
	Co_9S_8	CoMoS	Co^{2+}	Co_9S_8	CoMoS	Co^{2+}
$CoMo/Al_2O_3$	779.3	777.5	786.0	791.4	794.4	798.2
$CoMo\text{-}EDTA/Al_2O_3$	770.5	779.6	783.3	791.2	794.3	797.9

Table 3.14: Percentage abundance of Co 2p and Mo 3d for $CoMo/Al_2O_3$ and $CoMo\text{-}EDTA/Al_2O_3$ catalysts.

Catalysts	Co distribution (%)			Mo distribution (%)		
	Co_9S_8	CoMoS	Co^{2+}	Mo^{4+}	Mo^{5+}	Mo^{6+}
$CoMo/Al_2O_3$	37	45	18	45	48	7
$CoMo\text{-}EDTA/Al_2O_3$	17	68	14	63	21	16

3.5.5 Energy Dispersion Spectroscopy (EDS)

(a) CoMo Oxide catalysts

EDS analysis studies the composition and the elements present in the compound; in this case it studies the elements present on the bulk sample of the synthesized catalyst. This technique makes it possible to obtained information on elemental composition of a certain area of the catalyst sample, which helps in learning the distribution and atomic composition. The EDS of $CoMo/Al_2O_3$, $CoMo\text{-}EDTA/Al_2O_3$, $CoMo\text{-}AA/Al_2O_3$ and $CoMo\text{-}CA/Al_2O_3$ are presented in **Figure 3.22**. Qualitative atomic percentage of Co and Mo in HDS catalysts are shown in **Table 3.15**.

The presence of Co, Mo, O, C, and Al is shown in **Figure 3.15**, and the elemental distribution was shown in **Table 3.8**. The presence of aluminium is an indication that the catalyst is supported. The abundance oxygen could also be due to absorbed air on the catalytic surface. The peaks were observed at ~ 0.65, ~6.9 and 7.5 KeV corresponding to the theoretical L_α K_α, and K_β values of Co, O peak at (~0.5 KeV), carbon peak is observed at (~0.28 KeV), the presence of Mo peaks (~2.37, ~2.82 KeV) in the EDS micrograph of $CoMo/Al_2O_3$ and Al peak (~1.5 KeV) are also observed. The EDS results show that that no impurities were present (Umapathy *et al*., 2017), the corresponding carbon is derived from the that tape was detected.

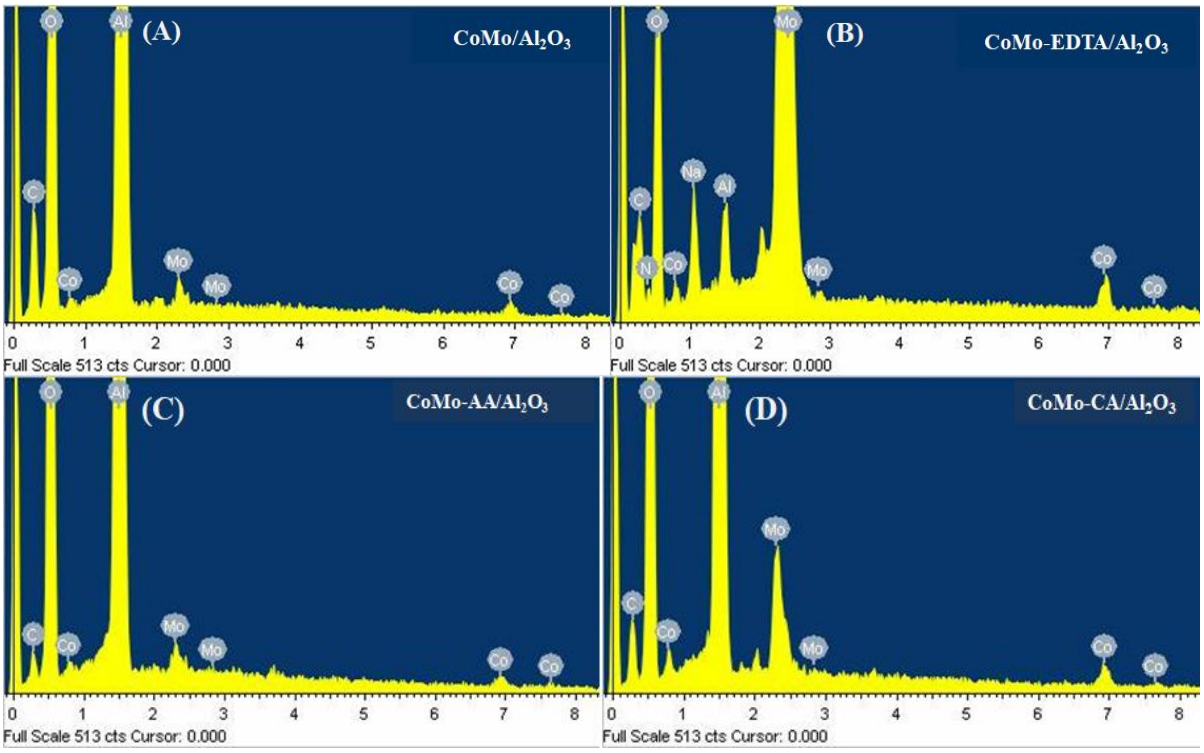

Figure 3.22: EDS spectrum for (a) $CoMo/Al_2O_3$, (b) $CoMo\text{-}EDTA/Al_2O_3$, (c) $CoMo\text{-}AA/Al_2O_3$, (d) $CoMo\text{-}CA/Al_2O_3$ catalysts. (Co, Mo appears in different k, l, m, regions).

Table 3.15: Qualitative atomic percentage of Co, and Mo in HDS catalysts.

	Atomic Percentage (wt.%)						Ratio of Co% to Mo%
	C K	O K	Al K	N K	Mo L	Co K	
$CoMo/Al_2O_3$	14.71	60.99	23.47	-	0.46	0.37	0.804
$CoMo\text{-}EDTA/Al_2O_3$	7.28	62.08	27.19	2.72	0.57	0.16	0.281
$CoMo\text{-}AA/Al_2O_3$	38.93	46.34	14.08	-	0.29	0.37	1.276
$CoMo\text{-}CA/Al_2O_3$	7.84	61.20	30.56	-	0.71	0.22	0.549

(b) Sulfided CoMo catalysts

The EDX of $CoMo/Al_2O_3$, $CoMo\text{-}EDTA/Al_2O_3$, $CoMo\text{-}AA/Al_2O_3$, and $CoMo\text{-}CA/Al_2O_3$ are presented in **Figure 3.23**. EDX analysis was performed in to check the composition of mentioned catalysts. All the sulfided catalysts share similar elemental composition at a similar environment, the difference was the intensity. Sulfided CoMo catalysts confirmed that the material is made of Co K, Mo L, O K, S K, C K and Al K elements. Peaks at ~ (0.75, ~6.98 and ~ 7.62 KeV), (~2.37, ~2.82) KeV), ~0.5 KeV,

~2.37 KeV, ~0.28 KeV, and the additional peak of~ 1.5 KeV corresponds to theoretical K_{α}, L_{α}, K_{α}, and K_{β} this confirmed that the sample is made up of these elements (**Fig.3.23**). For all catalysts, the additional peak of C K (~0.28 KeV) was due to the tape used for holding the samples. The increase in carbon for the chelated catalysts may be due remaining organic residue as they might have not completely decomposed during sulfidation process. Qualitative atomic percentage of the present elements for sulfided HDS catalysts are shown in **Table 3.1.**

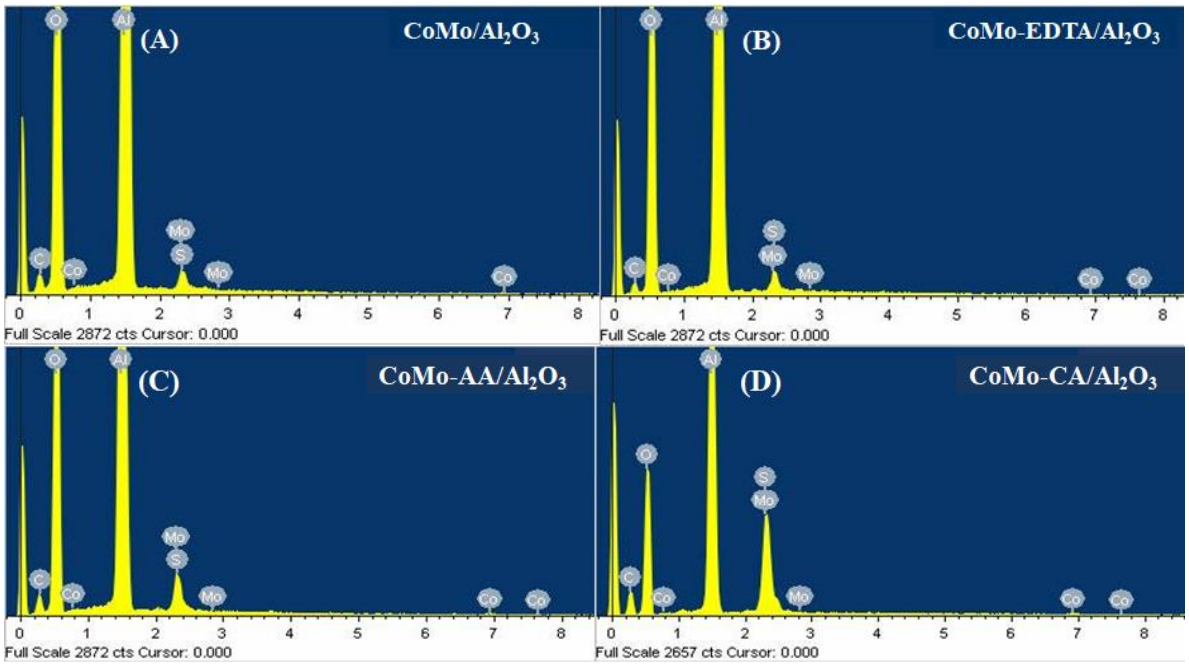

Figure 3.23: EDS analysis for (a) $CoMo/Al_2O_3$, (b) $CoMo\text{-}EDTA/Al_2O_3$, (c) $CoMo\text{-}AA/Al_2O_3$, (d) $CoMo\text{-}CA/Al_2O_3$ catalysts.

Table 3.16: Qualitative atomic percentage of Co, and Mo for sulfided HDS catalysts.

	Atomic Percentage (wt. %)						**Ratio of Co% to Mo%**
	C K	O K	Al K	S K	Co K	Mo L	
$CoMo/Al_2O_3$	13.50	60.21	25.03	0.79	0.11	0.36	0.306
$CoMo\text{-}EDTA/Al_2O_3$	12.34	56.82	29.68	0.69	0.13	0.33	0.394
$CoMo\text{-}AA/Al_2O_3$	32.32	46.52	18.47	3.28	0.15	1.27	0.126
$CoMo\text{-}CA/Al_2O_3$	10.27	61.13	26.80	0.70	0.10	0.98	0.102

3.5.7 X-ray diffraction (XRD)

The XRD patterns of chelated and non-chelated CoMo catalysts in oxide phases are shown in **Figure 3.24**. All catalysts gave similar reflections at 2θ = 32.0°, 37.6°, 39.5°, 45.5°, 60.9° and 67.0˚, corresponding to (220), (311), (222), (400), (511) and (440) planes, respectively and it is characteristic of γ-Al_2O_3 face-centered cubic phase. Furthermore, CoMo/Al_2O_3 showed characteristic reflections at 2θ = 19.1°, 26.5°, 33.9° which correspond to (201), (002), and (222) basal plane belonging to crystalline monoclinic β-$CoMoO_4$. The non-chelated catalyst (CoMo/Al_2O_3) exhibited the formation of crystalline phases, the metal agglomeration in this catalyst is an undesirable effect, CoMo-EDTA/Al_2O_3 showed a very clear contribution at 2θ = 23.3° (021) and 28.5° (220) belonging to MoO_3, no other characteristic reflections were obtained. For all the chelated catalyst, CoMo-EDTA/Al_2O_3 showed to have large particles (and this was shown in TEM). In general, the higher molecular weight chelating agent resulted in low degree of crystallinity, which can be contributed to high carbon content remaining on the surface after the activation step. The presence of MoO_3 was visible as the molecular weight of the chelating agent decreases. This can be explained because the metals are more susceptible to contact with oxygen in the catalysts synthesized with chelating agents of smaller molecules (AA and CA) (Beltrán *et al*., 2018).

The XRD analysis of CoMo-AA/Al_2O_3 presented MoO_3 as the major phase. The prominent reflections at 2θ = 16.0°, 28.5°, and 29.1° corresponds to (111), (220) and (310) planes of MoO_3 base-centered monoclinic. A very weak contribution peaks at 2θ = 26.5° (002) correspond to β-$CoMoO_4$ monoclinic phase. Lastly, for CoMo-CA/Al_2O_3 no characteristic reflections were observed, this indicated that Co and Mo citrate species were either present as small nano-sized particles and well dispersed on the surface of the alumina support, which cannot be detected by XRD method. This showed that CA could transform metal oxides from tetrahedral MoO_4^{2-} or β-$CoMoO_4$ into octahedral polymolybdate species (Zhang *et al*., 2016)

Generally, the formation of β-$CoMoO_4$ indicated that Co and Mo species are able to interact more with the support. Catalyst with AA exhibited weak formation of β-$CoMoO_4$ and MoO_3, this showed that the use of chelating agents during impregnation of the metal species to the support led to better dispersion. The absence of oxide phases for CoMo-CA/Al_2O_3 catalyst was because of citric acid, resulting in the formation of well dispersed or amorphous species. These amorphous species hindered the formation of mixed-metal oxides such as $CoMoO_4$ and likely $CoAl_2O_4$ and could enhance the formation of small domain size of Co and Mo-oxo species. It can be concluded that CA mitigates the aggregation of the metal component particles. The well dispersed species have weak interaction with the alumna surface, which enhancing the formation of type II CoMoS structure upon the sulfidation process (González-Cortés *et al*., 2015).

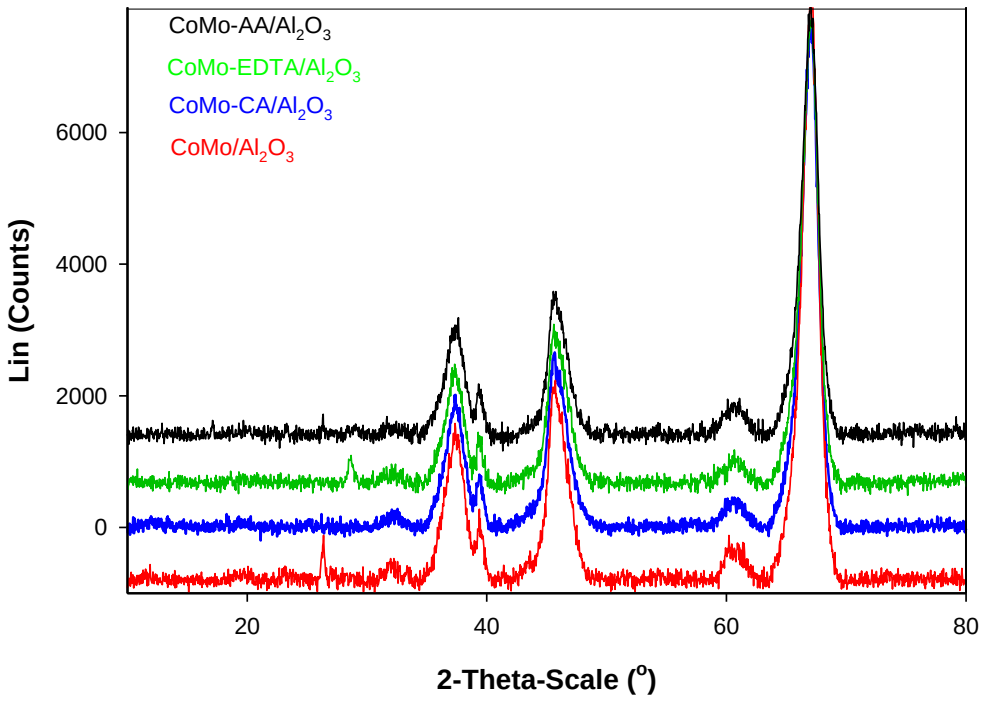

Figure 3.24: XRD diffraction pattern of $CoMo/Al_2O_3$, $CoMo\text{-}EDTA/Al_2O_3$, $CoMo\text{-}AA/Al_2O_3$, and $CoMo\text{-}CA/Al_2O_3$ catalysts.

All sulfided CoMo catalysts (**Figure 3.25**) showed similar reflections at 2θ = 19.6° (111), 32.0° (220), 37.6° (311), 39.5° (222), 45.5° (400), 60.9° (511) and 67.0° (440) and characteristic of γ-Al_2O_3 face-centered cubic phase. $CoMo/Al_2O_3$ showed a broad reflection at 2θ = 12.0˚ due to MoO_3 phase. For all catalysts typical diffraction patterns of poorly crystalline MoS_2 with the characteristic reflections at 2θ = 14.4°, 33°, 58° were observed (Huang *et al*., 2008). As shown in **Figure 3.25** $CoMo\text{-}EDTA/Al_2O_3$, no reflections corresponding to Co or Mo phases were detected. In contrast, $CoMo\text{-}AA/Al_2O_3$ showed a very weak reflection at 25.5° which corresponds to octahedral MoO_3 phase (Badoga *et al*., 2012a), this suggested that some of the oxides formed were not sulfided. $CoMo\text{-}CA/Al_2O_3$ showed a reflection that appeared at 2θ = 11.5°, 18°. A very weak reflection appeared at 2θ = 23.5˚ which could be ascribed as MoO_3 (Singh *et al*., 2016). Weak XRD peak, indicated a very poorly crystalline structure characteristic of metal species. The XRD pattern of $CoMo/Al_2O_3$ confirmed that not all the metal oxide form was converted during sulfidation, and this was evident by the broad peak obtained at 2θ = 12.5° and poor redispersion of bulk MoO_3 (Singh *et al*., 2016). No multi-layered MoS_2 reflections at 2θ = 14.1° were observed on the XRD patterns, and this could be that the phase was presented in a very small nano-crystalline or very dispersed on the support.

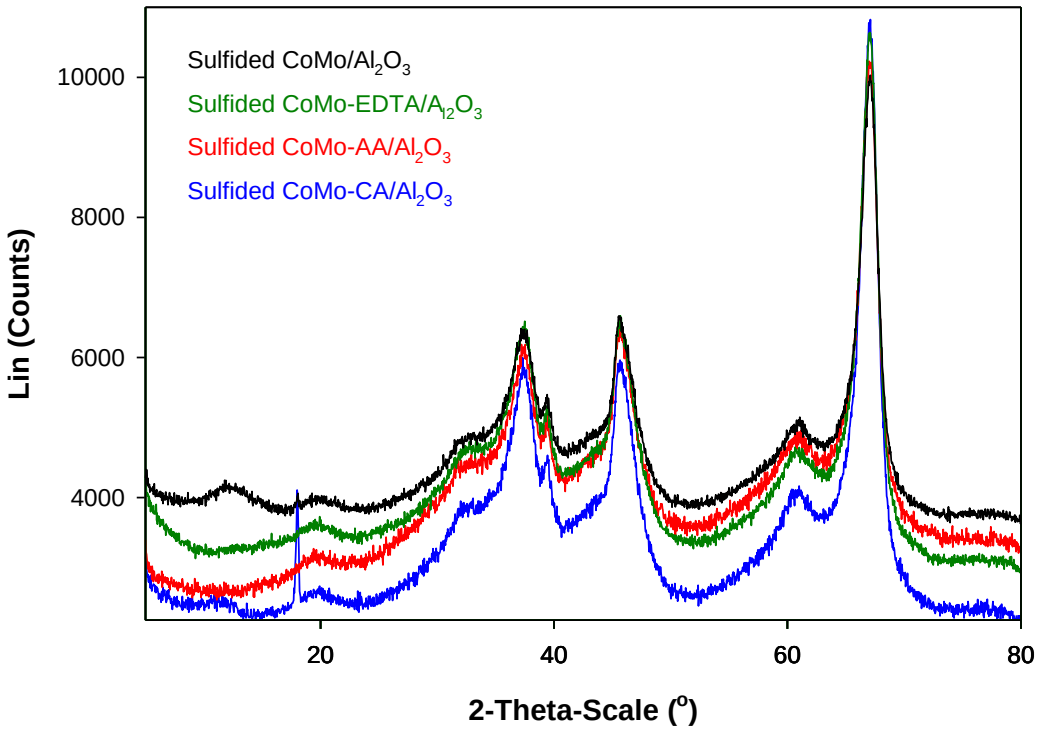

Figure 3.25: XRD patterns of sulfided $CoMo/Al_2O_3$, $CoMo\text{-}EDTA/Al_2O_3$, $CoMo\text{-}AA/Al_2O_3$, and $CoMo\text{-}CA/Al_2O_3$ catalysts.

3.5.9 Transmission electron microscopy (TEM)

TEM measurements of the sulfide catalysts were performed to gain more insight into the changes in the morphology and dispersion of MoS_2 crystallites on the alumina support. CoMo catalysts with and without chelating agents were used in the analysis. The morphology of MoS_2 particles has great influence on the HDS activity and selectivity of catalysts (Peña *et al*., 2014). Representative micrographs were selected for each catalyst (**Fig. 3.26-3.29**), with circles and arrows denoting the MoS_2 crystallites slab distribution.

The micrographs showed typical fringes representing MoS_2 crystallites, and distribution with average length shown in **Table 3.17**. The morphology of MoS_2 crystallites were modified by EDTA, AA and CA addition in the impregnation solution. It was clear from **Figure 3.27-3.29** that incorporation of chelating agents in catalysts had a significant impact on slab length and aggregation of particles, and this pointed out a good dispersion of the sulfide catalysts (Peña *et al*., 2014) which could result in an improved catalytic activity. $CoMo/Al_2O_3$ catalyst had MoS_2 crystallites with 5.57 nm average slab length. The average slab length for $CoMo\text{-}EDTA/Al_2O_3$ was 3.95 nm, for $CoMo\text{-}AA/Al_2O_3$ it was 3.37 nm, and for $CoMo\text{-}CA/Al_2O_3$ it was 3.11 nm (**Table 3.17**). According to the obtained results, it appeared that all chelated catalysts exhibit shorter length, with $CoMo\text{-}CA/Al_2O_3$ catalyst exhibiting the largest distribution of smaller crystallites particles and shorter slabs. The use of chelating agents resulted in a

decrease in the length of MoS_2 catalytically particles. The formation of shorter slabs was due to the reduction of metal-support interaction (Chen *et al*., 2017; Escobar *et al*., 2009). Studies have shown that MoS_2 layers are stacked *via* Van der Waals interaction (Han *et al*., 2011).

For alumina-supported catalysts, a polarization field can be generated due to the polarization effect of Al^{3+}. The Van der Waals interaction between the layers of the MoS_2 can be weakened by the polarization effect of Al^{3+} affecting the stacking of MoS_2 (Zhang *et al*., 2017). The larger pore size weakens the effect of polarization on the Van der Waals interactions, and the active phase is more stacked. While smaller pore size limits the stacking due to the strong polarization effect, and the active phase was inclined to grow along the slab, hence, the reason for $CoMo/Al_2O_3$ to obtain longer slab length. $CoMo/Al_2O_3$ proved to have poor dispersion than all the synthesized catalysts. The poor dispersion of active metal species was due to the intimate contact between Mo and Al, resulting in a strong interaction between Mo and Al_2O_3 (Mo-O-Al linkages) and the formation of larger percentage of Type I CoMoS phases due to calcination.

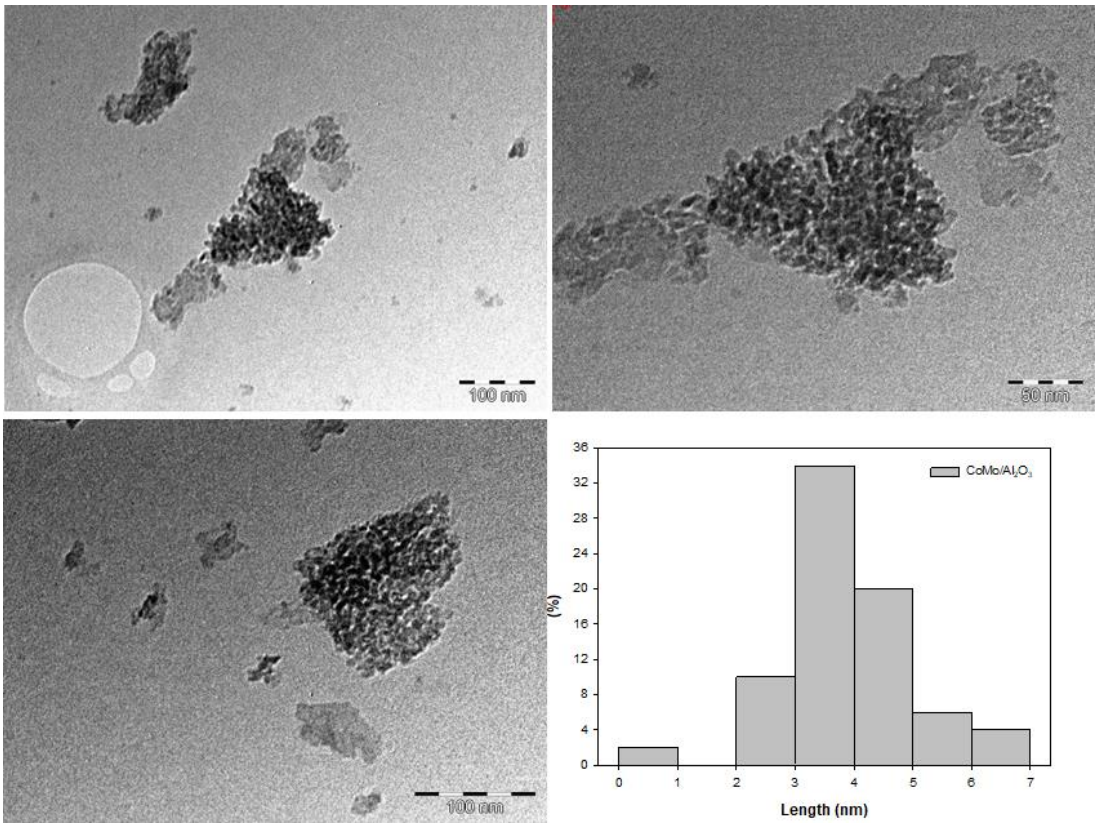

Figure 3.26: TEM images showing the slab length distribution of MoS_2 crystallites for $CoMo/Al_2O_3$ catalyst.

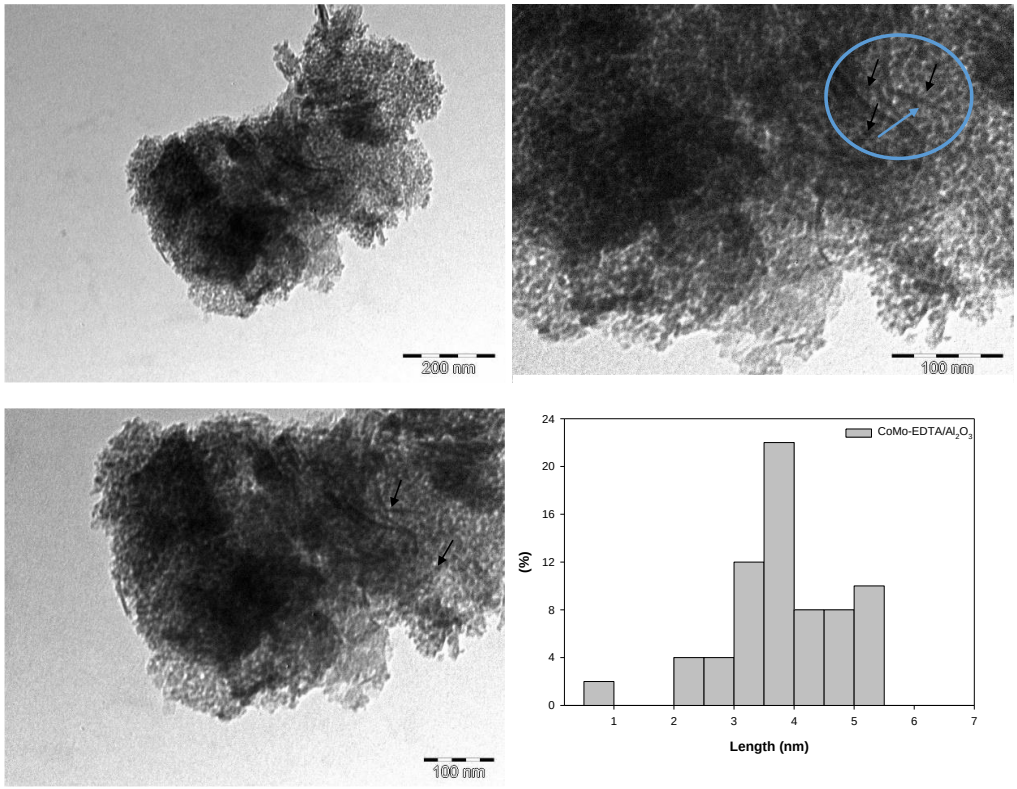

Figure 3.27: TEM images showing the slab length distribution if MoS_2 crystallites for CoMo-EDTA/Al_2O_3 catalyst.

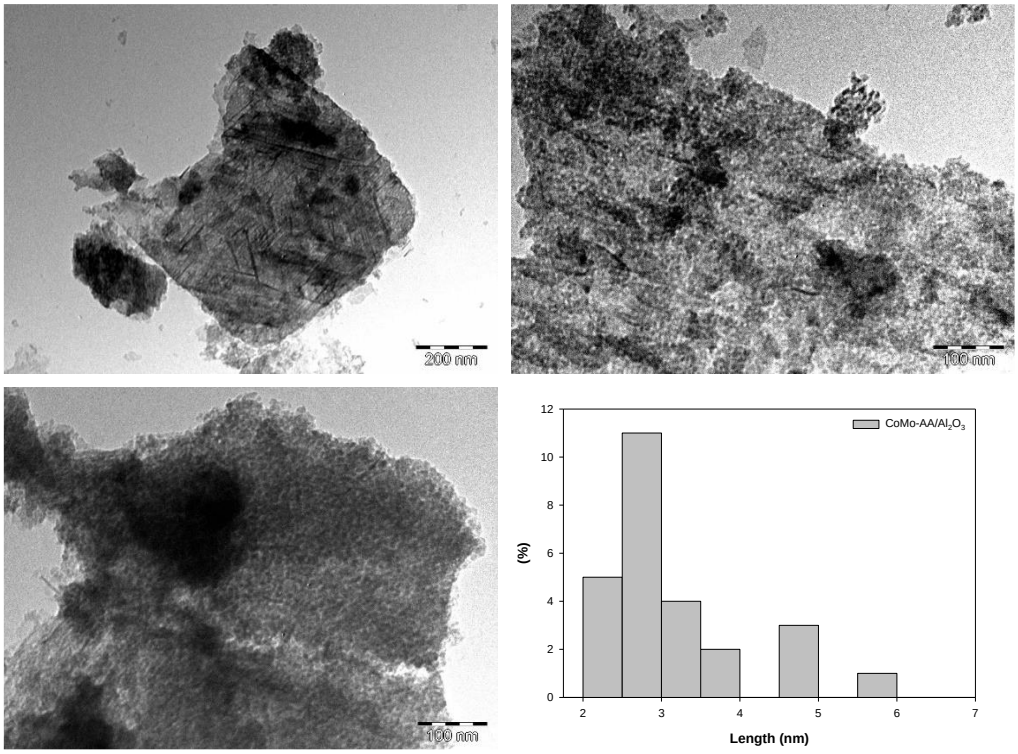

Figure 3.28: TEM images showing the slab length distribution if MoS_2 crystallites for CoMo-AA/Al_2O_3 catalyst.

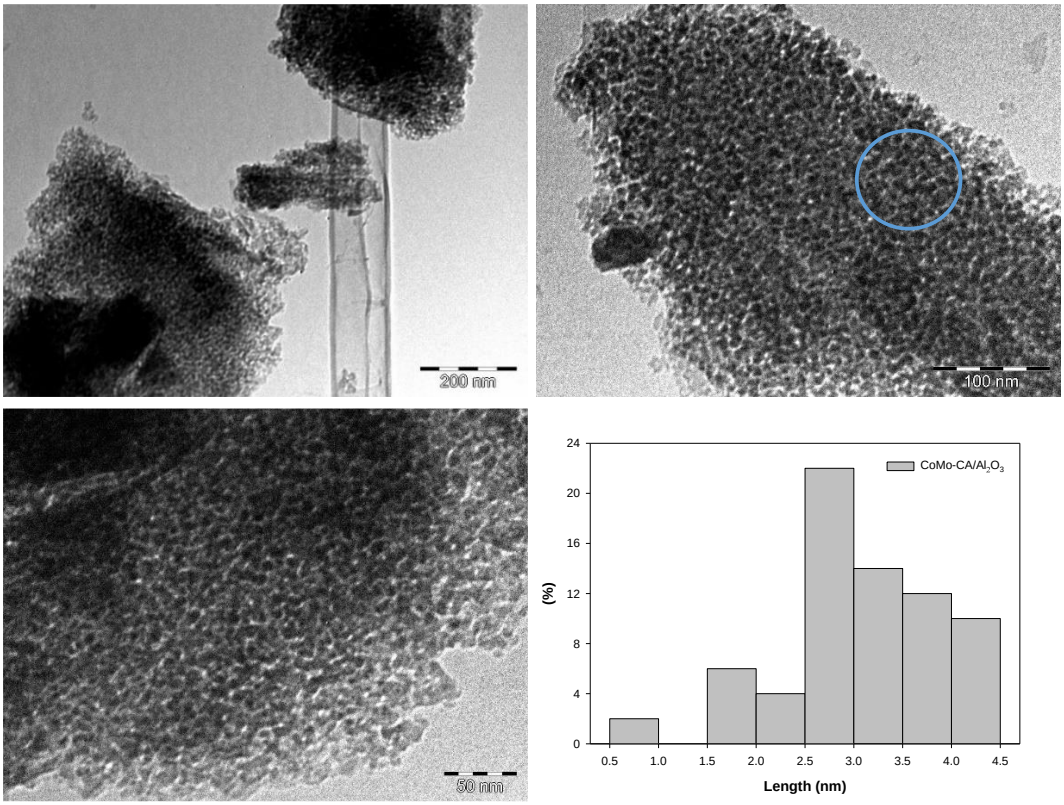

Figure 3.29: TEM images showing the slab length distribution of MoS_2 crystallites for CoMo-CA/Al_2O_3 catalyst.

Table 3.17: Average length of MoS_2 crystallites in CoMo/Al_2O_3 and CoMo-x/Al_2O_3 (x = EDTA, AA, CA).

Catalysts	**Average diameter ± SD (nm)**
CoMo/Al_2O_3	5.57 (± 1.048)
CoMo-EDTA/Al_2O_3	3.95 (± 1.047)
CoMo-AA/Al_2O_3	3.37 (± 0.988)
CoMo-CA/Al_2O_3	3.11 (± 0.803)

3.5.10 Scanning Electron Microscopy (SEM)

(a) Alumina supported CoMo catalysts

To investigate the morphology and shape of the catalysts, SEM images were collected using TESCAN Vega TS 5136LM SEM. The images of $CoMoO_x$ are presented in **Figures 3.30-3.33**. $CoMo/Al_2O_3$ showed spherical-like particles which are agglomerated with small particles present on the surface of the support (**Figure 3.30**). CoMo-EDTA/Al_2O_3 (**Figure 3.31**) shows irregular shaped crystallites with small needle-like particles that are highly agglomerated, as a result the average size distribution could not be measured. $CoMo/Al_2O_3$, CoMo-AA/Al_2O_3 and CoMo-CA/Al_2O_3 images revealed agglomerated spherical-like material with the average size between 107-133 μm (diameter).

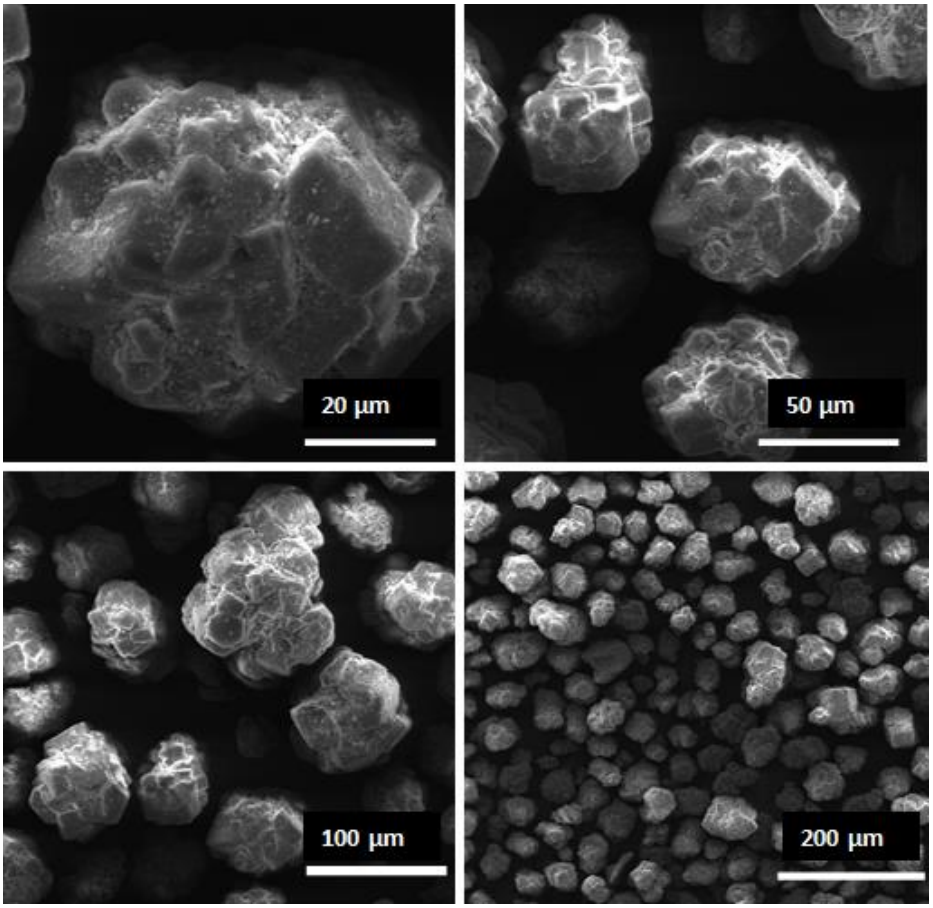

Figure 3.30: SEM images for $CoMo/Al_2O_3$ catalyst at different magnifications.

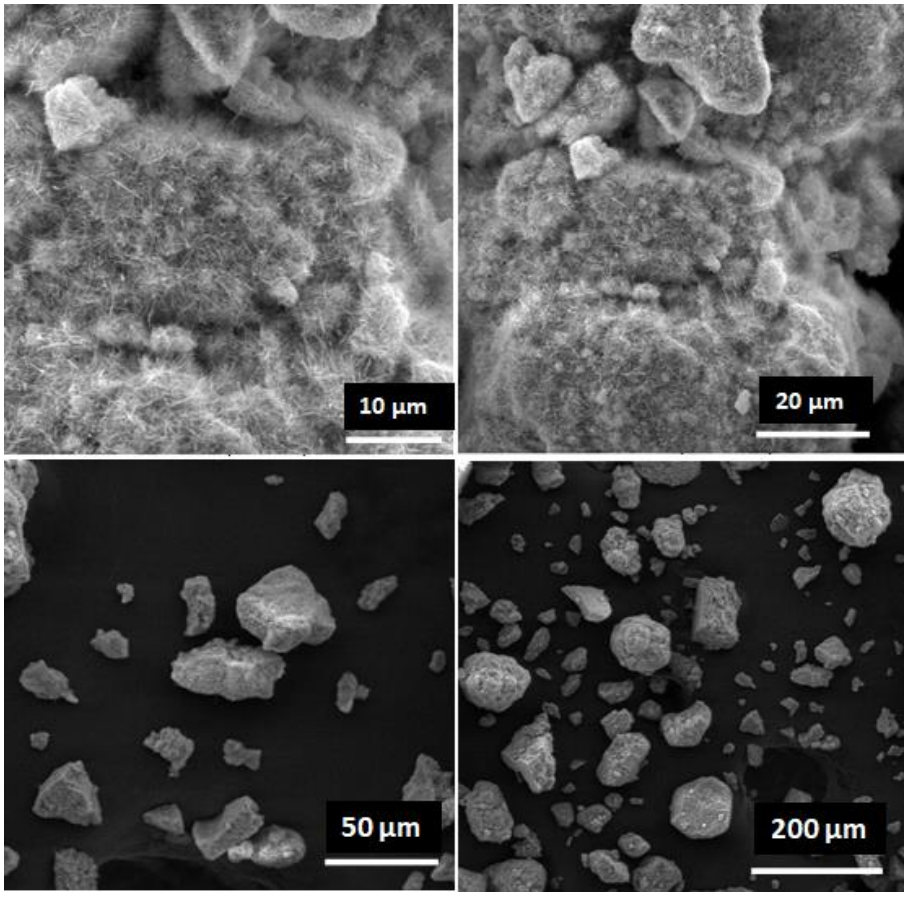

Figure 3.31: SEM images for CoMo-EDTA/Al_2O_3 catalyst at different magnifications.

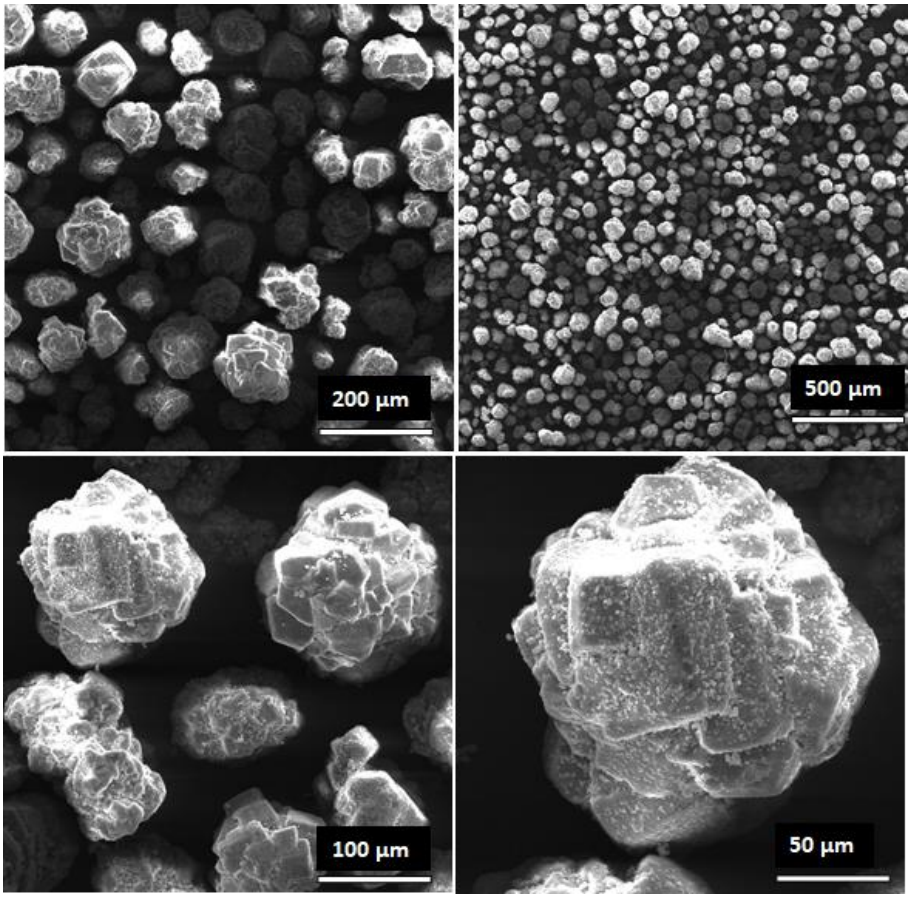

Figure 3.32: SEM image for CoMo-AA/Al_2O_3 catalyst at different magnifications.

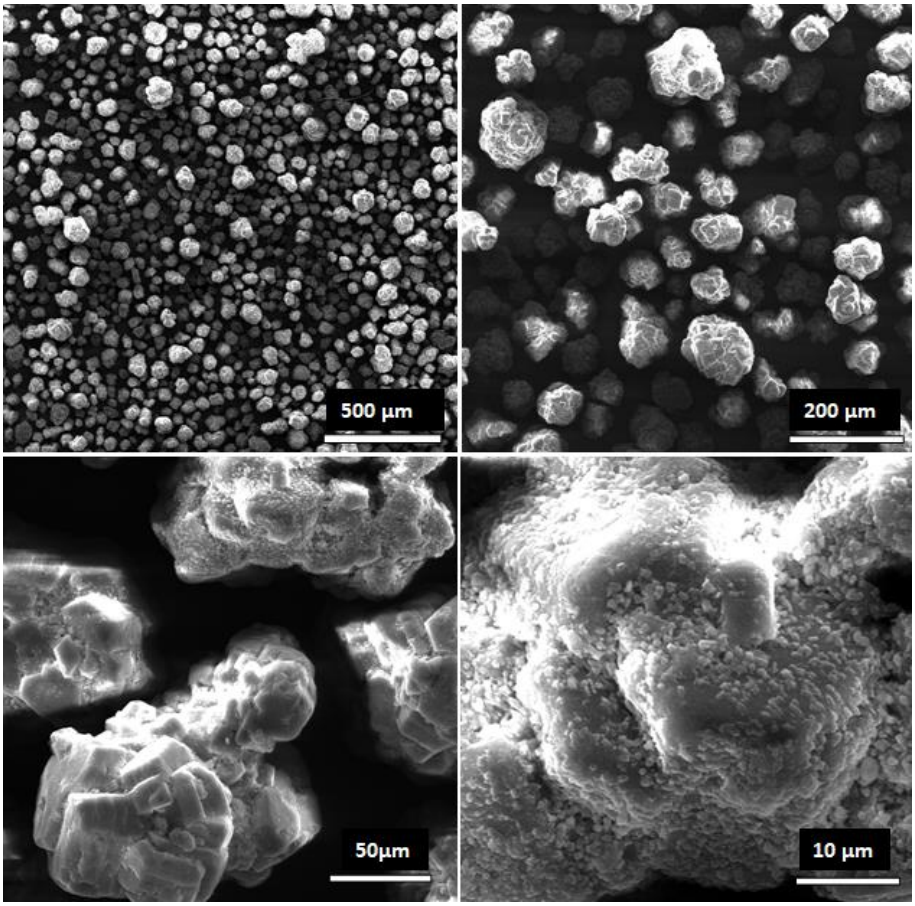

Figure 3.33: SEM images for CoMo-CA/Al_2O_3 catalyst at different magnifications.

(b) Sulfided CoMo catalysts

The sulfided CoMo catalysts are displayed in **Figure 3.34-3.37**. The SEM images confirmed spherical-shaped and agglomerated particles with small fluffy like particles, which could indicate that the catalysts are porous in nature. Particle distributions vary in size and were measured to be between 98.3-104.8 µm (in diameter), and for sulfided CoMo-AA/Al_2O_3 the particles were too agglomerated for the measurements to be possible.

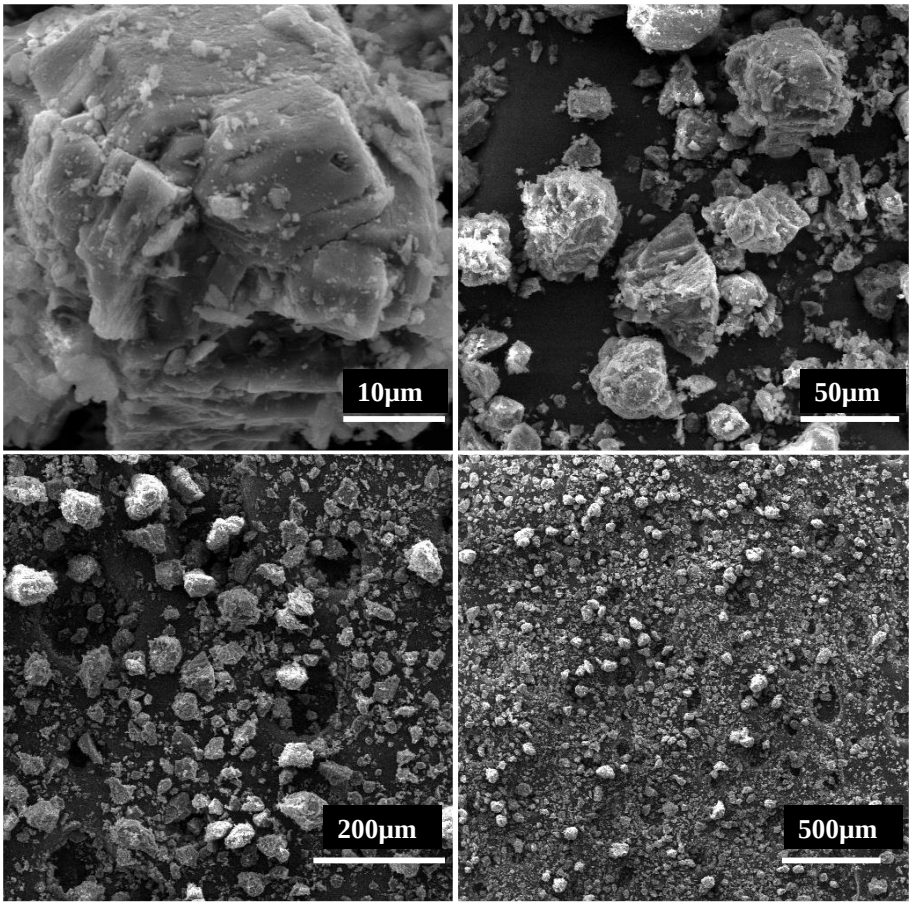

Figure 3.34: SEM images for the sulfided $CoMo/Al_2O_3$ catalyst at different magnifications.

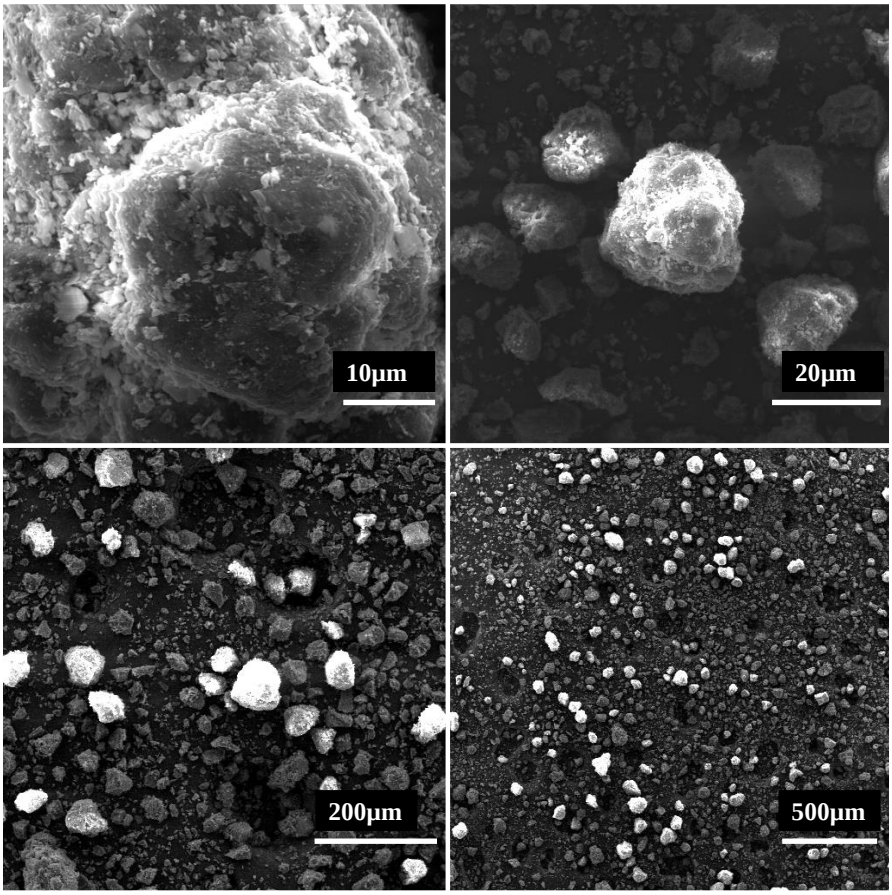

Figure 3.35: SEM images for the sulfided CoMo-EDTA/Al_2O_3 catalyst at different magnifications.

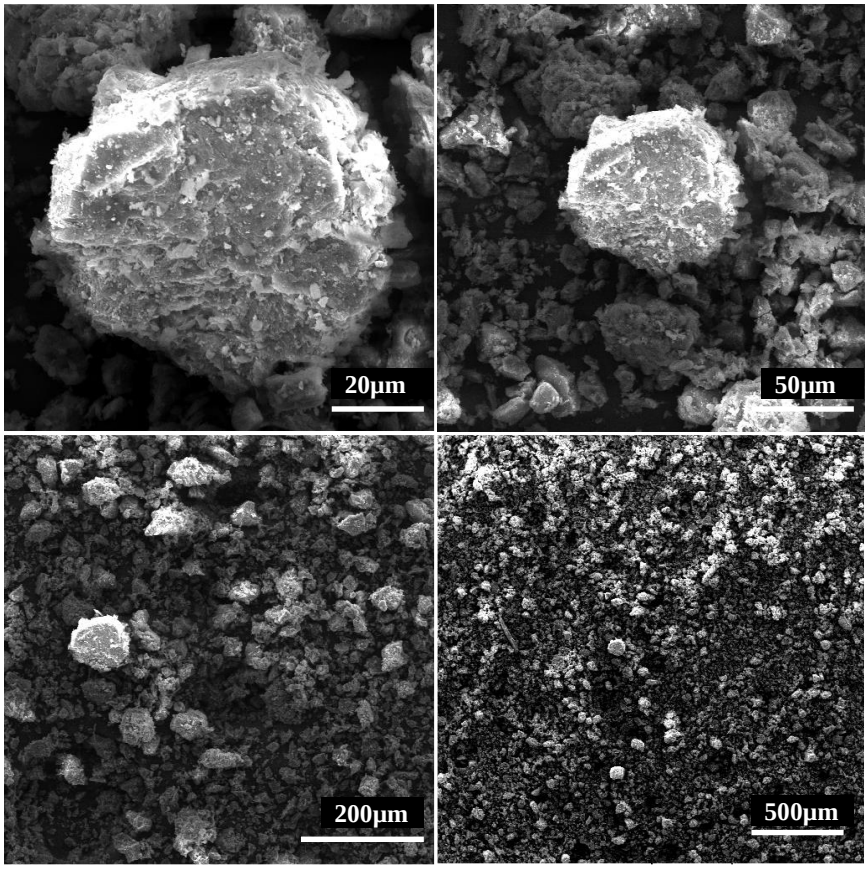

Figure 3.36: SEM images for the sulfided CoMo-AA/Al_2O_3 catalyst at different magnifications.

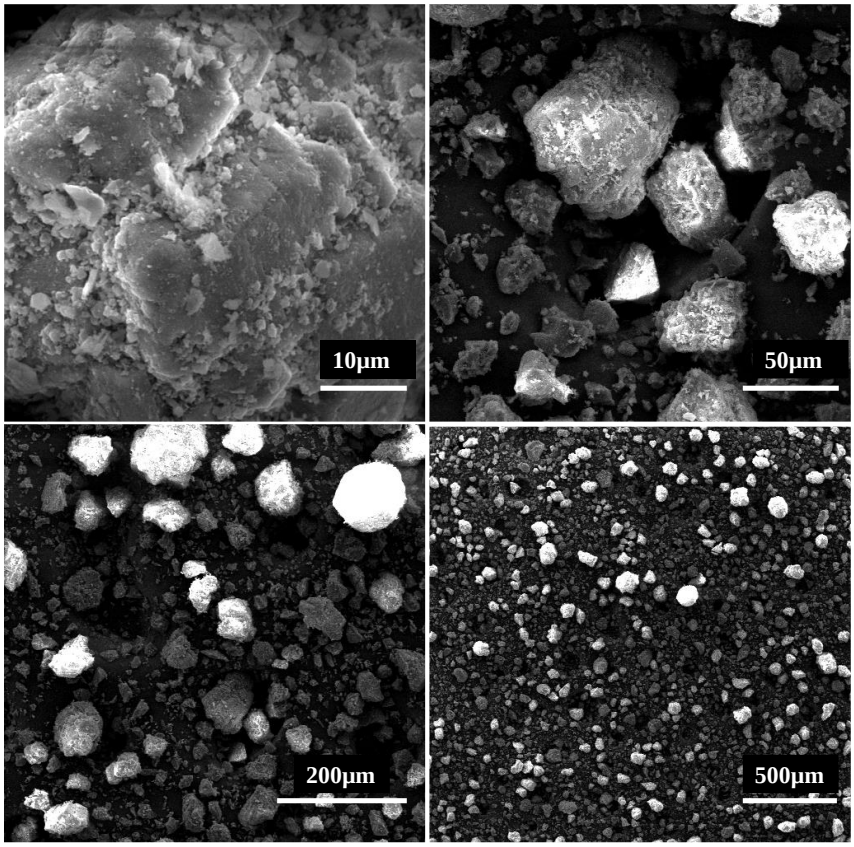

Figure 3.37: SEM images for the sulfided CoMo-CA/Al_2O_3 catalyst at different magnifications.

3.5.11 Stability of catalysts-TGA and DSC thermal analyses

The first weight loss of 4.5 % for CoMo/Al_2O_3occurred below 150 ˚C due to the desorption of physically adsorbed water (**Fig. 3.38**). The second weight loss occurred in the range of 180-410 ˚C, leading to the weight loss of 2.5 % associated with the decomposition. This weight loss could be due to support dihydroxylation and further elimination of coordinated water molecules. The weight loss was also reflected by a weak and broad exothermic peak between 160-210 ˚C. Another weight loss obtained 220-410˚C, was due to complex overlapping chemical reactions such as dihydroxylation of alumina and partial dehydration of cobalt nitrate and heptamolybdate species (González-Cortés *et al*., 2005). From 650˚ no weight loss was observed, this could indicate a subsequent total transformation of the Co and Mo precursor species into the catalyst oxidic precursor (González-Cortés *et al*., 2005). Weak endothermic peak < 150˚C was mainly due to water desorption, while the weak and broad exothermic peak between 170-360˚C was associated to partial dehydration-composition of Co and Mo species, and combustion of residual organic matrix. Weak and endothermic peak between 400-780˚C was due to further combustion of residual organic matrix and the formation of stable metal oxides.

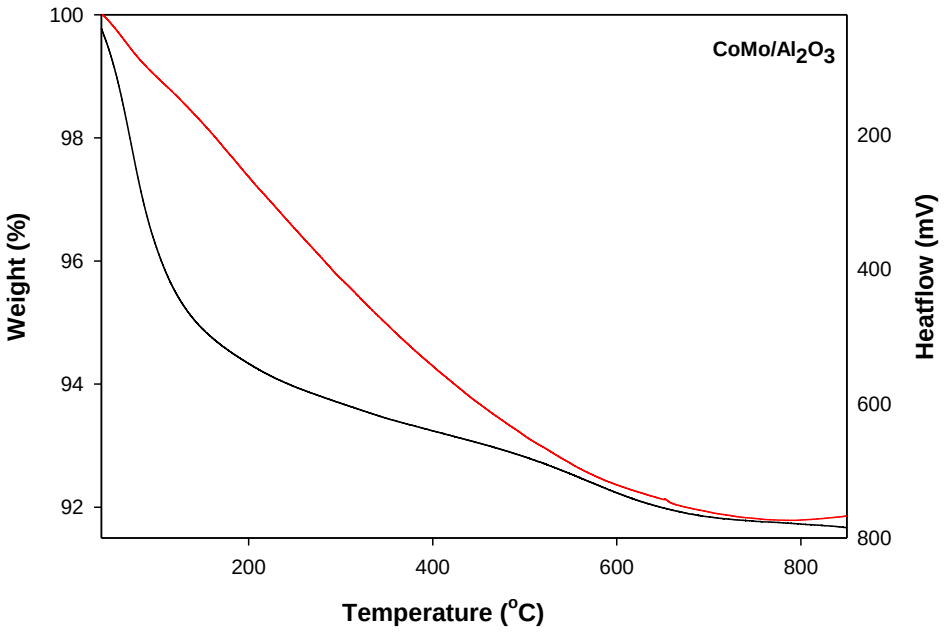

Figure 3.38: TGA-DSC curves of $CoMo/Al_2O_3$ catalyst.

TGA-DSC patterns of CoMo-AA/Al_2O_3, CoMo-AA/Al_2O_3 crystal, CoMo-EDTA/Al_2O_3, CoMo-EDTA crystal and CoMo-CA/Al_2O_3 are presented in **Figures 3.39-3.5.43**. **Figure 3.39** showed the TGA-DSC of CoMo-EDTA/Al_2O_3 curve. The first weight loss of 3.52 % occurred below 150˚C and was attributed to the desorption of physically adsorbed water from the alumina and partial dehydration of citric acid on alumina. The second weight loss took place in the region of 150-220˚C leading to 3.4 % weight loss and being associated with an endothermic peak at a maximum of 180˚C and was due to the support losing adsorbed water on the surface and the loss of crystal water in the cobalt complex. According to Wyrzykowski and co-workers, this peak can be attributed to the melting or decomposition from the dehydration of EDTA. The third weight loss occurred from 220-410˚C could be assigned to complex series of overlapping chemical reactions which involved partial dehyroxylation-decomposition of EDTA and partial dehydroxylation of alumina (González-Cortés *et al*., 2015). The broad exothermic peak at maximum 210˚C, 380˚C and a strong exothermic peak around 410˚C was due to dehydroxylation process with weight loss of 2.2 % and 1.8 % (Bui *et al*., 2019). A weak endothermic peak at 240˚C was attributed to the oxidation of the remaining residue of EDTA produced. Stable phases are formed from 600-800˚C accompanied by a weak broad exothermic peak, which was attributed to the formation of stable MoO_3 phases. No weight loss was observed above 600˚C, this indicated a formation of stable metal oxides.

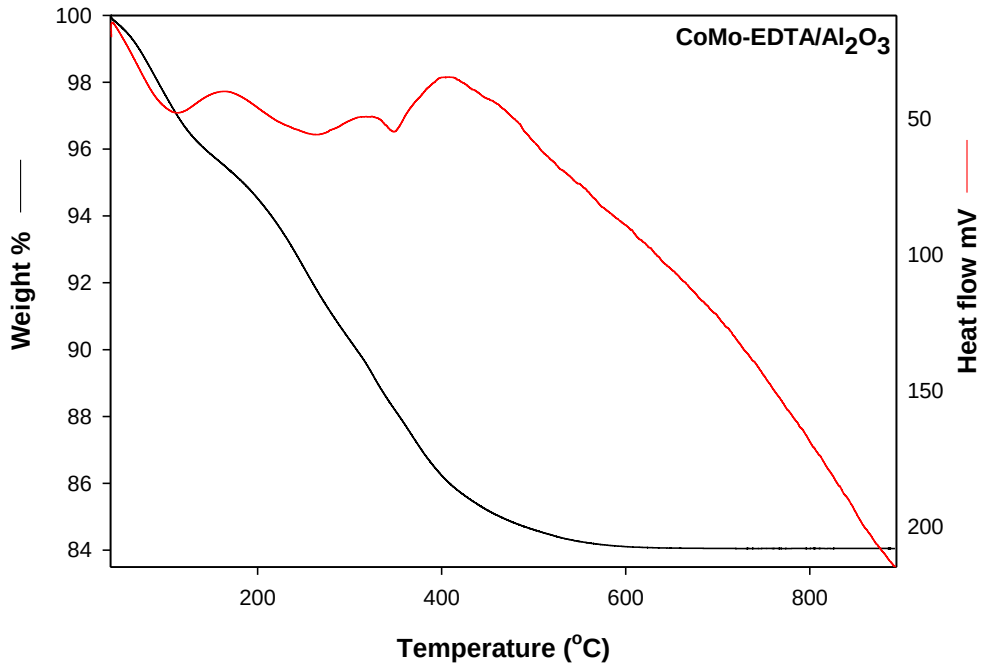

Figure 3.39: TGA-DSC curves of CoMo-EDTA/Al_2O_3 catalyst.

The first weight loss for CoMo-EDTA crystal in (**Figure 3.40**) was 7.1 % occurred < 150˚C due to the desorption of physically adsorbed water and partial dehydration of EDTA. The second weight loss occurred between 150-190˚C, leading to 13.5 % weight was loss associated with the decomposition of EDTA ligand. The weight loss was also reflected by the endothermic peak at 120˚C and a strong endothermic peak at 170˚C which could be attributed to the melting/decomposition temperature of chelated agent from the dehydration of EDTA. Another weight loss was obtained at 250˚C and 390˚C with weight loss of 3 % and 18 %, respectively, and could be assigned to full decomposition of EDTA, subsequent total transformation of Co and Mo precursors species into the catalyst oxidic precursor (González-Cortés *et al*., 2005) and the formation of molybdenum trioxide (MoO_3). These weight losses were also reflected by an exothermic peak at 250˚C and 340˚C due to further combustion of residual organic matrix and a broad endothermic peak at 280˚C followed by a strong endothermic peak at 390˚C attributed to a fully decomposition of residual organic matrix (EDTA). Above 400˚C there was no weight loss, this indicated that all the Co-EDTA complexation had decomposed leaving Co^{2+} ions to complex with Mo ions which resulted in the formation CoMoS type II during sulfidation (Badoga, 2012).

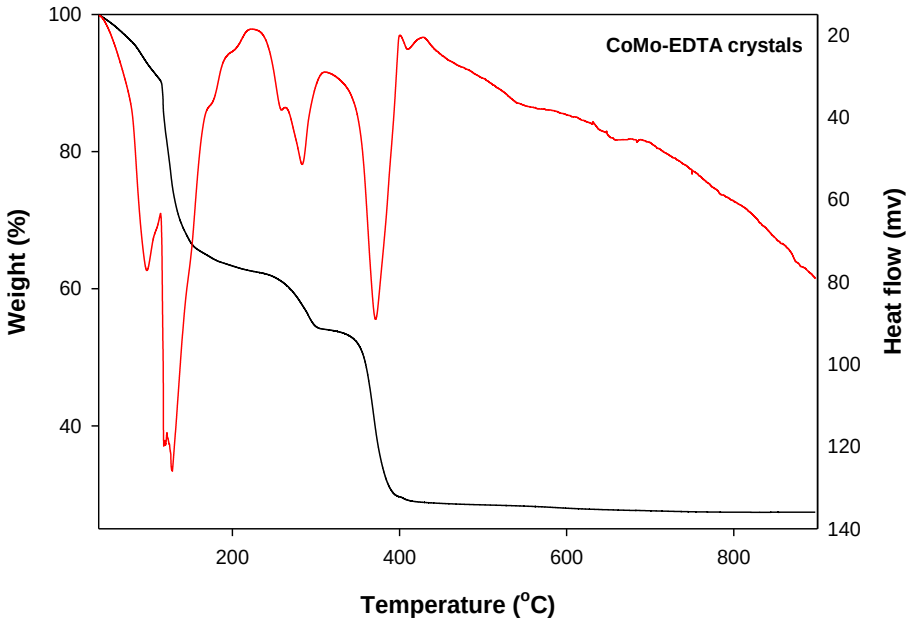

Figure 3.40: TGA-DSC curves for CoMo-EDTA crystals.

The results obtained in CoMo-AA/Al_2O_3 (**Figure 3.41**) showed the weight loss of 3.1 % between 80-180˚C was associated to the desorption of water molecules from alumina surface and partial dehydration of acetic acid. The latter was accompanied by a broad exothermic peak 185˚C which was attributed to partial decomposition of the complex. The second weight loss occurred in the range of 190-400˚C, leading to 1.2 % weight loss associated with the dehydroxylation process and decomposition of burning of carbon residua from acetic acid, corresponding to weak and broad endothermic peak between 210-620˚ due to further combustion of residual organic matrix (González-Cortés *et al*., 2005). After 400˚C there was not much definite weight loss obtained, a narrow endothermic peak was observed at 860˚C indicated the formation of stable metal oxides. The increase in mass from 750˚C was due forming of metal oxide due to oxidation taking place.

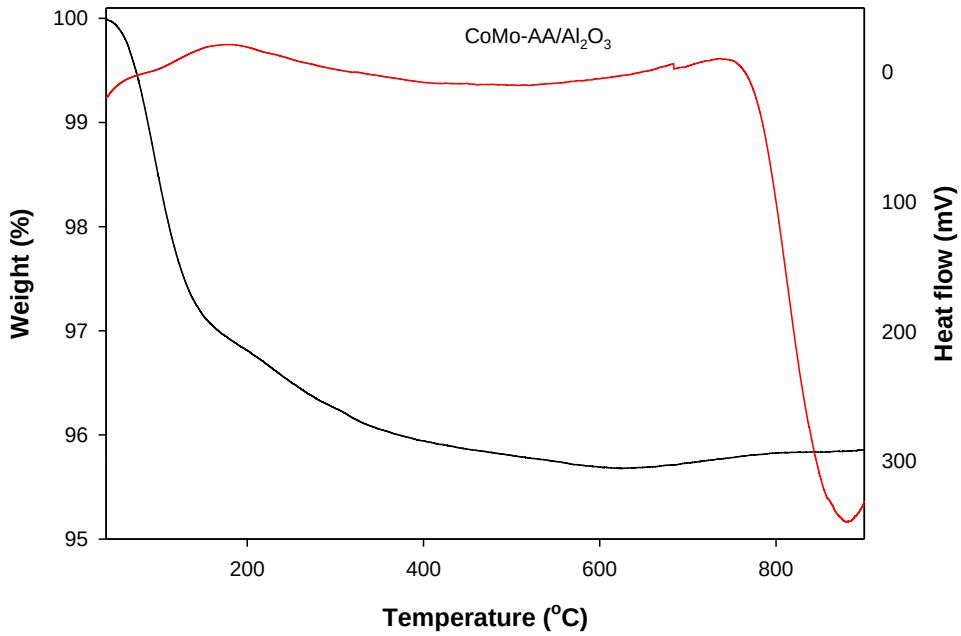

Figure 3.41: TGA-DSC curves for CoMo-AA/Al_2O_3 catalyst.

The first weight loss at150˚ (31 %) for CoMo-AA/Al_2O_3 was assigned to the desorption of physically adsorbed water molecules on alumina surface, it was accompanied by an exothermic peak at 80˚C which correspond to the loss of water (**Figure 3.42**). The second (2%) and third weight loss (20%) was observed at 250˚C and 380˚C, the minor weight loss was due to overlapping chemical reactions (partial-decomposition and combustion of metal species and the latter was assumed to be the full decomposition of acetic acid and the formation of molybdenum trioxide. After 400˚C no weight loss was observed which indicated the formation of stable metal oxides. The DSC curve for this catalyst exhibited endothermic peaks at 150˚C, 240˚C, 380˚C and narrow exothermic peaks at 200˚ and 270˚C (González-Cortés *et al*., 2005). The first stage was mainly due to the decomposition and combustion of acetic acid, the second stage was associated to the partial hydration-decomposition of the metal precursor salts, respectively, and the third stage of endothermic peak was assigned to the formation of stable metal oxide.

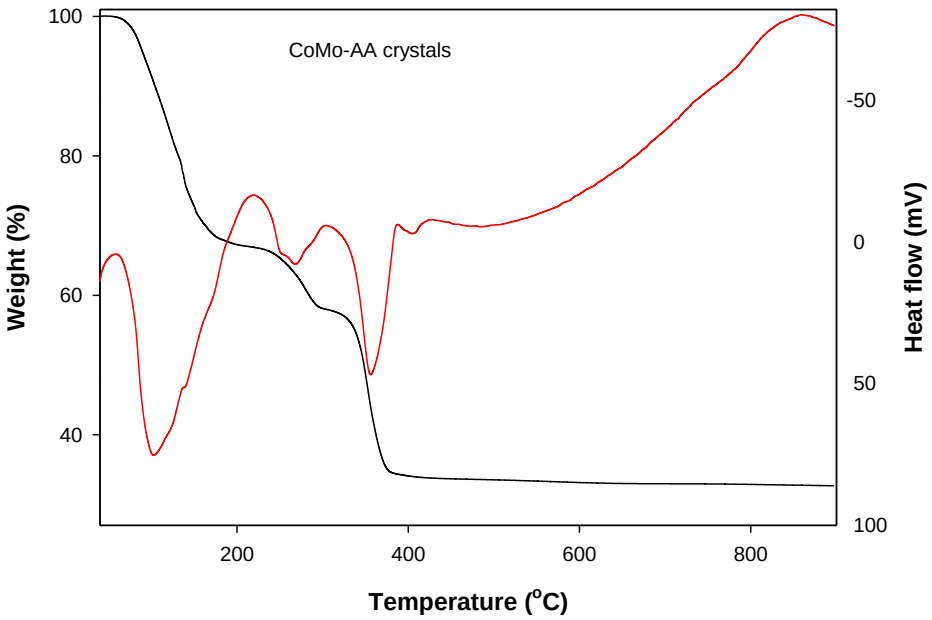

Figure 3.42: TGA-DSC curves for CoMo-AA crystals.

The first weight loss of 1.1 % between 50-180˚C for CoMo-CA/Al_2O_3 was associated to desorption of water molecules from the alumina surface and partial dehydration of citric acid on alumina (Escobar *et al*., 2017), accompanied by a weak endothermic peak at a maximum temperature at 80˚C associated to the dehydration reaction (**Figure 3.43**). The slope change at 180˚C indicated the onset of decomposition of citric acid. The second weight loss (15.5%) observed from 210-290˚C, was attributed to a complex series of overlapping chemical reactions such as partial hydroxylation-decomposition of metal-citrate complex (Stanislaus *et al*., 2010), partial dehydroxylation (Knözinger & Ratnasamy, 1978) and full decomposition of citric acid and the formation of MoO_3 and $CoMoO_4$ (Escobar *et al*., 2017). This weight loss was accompanied by a sharp exothermic peak at a maximum temperature of 200˚C which was attributed to the melting or decomposition temperature of trans-aconitic acid produced from the dehydration reaction of citric acid (Wyrzykowski and co-workers, 2011). A third weight loss (2.8 %) between 300-600˚C was associated with the evolution of remaining residue of citric acid (González-Cortés *et al*., 2015). At 350-450˚C there was a broad exothermic peak associated with further destruction of organic fragments. This weight loss was also reflected by ta broad exothermic peak at 560-650˚C. A weak exothermic peak at 770˚C was associated with the generation of MoO_3.

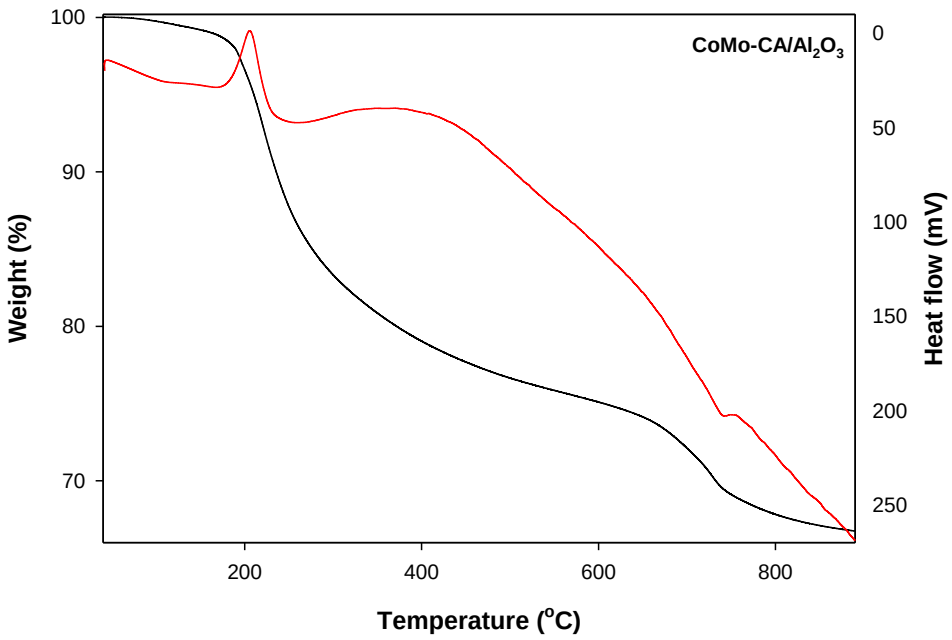

Figure 3.43: TGA-DSC curves for CoMo-CA/Al_2O_3 catalyst.

3.5.12 Catalytic activity

Hydrodesulfurization (HDS) was used to determine the catalytic activity of the catalysts. In this study, the catalytic activity of CoMo catalysts was evaluated in the DBT reaction. The best catalyst was used to perform HDS study for BT, DBT, and 4,6-DMDBT model fuel. Hydrotreating reactions were carried out under industrial conditions. The HDS of DBT was carried out at 300 ˚C and 4 MPa for different catalysts and the results are presented in **Table 3.18**. HDS of DBT occurs via two routes: direct desulfurization (DDS) leading to the formation of biphenyl (BP) and hydrogenation (HYD) route which leads to the formation of tetrahydrodibenzothiophene (TH-DBT), cyclohexylbenzene (CHB) and finally, bicyclohexyl (BCH) (Vatutina *et al*., 2019). The increase in BP selectivity and a decrease in CHB selectivity in all catalysts was evidence that DBT desulfurization degree was mostly *via* the DDS pathway. All the investigated catalysts achieved 43-98% conversion of DBT. The maximal DBT conversion was observed for CoMo-CA/Al_2O_3 (98%), and CoMo/Al_2O_3 catalyst has the lowest activity with the conversion of 43%. The sulfur conversion follows the order: CoMo-CA/Al_2O_3 > CoMo-AA/Al_2O_3 > CoMo-EDTA/Al_2O_3 > CoMo/Al_2O_3. According to obtained results, all chelated catalysts lead to higher hydrotreating activity, and this was due to; (i) the chelating ligands forming a complex with almost all Co present and delay the Co sulfidation temperature, (ii) better dispersion of Co and Mo active species, and the formation of more dispersed type II CoMoS active phases. The low activity for CoMo/Al_2O_3 was due to strong interaction between the metal and support due to calcination forming tetrahedral aluminium molybdenum complex which resulted in the formation of more type I active

phases and fewer CoMoS type II. The results correlate with the results obtained from the theoretical studies (Section 3.2.3).

The activity of the catalysts was estimated using equation 1:

$$X_{HDS}(\%) = \frac{C^0_{DBT} - C_{DBT}}{C^0_{DBT}} \times 100 \qquad \text{equation 1}$$

where C^0_{DBT} is the DBT content in the feedstock (wt.%) and C_{DBT} was the DBT content in the products (wt. %) (Vatutina *et al*., 2019).

Selectivity was calculated by the following formula:

$$S = \frac{C_x}{C^0_{DBT} - C_{DBT}} \qquad \text{equation 2}$$

where C_x was the content of CHB or BP (Vatutina *et al*., 2019).

Figure 3.44 shows DBT model fuel before hydrodesulfization took place. **Figure 3.45** showed the product of DBT after hydrodesulfurization. The high activity for the chelated catalysts could be due to weak metal support interaction which enhances the formation of polymolybdates. These are easy to sulfide, resulting to the formation of more type II CoMoS active phases which are responsible for high HDS activity. Of all chelated catalysts CoMo-CA/Al_2O_3 exhibited the highest activity, and this can be attributed to greater dispersion of active metals in the catalyst as shown by TEM analysis.

Acidity and hydrogenation are one of the two important characteristics of a catalyst, and they affect the catalytic activity. Low acidity and fewer Bronsted sites are responsible for low HDS conversion. Acetic acid played a role of a chelating agent, and it could be possible that it may act as an additive, which affects Bronsted acidity of the support. This will result in more interaction with the surface hydroxyl group of the support, leaving only few sites to which molybdenum oxide can anchor (Baddoga *et al*., 2012). Thereby leading to the formation of polymolybdates which are easier to sulfide. Another reason for a CoMo-AA/Al_2O_3 catalyst to have higher activity compared to CoMo-EDTA/Al_2O_3 may be that since the metals are more susceptible to contact with oxygen in the catalysts synthesized with chelating agents of smaller molecules (AA and CA) (Beltrán *et al*., 2018). This will result in more Co-AA or CA ligand complexation, resulting in weak metal-support interaction and more Type II CoMoS. From the obtained results (**Table 3.18**), CoMo-CA/Al_2O_3 had higher selectivity towards the removal of sulfur via DDS route. The HYD/DDS molar ratio for catalysts was between (0.19-0.38), chelated catalysts showed higher HYD/DDS molar ratio, and this implied that the addition of chelating ligands enhanced both DDS and HYD routes. The obtained results are presented in (**Table 3.18**) and for all the catalysts the selectivity favours the DDS pathway (HYD/DDS < 1).

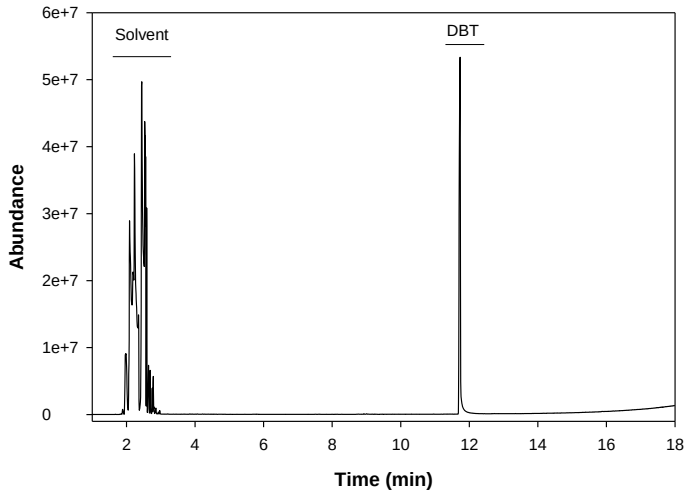

Figure 3.44: GC chromatogram of DBT before HDS.

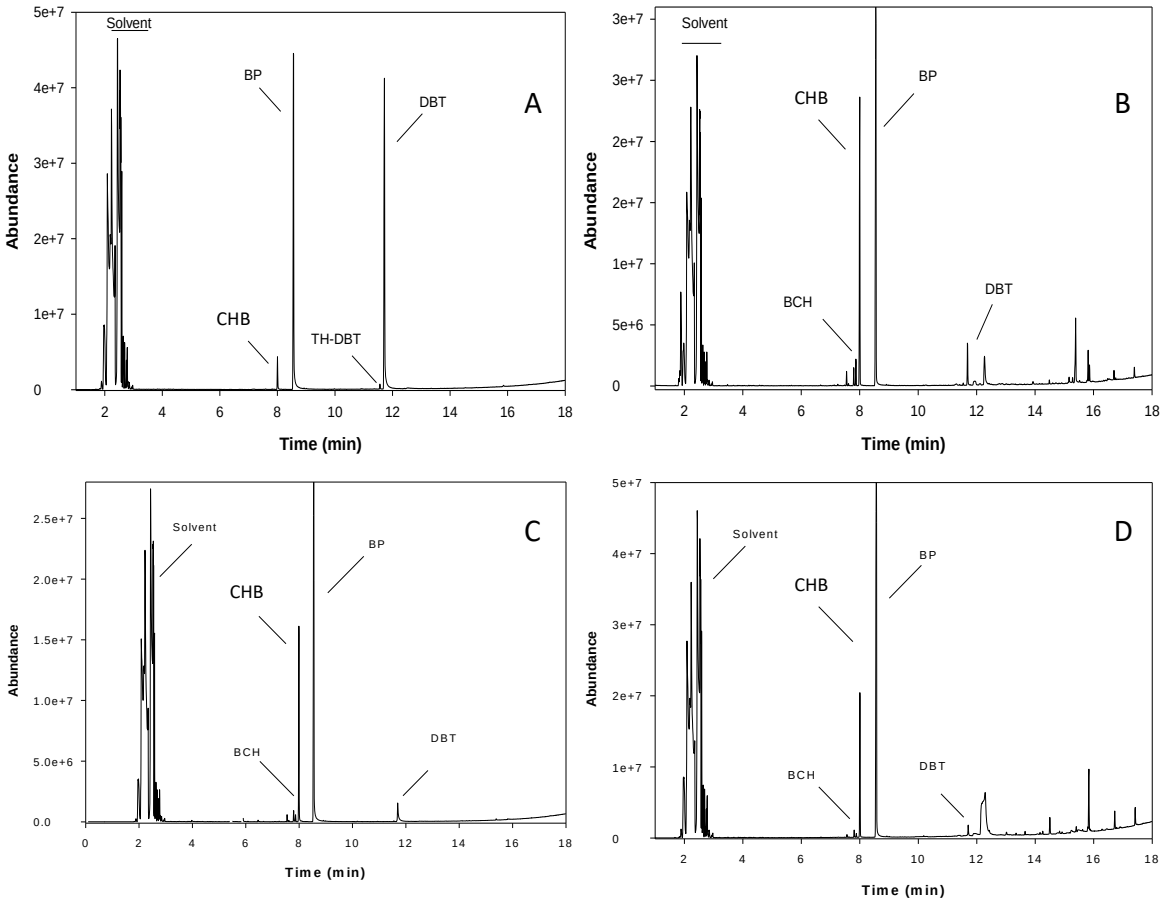

Figure 3.45: GC chromatogram of DBT after HDS using (A) CoMo/Al_2O_3, (B) CoMo-EDTA/Al_2O_3, (C) CoMo-AA/Al_2O_3, and (D) CoMo-CA/Al_2O_3. DBT = dibenzothiophene, BP = biphenyl, Cyclohexylbenzene (CHB), BCH = bicyclohexyl (clean), TH-DBT = tetrahydrodibenzothiophene.

Table 3.18: Catalytic performances of $CoMo/Al_2O_3$ and $CoMo\text{-}x/Al_2O_3$ (x = EDTA, AA, CA) in hydrotreating of DBT as a simulated fuel.

Catalysts	HDS (%)	BP	CHB	HYD/DDS ratio	TOF (h^{-1})
$CoMo/Al_2O_3$	43	21	4	0.19	31
$CoMo\text{-}EDTA/Al_2O_3$	90	63	23	0.37	56
$CoMo\text{-}AA/Al_2O_3$	94	71	27	0.38	84
$CoMo\text{-}CA/Al_2O_3$	98	76	18	0.24	150

Catalyst (Molybdenum content) employed = 0.1 g (1.66×10^{-5} moles). Time of reaction for each of the oxidation system was 6 h. [a]TOF, h^{-1}: (turnover frequency) moles of substrate converted per mole of metal ion (in the solid-state catalyst) per hour.

The best catalyst ($CoMo\text{-}CA/Al_2O_3$) was used for HDS activity of model fuel containing benzothiophene (BT) ($1.192 \times 10^{-3} moles$), dibenzothiophene (DBT) ($1.194 \times 10^{-3} moles$), and 4,6-dimethyldibenzothiophene (4,6-DMDBT) ($1.083 \times 10^{-3} moles$). The same procedure for catalytic activity was followed. It was observed that the amount of BT, DBT, 4,6-DMDBT was reduced by 100%, 63%, and 24%, respectively. The obtained product for 4,6-DMDBT was 3,3'dimethylbiphenyl, and for DBT the final products are biphenyl and cyclohexylbenzene, BT HDS catalytic activity produced a product of ethylbenzene. The low conversion observed for model fuel was due to the amount of the catalyst employed (~2 g) and the reaction time (6 h). The study of HDS for DBT was conducted for 6 h and ($1.66 \times 10^{-5} moles$) of Mo in the catalyst was required to convert ($1.194 \times 10^{-3}\ moles$) of DBT. Therefore, more Mo moles (about 20 times more) in the catalyst will be required to convert the mixture of ($1.112 \times 10^{-3} moles\ of\ BT$), ($1.194 \times 10^{-3}\ moles\ of\ BDT$), and ($7.065 \times 10^{-4} moles\ of\ 4{,}6-DMDBT$) model fuel at a longer reaction time. The results are illustrated in **Figure 4.46**.

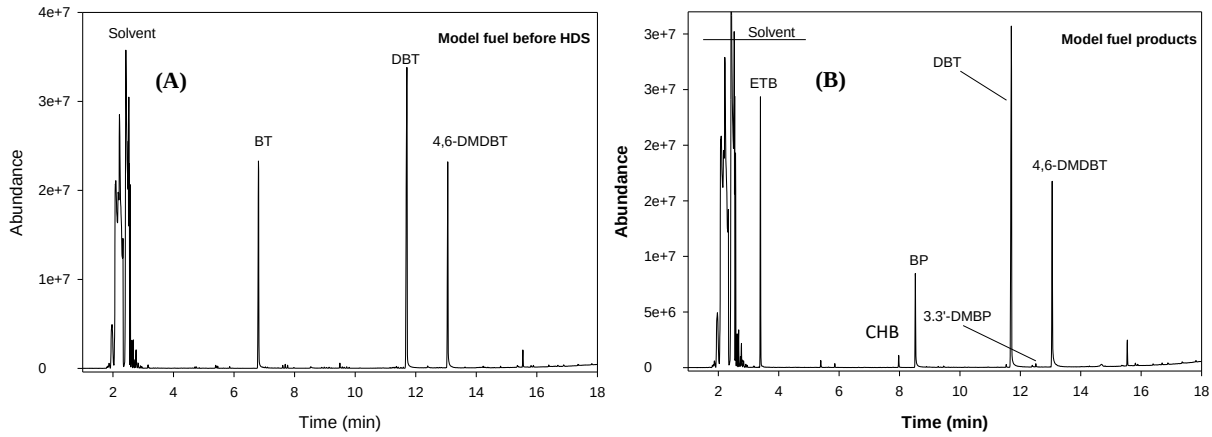

Figure 3. 46: GC chromatogram for BT, DBT, 4,6-DMDBT (a) Model fuel before HDS and (b) Model fuel after HDS activity using CoMo-CA/Al_2O_3 catalyst. BT = benzothiophene, DBT = dibenzothiophene, 4,6-DMDBT = 4,6-dimethyldibenzothiophene, 3.3'DMBP = 3.3'-dimethylbiphenyl, BP = biphenyl, CHB = cyclohexylbenzene, ETD = ethlybenzene.

3.5.13 EDS analysis for CoMo catalysts after HDS activity

The EDS analysis (**Figure 3.47**) showed the elemental composition and the atomic ratios (**Table 3.19**) of the CoMo catalysts after HDS activity. According to the obtained results the atomic percentage of elements present on the catalysts decreased (**Table 3.19**). The obtained results showed that after HDS activity the catalysts can be reusable, as their metals are still available in appropriate amounts.

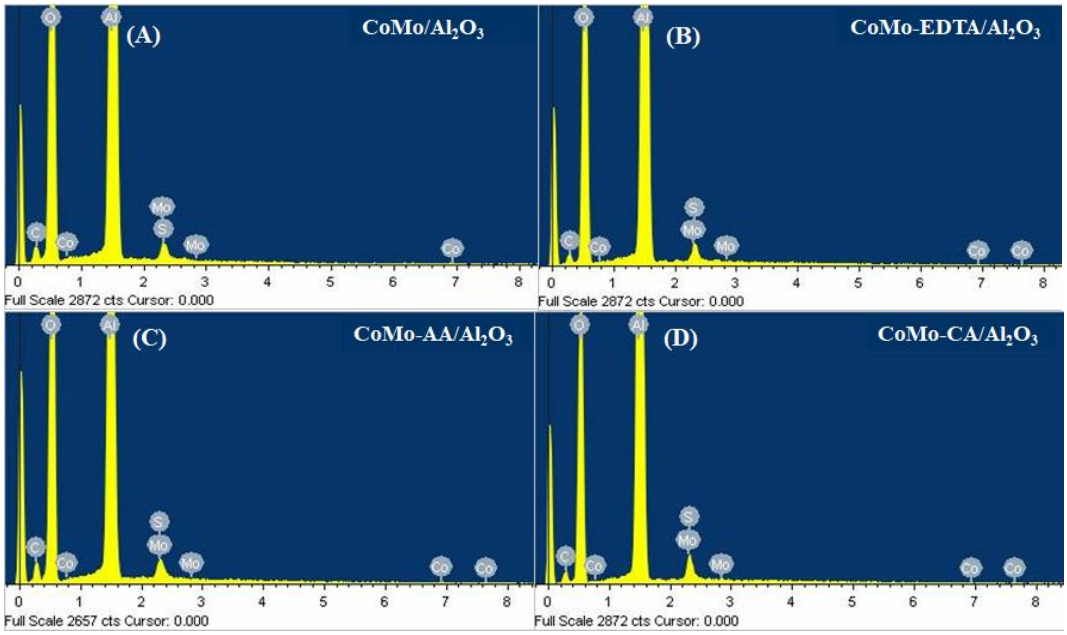

Figure 3.47: EDS analysis for sulfided (a) CoMo/Al_2O_3, (b) CoMo-EDTA/Al_2O_3, (c) CoMo-AA/Al_2O_3, (d) CoMo-CA/Al_2O_3 catalysts after HDS activity.

Table 3.19: Qualitative atomic percentage of Co, and Mo for sulfided HDS catalysts.

	Atomic Percentage (wt. %)						Ratio of Co% to Mo%
	C K	O K	Al K	S K	Co K	Mo L	
$CoMo/Al_2O_3$	9.60	60.73	28.91	0.51	0.07	0.18	0.389
$CoMo\text{-}EDTA/Al_2O_3$	14.06	60.02	25.33	0.25	0.06	0.29	0.207
$CoMo\text{-}AA/Al_2O_3$	17.00	60.18	19.91	1.94	0.13	1.27	0.126
$CoMo\text{-}CA/Al_2O_3$	8.16	62.16	28.70	0.67	0.07	0.25	0.280

3.6 Conclusion

A series of CoMo-based catalysts ($CoMo/Al_2O_3$, $CoMo\text{-}EDTA/Al_2O_3$, $CoMo\text{-}AA/Al_2O_3$, $CoMo\text{-}CA/Al_2O_3$) were successfully synthesized. The catalysts were tested for the DBT and model fuel HDS activity. Characterization by SC-XRD pointed out that Co complexed with chelating agents, and this agreed with the results obtained by TGA-DSC. Theoretical studies revealed that CoMo-EDTA complex was highly stable and low reactive, these findings played a role in HDS activity where $CoMo\text{-}EDTA/Al_2O_3$ resulted in lower HDS activity compared to other chelated catalysts. UV-vis spectrophotometric analysis showed the presence of new band at 545, 585, and 630 nm due to the addition of chelating agents. The band gaps of 3.195 ($CoMo/Al_2O_3$), 3.525 ($CoMo\text{-}AA/Al_2O_3$), 3.859 ($CoMo\text{-}EDTA/Al_2O_3$), 3.867 ($CoMo\text{-}CA/Al_2O_3$) catalysts were obtained. XPS analysis showed that the presence of chelating ligand led to better a dispersion, and this agrees with XRD and TEM analysis, this was indicated by the shift of binding energies to lower energy in the presence of EDTA. It was also discovered that the percentage of CoMoS and MoS_2 increased with the addition of EDTA. TEM analysis confirmed that chelated catalysts resulted in shorter MoS_2 slabs. EDS analysis confirmed the composition, and the elements present in the catalysts. TGA-DSC analysis was carried out and confirmed Co-chelating agent complex. The HDS activity results showed that chelated catalysts gave higher activity than unchelated catalyst, chelated $CoMo\text{-}CA/Al_2O_3$ had highest activity of 98% as compared to unchelated $CoMo/Al_2O_3$ with 43%.

Chapter Four

The effect of EDTA, AA and CA on the structure and catalytic properties of sulfided RhMo/Al_2O_3 catalysts for hydrotreating reactions

4.1 Introduction

Oil refining is one of the most important and large-scale chemical processes. In an oil refinery, crude oil is converted into well-known products such as LPG, gasoline, kerosene, and diesel oil. Crude oil is separated in different boiling fractions by atmospheric distillation, and the resulting streams are further treated and purified by a variety of catalytic processes to meet the legal and environmental specifications for the various products. The product streams undergo hydrotreating, in this process hetero atoms such as sulfur are removed from the molecules using catalysts based on transition metal sulfides. To meet the environmental regulations, the efficiency of the hydrotreating process must be increased. This can be achieved by modifying the type of catalyst, the conventionally used catalyst is molybdenum or tungsten impregnated on alumina support with Co (Ni) as a promoter (Satterfield, 1996). However, due to difficulty in the removal of the most refractory sulfur compounds, catalysts with enhanced activity and selectivity to meet the stringent environmental sulfur specifications for transportation fuel are needed (Rinaldi *et al*., 2010). Therefore, in recent years research has been primarily focused on increasing the activity of the catalyst by changing the type of promoter, type of support materials, modifying the catalyst preparation methods, using chelating ligands such as EDTA, citric acid etc. (Ninh *et al*., 2011; Sun *et al*., 2003). In certain cases, improvement have been achieved.

Many other metals have been shown to be active in HDS catalysis, and many papers have been published on the study of periodic trends in activities for transition metal sulfides (TMS) (Topsoe *et al*., 1996; Pecararo & Chianelli, 1981; Array & Rodruguez, 2000). Both pure metal sulfides and supported metal sulfides have been considered and experimental studies show that the activities of HDS for the desulfurization of DBT (or of thiophene are related to the position of the metal in the periodic table (Pecararo & Chianelli, 1981; Vissers *et al*., 1984; Ledoux *et al*., 1986). All studies agreed that the second and the third-row metals display a characteristic volcano-type dependence of activity on the periodic position, and they are considerably more active that their first-row counterparts. Rhodium is one of the metals which was found to have maximum activity. These periodic trends have been explained in several ways by different authors, always in terms of the strength of the metal sulfur bond. Another model conducted by Toulhoat *et al.*, (1997) suggested the idea that the maximum HDS activity is related to an optimum metal-sulfur bond strength (Raybaud e*t al*., 1997; Toulhoat *et al*., 1997). Therefore, it can be assumed that Rh will yield higher activity based on the discussed theory. According to this study we can assume that rhodium will act as a promoter; its presence enhances the C-S bond

cleavage activity of the catalyst *via* weakening the metal-sulfur bond and increase the electron density on the sulfur atoms (Bataille, *et al*., 2000).

The catalytic activity depends on various factors, with active metal dispersion and morphology being one of the most important factors. The interaction between the support and the metal affects metal dispersion. Moderate metal-support interaction is required to achieve optimum dispersion and the formation of type II active phase, this is because strong metal-support interaction result in high dispersion, but less reduction of metals is achieved (Stanislaus *et al*., 2010) and incomplete sulfidation of Mo oxide. While weak metal-support interaction results in the formation of bigger active metal crystals which leads to less dispersion of MoS_2. It is well established that, to increase the activity of the catalysts, the formation of more type II active sites is important. Using chelating agents or using different promoters is one of the tools which can be used to increase HDS catalyst activity.

Chelating ligands are molecules with two or more donor atoms, available to bind a metal cation (Sun et al. 2003). The use of chelating agent such as EDTA, CA on HDS catalysts show better effect on hydrotreating activity (*Rana et al*., 2007; Stanislaus *et al*., 2010). The addition of these agents favours the formation of stable complex with a promoter such as Co (Ni) as compared to Mo. Without chelating agent Co starts to sulfide at 50 ˚C and completes around 150 ˚C, while the sulfidation of Mo starts at 175 ˚C (Cattaneo *et al*., 2003). As discussed, in active phase Co(Ni)MoS_2, where Co (Ni) is located at the edges of MoS_2 slabs, the sulfidation of the promoter prior to the sulfidation of Mo results in less chances of the promoter to sit on the corner and edges of MoS_2 slabs. The sulfidation step is the most important step, it leads to the formation of type I and type II active phase of the catalysts. The addition of chelating ligands forms a complex the promoter (Co) and above 200 ˚C the complex starts to decompose, leaving the promoter (Badoga, 2012). Thus, chances of the released promoter ions to move to the edges and corners of already formed MoS_2 slabs are high, and this results in the formation of more CoMoS active phases (Sandaramurthy *et al*., 2005). This shows that the addition of the chelating agent delays the sulfidation of the promoter to higher temperatures where Mo has already started to sulfide and this leads to the formation of type II active phase, hence increasing the activity of the catalysts. Chelating agents also help catalytic activity by reducing metal-support interactions, which results in the formation of more type II active sites, and this was also confirmed by Extended X-ray absorption fine structure (EXAFS) analysis of $CoMo/Al_2O_3$ catalyst with and without chelating agent (Cattaneo *et al*., 2000). Gonzalez-Cortés *et al* conducted the study for $CoMo/Al_2O_3$ catalysts with EDTA, the TEM study showed that there is an increase in the length and stacking degree of MoS_2 slabs. Several studies have shown that the use of chelating ligands show the potential to increase the catalytic activity. However, there is rare reference in literature on the combined effects of chelating ligands and rhodium on catalytic activity of molybdenum sulfide on the Al_2O_3 support which is the main focus in this study. Among monometallic sulfides, rhodium sulfide (Rh_2S_3) has been observed to be one of the most active for the hydrodesufurization of the organosulfur compounds of thiophene (Th),

dibenzothiophene (DBT), and 4,6-dimethyldibenzothiophene (4,6-DMDBT) (Pecoraro & Chianelli, 1981; Hansel *et al*., 2000; Hayes *et al*., 2010). However, no RhMoS catalyst has been tested previously.

Table 4.1: Findings on the use of chelating agents on the HDS activity of alumina supported CoMo catalysts (Bagogga, 2015).

Chelating Ligand	**Support material**	**Active metal**	**Feed**	**Findings**	**Reference**
Ethylene Diamene	Al_2O_3	CoMo	Thiophene model feed	Pre-sulfidation heat treatment studies -EXAFT analysts	Leonova *et al*., 2014
EDTA	Al_2O_3	CoMo	2,6-dimethylanline thiophene	EDTA content used is 27 wt%	Lelias *et al*., 2010
Citric acid	Al_2O_3	CoMo	SRGO	Effect of drying condition of catalyst at 110, 220, 300, 400˚C on HDS was studied. 110 and 220 ˚C were preferred due to high activity.	Pashigreva *et al*., 2010

In literature there are some contradictions regarding the role played by chelating ligands on the HDS activity. Therefore, one of the objectives of this study is to determine the effect of promoter and chelating agents on active phase dispersion and morphology and relate it to the activity of the catalysts. The aim of this work is to meet current environmental challenges by improving catalytic activity. This chapter discusses the results of a study on the effect a promoter (Rh) in $RhMo/Al_2O_3$ catalyst and the effect of chelating agents (EDTA, CA, AA) on the activity of $RhMo/Al_2O_3$ catalyst for HDS of DBT. The catalysts were synthesized with different chelating agent/Rh molar ratios. All the catalysts, with and without chelating agents were characterized by FTIR, UV-Vis, ICP-OES, XRF, DSC-TGA, SEM, TEM, XRD, and XPS. The catalytic activity was measured in terms of HDS for hydrotreating of model fuel in a Parr reactor under industrial conditions. The catalytic activity is related to the results obtained from characterization techniques. The best activity was obtained for $RhMo/Al_2O_3$ (88%) catalyst.

4.5 Results and discussion

4.5.1 UV-Vis Spectroscopy

UV-vis absorption curves for $RhMo/Al_2O_3$, $RhMo\text{-}EDTA/Al_2O_3$ and $RhMo\text{-}CA/Al_2O_3$ are shown in **Figure 4.2-4.5**, respectively.

$RhMo/Al_2O_3$: Obtained results in (**Figure 4.1**) this catalyst exhibited a broad absorption band at 210-290 nm could be assigned to the ligand-metal charge transfer transitions $O^{2-} \rightarrow Mo^{6+}$ in octahedral coordination (Bui *et al*., 2019). A weak band observed in the region of 340-360 nm at a maximum of 346 nm was associated with Rh(III) oxides, and another weak broad band at a visible region displayed at 452 nm was due to the presence of Rh(III) in oxide form (Mendes & Schmal, 1997; Hung *et al*., 2010). A shoulder at 530 nm provided a strong evidence of well-dispersed octahedral Rh oxide species (Graselli & Bulkin, 1991), which are known to be easily reduced and sulfided and therefore susceptible to develop the active sites for the HDS reaction (Matralis *et al*., 1994, Papadopoulou *et al*., 2004; Huirache-Acuña *et al*., 2015). A broad band between 550-680 nm was due to Rh^{3+} interacting with Al_2O_3 support to form Rh/Al_2O_3 rhodium aluminate phase (Bui *et al*., 2019).

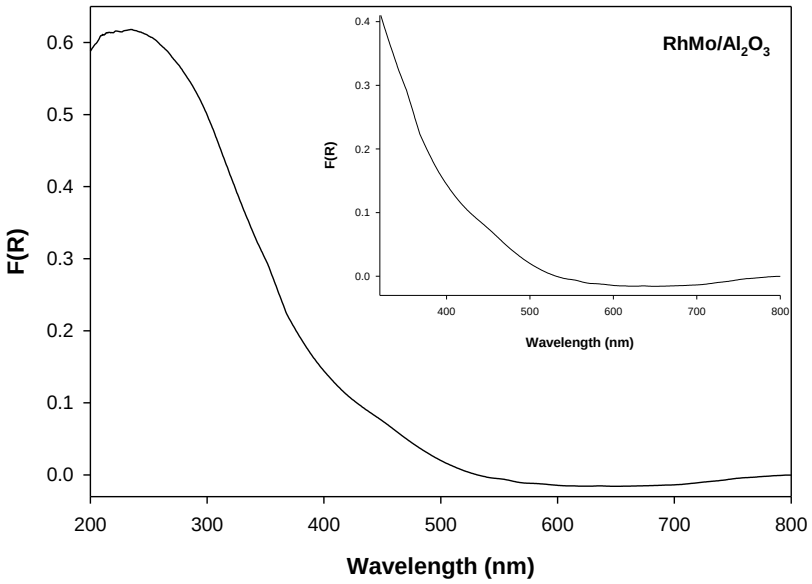

Figure 4.1: UV-Vis spectrum for $RhMo/Al_2O_3$ catalyst.

$RhMo\text{-}EDTA/Al_2O_3$: The electronic spectrum of uncalcined catalyst in (**Figure 4.2**) indicated that there was no evidence of $Rh^{3+}{}_{Td}$ observed in the spectrum, and this was expected. The incorporation of EDTA to the catalyst results in the formation of $Rh^{3+}{}_{Oh}$, and led to an improvement in the promotion, hence more O_h Rh^{3+} species (346 nm) will be coordinate with EDTA, favouring the formation of sites during sulfidation. A band at 240 nm with a shoulder between 250-320 nm were observed. The band was associated to ligand-to-metal charger transfer of O^{2-} to Mo^{6+} (Zhang *et al*., 2019), while the shoulder

was attributed to O^{2-} to Mo^{6+} ions in an octahedral coordination. The visible region of the spectrum displays a weak broad band in the 410-480 nm region, which was ascribed to ligand field transition of Rh (III).

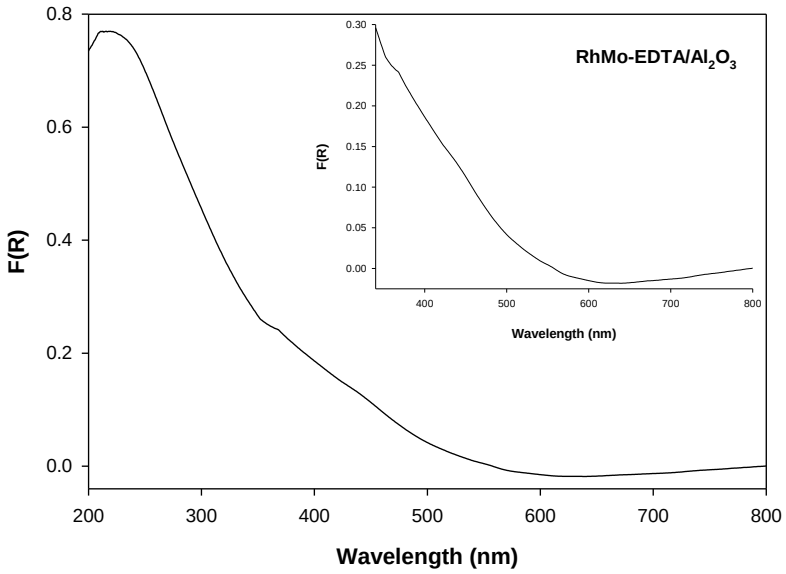

Figure 4.2:UV-Vis spectrum for RhMo-EDTA/Al_2O_3 catalyst.

RhMo-AA/Al_2O_3: The weak absorption band at 250 nm was an indication of the presence of isolated individual T_d coordinated Mo sites. A broad displayed in the region of 380-480 nm, was ascribed to ligand field transition of Rh (III) oxides (Hung *et al*., 2010). In the addition to the CT bands was due to Mo appearing in the UV-region. A band in the region of 750 nm was associated with Rh oxide species.

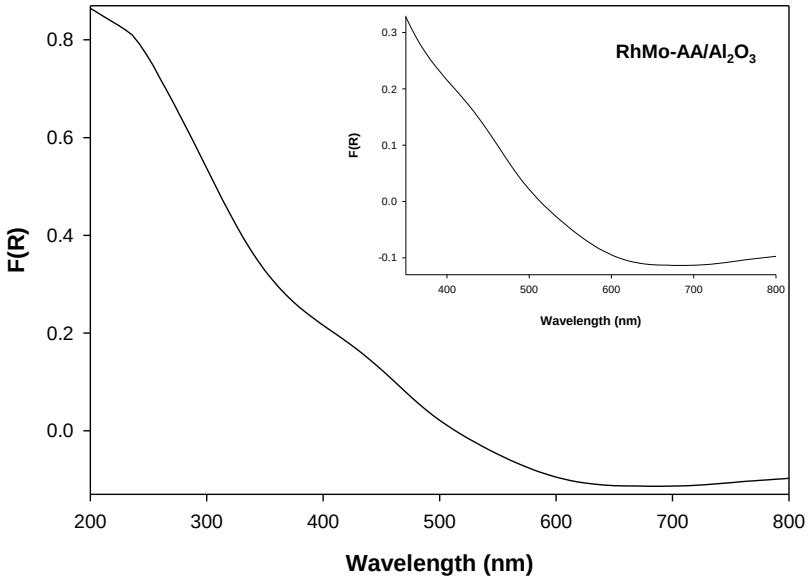

Figure 4.3: UV-Vis spectrum for RhMo-AA/Al_2O_3 catalyst.

RhMo-CA/Al_2O_3: The use of citric acid in the formulation induced deep changes in the region where promoter ion (Rh^{3+}) species are observed. After impregnation, maturation and drying, the d-d transition band shifted to lower wavelength. This shift to lower wavelength indicated a weak interaction of Rh oxide species with the alumina support which could result from CA complexation with Rh as suggested by Rinalda *et al.,* (2009) in case of citric acid (Rinaldi *et al*., 2009; Bui *et al*., 2019). The shift to a lower wavelength also indicated a decreased agglomeration of Mo species (Zhang *et al*., 2016). (**Figure 4.4**) showed a broad band between 200-400 nm due to O^{2-} to Mo^{6+} ligand-to-metal charge transfer band, and the observed shift to lower wavelength showed the formation of less polymerized molybdate species and heteropolymolybdates (Weber *et al*., 1995; Bui *et al*., 2019). A shoulder at 350 nm corresponds to d-d transitions of Rh^{3+} ions in octahedral environment of oxygen atoms in the Rh-Mo complex (Bergwerff *et al*., 2008; Vatutina *et al*., 2019; Hung *et al*., 2010). A low shoulder at about 400-420 nm confirmed the octahedral coordination of the Rh oxide species and it was attributed to the d-d electronic transitions.

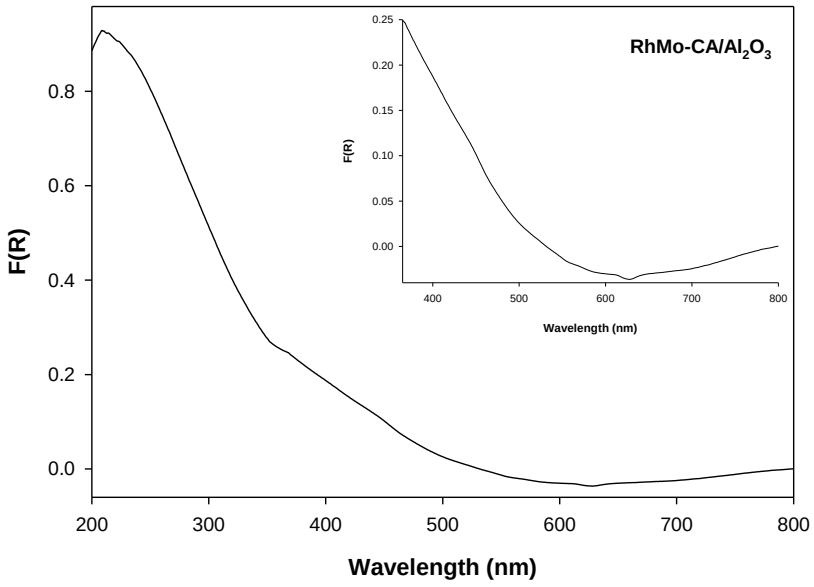

Figure 4.4: UV-Vis spectrum for RhMo-CA/Al_2O_3 catalyst.

4.5.1.1 Band gap of RhMo catalysts

The E_g value demonstrate the dispersion of the Mo species. The band gaps for RhMo/Al_2O_3, RhMo-EDTA/Al_2O_3, RhMo-CA/Al_2O_3 and RhMo-AA/Al_2O_3 were determined and are displayed in (**Figure 4.5-4.8**). The band gap energy (E_g) values are used to compare the dispersion of Mo species of the oxidic catalysts (Zhang *et al*., 2019). According to literature (Weber, 1995), the band gap energy increases as the size of the metal particles decreases, therefore, a catalyst with higher E_g value possesses

smaller and more dispersed particles (Xu *et al*., 2017; Shan *et al*., 2015). Chelated catalysts had the highest E_g values compared to the unchelated catalyst, hence are had more dispersed Mo species (Shan *et al*., 2015). The obtained band gap for $RhMo/Al_2O_3$ was 3.779 eV (**Figure 4.5**), the E_g value obtained for $RhMo\text{-}EDTA/Al_2O_3$ was 4.341 eV, the E_g value $RhMo\text{-}AA/Al_2O_3$ was E_g = 4.394 eV, and E_g value for $RhMo\text{-}CA/Al_2O_3$ was 4.478 eV for. $RhMo\text{-}CA/Al_2O_3$ catalyst exhibited the highest E_g value, this implies a further decrease in the average particle size of the metals. This could also be due the structural transformation of MoO_3 from amorphous to the crystalline phases as it is known to give rise to higher E_{gap}. Weber *et al*., (1995) found that larger iso-polymolybdates aggregates have lower band gap energy. Conversely, a decreased band gap energy corresponds to increased estimated average aggregation degree of oxidic molybdenum clusters. Thus, enhanced E_g suggests higher Mo dispersion (Escobar *et al*., 2017).

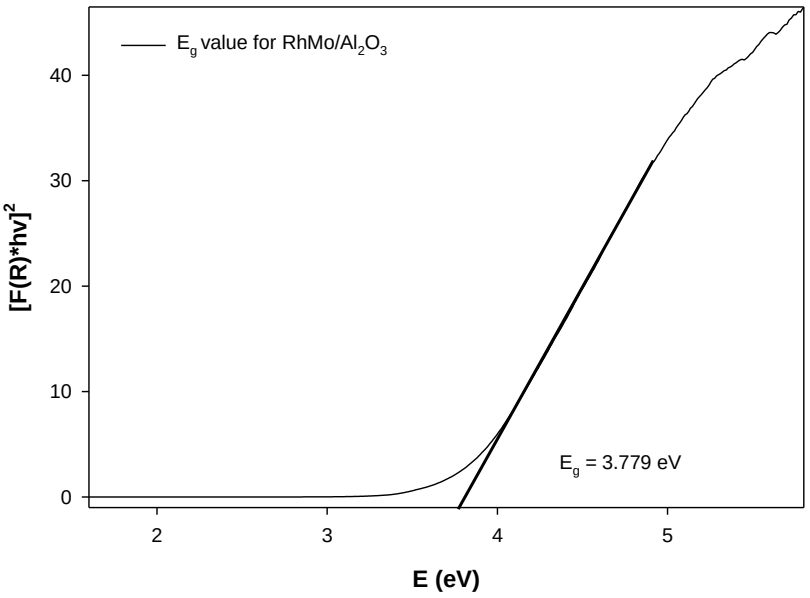

Figure 4.5: The E_g value for $RhMo/Al_2O_3$ obtained from a UV-Vis spectrum.

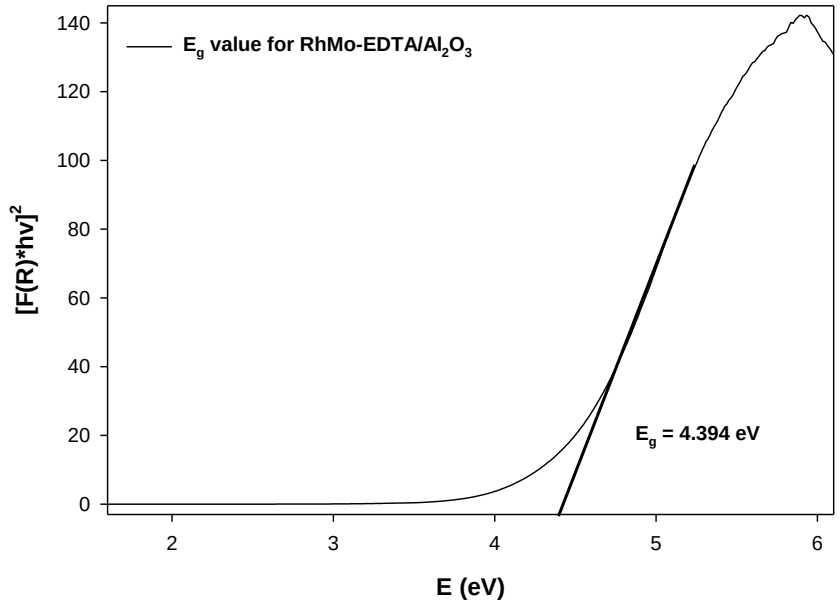

Figure 4.6: The E_g value for RhMo-EDTA/Al_2O_3 obtained from a UV-Vis spectrum.

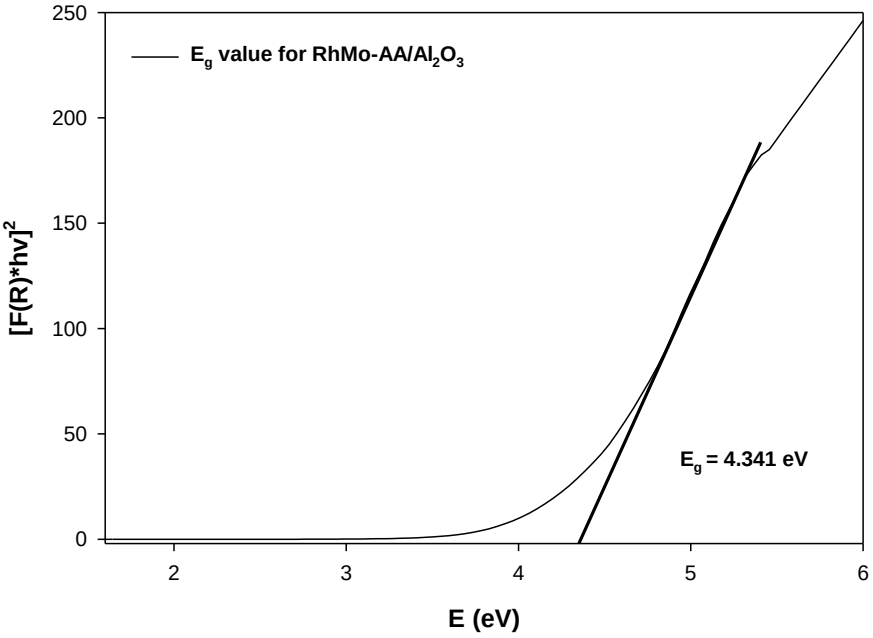

Figure 4.7: The E_g value for RhMo-AA/Al_2O_3 obtained from a UV-Vis spectrum.

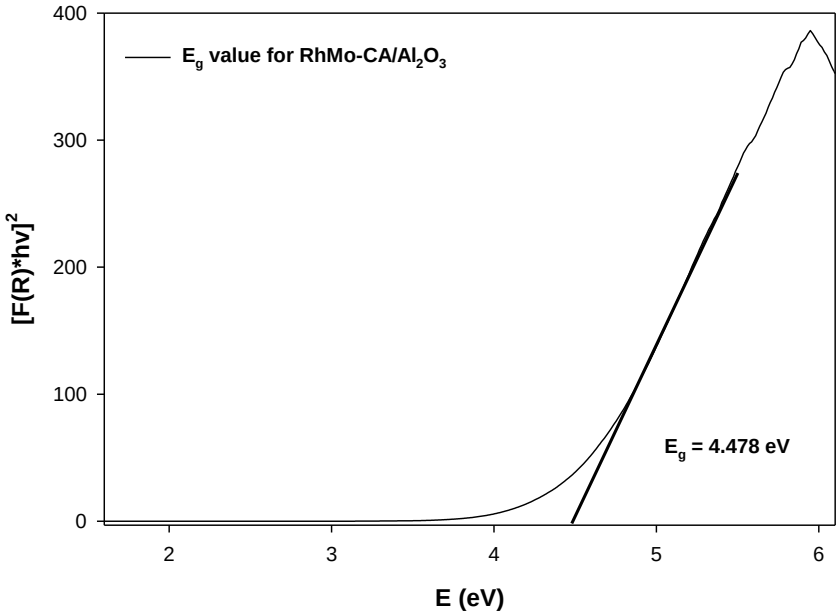

Figure 4.8: The E_g value for RhMo-CA/Al_2O_3 obtained from a UV-Vis spectrum.

Table 4.2: Band gap energy and average number of (covalent bridging of the central Mo^{6+} cation) nearest Mo^{6+} neighbors ($N_{Mo\text{-}O\text{-}Mo}$) in deposited clusters, as determined from UV spectra of the oxide CoMo catalysts.

Catalysts	**E_g values**	**$N_{Mo\text{-}O\text{-}Mo}$**
RhMo/Al_2O_3	3.779	1.975
RhMo-AA/Al_2O_3	4.341	0.5134
RhMo-EDTA/Al_2O_3	4.394	0.3756
RhMo-CA/Al_2O_3	4.478	0.1572

$N_{Mo\text{-}O\text{-}Mo} = 11.8\text{-}2.6E_g$ (Tian *et al.*, 2010)

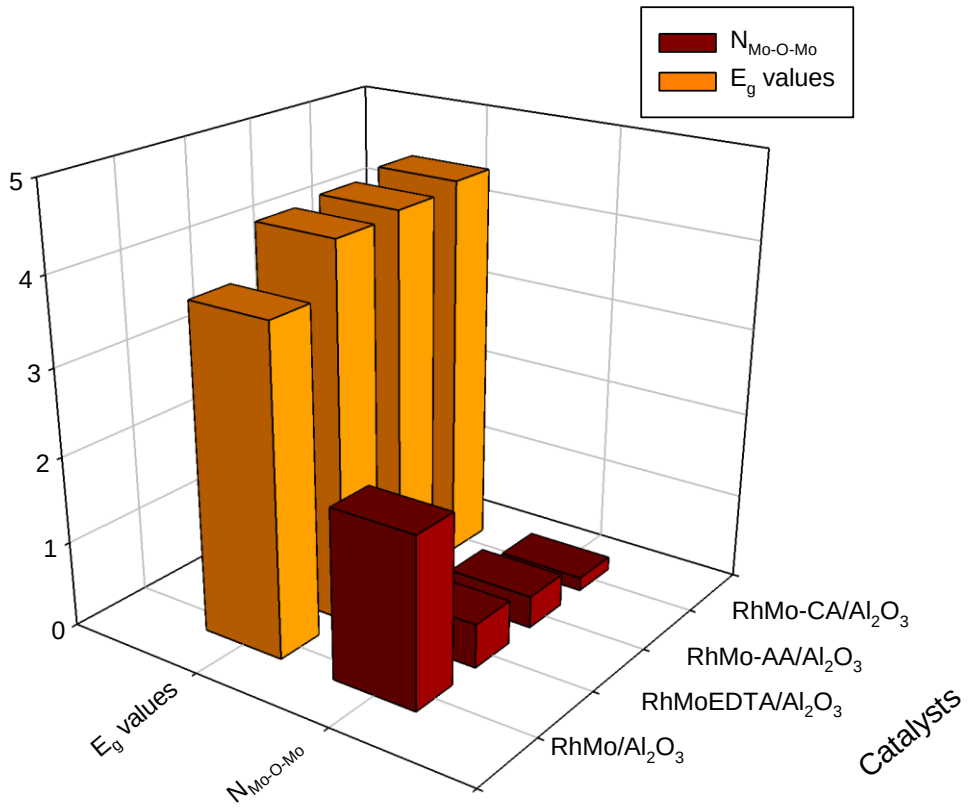

Figure 4.9: The number of covalent bridging Mo-O-Mo bonds of the central Mo^{6+} ($N_{Mo\text{-}O\text{-}Mo}$) cation and E_g values estimated from the UV-Vis absorption edge energies.

Table 4.2 shows determined number of covalent bridging Mo-O-Mo bonds or the degree of polymerization of the central Mo^{6+} cation. E_g values can qualitatively establish the extent of polymerization of metal oxides, and this helps in determining or identifying the molecular structures of different Mo (IV) oxide species present (Cattaneo *et al*., 2019). According to E_g values and ($N_{Mo\text{-}O\text{-}Mo}$) in (**Table 4.2**), RhMo/Al_2O_3 consist of $[Mo_7O_{24}]^{6-}$ clusters and trances of isolated $[MoO_4]^{2-}$ structures present, RhMo-EDTA/Al_2O_3 resulted in isolated MoO_4/MoO_6 and $[Mo_7O_{24}]^{6-}$ clusters, RhMo-AA/Al_2O_3 resulted in isolated MoO_6 clusters, and isolated $[MoO_4]^{2-}$, while RhMo-CA/Al_2O_3 had isolated $[MoO_4]^{2-}$ and traces of $[Mo_7O_{24}]^{6-}$. **Figure 4.9** showed 3D graph of the number of covalent bridging Mo-O-Mo bonds of central Mo^{6+} ($N_{Mo\text{-}O\text{-}Mo}$) vs E_g values, the results showed that the higher the E_g value the lower the $N_{Mo\text{-}O\text{-}Mo}$ values.

The increasing demand for efficient removal of sulfur has made it important to clarify the structures and the related catalytic activity of these complex catalyst systems. Molybdenum is considered the active ingredient, Mo species in HDS catalysts is present on the support as a mixture of MoO_4^{2-} and polymolybate clusters, the former being the main species (Cattaneo *et al*., 1999). The explanation of the structure of the oxidic precursors help to understand the factors that influence the formation of the

active sites on the support during sulfidation and this study was conducted using EXAFS, UV-Vis, and Raman spectroscopy (Cattaneo *et al*., 1999). The structure of the catalyst precursors werecorrelated with the catalytic activity of the final sulfided catalysts in the HDS process (Cattaneo *et al*., 1999). The smaller molybdates are easier to sulfide, since no Mo-O-Mo bridging bonds must be cleaved (Cattaneo *et al*., 2001), therefore, in this study we would expect more MoS_2 sulfidation for RhMo-AA/Al_2O_3 as it possessed less complex Mo structures.

4.5.2 Fourier transform infrared spectroscopy (FTIR)

FTIR was done to identify the functional groups present in the catalyst. The absorption bands at 3600-2800 cm^{-1} corresponds to the OH (from H_2O) stretching. At region between 550 cm^{-1} the corresponding band was assigned to Mo-O-Mo bridge stretching, while bands found and Mo=O stretching was located at 950 cm^{-1} (Cabello *et al*., 2002). RhMo-EDTA/Al_2O_3 showed an absorption band at 978 cm^{-1} which could be assigned to Mo-N band (Vatutina *et al*., 2019). At 1588 cm^{-1} the absorption band could be assigned to -COO^- vibrations with H_2O (Valencia & Klimova, 2002) (**Figure 4.10**).

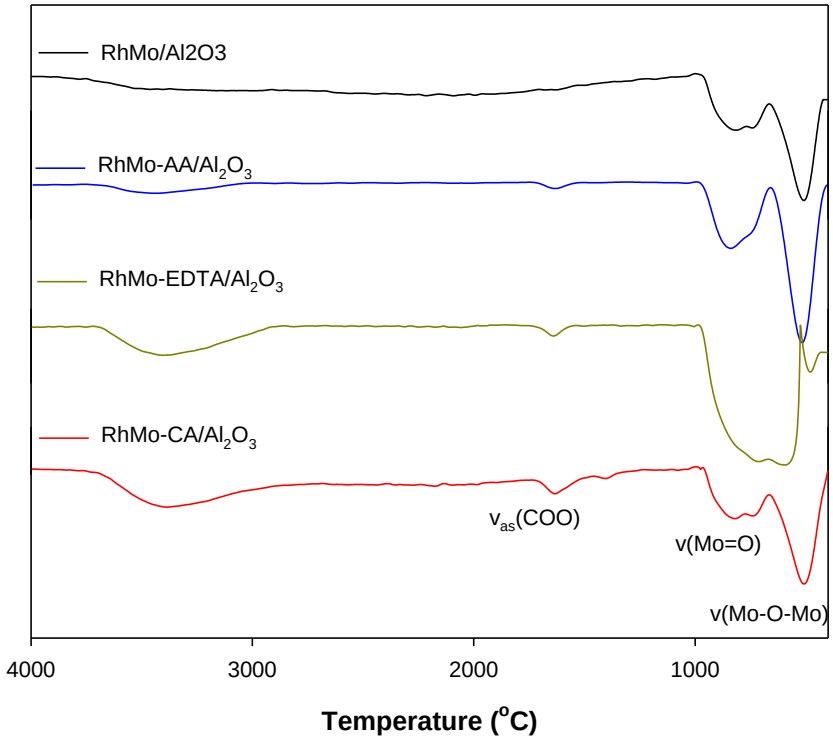

Figure 4.10: FT-IR for RhMo/Al_2O_3, RhMo-x/Al_2O_3 (where x = EDTA, AA and CA) catalysts.

4.5.3 XPS analysis of sulfided catalysts

To attain further insight into the chemical state, surface composition, dispersion, and sulfidation degree of metal species in the prepared catalysts, XPS analysis was carried out for sulfided $RhMo/Al_2O_3$ and $RhMo\text{-}EDTA/Al_2O_3$ catalysts. The survey scan spectrum, shown in **Figure 4.11a** and **Figure 4.12a**, demonstrated the presence of the key elements, O 1s, S 2p, C 1s, Al 2p and 2s, Rh 3d and Mo 3d in the catalysts. Highly resolved measurements of these individual elements are demonstrated in **Fig. 4.11b-h** and **Fig. 4.12b-h**. The binding energies of these elements are shown in (**Table 4.3**); these energies signify the presents of the elements on the catalysts. The XPS result of Rh 3d peaks for $RhMo/Al_2O_3$ showed doublet at the binding energies of 306.5 and 310.6 eV, and for $RhMo\text{-}EDTA/Al_2O_3$ the Rh 3d binding energies were obtained at 305.0 and 310.1 eV, respectively (Manolova *et al*., 2007; Muhammad *et al*., 2010). Mo 3d showed three characteristic peaks observed at 226, 230.0, and 233.2 eV for $RhMo/Al_2O_3$ and two visible peaks at 226 and 230.0 eV for $RhMo\text{-}EDTA/Al_2O_3$, respectively.

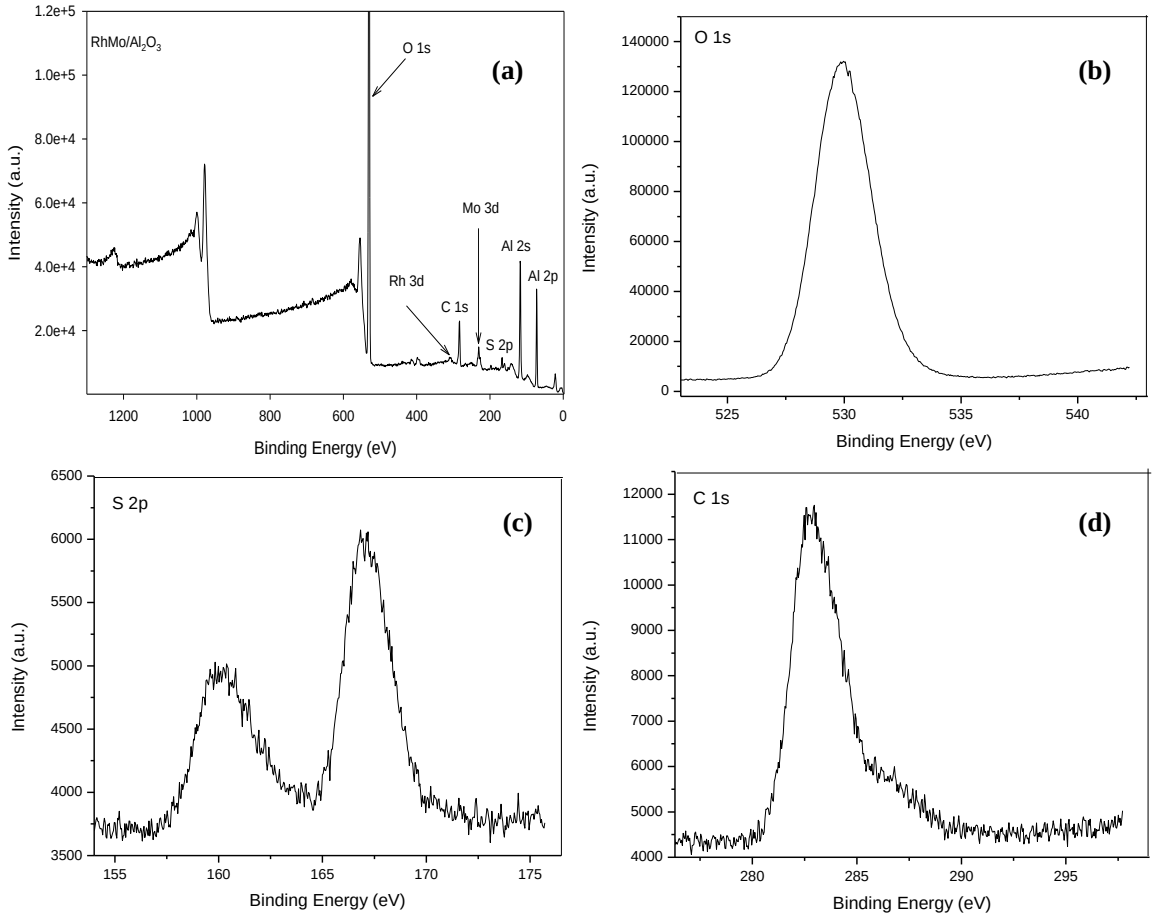

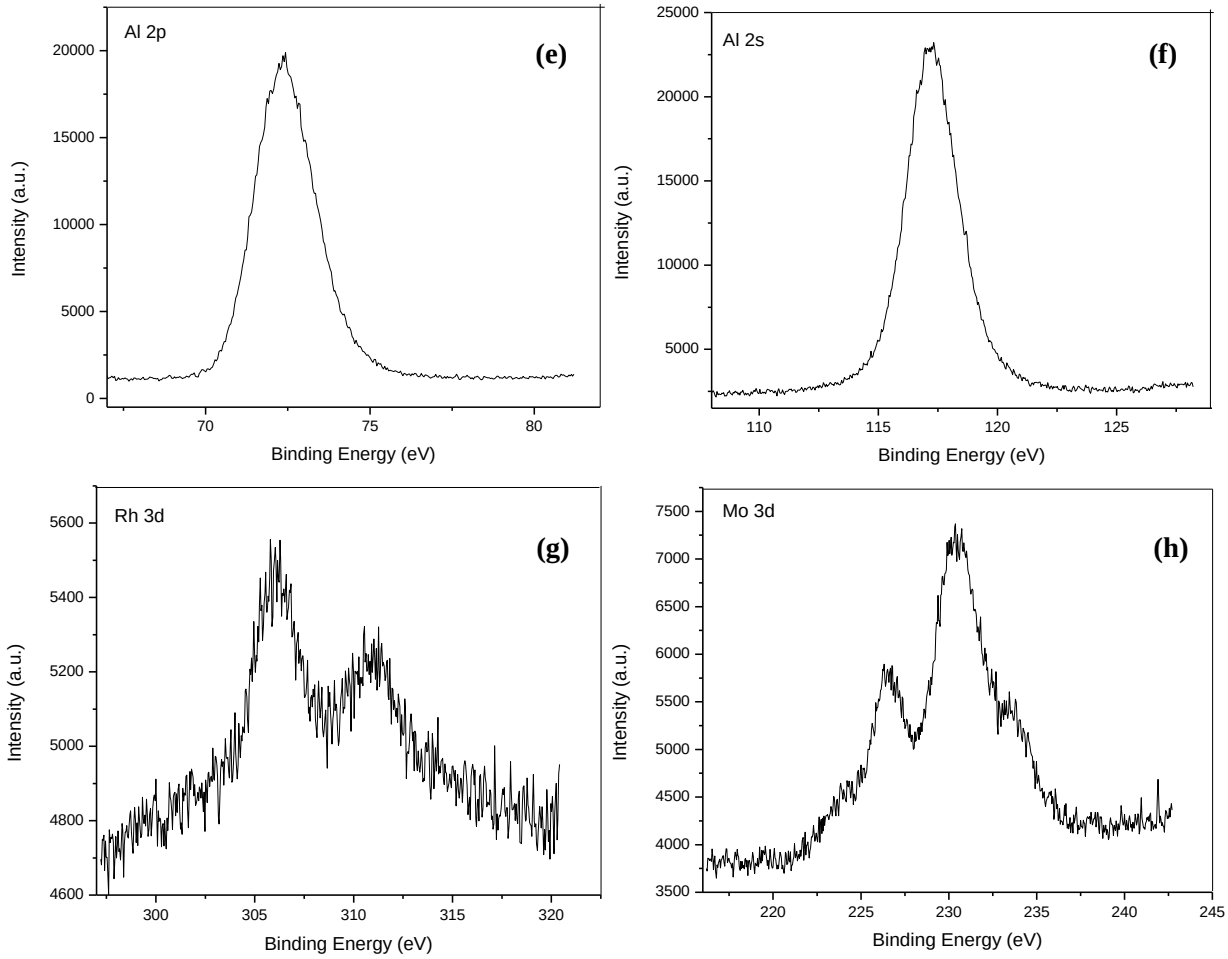

Figure 4.11: XPS spectra for (a) $RhMo/Al_2O_3$ survey spectrum with different elemental contributions, (b) O 1s, (c) S 2p, (d) C 1s, (e) Al 2p, (f) Al 2s, (g) Rh 3d, (h) Mo 3d.

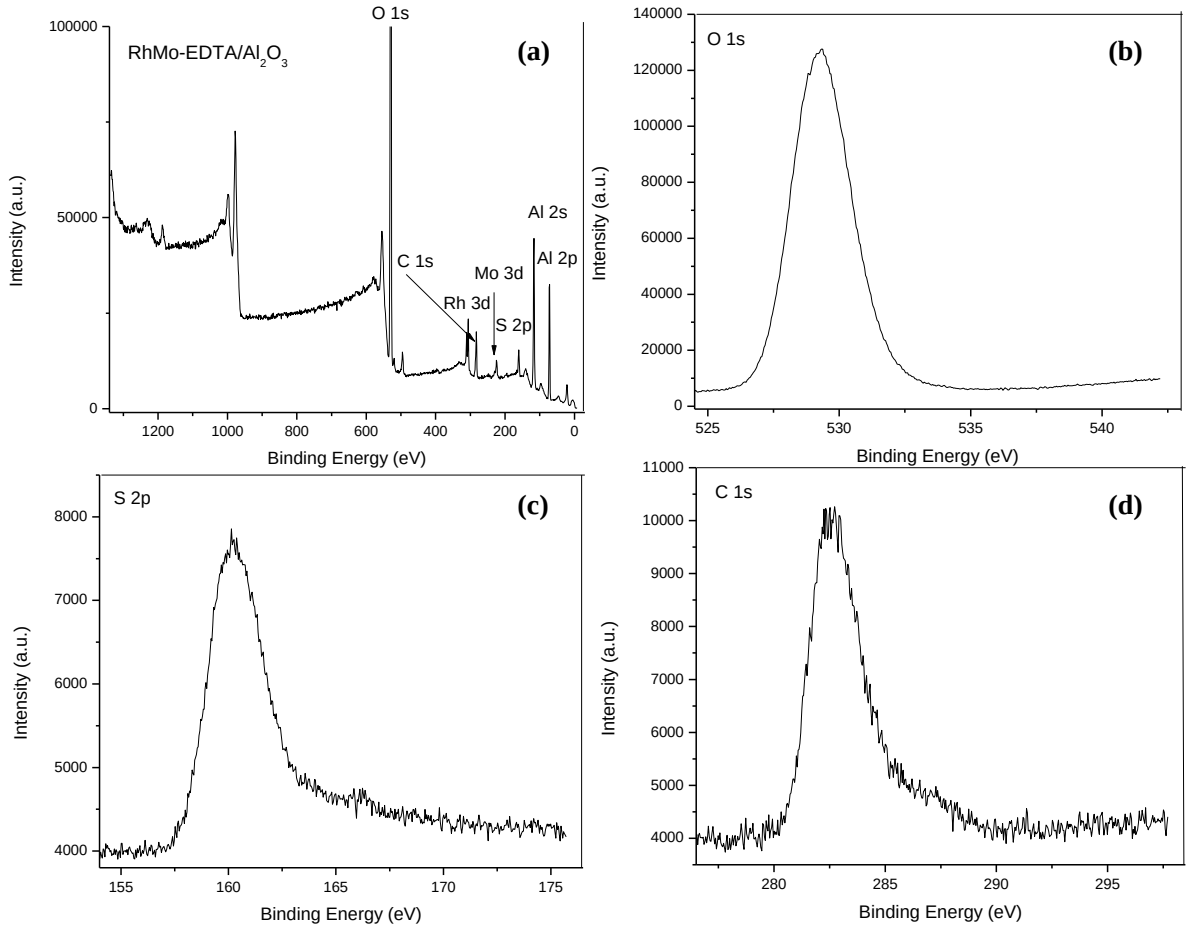
RhMo-EDTA/Al2O3
(a)
O 1s
C 1s
Rh 3d
Mo 3d
S 2p
Al 2s
Al 2p
Intensity (a.u.)
Binding Energy (eV)
(b)
O 1s
(c)
S 2p
(d)
C 1s

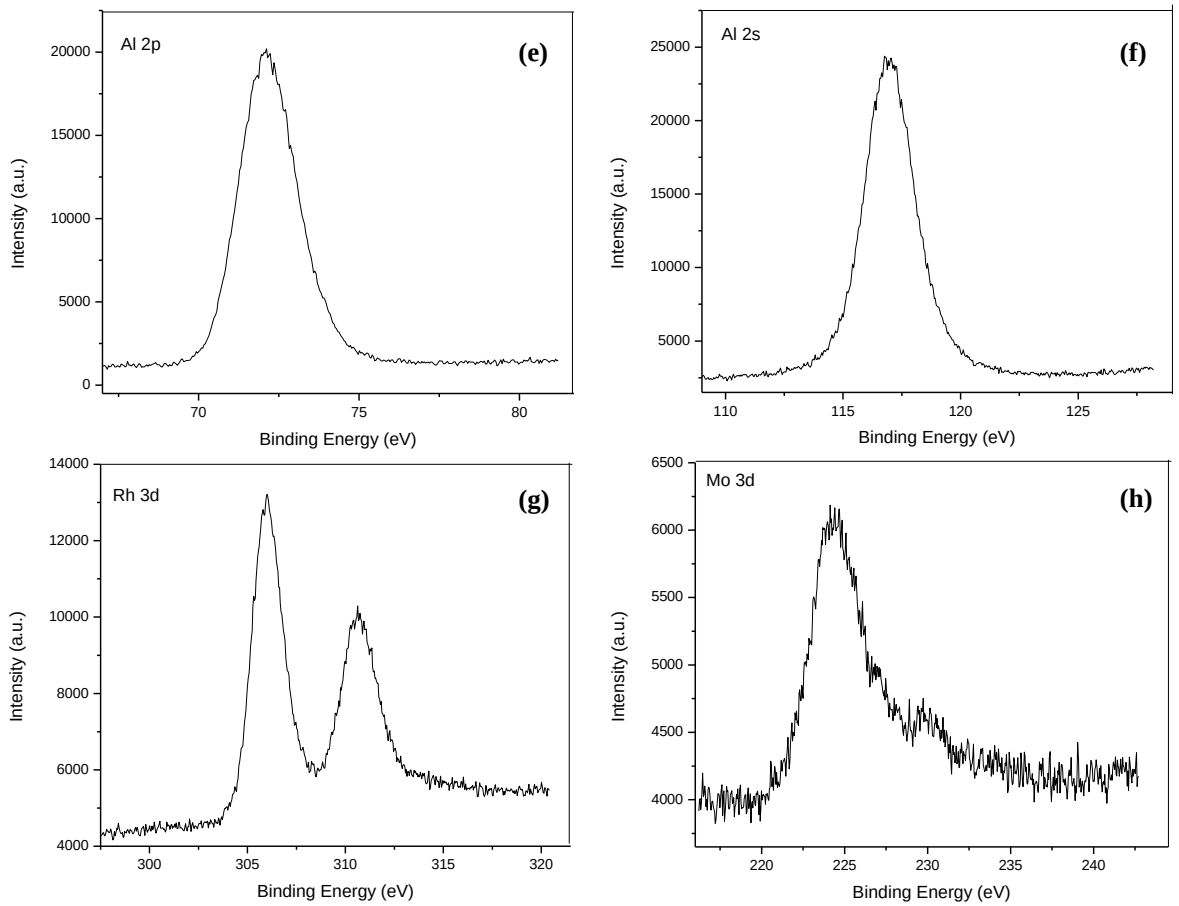

Figure 4.12: XPS spectra for (a) RhMo-EDTA/Al_2O_3 survey spectrum with different elemental contributions, (b) O 1s, (c) S 2p, (d) C 1s, (e) Al 2p, (f) Al 2s, (g) Rh 3d, (h) Mo 3d.

Table 4.3: Binding energies determined in XPS experiments.

Elements (eV)	**RhMo/Al_2O_3**	**RhMo-EDTA/Al_2O_3**
C 1s	289.5	285.5
O 1s	530.0	529.0
Mo 3d	226.2; 230.0; 233.2	226.0; 230.0
Rh 3d	306.5; 310.6	305.0; 310.1
S 2p	160.1; 167.0	160.5; 166.1
Al 2p	72.4	72.0
Al 2s	117.0	117.0

To investigate different phases within the samples Rh 3d and Mo 3d for sulfided $RhMo/Al_2O_3$ and $RhMo\text{-}EDTA/Al_2O_3$ spectra were carefully deconvoluted and the obtained results are presented in **Figure 4.13** and **Figure 4.14**. The surface chemistry of the sulfided $RhMo/Al_2O_3$ and $RhMo\text{-}EDTA/Al_2O_3$ samples was studied by XPS. Rh_2S_3 phase showed a doublet at the binding energies of 307-309.2 and 312.7-314. eV, corresponding to the Rh $3d_{5/2}$ and Rh $3d_{3/2}$ states for rhodium sulfide, respectively (Manolova *et al*., 2007; Masud *et al*., 2015). Rhodium oxide (Rh_2O_3) showed characteristic peaks between 307-310 for Rh $3d_{5/2}$, and for Rh $3d_{3/2}$ showed characteristic peaks at a region between 312-315 eV (Masud *et al*., 2015; Chen *et al*., 2009), and the corresponding results are presented in **Figure 4.13a** and **Figure 4.14a**. The Mo 3d XPS core-level spectra are generally decomposed into three main contributions corresponding to the different degrees of oxidation: +V (oxide), +V (oxysulfide), and +IV (sulfide) (Galtayries *et al*., 1997; Venezia *et al*., 2003; Dupin *et al*., 2001). **Figure 4.13b** and **Figure 4.14b** showed the deconvolution of the Mo 3d spectra. In the case of Mo, its deconvolution consisted of Mo^{4+} (228.4-229.1 eV, sulfide MoS_2), Mo^{5+} (229.7-230.5 eV, oxysulfide MoS_xO_y), Mo^{6+} (232.1-232.7 eV, oxide MoO_3) (Budukva *et al*., 2019).

The doublet at binding energy (BE) of (±) 229 eV and (±) 232.1 0.1 eV was attributed to Mo $3d_{5/2}$ and Mo $3d_{3/2}$ levels of MoS_2 (Mo^{4+}), two contributions observed at (±) 230.0 eV and (±) 235.3 0.1 eV were assigned to Mo $3d_{5/2}$ and Mo $3d_{3/2}$ of Mo oxysulfide (MoO_xS_y, Mo^{5+}) (Budukva *et al*., 2019), the binding energy of Mo $3d_{5/2}$ component located at (±) 232.2 0.1 eV was assigned to Mo^{6+} (MoO_x) species (Xu *et al*., 2019) and for Mo $3d_{3/2}$ energy level, the binding energy was (±) 236.0 eV, respectively (Huang *et al*., 2018). The peak presented at 226.3 and 226.1 eV was ascribed to S 2s level of sulfur (**Figure 4.13c** and **Figure 4.14c**). The analysis results, including the detailed binding energies and sulfidation degree of Mo species obtained by the deconvolution are shown in (**Table 4.4**), and the different phase compositions of the catalysts are calculated from the area of the deconvoluted peaks. **Figure 4.13c** and **Figure 4.14c** displayed a contribution at 162.1 eV at the lower binding energy of S 2p peak originating from S^{2-} precursor (Matsumoto *et al*., 1996; Grumelli *et al*., 2007) and it was clearly visible in both catalysts. S 2p region suggesting the existence of S^{2-}, S_2^{2-}, SO_4^{2-} species (Tang *et al*., 2015; Li *et al*., 2015). The peaks at 162.3 and 163.5 eV are assigned to S^{2-} $2p_{3/2}$ and S^{2-} $2p_{1/2}$, respectively, and are indicative of the presence of S^{2-} in MoS_2 (Han *et al*., 2016; Tang *et al*., 2015; Wang *et al*., 2019) and the characteristic peak in S 2p at 166.7 eV was attributed to SO_4^{2-} (Rashidi *et al*., 2013). The sulfidation degree of Mo species was calculated by the following formula:

$$[Mo^{4+}](\%) = \frac{A_{Mo^{4+}}}{A_{Mo^{4+}} + A_{Mo^{5+}} + A_{Mo^{6+}}} \times 100\% \qquad (1)$$

where $[Mo^{4+}]$ is the sulfidation degree of the samples, $A_{Mo}{}^{4+}$, $A_{Mo}{}^{5+}$, $A_{Mo}{}^{6+}$ are the areas of the peaks which assigned to Mo^{4+}, Mo^{5+}, and Mo^{6+} species, respectively (Wang *et al*., 2017; Nikulshina *et al*., 2019).

A catalyst with higher sulfidation degree (MoS_2) would suggest that there was a lower metal-support interaction with the active metal, resulting in easier reduction and sulfidation, thus improving HDS performance (Wang *et al*., 2017). The slight shift towards lower BE of Mo 3d in $RhMo/Al_2O_3$ catalyst (**Table 4.4**) could be attributed to weaker metal-support interaction (caused by electron effects of the defects at the surface on the alumina support), which can play a role in enhancing the catalytic activity towards the conversion of DBT (Muhammad *et al*., 2019). $RhMo/Al_2O_3$ catalyst resulted in higher percentage of MoS_2 (63%) species, this would suggest that $RhMo/Al_2O_3$ will have higher Mo sulfidation, thus increasing HDS activity.

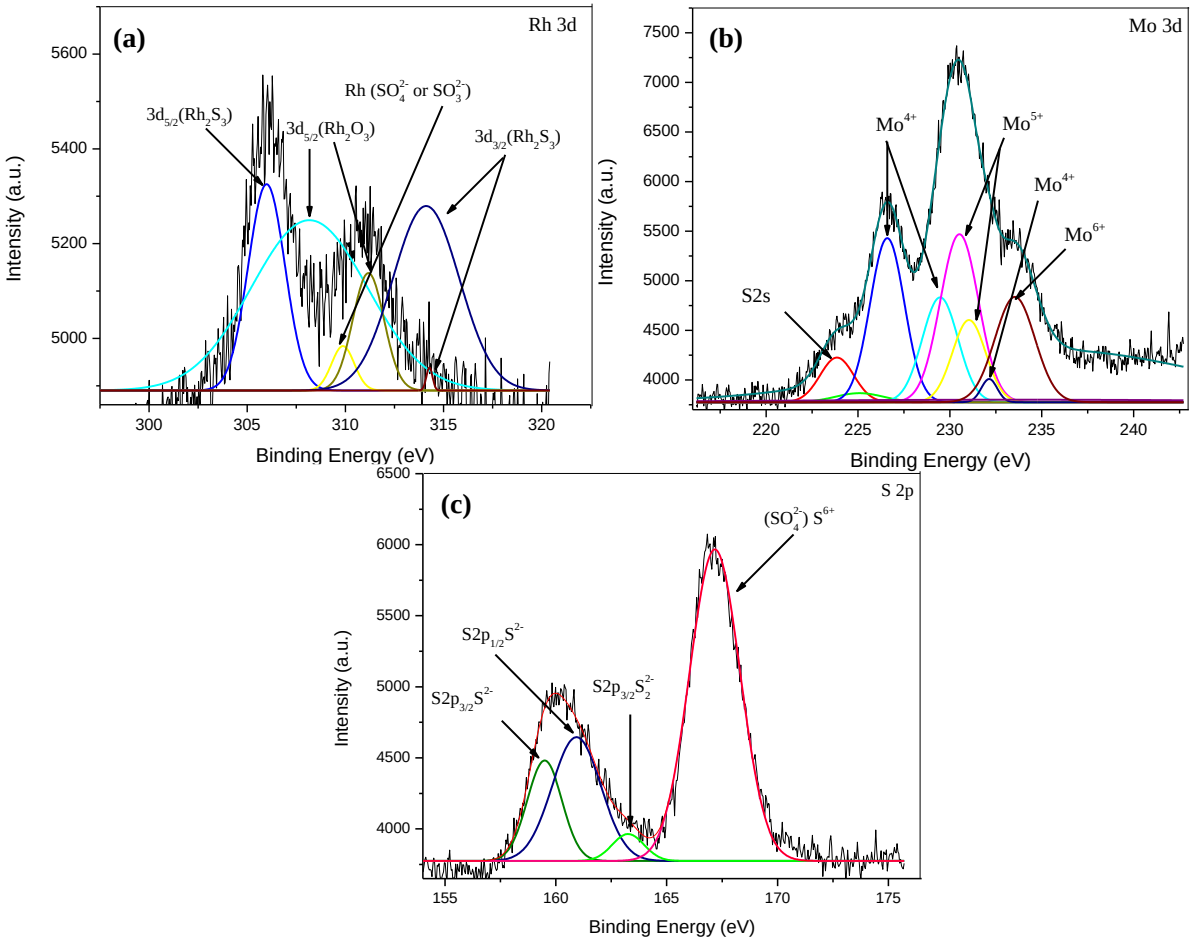

Figure 4.13: XPS deconvolution of $RhMo/Al_2O_3$ catalyst where (a) Rh 3d, (b) Mo 3d, (c) S 2p.

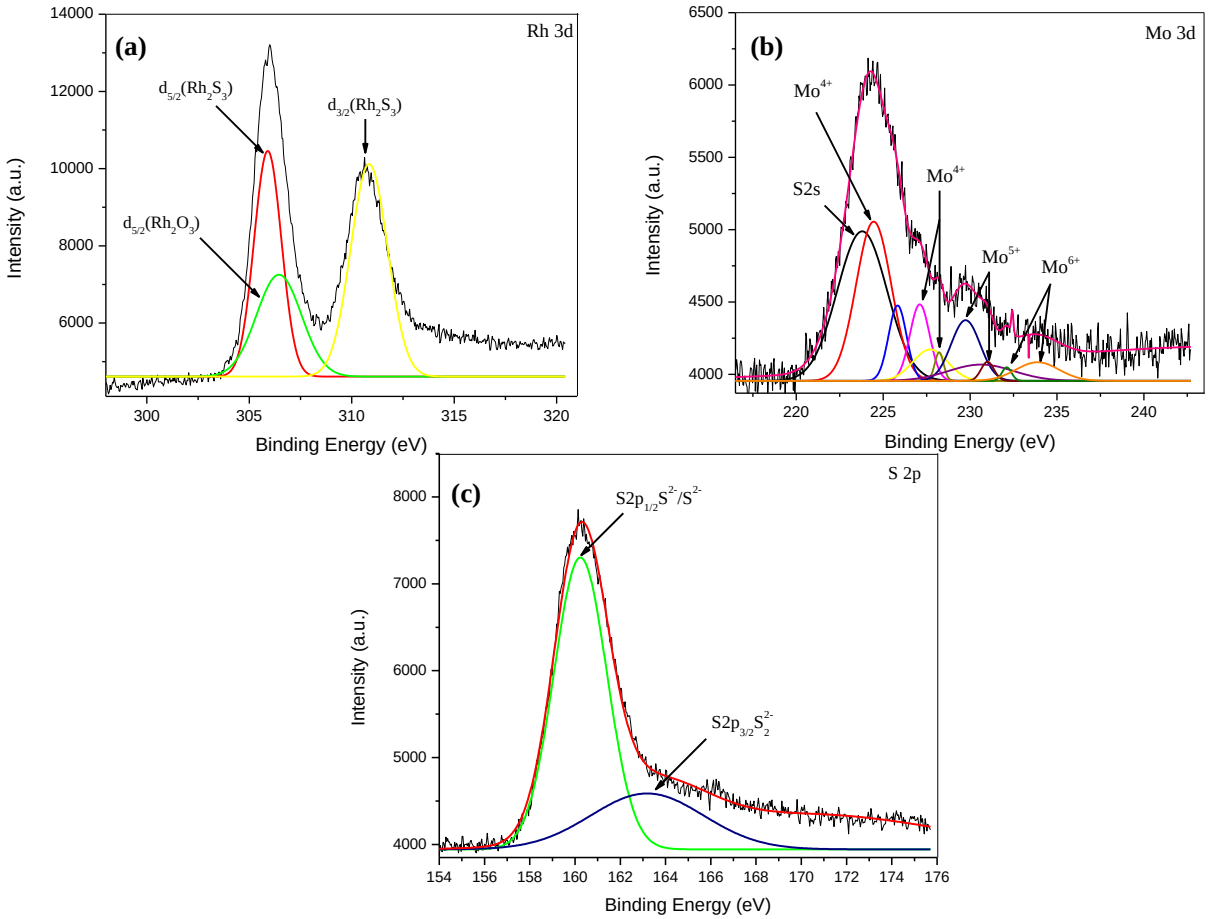

Figure 4.14: Deconvolution of RhMo-EDTA/Al_2O_3 catalyst for (a) Rh 3d, (b) Mo 3d, and (c) S 2p spectra.

Table 4.4: Binding energies of various species in sulfided RhMo/Al_2O_3 and RhMo-EDTA/Al_2O_3 catalysts and percentage of different contributions of Mo 3d phases.

Catalysts	BE (eV) Mo $3d_{5/2}$			BE (eV) S 2p		Mo distribution (%)		
	Mo^{4+}	Mo^{5+}	Mo^{6+}	S $2p_{3/2}$	S $2p_{1/2}$	Mo^{4+}	Mo^{5+}	Mo^{6+}
RhMo/Al_2O_3	229.2	230.1	233.4	162.3	163.5	63	17	21
RhMo-EDTA/Al_2O_3	229.9	230.0	233.0	160.1	163.5	60	27	13

Table 4.5: Phase composition of the different contribution of Rh 3d for $RhMo/Al_2O_3$ and RhMo-EDTA/Al_2O_3 catalysts.

Catalysts	BE (eV) Rh $3d_{5/2}$			BE (eV) Rh $3d_{3/2}$		
	Rh_2O_3	Rh_2S_3	$RhSO_x$	Rh_2O_3	Rh_2S_3	$RhSO_x$
$RhMo/Al_2O_3$	306.1	307.7	309.3	313.2	311.2	310.2
RhMo-EDTA/Al_2O_3	308.3	310.5			311.4	

4.5.4 Inductively Coupled Plasma Optical Emission spectroscopy (ICP-OES)

ICP-OES analysis was performed to provide information on the amount of elemental composition present in catalysts (metals). For the RhMo catalysts, the Mo content was in the range of 3.95-0.349 wt. % and the Rh content was in the range of 0.912-0.549 wt. %, respectively (**Table 4.6**).

Table 4.6: ICP-OES analysis for RhMo catalysts.

Catalysts	ICP-OES	
	Rh (wt.%)	**Mo (wt.%)**
$RhMo/Al_2O_3$	0.7203	3.9522
RhMo-EDTA/Al_2O_3	0.6374	1.3061
RhMo-AA/Al_2O_3	0.5486	1.0236
RhMo-CA/Al_2O_3	0.9116	0.3490

4.5.5 Energy Dispersive X-Ray Analysis (EDS)

(a) Oxide catalysts

EDS was used to measure the elemental compositions present in the catalysts. (**Table 4.7**) showed the atomic ratio of rhodium to molybdenum, and the Rh/Mo atomic ratio for the precursors are about ~0.5-1.1. The EDS analysis of the catalysts are presented in **Figure 4.15** and showed the presence of C, Rh, Mo, Al, and O by the appearance of C, O, Al, Mo and Rh. The peaks were observed at ~2.4, ~2.8, and ~3.4 KeV corresponding to the theoretical L_α, K_α, and K_β values of Rh, O peak (~0.5 KeV) and Mo peaks (~2.8 and ~3.4 KeV). The presence of additional Al (~1.5 KeV) peak was a results of alumina support, while the C peak was due to carbon tape used for the sample analysis (Yurum & Karas, 2017),

and the increase in carbon intensity for the chelated catalysts was a results of carbon present in chelated catalysts. The results are perfect evidence to propose that the sample did not contain impurities. Furthermore, the Ratio of Co% to Mo% was investigated by EDS analysis (**Table 4.7**), and it was between ~0.33 to ~0.61.

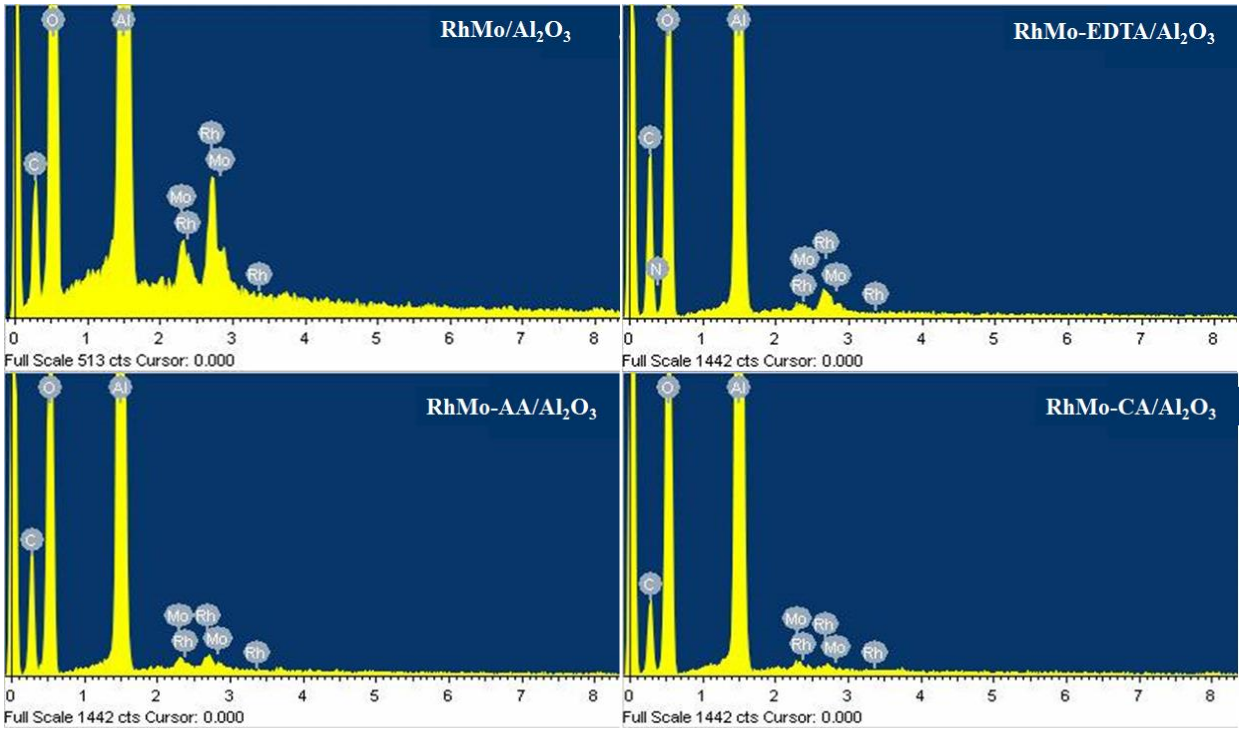

Figure 4.15: EDS spectrum for sulfided (a) $RhMo/Al_2O_3$, $RhMo\text{-}EDTA/Al_2O_3$, (c) $RhMo\text{-}AA/Al_2O_3$, (d) $RhMo\text{-}CA/Al_2O_3$ catalysts after HDS activity.

Table 4.7: Qualitative atomic percentage of Rh, and Mo in HDS catalysts.

Catalysts	**Atomic Percentage (wt.%)**						**Ratio of Co% to Mo%**
	C K	O K	Al K	N K	Mo L	Rh L	
$RhMo/Al_2O_3$	14.71	60.99	23.47	-	0.46	0.37	0.804
$RhMo\text{-}EDTA/Al_2O_3$	43.73	43.28	12.71	0.21	0.11	0.17	1.545
$RhMo\text{-}AA/Al_2O_3$	37.26	46.96	15.45	-	0.16	0.17	1.063
$RhMo\text{-}CA/Al_2O_3$	29.32	52.09	18.41	-	0.13	0.06	0.462

(b) Sulfided catalysts

The EDS of sulfided $RhMo/Al_2O_3$, $RhMo\text{-}EDTA/Al_2O_3$, $RhMo\text{-}AA/Al_2O_3$, and $RhMo\text{-}CA/Al_2O_3$ catalysts confirmed that the catalysts are made up of Rh, Mo, O, S, C, and Al (**Figure 4.16**). The peaks at ~2.37, ~2.7, ~2.81, and ~3.28 KeV corresponded to theoretical L_α, K_α, and K_β of Rh, respectively. The peaks at ~2.3, and 2.81 KeV corresponded to theoretical L_α, K_α, and K_β of Mo, the O peak was obtained at ~0.5 KeV and S at ~2.3 KeV. The additional peak at ~1.5 KeV corresponded to Al from the support, and the presence of carbon (~0.28 KeV) was due to carbon tape that was used for sample analysis (Yurum & Karas, 2017). **Table 4.8** illustrates qualitative atomic percentage of the present elements for each HDS catalyst.

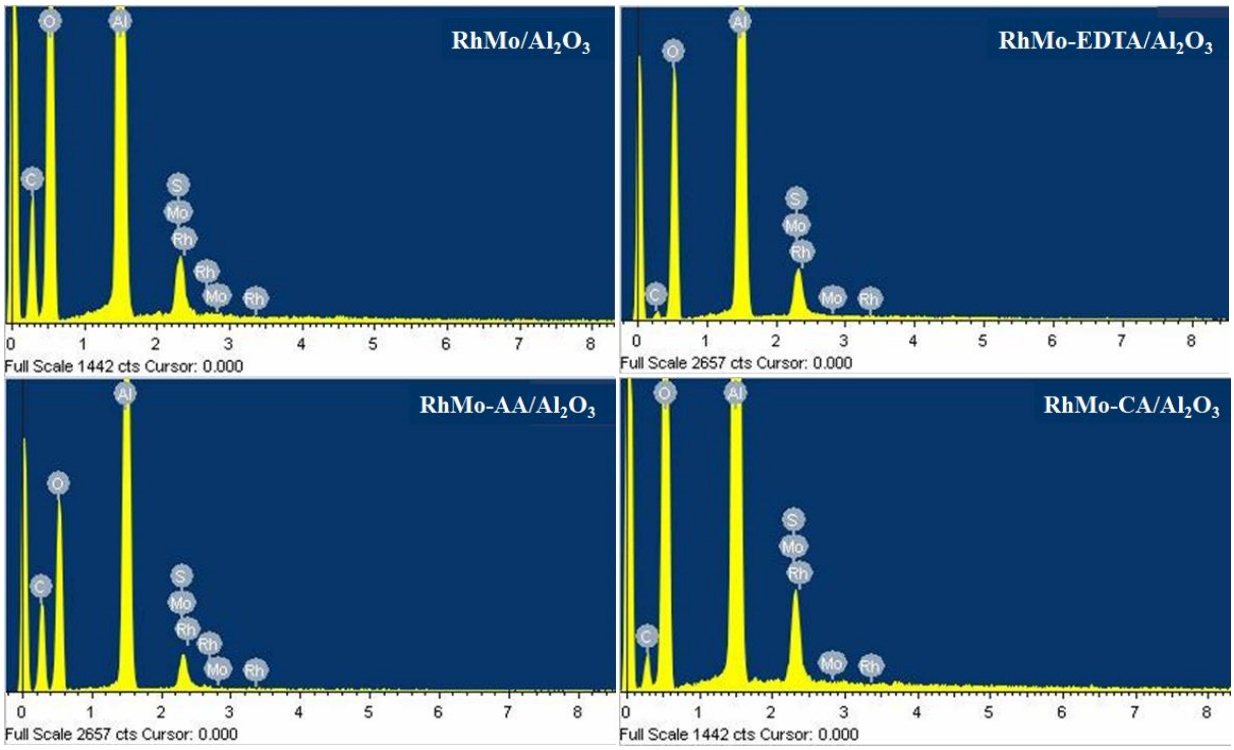

Figure 4.16: EDS spectra for sulfided (a) $RhMo/Al_2O_3$, (b) $RhMo\text{-}EDTA/Al_2O_3$, (c) $RhMo\text{-}AA/Al_2O_3$, (d) $RhMo\text{-}CA/Al_2O_3$ catalysts.

Table 4. 8: Qualitative atomic percentage of Rh, and Mo in HDS catalysts.

Catalysts	**Atomic Percentage (wt. %)**						**Ratio of Rh% to Mo%**
	C K	O K	Al K	S K	Rh L	Mo L	
$RhMo/Al_2O_3$	7.97	63.24	26.47	0.68	0.17	1.46	0.116
$RhMo\text{-}EDTA/Al_2O_3$	10.20	57.52	30.03	1.48	0.44	0.32	1.38
$RhMo\text{-}AA/Al_2O_3$	9.38	62.61	25.63	1.35	0.19	0.73	0.260
$RhMo\text{-}CA/Al_2O_3$	12.07	57.56	26.88	1.60	0.94	0.90	1.04

4.5.6 X-ray diffraction of oxide and sulfide catalysts

The XRD analysis was performed to determine the structural information of the synthesized $RhMo/Al_2O_3$ and $RhMo\text{-}x/Al_2O_3$ (x = EDTA, acetic acid (AA), citric acid (CA) catalysts. **Figure 4.17** showed that all RhMo catalysts in oxide phase had similar diffraction patterns at 2θ = 19.6˚, 32.0˚, 37.6˚, 39.5˚, 45.5˚, 60.9˚ and 67.0˚ and were assigned to (220), (311), (222), (400), (511) and (440), characteristic of γ-Al_2O_3 face-centered cubic phase, respectively. For $RhMo/Al_2O_3$ catalyst more pattern was observed at 2θ = 12.1˚, 18.5˚, 28.5˚ which was due to orthorhombic MoO_3 crystalline phase (Cheng *et al*., 2010; Badoga *et al*., 2012a), the diffraction pattern at 49.0˚ could be ascribed to the monoclinic crystalline phase of MoO_3. The pattern observed at 2θ = 34.1˚ could be attributed to Rh_2O_3 phase, the diffraction patterns at 56.0˚,57.8˚ were also observed. All chelated catalysts showed alumina support characteristic reflections and very weak reflection peaks for $RhMo\text{-}CA/Al_2O_3$, and this indicated that the addition of chelating agent could promote the redispersion of bulk MoO_3 (Zhang *et al*., 2016). $RhMo\text{-}EDTA/Al_2O_3$ and $RhMo\text{-}AA/Al_2O_3$ had no metal species present this would indicate small particle sizes below 2-3 nm and a high degree of dispersion of catalyst nanoparticles (Chen *et al*., 2009), while $RhMo\text{-}CA/Al_2O_3$ had a weak and broad diffraction pattern at 2θ = 11.5˚. The broadness and amorphous nature of the diffraction pattern observed in chelated catalysts indicated the absence of crystalline MoO_3 ($RhMo\text{-}CA/Al_2O_3$). According to the obtained results, it was shown that the addition of chelating ligands resulted in better dispersion of molybdenum oxide (Gutierrez *et al*., 2008).

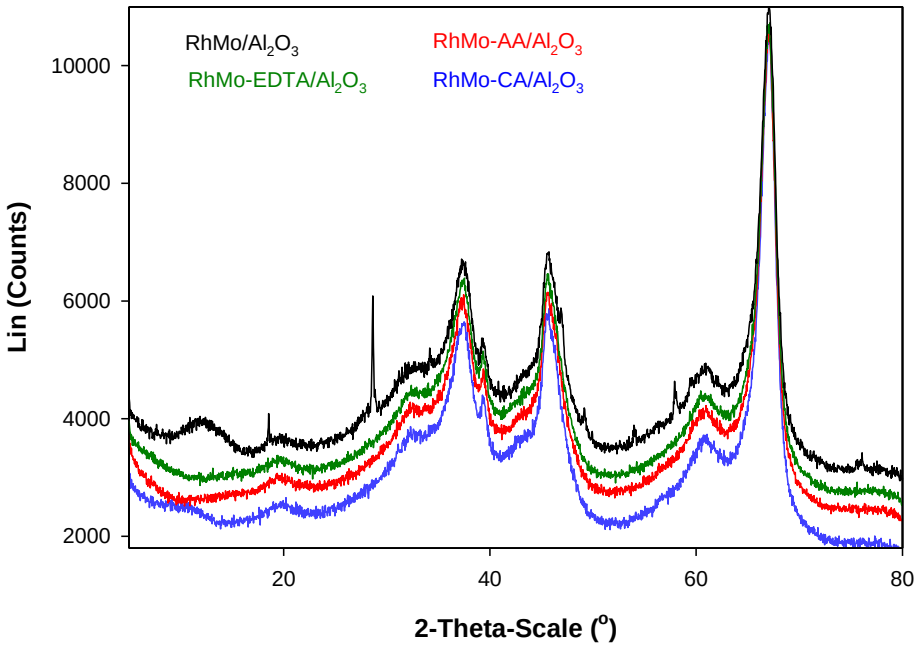

Figure 4.17: XRD patterns for RhMo/Al_2O_3, RhMo-EDTA/Al_2O_3, RhMo-AA/Al_2O_3, and RhMo-CA/Al_2O_3 catalysts.

The XRD patterns for sulfided RhoMo/Al_2O_3, RhMo-x/Al_2O_3 (x = EDTA, AA, CA) catalysts are shown in **Fig.4.18**. All catalysts showed similar diffraction patterns at 2θ = 32.0˚, 37.6˚, 39.5˚, 45.5˚, 60.9˚ and 67.0˚ and were assigned to (220), (311), (222), (400), (511) and (440), characteristic of γ-Al_2O_3 face-centered cubic phase, respectively. Sulfided RhMo/Al_2O_3 showed more and sharper crystalline pattern, the characteristic patterns were observed at 2θ = 15.1˚, 25.2˚ and could be due to octahedral MoO_3 crystalline phase (Eswaramoorthi *et al*., 2008; Badoga *et al*., 2012a). The diffraction patterns at 2θ = 29.5˚, 61.4˚, 47.2˚ could be ascribed as orthorhombic Rh_2S_3 (Parthe *et al*., 1967; Sosibono & Revaprasadu, 2008). A diffraction peak obtained at 2θ = 17.8˚ was attributed to Rh_2O_3 (Musić *et al*., 2009), and diffraction patterns at 2θ = 14,6˚, 39.1, 47.2˚, 52.1˚,60.1 were attributed to MoS_2 (Yoosuk *et al*., 2008; Beltrán *et al*., 2018), while 2θ = 55.5˚, 57.5˚, 73.1˚ and 78.3˚ were also observed. For sulfided RhMo-EDTA/Al_2O_3 there were no characteristic patterns observed, and this indicated that both Rh and Mo species were poorly crystalline or nano-sized particles resulting in well dispersed species on the alumina support (Ziegebauer *et al*., 2009; Chen *et al*., 2009). RhMo-AA/Al_2O_3 showed a very small diffraction pattern at 2θ = 14.1˚ which corresponded to MoS_2 crystallites. Sulfided RhMo-CA/Al_2O_3 showed a sharp pattern at 2θ = 18.0˚. The addition chelating ligand helped in dispersing the metal species on the support, and this could be the reason that led to a decrease in the intensity of peaks. The absence of the patterns for the chelated catalysts are due to high dispersion.

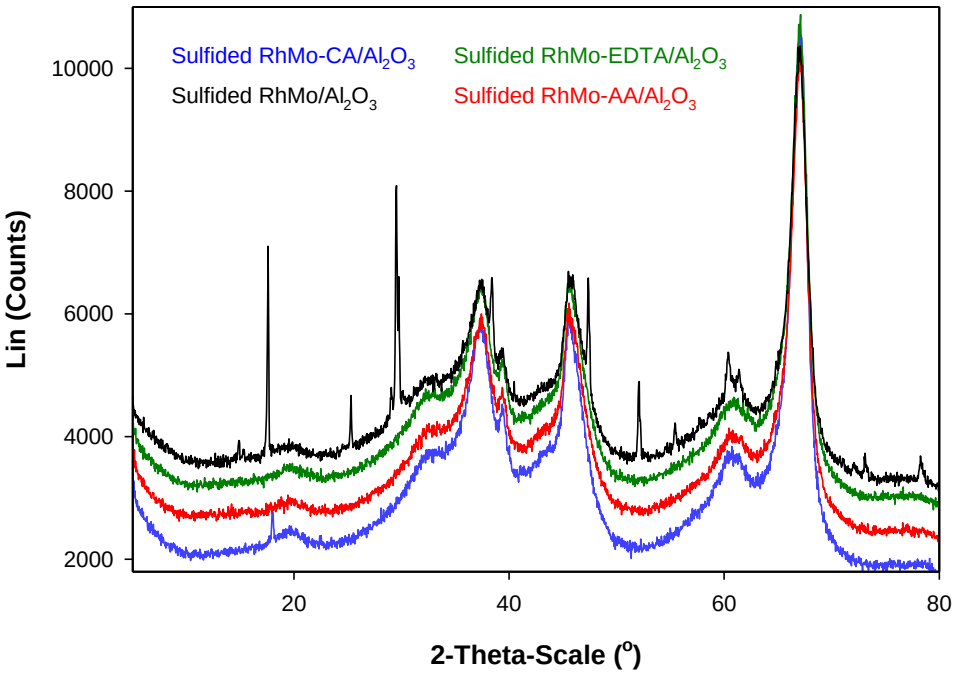

Figure 4.18: XRD patterns for sulfided $RhMo/Al_2O_3$, $RhMo\text{-}EDTA/Al_2O_3$, $RhMo\text{-}AA/Al_2O_3$, and $RhMo\text{-}CA/Al_2O_3$ catalysts.

4.5.7. Transmission Electron Microscopy (TEM)

TEM measurements of the sulfided $RhMo/Al_2O_3$ and $RhMo\text{-}x/Al_2O_3$ (where x = AA, EDTA, CA) catalysts were performed to gain more insight into the changes in the morphology and dispersion of active MoS_2 crystallites induced by chelating agent loading**. Figure 4.19-4.22** showed the distribution of MoS_2 crystallites in sulfided catalysts with and without chelating agents, and their statistical distribution results length of MoS_2 slab. The addition of chelating agents influenced particle size distribution. $RhMo\text{-}CA/Al_2O_3$ had the lowest average diameter (1.856 nm), and the $RhMo/Al_2O_3$ resulted in highest average diameter (4.72 nm). The carbon formed during decomposition of citrate ligands can perform an isolating function and prevent an increase in the length of MoS_2 slabs (Pereyma *et al*., 2018). The decrease of MoS_2 slabs improves the dispersion of the active phase (Fan *et al*., 2017). The average slab length in diameter observed for the catalysts are shown in (**Table 4.9**), and the average slab length of MoS_2 slab with the highest frequency distributed between 2.5-6.0 nm. Along with these crystallites, there were few regions with big agglomerations of molybdenum sulfide confirmed by strings of highly stacked crystallites.

The results for the MoS_2 slab average diameter in (**Table 4.9**) indicated that the MoS_2 dispersion obtained for the RhMo catalysts decreased in the order of $RhMo\text{-}CA/Al_2O_3$ > $RhMo\text{-}AA/Al_2O_3$ > $RhMo/Al_2O_3$ > $RhMo\text{-}EDTA/Al_2O_3$. $RhMo/Al_2O_3$ catalyst had highest average slab length, and this could be due to the intimate contact between Mo and Al results in a strong interaction Mo and Al_2O_3

(Mo-O-Al linkages). The higher dispersion for chelated catalysts was due to the complexation of metal-chelating ligand, reducing the metal-support interaction and leading to the delay of sulfidation of the metals. The high MoS_2 dispersion could facilitate the generation of more active sites (Shimizu *et al*., 1998; Okamoto *et al*., 2004). The effect of chelating agents on the size of MoS_2 slabs might be explained by the decoration of the promoter at the edges of MoS_2 slabs which prevent further growth of MoS_2 crystallites (Yoosuk *et al*., 2008).

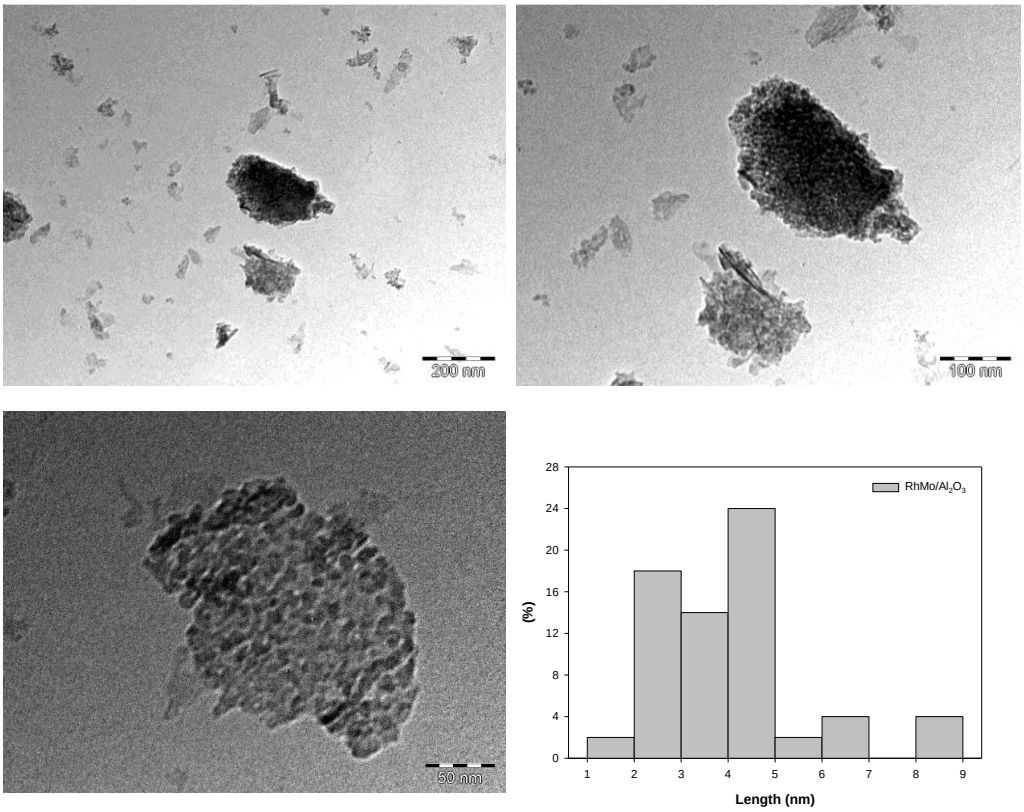

Figure 4.19: TEM images showing the slab length distribution of MoS_2 for $RhMo/Al_2O_3$ catalyst.

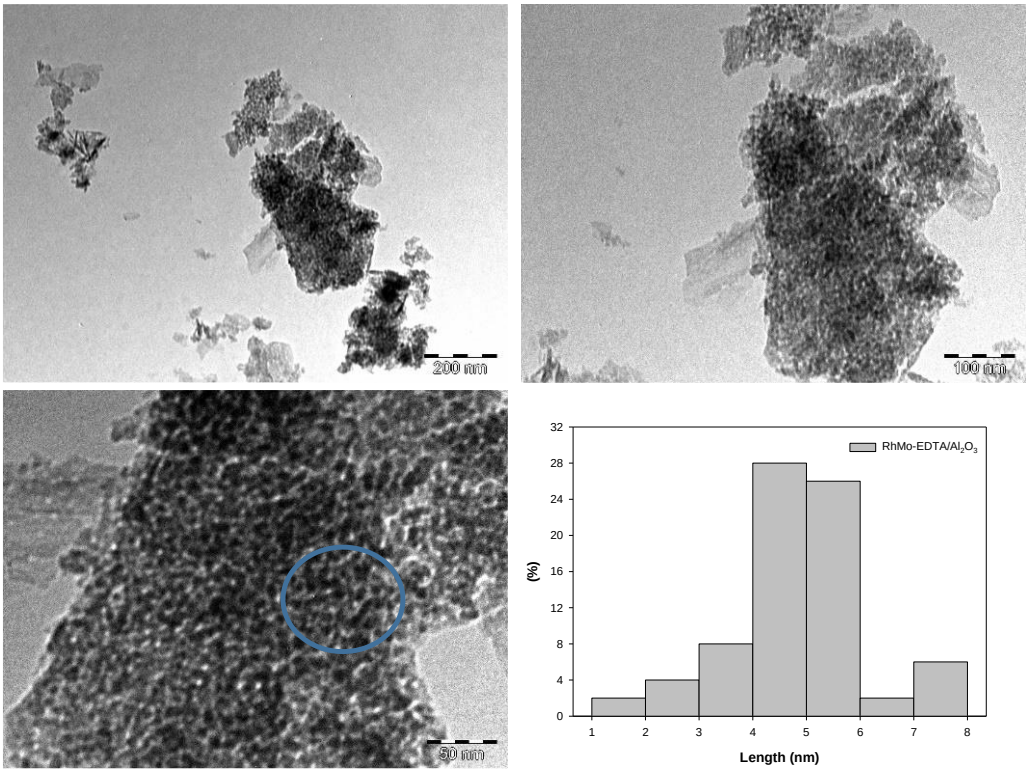

Figure 4.20: TEM images showing the slab length distribution of MoS_2 for RhMo-EDTA/Al_2O_3 catalyst.

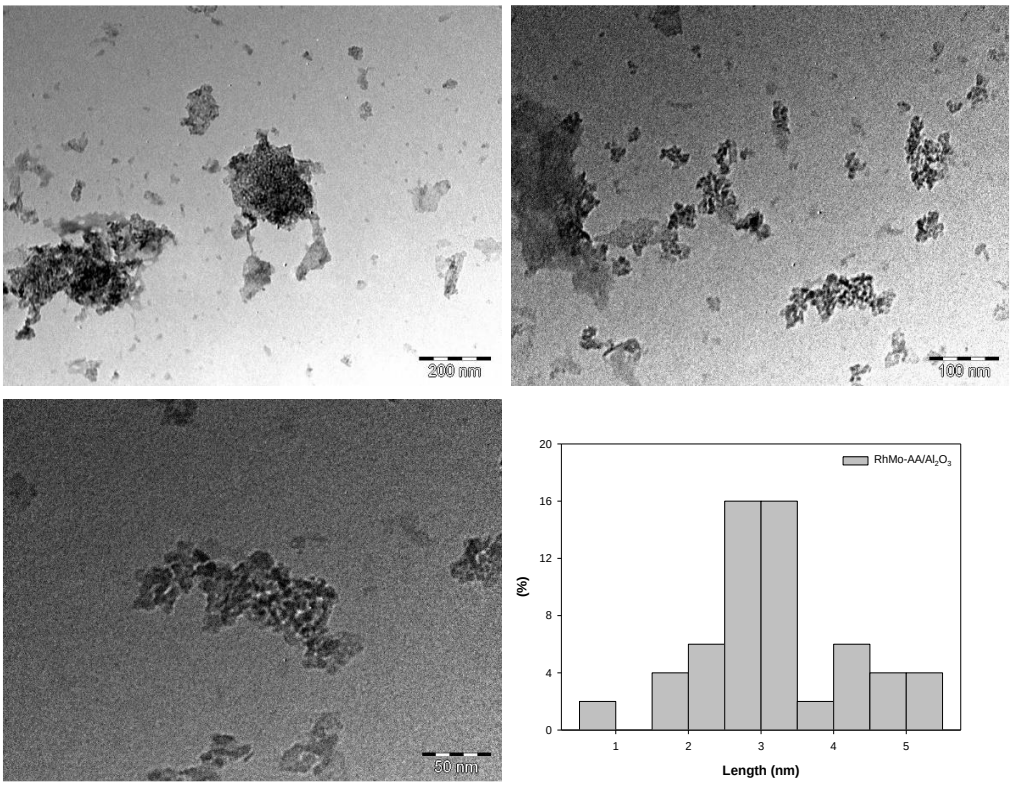

Figure 4.21: TEM images showing the slab length distribution of MoS_2 for RhMo-AA/Al_2O_3 catalyst.

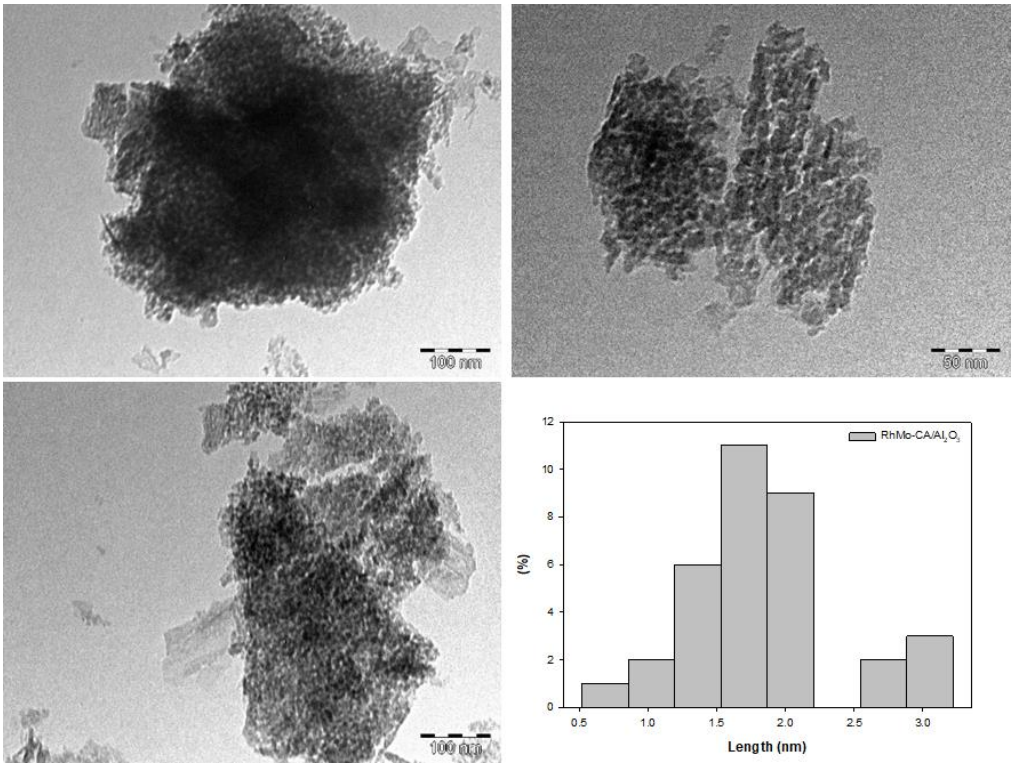

Figure 4.22: TEM images showing the slab length distribution of MoS_2 for RhMo-CA/Al_2O_3 catalyst.

Table 4.9: Average length of MoS_2 crystallites in RhMo/Al_2O_3 and RhMo-x/Al_2O_3 (x = AA, EDTA, CA) catalysts.

Samples	**Average diameter ± SD (nm)**
RhMo/Al_2O_3	4.4 (± 1.38)
RhMo-EDTA/Al_2O_3	4.1 (± 1.220)
RhMo-AA/Al_2O_3	3.3 (± 0.757)
RhMo-CA/Al_2O_3	1.6 (± 0.860)

4.5.8 Scanning Electron Microscopy (SEM)

(a) Alumina supported RhMo catalysts

In order to investigate the surface morphology and shape of the catalysts, SEM was used. The samples were coated with gold and views using TESCAN Vega TS 5136LM, and SEM images were taken at different magnifications as shown in (**Fig**. **4.23-4.26**). The images showed that particles are closely spherical in shape with average uniform distribution. All samples had average particle size (82.5-102.6

μm) and highly agglomerated in nature. The SEM images showed that all chelated catalysts had metal particles on the surface as compared to calcined catalyst ($RhMo/Al_2O_3$).

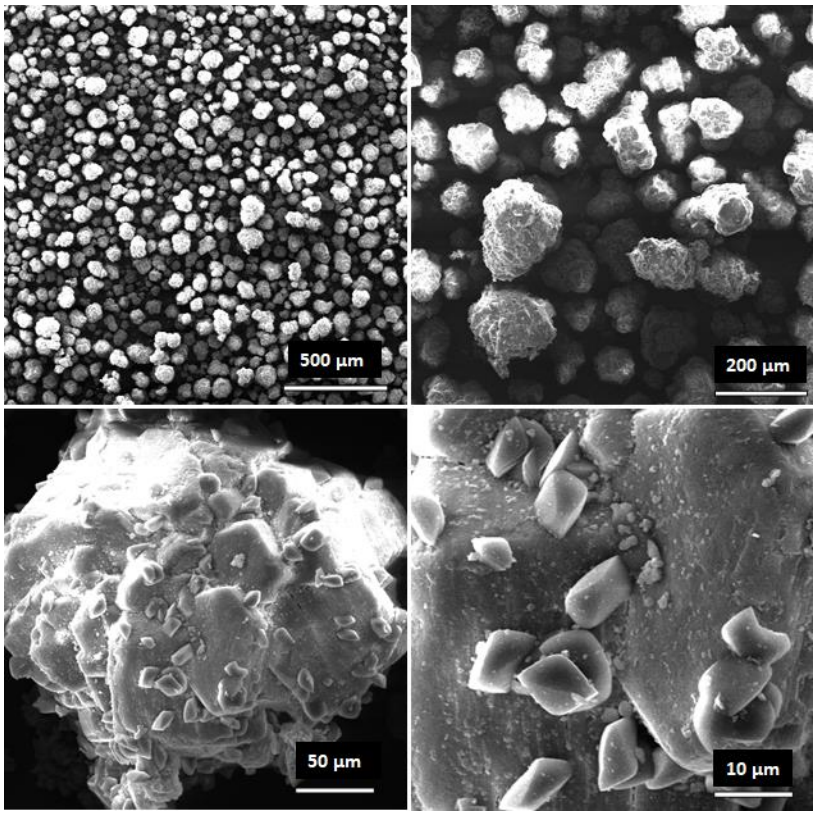

Figure 4.23: SEM images for $RhMo/Al_2O_3$ catalyst at different magnifications.

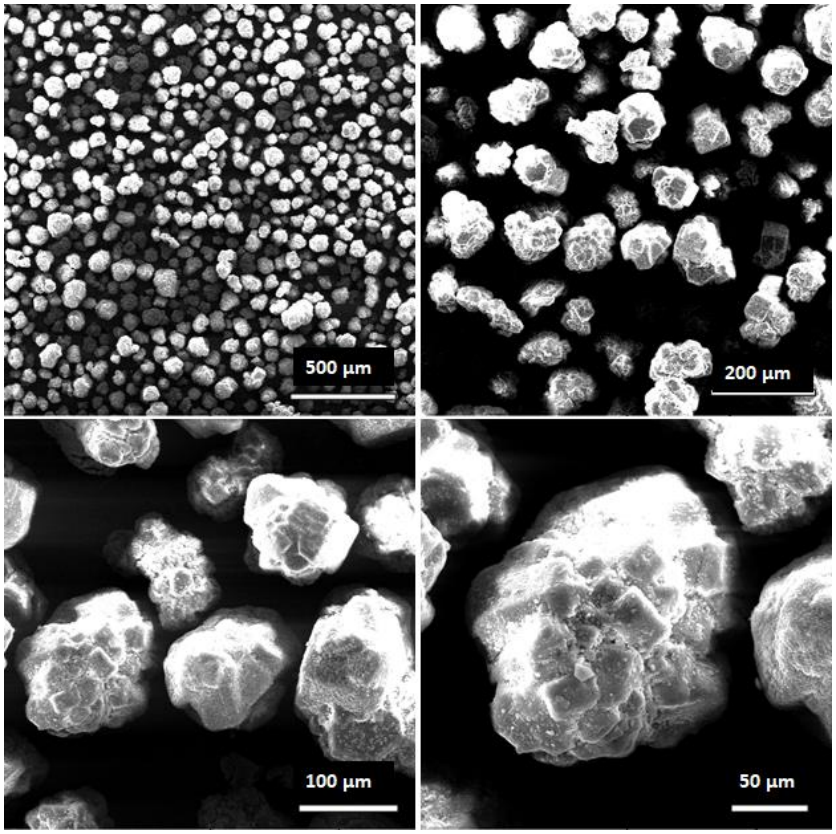

Figure 4.24: SEM images for RhMo-EDTA/Al_2O_3 catalyst at different magnifications.

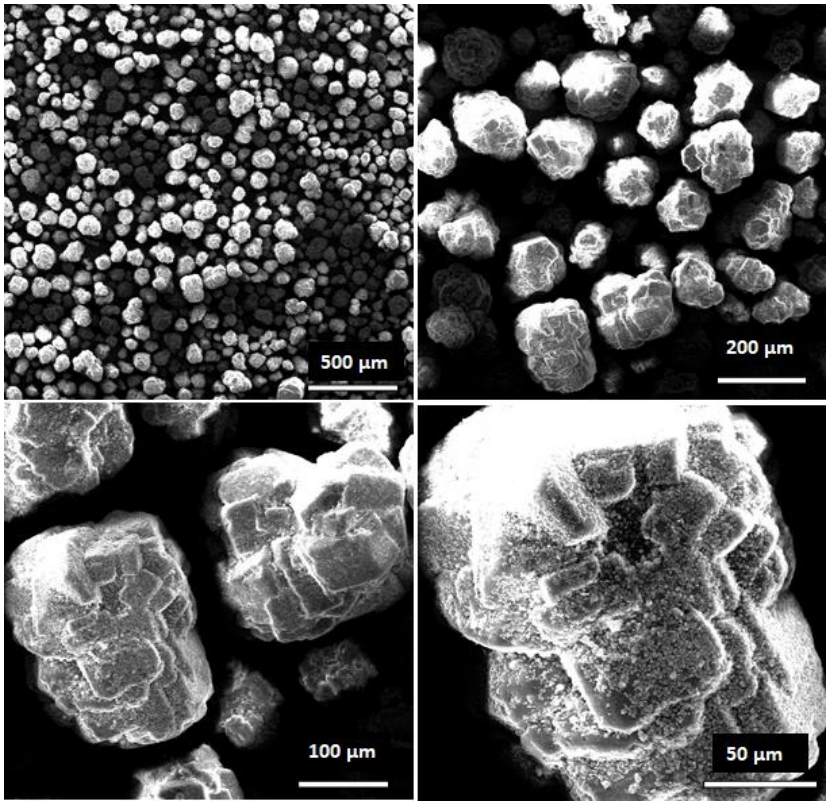

Figure 4.25: SEM images for RhMo-AA/Al_2O_3 catalyst at different magnifications.

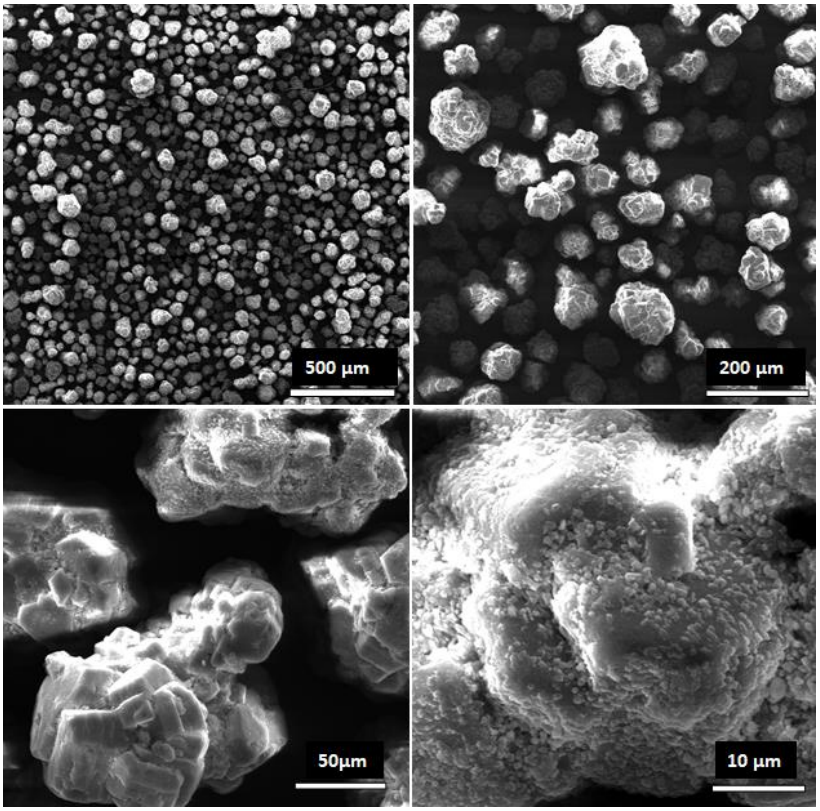

Figure 4.26: SEM images for RhMo-CA/Al_2O_3 catalyst at different magnifications.

(b) Sulfided RhMo catalysts

To investigate the morphology and the shape of sulfided alumina support RhMo catalysts SEM analysis was conducted. From the obtained results all the catalysts, showed particles that are closely spherical in nature with non-homogeneous size (**Figure 4.27-4.30**). Smaller magnification showed that RhMo /Al_2O_3, RhMo-EDTA/Al_2O_3, RhMo-AA/Al_2O_3, and RhMo-CA/Al_2O_3 are porous in nature, and the surface consists of smaller agglomerated particles.

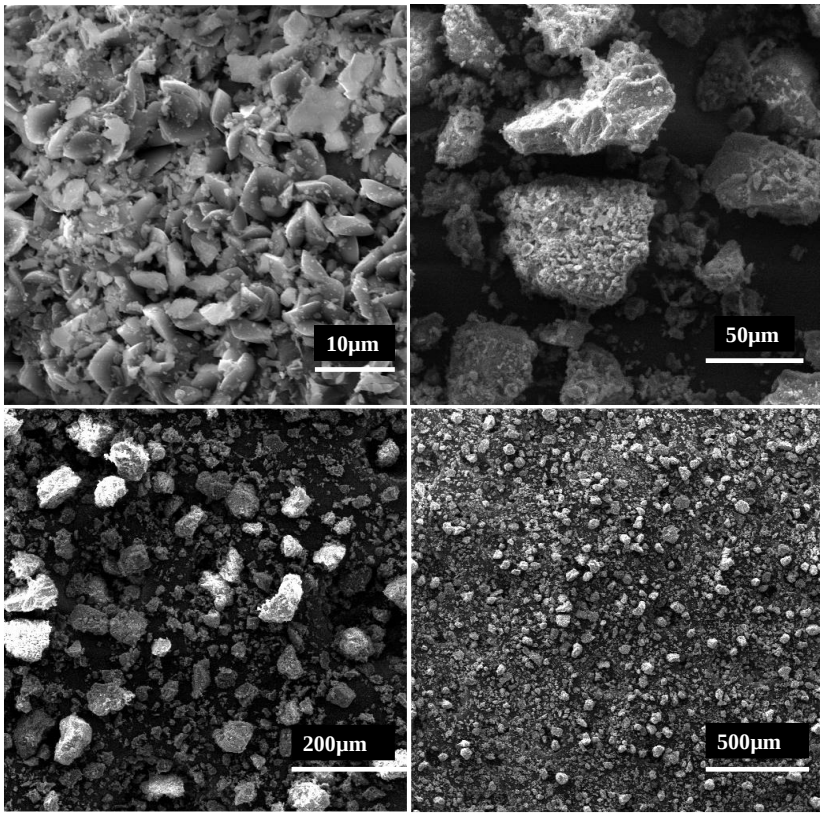

Figure 4.27: SEM images for the $RhMo/Al_2O_3$ catalyst at different magnifications.

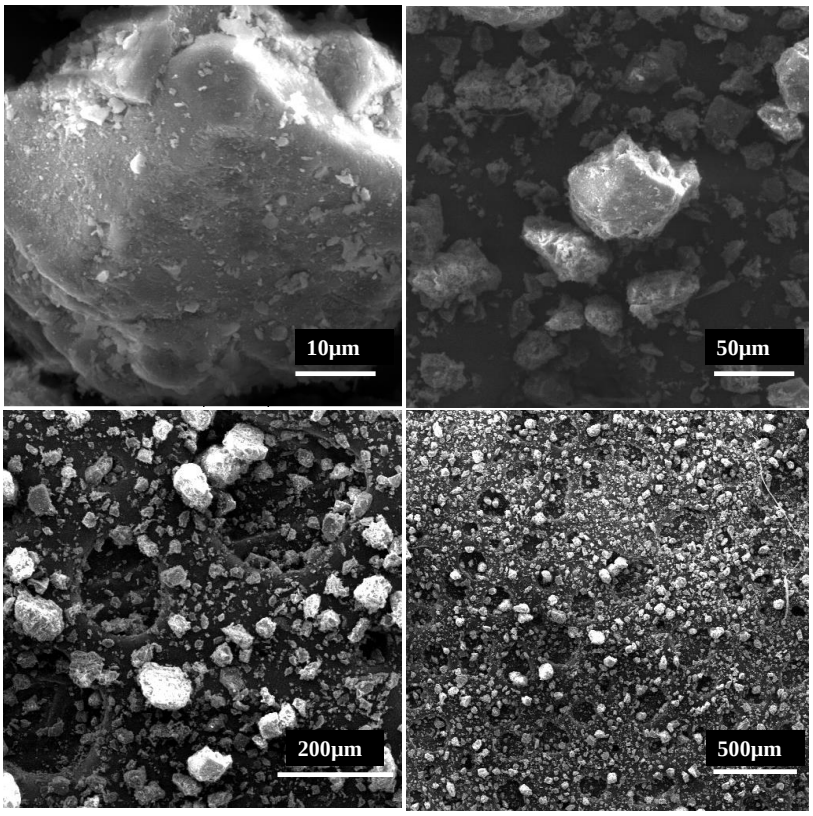

Figure 4.28: SEM images for the RhMo-EDTA/Al_2O_3 catalyst at different magnifications.

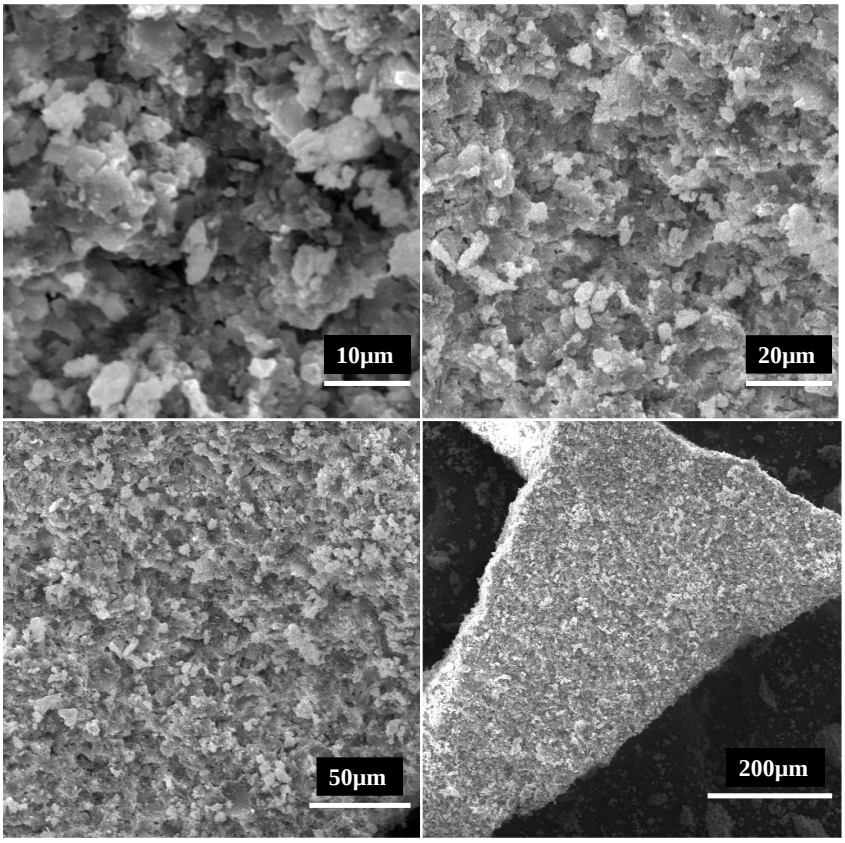

Figure 4.29: SEM images for the RhMo-AA/Al_2O_3 catalyst at different magnifications.

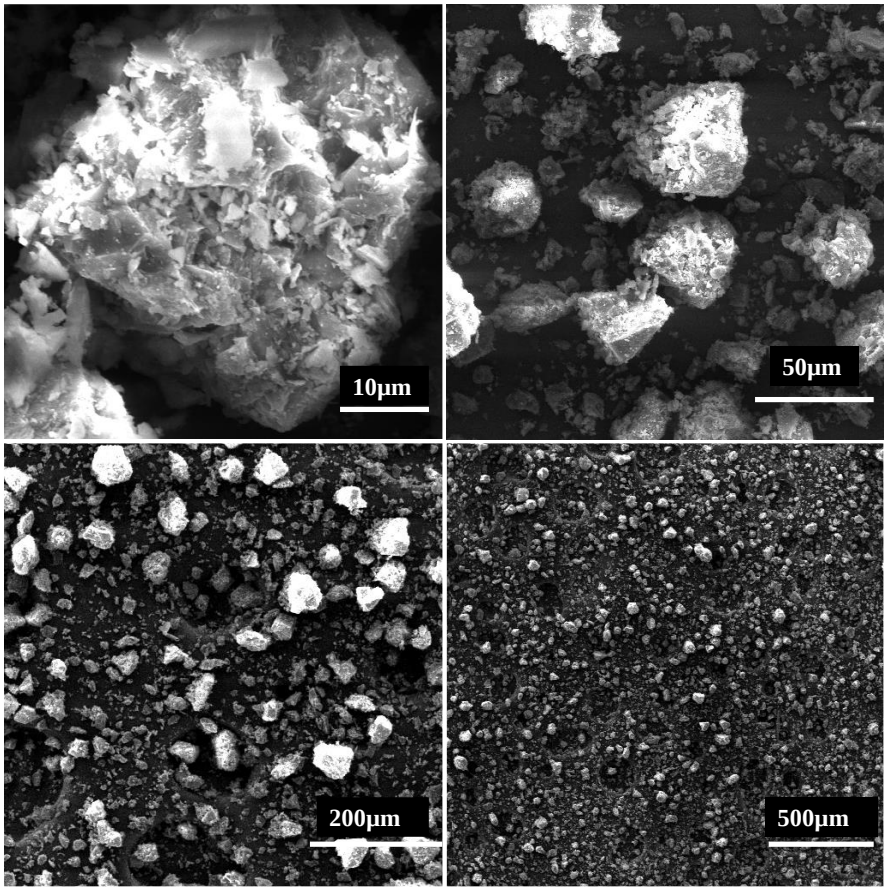

Figure 4.30: SEM images for the RhMo-CA/Al_2O_3 catalyst at different magnifications.

4.5.9 Thermal stability of catalysts-TGA and DSC studies

TGA-DSC is a technique used for thermal analysis, to characterize materials by measuring their change in mass as a function of temperature. It is coupled with DSC to provide complementary information such as measuring heat flow as a function of time and temperature at a controlled environment.

The first weight loss (2.5%) for RhMo/Al_2O_3 occurred in the range of 50-150˚C due to the desorption of physically adsorbed water from the surface of the catalyst, this was accompanied by a broad exothermic peak in the range of 120-210˚C (**Figure 4.31**). A second weight loss of 3 % was observed between 200-580 ˚C, it was reflected by a very weak endothermic peak between 360-610˚C associated with the decomposition of nitrate radical, hexaammonium molybdate (Wei *et al.*, 2019) and dehydroxylation. An endothermic peak at 810˚C was observed and it was attributed to the formation of stable MoO_3 phase.

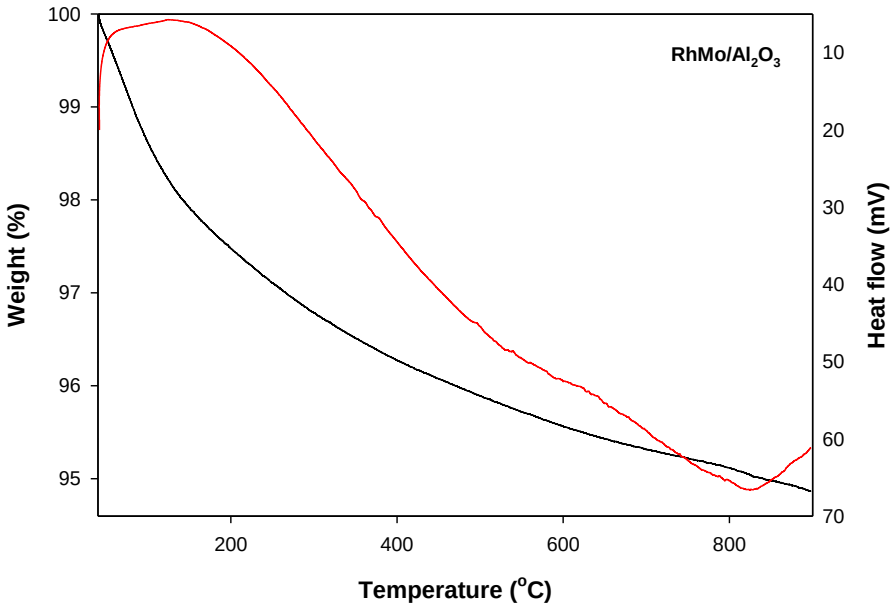

Figure 4.31: TGA-DSC curves of $RhMo/Al_2O_3$ catalyst.

The first weight loss (5.2%) in **Figure 4.32** below 100˚C and was mainly due to water desorption. From 160-800˚C, there was a gradual weight loss of 3% and not many events were happening in those stages. This weight loss was associated with the loss of complex, partial dehydration-decomposition of the Rh and Mo species of RhMo-EDTA/Al_2O_3 catalyst. The first and second weight loss was accompanied by a broad exothermic peak at maximum of 180˚C corresponding to the decomposition of the complex. A broad exothermic peak between 280-670˚C was observed and it was due to the decomposition of EDTA and further combustion of residual organic matrix (Yu *et al*., 2018; González-Cortés *et al*., 2004), and total transformation of partially decomposed Rh and Mo precursor species into the catalyst oxidic precursor (González-Cortés *et al*., 2005).

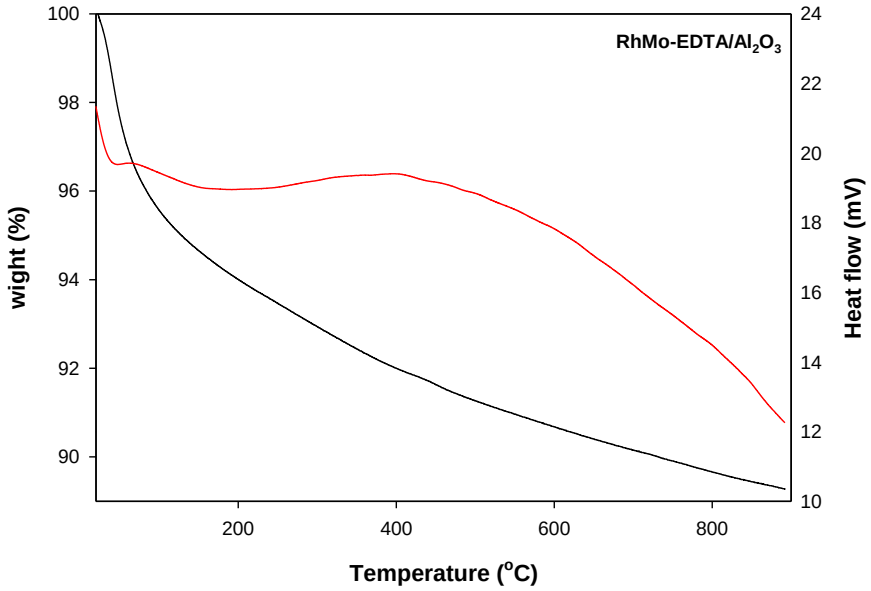

Figure 4.32: TGA-DSC curve of RhMo-EDTA/Al_2O_3 catalyst.

The results obtained for RhMo-AA/Al_2O_3 (**Figure 4.33**) showed a weight loss (3.6%) taking place in the range of 50-150˚C followed by an exothermic peak 90˚C and was mainly due to water desorption. The second weight loss of 2.8% between 180-410˚C was attributed to a series of overlapping chemical reactions (partial dehydration-decomposition and the subsequent combustion of the precursor species and partial dehydroxylation of alumina) (González-Cortés *et al*., 2015). A second exothermic peak occurred at a maximum of 280˚C corresponded to the decomposition of the complex (metal-AA) and total decomposition of partial hydration-decomposition of the Rh and Mo precursor species. A third weight loss (1.8%) between 410-850˚C was due to the formation of monometallic oxidic precursor. The DCS curve displayed an endothermic peak at a maximum of 580˚C.

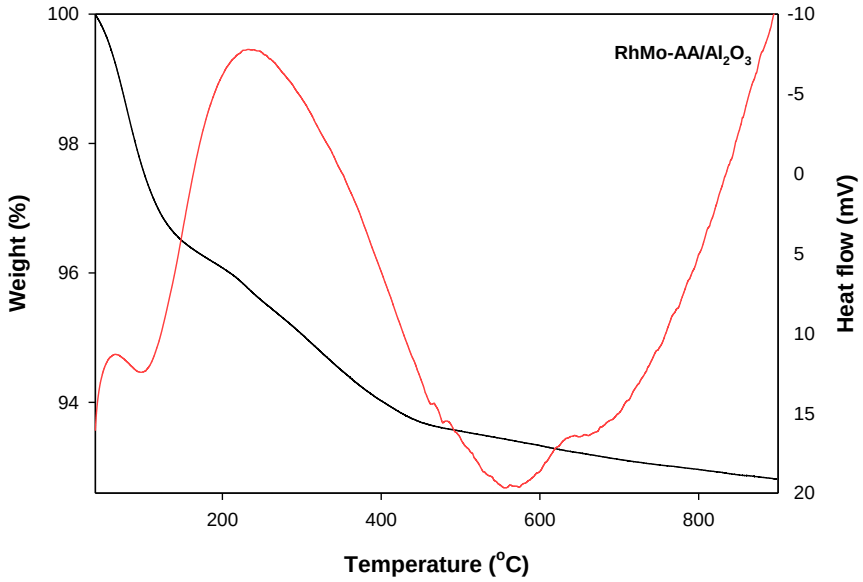

Figure 4.33: TGA-DSC curves for RhMo-AA/Al_2O_3 catalyst.

The results obtained for RhMo-CA/Al_2O_3 (**Figure 4.34**) showed a weight loss of (5.2%) below 150˚C followed by an endothermic peak 80˚C was mainly due to water desorption. The second weight loss of 2.8% between 180-400˚C was attributed to a series of overlapping chemical reactions (partial dehydration-decomposition and the subsequent combustion of the precursor species, and full decomposition of citric acid and the formation of molybdenum trioxide (Valencia *et al*., 2012). A broad and weak exothermic peak occurred at a maximum of 400˚C corresponded to the decomposition of the remaining complex (metal-CA) and the total decomposition of partial hydration-decomposition of the Rh and Mo precursor species. Above 400˚C not much loss of weight loss was observed, this indicated the formation of stable metallic oxidic precursors.

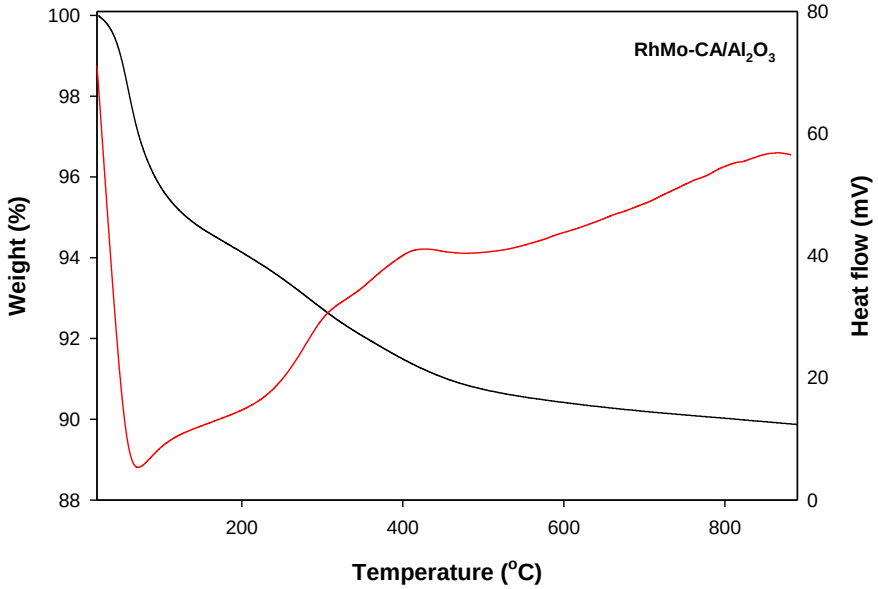

Figure 4.34: TGA-DSC curves for RhMo-CA/Al_2O_3 catalyst.

4.5.10 Catalytic activity

To estimate the catalytic activity, the alumina supported RhMo catalysts with and without chelating ligands were tested in hydrotreating DBT. The hydrodesulfurization (HDS) was carried out at 300˚C and 4 MPA for different catalysts (**Table 4.10**). The conversion of dibenzothiophene (DBT) (X) was used to estimate the catalytic activity in HDS, and it was calculated by the following formula:

$$X = \frac{C_0 - C}{C_0} \times 100 \qquad (1)$$

where C_0 is the initial DBT content and C is the DBT content in the reaction product. DBT consists of two pathways, direct desulfurization (DDS) and hydrogenation (HYD) pathway (**Figure 4.37**). For DDS, the corresponding products are biphenyl (BP), and for HYD the corresponding products are cyclohexylbenzene (CHB), bicyclohexyl (BCH), and tetrahydrodibenzothiophene, respectively. The obtained results showed that BP and CHB were the main reaction products accompanied by small amounts of BCH and tetrahydrodibenzothiophene. However, the proportion of BP and CHB in the reaction products changed depending on the catalyst used. A chromatogram of DBT model fuel before sulfidation was shown in **Figure 4.35**, while **Figure 4.36** showed GC chromatogram of DBT model fuel after HDS process for all the catalysts. Obtained products allowed the determination of the selectivity values for both pathways, and the selectivity was calculated by the following formula:

$$S = \frac{C_x}{C_0 - C} \times 100 \qquad (2)$$

where C_x is the content of BCH, BP, or CHB.

$RhMo/Al_2O_3$ (88%) had the highest catalytic activity and the activity for the chelated catalyst followed this order; RhMo-AA/Al_2O_3 (73%) > RhMo-CA/Al_2O_3 (72%) > RhMo-EDTA/Al_2O_3 (68%) (**Table 4.10**). An increase in activity was associated with the introduction of rhodium (Rh) as a promoter. The formation of the active phase was related to the electron donation of the promoter to Mo decreasing Mo-S bond strength to an optimum range, thus increasing the activity of the catalyst (Pecoraro & Chianelli *et al*., 1981). This study was investigated by Pecoraro & Chianelli using volcano plot to explain periodic trend. The results showed that the second and third row of metals in the periodic table are more active, with rhodium being one of the metal-sulfides with maximum activity. The higher electron density from a promoter (Rh) resulted in weaker Mo-S bond strength, higher concentration of CUS and higher HDS activity (Chianelli *et al*., 2012). Similar study was reported by Huang *et al*., (2018) about the effect cobalt in HDS catalysts. It was found that Co donates electrons to Mo, and an increase in number of electrons on Mo resulted in stronger binding to the heterocyclic ring sulfur and further weakened the C-S bod in the ring through back-donation into the ring π^* orbital, which enhanced the breaking of C-S bonds in DBT and thereby improving the HDS activity of the catalyst (Huang *et al*., 2018). The studies conducted by these researchers can be applied in this work study since the addition of Rh influenced the activity of HDS catalyst.

$RhMo/Al_2O_3$ chelated catalysts resulted in lower catalytic activity compared to unchelated catalyst ($RhMo/Al_2O_3$). This could be due to the formation of Rhodium-chelating ligand and molybdenum-chelate complex. For the chelating ligands to work efficiently, it should be present in appropriate amount in the catalyst to retard the sulfidation of promoter effectively, so that the sulfidation takes place simultaneously with Mo at high temperatures, forming more active phase (Paryari & Moradi, 2011). Therefore, it is important to determine the optimal amount of organic additive to impregnate, as this parameter seemed to be decisive in obtaining more active phases which will result in an increased catalytic activity (Paryari & Moradi, 2011). The excess of EDTA could chelate some Mo^{6+} species forming stable Mo-chelating complex, and the high stability of Mo- chelated species (Cattaneo *et al*., 1999) could severely limit the formation of active MoS_2. This could decrease the amounts of crystallites in which the sulfiding promoter would properly integrate (Escobar *et al*., 2008), and could be responsible for the decrease in HDS activity for RhMo-EDTA/Al_2O_3 catalyst. The addition of citric acid could form Mo-citrate complexes; dimers, trimers, and tetramers, and have proved to be detrimental to the sulfidation of molybdenum (Mohanty, 2011). The formation of such complexes severely retards the sulfidation of Mo, resulting in incomplete sulfidation, hence lower HDS activity.

For all catalysts studied, the DBT converted mainly *via* DDS pathway (**Table 4.10**). There was not much difference obtained in terms of selectivity when comparing the HYD/DDS selectivity ratio. $RhMo/Al_2O_3$ showed a slightly higher HYD/DDS ratio of ~0.20 as compared to the chelated catalysts. The addition of chelating ligands showed a slight difference and therefore we can conclude that the addition of chelating ligand on the catalysts had not much influence on the selectivity (**Table 4.10**). The

HDS selectivity correlated linearly with slab length of MoS_2 phase (TEM), longer slab length indicate high ratio of edge/corner and better HDS selectivity (Li *et al*., 2010). Among all the catalysts, $RhMo/Al_2O_3$ had the longest slab length. The catalytic selectivity differences might be related to the different type of proportions of the active sites. There are there are two kinds of active sites on MoS_2 slabs: the edge and corner sites. It was believed that the corner sites could catalyse both HDS and HYD reactions, due to its high degree of coordinative unsaturation than that of the edge sites (Bin *et al*., 2014; Gonziález-Cortéz *et al*., 2004), and the edge sites only catalyse the HDS reaction (Bin *et al*., 2018). With increasing slab length of MoS_2 particles for $RhMo/Al_2O_3$, relatively less corner sites for HYD were formed and consequently the olefin saturation was exceedingly suppressed (Bin *et al*., 2014). Therefore, higher slab length would exhibit higher HDS selectivity, and this was seen in $RhMo/Al_2O_3$ catalytic activity. From the obtained results the addition of chelating agents did not facilitate higher HDS activity. In all the catalysts high amounts of BP was observed, and this indicated that all the respective catalysts favoured DDS pathway for the HDS of DBT.

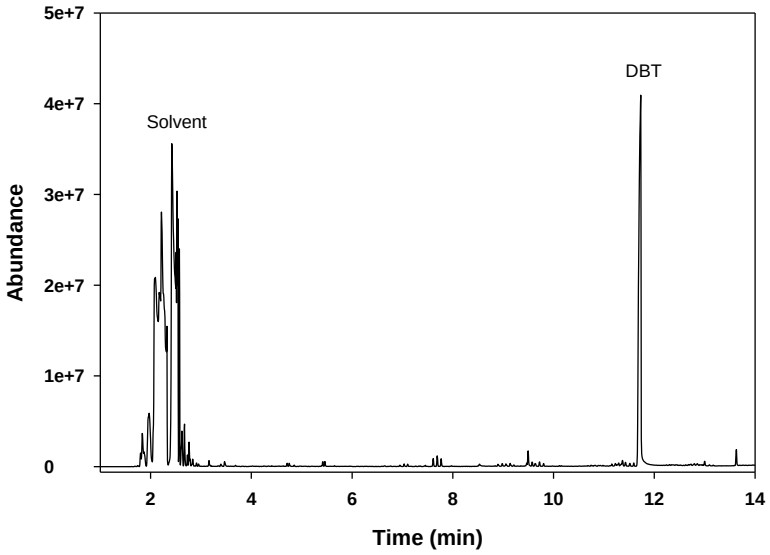

Figure 4.35: GC chromatogram of DBT before HDS.

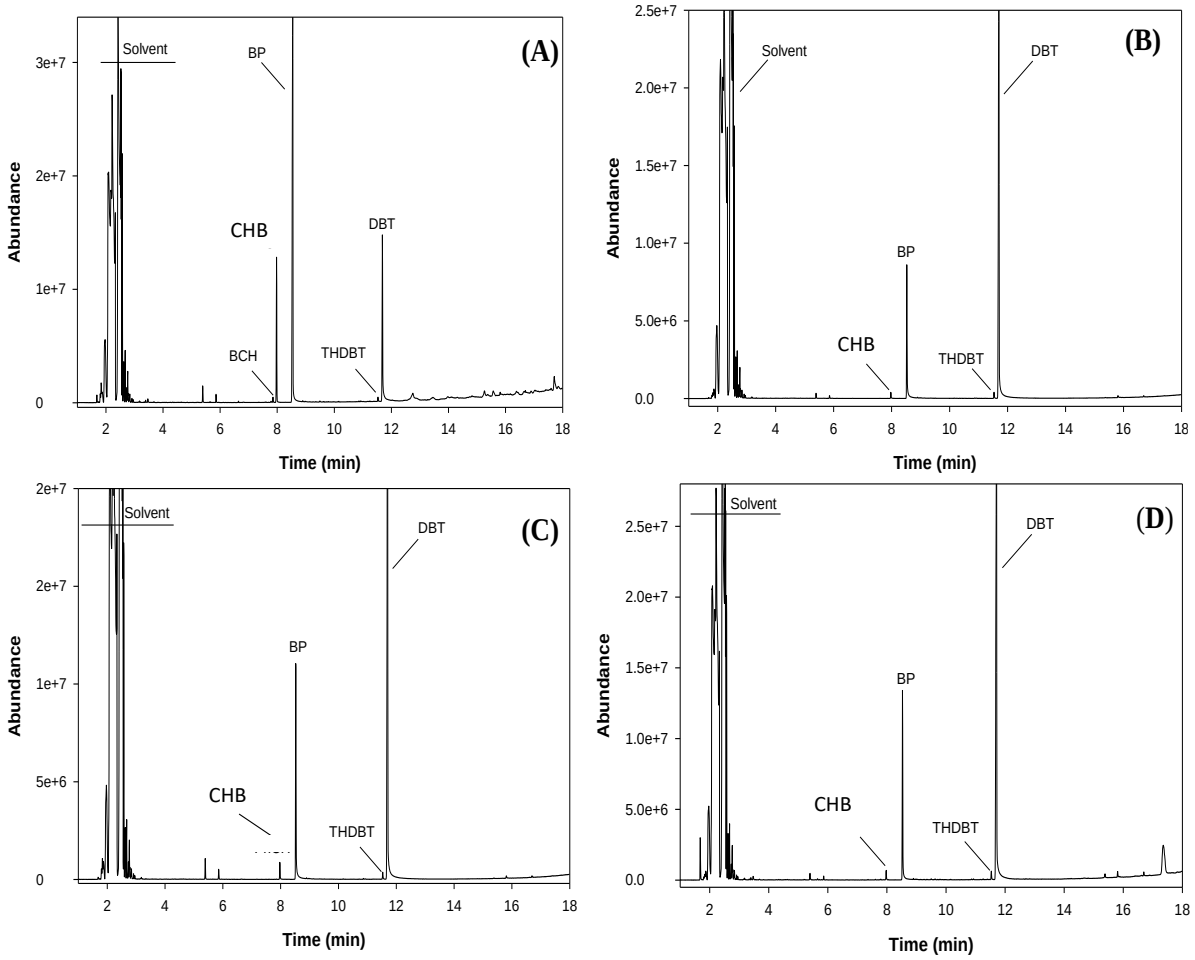

Figure 4.36: GC chromatogram of DBT after HDS using (A) $RhMo/Al_2O_3$, (B) $RhMo\text{-}EDTA/Al_2O_3$, (C) $RhMo\text{-}AA/Al_2O_3$, (D) $RhMo\text{-}CA/Al_2O_3$, DBT = dibenzothiophene, BP = biphenyl, CHB = cyclohexylbenzene, BCH = bicyclohexyl, THDBT= tetrahydrodibenzothiophene.

Table 4.10: Conversion and product yield in the HDS of DBT over $RhMo/Al_2O_3$, and $RhMo\text{-}x/Al_2O_3$ (where x = EDTA, AA, CA).

Catalysts	**HDS (%)**	**BP**	**CHB**	**HYD/DDS ratio**	**TOF (h^{-1})**
$RhMo/Al_2O_3$	88	65	13	0.20	51
$RhMo\text{-}EDTA/Al_2O_3$	68	16	1	0.06	60
$RhMo\text{-}AA/Al_2O_3$	73	65	3	0.05	79
$RhMo\text{-}CA/Al_2O_3$	72	36	2	0.06	223

Catalyst (Molybdenum content) employed = 0.1 g (4.119×10^{-5} moles). Time of reaction for each of the oxidation system was 6 h. [a]TOF, h^{-1}: (turnover frequency) moles of substrate converted per mole of metal ion (in the solid-state catalyst) per hour.

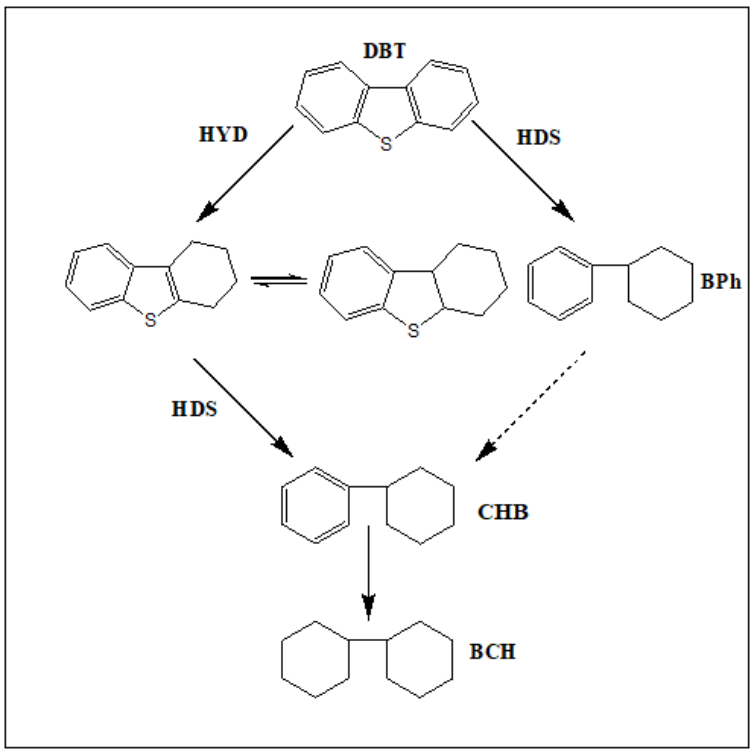

Figure 4.37: The pathways of HDS of DBT.

4.5.11: EDS analysis for RhMo catalysts after HDS activity

The EDS analysis (**Figure 4.38**) showed the elemental composition and the atomic ratios (**Table 4.11**) of the RhMo catalysts after HDS activity. According to the obtained results the atomic percentage of elements present on the catalysts decreased (**Table 4.11**). The obtained results showed that after HDS activity the catalysts can be reusable, as their metals are still available in appropriate amounts.

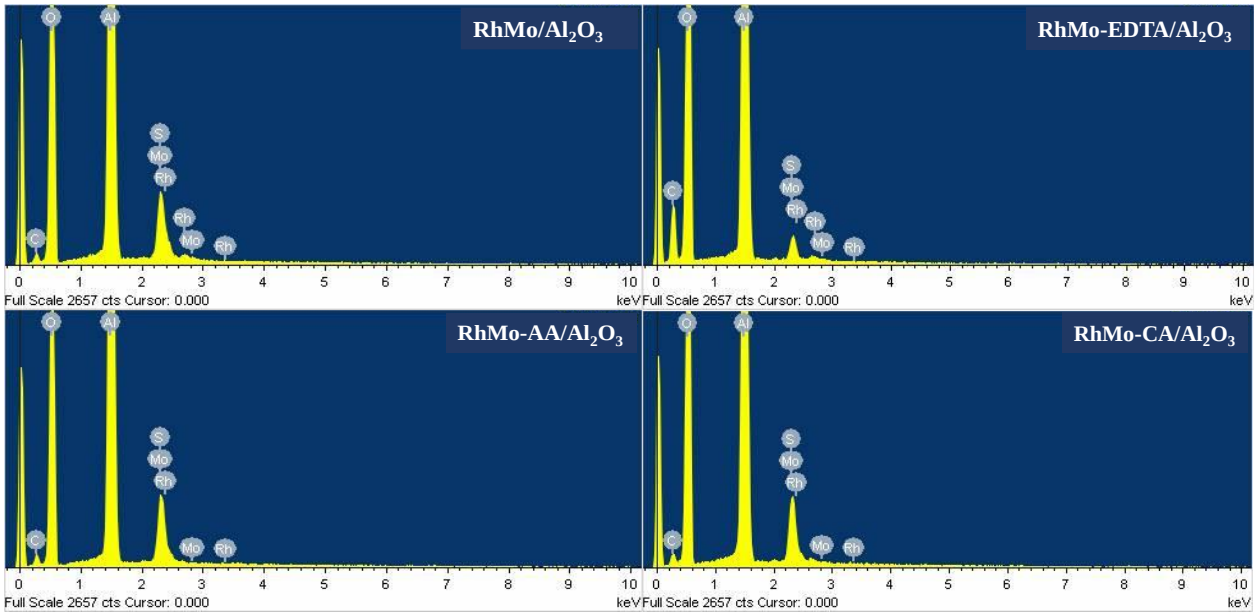

Figure 4.38: EDS analysis for (a) $RhMo/Al_2O_3$, (b) $RhMo\text{-}EDTA/Al_2O_3$, (c) $RhMo\text{-}AA/Al_2O_3$, (d) $RhMo\text{-}CA/Al_2O_3$ catalysts.

Table 4.11: Qualitative atomic percentage of Rh, and Mo in HDS catalysts.

Catalysts	**Atomic Percentage (wt. %)**						**Ratio of Co% to Mo%**
	C K	O K	Al K	S K	Rh K	Mo L	
$RhMo/Al_2O_3$	47.57	38.21	13.34	0.55	0.10	0.32	0.313
$RhMo\text{-}EDTA/Al_2O_3$	27.23	53.38	18.73	0.44	0.102	0.10	1.02
$RhMo\text{-}AA/Al_2O_3$	11.65	61.03	25.87	0.87	0.101	0.47	0.215
$RhMo\text{-}CA/Al_2O_3$	11.42	56.17	29.96	1.69	0.62	0.70	0.886

4.6 Conclusion

In present work, a series of new catalysts ($RhMo/Al_2O_3$, $RhMo\text{-}x/Al_2O_3$ (where x = EDTA, AA, CA) were successfully synthesized and characterized. All the catalysts were characterized by XRD, FT-IR, ICP-OES, XRD, XPS, SEM, EDS, TEM, TGA-DSC, and GC-MS. The activity test of the catalysts was conducted under industrial conditions with DBT as a model fuel, and the activity was determined in terms of HDS conversion. The UV-vis analysis confirmed the presence octahedral molybdate species between 320-360 nm for $RhMo/Al_2O_3$, and the shift to lower wavelength in the visible of 220 nm for the chelated catalysts was observed and indicated the formation of less polymerized molybdate species and heteropoplymolybdates. Band gaps of 3.779 eV ($RhMo/Al_2O_3$), 4.341 eV ($RhM\text{-}EDTA/Al_2O_3$), 4.394 eV ($RhMo\text{-}AA/Al_2O_3$), and 4.478 eV ($RhMo\text{-}CA/Al_2O_3$) were obtained. SEM imaging confirmed the morphology with spherical-like particles in nanorange, and TEM imaging confirmed that the materials had fringe-like morphology deemed as MoS_2 slabs. The chelated catalysts showed a greater dispersion compared with unchelated catalysts because of the absence of crystalline peaks, which was confirmed by XRD analysis. $RhMo/Al_2O_3$ resulted in higher catalytic activity compared with the chelated catalysts, and this was confirmed by XPS showing more MoS_2 phases of $RhMo/Al_2O_3$ catalyst to be (63%), and it was also confirmed by HDS activity where $RhMo/Al_2O_3$ exhibited the highest DBT conversion of (88%).

Chapter Five

Conclusions and recommendations

5.1 Conclusions

The overall objective of this study was to understand the roles of chelating ligands and promoters (Co and Rh) on HDS activity with the primary goal of promoting total sulfur reduction while minimizing hydrogenation of organics within the fuel matrix. Therefore, this chapter summarizes and concludes on the findings of the study. It further gives some recommendations pertaining to development of highly active HDS catalysts using chelating agents hence leading to future studies and investigations.

In Chapter three, CoMo catalysts chelated with acetic acid (AA), ethylenediaminetetraacetic acid (EDTA), and citric acid (CA) in a Co/chelate molar ratio of 1:1 and 1:2 was synthesized and characterized to study the effects of chelating ligands on sulfidation and HDS activity. All the catalysts were synthesized under (Co/Co+Mo) = 0.33 molar ratio. Single crystal data revealed that Co complexed with EDTA and acetic acid, and single crystals could not be isolated for CoMo-CA. The formation of the metal-chelating ligand was found to retard the sulfidation of the promoter (Co) and increased the sulfidation temperature of cobalt to the point where the sulfidation of molybdenum had already started sulfiding. This led to the formation of more type II CoMoS active sites responsible for increasing HDS catalytic activity. Characterization by SC-XRD pointed out that Co complexed with chelating agents (EDTA and AA) and the CoMo-EDTA (AA) complex was further confirmed by TGA-DSC analysis. The dispersion of molybdenum oxide was enhanced by the addition of chelating agents, and this was confirmed by TEM, XRD, and XPS analysis. XPS also showed that the presence of chelating ligand yielded more MoS_2 and CoMoS phases. An increase in HDS activity followed the order: CoMo-CA/Al_2O_3 (98%) > CoMo-AA/Al_2O_3 (94%) > CoMo-EDTA/Al_2O_3 (90%) > CoMo/Al_2O_3 (43%).

In Chapter four, rhodium (Rh) was employed as promoter in the synthesis of RhMo catalysts. Incorporating chelating agents changed the morphology of the catalysts surface, leading to highly dispersed metals as observed by XRD and TEM. Among monometallic sulfides, rhodium sulfide (Rh_2S_3) was observed as one of the most active phases for HDS process. Higher percentage of MoS_2 from XPS analysis of RhMo/Al_2O_3 catalyst was obtained and this indicated better sulfidation degree which led to high HDS activity. The formation of the active phase was related to the electron donation of the promoter to Mo decreasing Mo-S bond strength to an optimum range, thus increasing the activity of the catalyst. This study was supported by Pecoraro & Chianelli using volcano plot to explain periodic trend. Their studies showed that the second and third row of metals in the periodic table are more active than first row, with rhodium being one of the metal-sulfides with maximum activity. One of the conclusions was that the highest activity for desulfurization is linked to TMS with the lowest sulfur

bond energy resulting to larger number of sulfur vacancies, hence high activity. Therefore, the results obtained in this study proved to follow these findings since changing the promoter played the role in enhancing HDS activity due to its electronic nature it possesses. RhMo/Al_2O_3 presented HDS activity of 88% while chelated catalysts showed low HDS activity in decreasing order of; RhMo-AA/Al_2O_3 (73%) > RhMo-CA/Al_2O_3 (72%) > RhMo-EDTA/Al_2O_3 (68%). The low HDS activity could be due to the excess of chelating agent complexing with both rhodium and molybdenum, thus forming Mo-chelate complex formation (see FT-IR in Section 4.5.2), hindering the formation of MoS_2 (during sulfidation) phase due to high stability of the formed molybdenum species. Thus, integration of sulfidic promoter from Rh-chelate complex decomposition could be limited by the decreased MoS_2 edges availability.

RhMo/Al_2O_3 (88%) showed higher activity compared to CoMo/Al_2O_3 (43%), which was expected. On the contrary, all CoMo chelated catalysts resulted in higher activity compared to RhMo chelated catalysts. This could be due to a lot of reasons, one being that there is lacking information based Rh:Chelate molar ratio to impregnate on RhMo catalysts. Therefore, studies need to be conducted to optimize the Rh:Chelating ligand molar ratio, because for the chelating ligand to work effectively, the amounts used should be presented in appropriate concentration in the catalyst network to effectively retard the sulfidation of Rh so that it would take place after Mo at high temperatures, forming more active phases. The selection of ligands might not have been in line with HSAB theory for this study since only hard ligands were used, and soft ligands could be used to study their influence on the catalytic activity. For CoMo catalysts, Co:Chelating ligand molar ratio have been studied extensively and the chosen ratios are known to produce high catalytic activity, therefore similar study need to be conducted for Rh:Chelating ligands.

5.2 Recommendations

For CoMo catalysts, low HDS conversion was observed in model fuel. The low activity could be due to the following factors (i) conducting the catalytic activity with the same reaction time used for DBT HDS activity, (ii) using a catalyst with the same concentration used for hydrodesulfurization of DBT. For RhMo catalysts, low HDS activity was observed for chelated catalysts. Some key factors which limit the HDS catalytic activity are (i) using the same promoter:Chelating ligand molar ratio as CoMo catalysts without optimizing, (ii) using hard ligands without looking into soft ligands. RhMo catalysts are new catalysts that have not been explored yet, therefore a lot of optimizations is required to obtain the best HDS catalyst that will yield high HDS catalytic activity. For future studies, reusability studies will be conducted to check stability of catalysts. Furthermore, kinetic studies to determine the desulfurization rate and inhibitory effects will be carried out. It is important to check the influence of other chelating ligands or additives on the activity of RhMo catalysts, hence, the study will look into the use of soft ligands and additives at different molar ratios. Modifying the alumina support would be beneficial as it known to form strong metal-support interaction inhibiting the formation of more active phase, therefore, improving surface area, acidity sites will play a role in increasing the HDS activity for the refractory sulfur containing compounds. It is also important to further study the H_2 chemisorption properties of the synthesized catalysts to determine the actual dispersion of the metals on the support, to conduct TPR analysis to study the reducibility of the catalysts. HDS catalysts are reported to struggle with 4,6-DMDBT during desulfurization, and this is due to the steric nature of the compound, hence future work will focus on these classes of sulfur containing compounds.

References

1. Kaluza, L., Zdrazil, M., Gulkova, D., & Vit, Z. (2013). The Influence of the Chelating Agent Nitrilotriacetic Acid on Promotion of Hydrodesulfurization Activity by Co in CoMo Catalysts Prepared on Al_2O_3, C, and ZrO_2 Supports. *Chemical Engineering Transactions*, 32, 841-846.
2. Mazoyer, P., Geantet, C., Diehl, F., Loridant, S., & Lacroix, M. (2008). Role of chelating agent on the oxidic state of hydrotreating catalysts. *Catalysis Today*, 130(1), 75-79.
3. Xu, J., Guo, Y., Huang, T., & Fan, Y. (2019). Hexamethonium bromide-assisted synthesis of CoMo/graphene catalysts for selective hydrodesulfurization. *Applied Catalysis B: Environmental*, 244, 385-395.
4. Kobayashi, K., & Nagai, M. (2017). Active sites of sulfided $NiMo/Al_2O_3$ catalysts for 4, 6-dimethyldibenzothiophene hydrodesulfurization-effects of Ni and Mo components, sulfidation, citric acid and phosphate addition. *Catalysis Today*, 292, 74-83.
5. Al-Dalama, K., & Stanislaus, A. (2006). A comparative study of the influence of chelating agents on the hydrodesulfurization (HDS) activity of alumina and silica− alumina-supported CoMo catalysts. Energy & fuels, 20(5), 1777-1783.
6. Bui, N. Q., Geantet, C., & Berhault, G. (2019). Activation of regenerated $CoMo/Al_2O_3$ hydrotreating catalysts by organic additives–The particular case of maleic acid. *Applied Catalysis A: General*, 572, 185-196.
7. González-Cortés, S. L., Qian, Y., Almegren, H. A., Xiao, T., Kuznetsov, V. L., & Edwards, P. P. (2015). Citric acid-assisted synthesis of c-alumina-supported high loading CoMo sulfide catalysts for the hydrodesulfurization (HDS) and hydrodenitrogenation (HDN) reactions. *Appl Petrochem Res*, 5, 181-197
8. González-Cortés, S. L., Xiao, T. C., Costa, P. M., Fontal, B., & Green, M. L. (2004). Urea–organic matrix method: an alternative approach to prepare Co□ MoS_2/γ-Al_2O_3 HDS catalyst. *Applied Catalysis A: General*, *270*(1-2), 209-222.
9. González-Cortés, S. L., Xiao, T. C., Rodulfo-Baechler, S. M., & Green, M. L. (2005). Impact of the urea–matrix combustion method on the HDS performance of Ni-MoS_2/γ-Al_2O_3 catalysts. *Journal of Molecular Catalysis A: Chemical*, *240*(1-2), 214-225.
10. Valencia, D., & Klimova, T. (2013). Citric acid loading for MoS2-based catalysts supported on SBA-15. New catalytic materials with high hydrogenolysis ability in hydrodesulfurization. *Applied catalysis B: environmental*, 129, 137-145.
11. Peña, L., Valencia, D., & Klimova, T. (2014). CoMo/SBA-15 catalysts prepared with EDTA and citric acid and their performance in hydrodesulfurization of dibenzothiophene. *Applied Catalysis B: Environmental*, 147, 879-887.

12. Santolalla-Vargas, C. E., Toriello, V. S., De los Reyes, J. A., Cromwell, D. K., Pawelec, B., & Fierro, J. L. G. (2015). Effects of pH and chelating agent on the NiWS phase formation in NiW/γ-Al_2O_3 HDS catalysts. *Materials Chemistry and Physics*, 166, 105-115.
13. Pereyma, V. Y., Klimov, O. V., Prosvirin, I. P., Gerasimov, E. Y., Yashnik, S. A., & Noskov, A. S. (2018). Effect of thermal treatment on morphology and catalytic performance of NiW/Al_2O_3 catalysts prepared using citric acid as chelating agent. *Catalysis Today*, 305, 162-170.
14. International Energy Agency. (2015). Energy efficiency outlook for South Africa. *France, www.ieo.org*.
15. Wei, Q., Zhou, Y., Xu, C., & Liu, Y. (2011). Effects of citric acid as a chelating agent on the performance of a heavy oil hydrotreatment catalyst. In Production and Purification of Ultraclean Transportation Fuels (pp. 3-13). *American Chemical Society*.
16. Xia, B., Cao, L., Luo, K., Zhao, L., Wang, X., Gao, J., & Xu, C. (2019). Effects of the Active Phase of CoMo/γ-Al_2O_3 Catalysts Modified Using Cerium and Phosphorus on the HDS Performance for FCC Gasoline. *Energy & Fuels*, 33(5), 4462-4473.
17. Vatutina, Y. V., Klimov, O. V., Stolyarova, E. A., Nadeina, K. A., Danilova, I. G., Chesalov, Y. A., ... & Noskov, A. S. (2019). Influence of the phosphorus addition ways on properties of CoMo-catalysts of hydrotreating. *Catalysis Today*, 329, 13-23.
18. Suárez-Toriello, V. A., Santolalla-Vargas, C. E., De Los Reyes, J. A., Vázquez-Zavala, A., Vrinat, M., & Geantet, C. (2015). Influence of the solution pH in impregnation with citric acid and activity of Ni/W/Al_2O_3 catalysts. *Journal of Molecular Catalysis A: Chemical*, 404, 36-46.
19. Rinaldi, N., Al-Dalama, K., Kubota, T., & Okamoto, Y. (2009). Preparation of Co–Mo/B_2O_3/Al_2O_3 catalysts for hydrodesulfurization: Effect of citric acid addition. *Applied Catalysis A: General*, 360(2), 130-136.
20. Budukva, S. V., Klimov, O. V., Pereyma, V. Y., & Noskov, A. S. (2017). Reactivation of CoMo/Al_2O_3 hydrotreating catalysts with chelating agents. *Russian Journal of Applied Chemistry*, 90(9), 1425-1432.
21. Chen, J., Mi, J., Li, K., Wang, X., Dominguez Garcia, E., Cao, Y., ... & Maugé, F. (2017). Role of citric acid in preparing highly active CoMo/Al_2O_3 catalyst: from aqueous impregnation solution to active site formation. *Industrial & Engineering Chemistry Research*, 56(48), 14172-14181.
22. van de Water, L. G., Bezemer, G. L., Bergwerff, J. A., Versluijs-Helder, M., Weckhuysen, B. M., & de Jong, K. P. (2006). Spatially resolved UV–vis microspectroscopy on the preparation of alumina-supported Co Fischer–Tropsch catalysts: Linking activity to Co distribution and speciation. *Journal of Catalysis*, 242(2), 287-298.

23. Beltrán, K. A., Álvarez-Contreras, L., De la Cruz, A., & Aguilar-Elguezabal, A. (2018). Study of the impregnation of NiMo assisted by chelating agents for hydrodesulfurization-supported catalysts over mesoporous silica. *Journal of Materials Research*, 33(21), 3604-3613.
24. Rana, M. S., Ramírez, J., Gutiérrez-Alejandre, A., Ancheyta, J., Cedeño, L., & Maity, S. K. (2007). Support effects in CoMo hydrodesulfurization catalysts prepared with EDTA as a chelating agent. *Journal of Catalysis*, 246(1), 100-108.
25. van Haandel, L., Bremmer, G. M., Hensen, E. J. M., & Weber, T. (2017). The effect of organic additives and phosphoric acid on sulfidation and activity of (Co) Mo/Al_2O_3 hydrodesulfurization catalysts. *Journal of Catalysis*, 351, 95-106.
26. Sheibani, S., Zare, K., & Shahidian, Z. (2018). The Effects of pH and Chelating Agent on Characterization of Ni Mo/γ-Alumina Heavy Oil Hydrodesulphurization Nanocatalyst.
27. Nadeina, K. A., Kazakov, M. O., Danilova, I. G., Kovalskaya, A. A., Stolyarova, E. A., Dik, P. P., & Noskov, A. S. (2019). The influence of B and P in the impregnating solution on the properties of NiMo/γ-δ-Al_2O_3 catalysts for VGO hydrotreating. *Catalysis Today*, 329, 2-12.
28. Asadi, A. A., Royaee, S. J., Alavi, S. M., & Bazmi, M. (2019). Ultra-deep hydrodesulfurization of cracked and atmospheric gasoil blend: Direct and interactive impacts of support composition, chelating agent, metal and promoter loadings. *Fuel Processing Technology*, 187, 36-51.
29. Rashidi, F., Sasaki, T., Rashidi, A. M., Kharat, A. N., & Jozani, K. J. (2013). Ultradeep hydrodesulfurization of diesel fuels using highly efficient nanoalumina-supported catalysts: Impact of support, phosphorus, and/or boron on the structure and catalytic activity. *Journal of catalysis*, 299, 321-335.
30. Escobar, J., Barrera, M. C., Gutiérrez, A. W., & Terrazas, J. E. (2017). Benzothiophene hydrodesulfurization over NiMo/alumina catalysts modified by citric acid. Effect of addition stage of organic modifier. *Fuel Processing Technology*, 156, 33-42.
31. Zhang, C., Brorson, M., Li, P., Liu, X., Liu, T., Jiang, Z., & Li, C. (2019). $CoMo/Al_2O_3$ catalysts prepared by tailoring the surface properties of alumina for highly selective hydrodesulfurization of FCC gasoline. *Applied Catalysis A: General*, 570, 84-95.
32. Nikulshina, M., Kokliukhin, A., Mozhaev, A., & Nikulshin, P. (2019). $CoMo/Al_2O_3$ hydrotreating catalysts prepared from single Co_2Mo_{10}-heteropolyacid at extremely high metal loading. *Catalysis Communications*, 127, 51-57.
33. Klimov, O. V., Vatutina, Y. V., Nadeina, K. A., Kazakov, M. O., Gerasimov, E. Y., Prosvirin, I. P., ... & Noskov, A. S. (2018). $CoMoB/Al_2O_3$ catalysts for hydrotreating of diesel fuel. The effect of the way of the boron addition to a support or an impregnating solution. *Catalysis Today*, 305, 192-202.
34. Braggio, F. A., Mello, M. D., Magalhães, B. C., Zotin, J. L., & Silva, M. A. (2017). Effect of pH on Activity of $NiMo/Al_2O_3$ Catalysts Prepared with Citric Acid in Simultaneous

Hydrodesulfurization and Hydrodenitrogenation Reactions. *Catalysis Letters*, 147(5), 1104-1113.

35. Liu, B., Liu, L., Chai, Y., Zhao, J., Li, Y., Liu, D., ... & Liu, C. (2018). Effect of sulfiding conditions on the hydrodesulfurization performance of the ex-situ presulfided CoMoS/γ-Al_2O_3 catalysts. *Fuel*, 234, 1144-1153.
36. Akbarzadeh, O., Mohd Zabidi, N. A., Abdul Wahab, Y., Hamizi, N. A., Chowdhury, Z. Z., Aljunid Merican, Z. M., & Johan, M. R. (2019). Effects of Cobalt Loading, Particle Size, and Calcination Condition on Co/CNT Catalyst Performance in Fischer–Tropsch Reactions. Symmetry, 11(1), 7.
37. Nikulshin, P. A., Ishutenko, D. I., Mozhaev, A. A., Maslakov, K. I., & Pimerzin, A. A. (2014). Effects of composition and morphology of active phase of CoMo/Al_2O_3 catalysts prepared using Co_2Mo_{10}–heteropolyacid and chelating agents on their catalytic properties in HDS and HYD reactions. *Journal of catalysis*, 312, 152-169.
38. Mohanty, S. (2011). Effect of citric acid on hydrotreating activity of NiMo catalysts (Doctoral dissertation, university of Saskatchewan).
39. Badoga, S. (2015). Synthesis and characterization of NiMo supported mesoporous materials with EDTA and phosphorus for hydrotreating of heavy gas oil. *University of Sakatchewan*.
40. Huang, T., Xu, J., & Fan, Y. (2018). Effects of concentration and microstructure of active phases on the selective hydrodesulfurization performance of sulfided CoMo/Al_2O_3 catalysts. *Applied Catalysis B: Environmental*, 220, 42-56.
41. Nikulshina, M., Mozhaev, A., Lancelot, C., Blanchard, P., Marinova, M., Lamonier, C., & Nikulshin, P. (2019). Enhancing the hydrodesulfurization of 4, 6-dimethyldibenzothiophene through the use of mixed $MoWS_2$ phase evidenced by HAADF. *Catalysis Today*, 329, 24-34.
42. Yang, L., Peng, C., Fang, X., Cheng, Z., & Zhou, Z. (2019). Hierarchically macro-mesoporous Ni-Mo/Al_2O_3 catalysts for hydrodesulfurization of dibenzothiophene. *Catalysis Communications*, 121, 68-72.
43. Tuktin, B., Zhandarov, E., Nurgaliyev, N., Tenizbayeva, A., & Shapovalov, A. (2019). Hydrotreating of gasoline and diesel oil fractions over modified alumina/zeolite catalysts. *Petroleum Science and Technology*, 37(15), 1770-1776.
44. Castillo-Villalón, P., Ramírez, J., Cuevas, R., Vázquez, P., & Castañeda, R. (2016). Influence of the support on the catalytic performance of Mo, CoMo, and NiMo catalysts supported on Al_2O_3 and TiO_2 during the HDS of thiophene, dibenzothiophene, or 4, 6-dimethyldibenzothiophene. *Catalysis Today*, 259, 140-149.
45. Kazakov, M. O., Nadeina, K. A., Danilova, I. G., Dik, P. P., Klimov, O. V., Pereyma, V. Y., & Dobryakova, I. V. (2019). Influence of USY zeolite recrystallization on physicochemical properties and catalytic performance of NiMo/USY-Al_2O_3 hydrocracking catalysts. *Catalysis Today*, 329, 108-115.

46. Zhang, C., Liu, X., Liu, T., Jiang, Z., & Li, C. (2019). Optimizing both the $CoMo/Al_2O_3$ catalyst and the technology for selectivity enhancement in the hydrodesulfurization of FCC gasoline. *Applied Catalysis A: General*, 575, 187-197.
47. Ameen, M., Azizan, M. T., Ramli, A., Yusup, S., & Yasir, M. (2016). Physicochemical properties of Ni-Mo/γ-Al_2O_3 catalysts synthesized via sonochemical method. *Procedia engineering*, 148, 64-71.
48. Zhang, D., Liu, W. Q., Liu, Y. A., Etim, U. J., Liu, X. M., & Yan, Z. F. (2017). Pore confinement effect of MoO_3/Al_2O_3 catalyst for deep hydrodesulfurization. *Chemical Engineering Journal*, 330, 706-717.
49. Huang, T., He, S., Chang, J., Xu, J., & Fan, Y. (2019). Preparation of a superior Co_4Mo_{12}/Al_2O_3 hydrodesulfurization catalyst by the hydrothermal deposition of heteropoly compounds on Al_2O_3. *Catalysis Communications*, 122, 68-72.
50. Liu, Q., Wang, W. Q., Yang, Y., Liu, X. G., & Xu, S. M. (2019). Recovery and regeneration of Al_2O_3 with a high specific surface area from spent hydrodesulfurization catalyst $CoMo/Al_2O_3$. *Rare Metals*, 38(1), 1-13.
51. Zhou, Z., Chen, S. L., Hua, D., Chen, A. C., Wang, Z. G., Zhang, J. H., & Gao, J. (2012). Structure and activity of NiMo/alumina hydrodesulfurization model catalyst with ordered opal-like pores. *Catalysis Communications*, 19, 5-9.
52. Dong, Y., Xu, Y., Zhang, Y., Lian, X., Yi, X., Zhou, Y., & Fang, W. (2018). Synthesis of hierarchically structured alumina support with adjustable nanocrystalline aggregation towards efficient hydrodesulfurization. *Applied Catalysis A: General*, 559, 30-39.
53. Saleh, T. A., Al-Hammadi, S. A., Abdullahi, I. M., & Mustaqeem, M. (2018). Synthesis of molybdenum cobalt nanocatalysts supported on carbon for hydrodesulfurization of liquid fuels. *Journal of Molecular Liquids*, 272, 715-721.
54. Okamoto, Y. (2014). Novel Molecular Approaches to the Structure–Activity Relationships and Unique Characterizations of Co–Mo Sulfide Hydrodesulfurization Catalysts for the Production of Ultraclean Fuels. *Bulletin of the Chemical Society of Japan*, 87(1), 20-58.
55. Abubakar, U. C., Alhooshani, K. R., Adamu, S., Al Thagfi, J., & Saleh, T. A. (2019). The effect of calcination temperature on the activity of hydrodesulfurization catalysts supported on mesoporous activated carbon. *Journal of Cleaner Production*, 211, 1567-1575.
56. Giraldo, S. A., Pinzón, M. H., & Centeno, A. (2008). Behavior of catalysts with rhodium in simultaneous hydrodesulfurization and hydrogenation reactions. *Catalysis today*, 133, 239-243.
57. Kanda, Y., Temma, C., Sawada, A., Sugioka, M., & Uemichi, Y. (2014). Formation of active sites and hydrodesulfurization activity of rhodium phosphide catalyst: Effect of reduction temperature and phosphorus loading. *Applied Catalysis A: General*, 475, 410-419.

58. Hayes, J. R., Bowker, R. H., Gaudette, A. F., Smith, M. C., Moak, C. E., Nam, C. Y., ... & Bussell, M. E. (2010). Hydrodesulfurization properties of rhodium phosphide: comparison with rhodium metal and sulfide catalysts. *Journal of Catalysis*, 276(2), 249-258.
59. Kanda, Y., Matsukura, Y., Sawada, A., Sugioka, M., & Uemichi, Y. (2016). Low-temperature synthesis of rhodium phosphide on alumina and investigation of its catalytic activity toward the hydrodesulfurization of thiophene. *Applied Catalysis A: General*, 515, 25-31.
60. Lee, J., Ishihara, A., Dumeignil, F., Miyazaki, K., Oomori, Y., Qian, E. W., & Kabe, T. (2004). Novel hydrodesulfurization catalysts derived from a rhodium carbonyl complex. *Journal of Molecular Catalysis A: Chemical*, 209(1-2), 155-162.
61. Lee, J., Ishihara, A., Dumeignil, F., Qian, E. W., & Kabe, T. (2004). Novel hydrodesulfurization catalysts derived from a supported rhodium carbonyl complex:-Effect of the support on the catalytic activity and the sulfur behavior. *Journal of Molecular Catalysis A: Chemical*, 213(2), 207-215.
62. Zhao, X., Cong, Y., Lv, F., Li, L., Wang, X., & Zhang, T. (2010). Mullite-supported Rh catalyst: a promising catalyst for the decomposition of N_2O propellant. *Chemical communications*, 46(17), 3028-3030.
63. Ito, S. I., Chibana, C., Nagashima, K., Kameoka, S., Tomishige, K., & Kunimori, K. (2002). CO hydrogenation over $RhVO_4/SiO_2$, Rh/V_2O_3 and Rh/SiO_2 catalysts: reduction and regeneration of $RhVO_4$. *Applied Catalysis A: General*, 236(1-2), 113-120.
64. Rao, Y., Zhang, L. M., Shang, X., Dong, B., Liu, Y. R., Lu, S. S., & Liu, C. G. (2017). Vanadium sulfides interwoven nanoflowers based on in-situ sulfurization of vanadium oxides octahedron on nickel foam for efficient hydrogen evolution. *Applied Surface Science*, 423, 1090-1096.
65. Hubaut, R. (2007). Vanadium-based sulfides as hydrotreating catalysts. *Applied Catalysis A*: General, 322, 121-128.
66. Guha, A., Banu, K. S., Das, S., Chattopadhyay, T., Sanyal, R., Zangrando, E., & Das, D. (2013). A series of mononuclear nickel (II) complexes of Schiff-base ligands having N, N, O-and N, N, N-donor sites: Syntheses, crystal structures, solid state thermal property and catecholase-like activity. *Polyhedron*, 52, 669-678.
67. Mudsainiyan, R. K., & Chawla, S. K. (2015). Synthesis, Characterizations, Crystal Structure Determination of μ6 Coordinated Complex of Co (III) with EDTA and Its Thermal Properties. *Molecular Crystals and Liquid Crystals*, 606(1), 237-245.
68. Myers, A. W., & Jones, W. D. (1996). Steric and Electronic Effects on the Insertion of a Rhodium Phosphine Complex into the C− S Bond of Substituted Dibenzothiophenes. Homogeneous Model for the Hydrodesulfurization Process. *Organometallics*, 15(13), 2905-2917.

69. Modak, R., Sikdar, Y., Mandal, S., & Goswami, S. (2013). Syntheses, crystal structures and catecholase activity of new dinuclear and cyclic trinuclear mixed valence cobalt (II, III) complexes. *Inorganic Chemistry Communications*, 37, 193-196.
70. Ayad, M. I. (2016). Synthesis, characterization and catechol oxidase biomimetic catalytic activity of cobalt (II) and copper (II) complexes containing N_2O_2 donor sets of imine ligands. *Arabian Journal of Chemistry*, 9, S1297-S1306.
71. Maji, A. K., Chatterjee, A., Khan, S., Ghosh, B. K., & Ghosh, R. (2017). Synthesis, crystal structure, catecholase and phenoxazinone synthase activities of a mononuclear cobalt (III) complex containing in situ formed tridentate N-donor Schiff base. *Journal of Molecular Structure*, 1146, 821-827.
72. Modak, R., Sikdar, Y., Mandal, S., Chatterjee, S., Bieńko, A., Mroziński, J., & Goswami, S. (2014). Syntheses, crystallographic characterization, catecholase activity and magnetic properties of three novel aqua bridged dinuclear nickel (II) complexes. *Inorganica Chimica Acta*, 416, 122-134.
73. Heidarinasab, A., Soltanieh, M., Ardjmand, M., Ahmadpanahi, H., & Bahmani, M. (2016). Comparison of Mo/MgO and Mo/γ-Al_2O_3 catalysts: Impact of support on the structure and dibenzothiophene hydrodesulfurization reaction pathways. *International journal of environmental science and technology*, 13(4), 1065-1076.
74. Kanchi, S., Chembeti, G., Sharma, D., Mdluli, P. S., Bisetty, K., Nuthalapati, V. N., & Sabela, M. I. (2016). Dithiocarbamate Induced Catalytic Hydrogen Wave for the determination of Iron (II) in Waters and Leafy Vegetables: Experimental and Computational Approach. *Int. J. Electrochem. Sci*, 11, 8027-8045.
75. Lu, B., Li, Y., & Xu, J. (2010). Electropolymerization study of benzothiophenes and characterization of novel poly (dibenzothiophene-S, S-dioxide). *Journal of Electroanalytical Chemistry*, 643(1-2), 67-76.
76. Coulier, L. (2001). Hydrotreating model catalysts: from characterization to kinetics. Eindhoven: *Technische Universiteit Eindhoven*.
77. Díaz de León, J. N., Ramesh Kumar, C., Antúnez-García, J., & Fuentes-Moyado, S. (2019). Recent insights in transition metal sulfide hydrodesulfurization catalysts for the production of ultra- low sulfur diesel: a short review. *Catalysis*, 9(1), 87.
78. Tanimu, A., & Alhooshani, K. (2019). Advanced hydrodesulfurization catalysts: a review of design and synthesis. *Energy & Fuels*, 33(4), 2810-2838.
79. Nie, H., Li, H., Yang, Q., & Li, D. (2018). Effect of structure and stability of active phase on catalytic performance of hydrotreating catalysts. *Catalysis Today*, 316, 13-20.
80. Hensen, E. J. M. (2000). Hydrodesulfurization catalysis and mechanism of supported transition metal sulfides. Technische *Universiteit Eindhoven*.

81. Vlasova, E. N., Deliy, I. V., Nuzhdin, A. L., Aleksandrov, P. V., Gerasimov, E. Y., Aleshina, G. I., & Bukhtiyarova, G. A. (2014). Catalytic properties of $CoMo/Al_2O_3$ sulfide catalysts in the hydrorefining of straight-run diesel fraction mixed with rapeseed oil. *Kinetics and Catalysis*, 55(4), 481-491.
82. Huirache-Acuña, R., Zepeda, T. A., Rivera-Muñoz, E. M., Nava, R., Loricera, C. V., & Pawelec, B. (2015). Characterization and HDS performance of sulfided CoMoW catalysts supported on mesoporous Al-SBA-16 substrates. *Fuel*, 149, 149-161.
83. Liu, B., Chai, Y., Li, Y., Wang, A., Liu, Y., & Liu, C. (2014). Effect of sulfidation atmosphere on the performance of the $CoMo/\gamma\text{-}Al_2O_3$ catalysts in hydrodesulfurization of FCC gasoline. *Applied Catalysis A: General*, 471, 70-79.
84. Huang, T., Xu, J., & Fan, Y. (2018). Effects of concentration and microstructure of active phases on the selective hydrodesulfurization performance of sulfided $CoMo/Al_2O_3$ catalysts. *Applied Catalysis B: Environmental*, 220, 42-56.
85. Bin, L. I. U., Lei, L. I. U., CHAI, Y. M., ZHAO, J. C., & LIU, C. G. (2018). Essential role of promoter Co on the MoS_2 catalyst in selective hydrodesulfurization of FCC gasoline. *Journal of Fuel Chemistry and Technology*, 46(4), 441-450.
86. Liu, X., Li, X., & Yan, Z. (2012). Facile route to prepare bimodal mesoporous $\gamma\text{-}Al_2O_3$ as support for highly active CoMo-based hydrodesulfurization catalyst. *Applied Catalysis B: Environmental*, 121, 50-56.
87. Bezverkhyy, I., Afanasiev, P., Geantet, C., & Lacroix, M. (2001). Highly active (Co) MoS_2/Al_2O_3 hydrodesulfurization catalysts prepared in aqueous solution. *Journal of Catalysis*, 204(2), 495-497.
88. Liu, B., Liu, L., Chai, Y., Zhao, J., Li, Y., Liu, Y., & Liu, C. (2018). Highly active $CoMoS/Al_2O_3$ catalysts ex situ presulfided with ammonium sulfide for selective hydrodesulfurization of fluid catalytic cracking gasoline. *Industrial & Engineering Chemistry Research*, 57(6), 2041-2049.
89. Yoosuk, B., Kim, J. H., Song, C., Ngamcharussrivichai, C., & Prasassarakich, P. (2008). Highly active MoS_2, $CoMoS_2$ and $NiMoS_2$ unsupported catalysts prepared by hydrothermal synthesis for hydrodesulfurization of 4, 6-dimethyldibenzothiophene. *Catalysis Today*, 130(1), 14-23.
90. Villalón, P. C., Ramırez, J., Cuevas, R., Vázquez, P., & Castaneda, R. (2015). Influence of the support on the catalytic performance of Mo, CoMo, and NiMo catalysts supported on Al_2O_3 and TiO_2 during the HDS ofthiophene, dibenzothiophene, or 4, 6-dimethyldibenzothiophene. *Catal Today*.
91. Zhang, D., Liu, W. Q., Liu, Y. A., Etim, U. J., Liu, X. M., & Yan, Z. F. (2017). Pore confinement effect of MoO_3/Al_2O_3 catalyst for deep hydrodesulfurization. *Chemical Engineering Journal*, 330, 706-717.

92. Huang, T., He, S., Chang, J., Xu, J., & Fan, Y. (2019). Preparation of a superior Co_4Mo_{12}/Al_2O_3 hydrodesulfurization catalyst by the hydrothermal deposition of heteropoly compounds on Al_2O_3. *Catalysis Communications*, 122, 68-72.
93. Breysse, M., Geantet, C., Afanasiev, P., Blanchard, J., & Vrinat, M. (2008). Recent studies on the preparation, activation and design of active phases and supports of hydrotreating catalysts. *Catalysis Today*, 130(1), 3-13.
94. van de Water, L. G., Bezemer, G. L., Bergwerff, J. A., Versluijs-Helder, M., Weckhuysen, B. M., & de Jong, K. P. (2006). Spatially resolved UV–vis microspectroscopy on the preparation of alumina-supported Co Fischer–Tropsch catalysts: Linking activity to Co distribution and speciation. *Journal of Catalysis*, 242(2), 287-298.
95. Moqadam, S. I., & Mahmoudi, M. (2013). Advent of nanocatalysts in hydrotreating process: benefits and developments. *Am J Oil Chem Technol*, 1, 13-21.
96. Badoga, S. (2015). Synthesis and characterization of NiMo supported mesoporous materials with EDTA and phosphorus for hydrotreating of heavy gas oil. *University of Sakatchewan*.
97. Mohanty, S. (2011). Effect of citric acid on hydrotreating activity of NiMo catalysts *(Doctoral dissertation, University of Saskatchewan*).
98. Liu, K. (2010). Hydrodesulfurization and Hydrodenitrogenation of Model Compounds Using in-situ Hydrogen over Nano-Dispersed Mo Sulfide Based Catalysts.
99. Silva, A. C., Corre, T., & Lemos, F. (2014). Study of the liquid activation of CoMo and NiMo catalysts. Tec. Lisboa, 1.
100. Théodet, M. (2010). New generation of" bulk" catalyst precursors for hydrodesulfurization synthesized in supercritical fluids (*Doctoral dissertation*).
101. Alamoudi, M. (2016). Hydrodesulphurization of dibenzothiophene using carbon supported NiMoS catalysts (*Doctoral dissertation, University of British Columbia*).
102. Hensen, E. J. M. (2000). Hydrodesulfurization catalysis and mechanism of supported transition metal sulfides. *Technische Universiteit Eindhoven*.
103. Tian, H., Roberts, C. A., & Wachs, I. E. (2010). Molecular structural determination of molybdena in different environments: Aqueous solutions, bulk mixed oxides, and supported MoO_3 catalysts. *The Journal of Physical Chemistry C*, 114(33), 14110-14120.
104. Medici, Á., & Prins, R. (1996). The influence of chelating ligands on the sulfidation of Ni and Mo in NiMo/SiO_2Hydrotreating catalysts. *Journal of Catalysis*, 163(1), 38-49.
105. de Jong, A. M., De Beer, V. H. J., van Veen, J. R., & Niemantsverdriet, J. W. (1996). Surface science model of a working cobalt-promoted molybdenum sulfide hydrodesulfurization catalyst: characterization and reactivity. *The Journal of Physical Chemistry*, 100(45), 17722-17724.

106. Shimizu, T., Hiroshima, K., Honma, T., Mochizuki, T., & Yamada, M. (1998). Highly active hydrotreatment catalysts prepared with chelating agents. *Catalysis today*, 45(1-4), 271-276.

107. Ohta, Y., Shimizu, T., Honma, T., & Yamada, M. (1999). Effect of chelating agents on HDS and aromatic hydrogenation over CoMo-and NiW/Al_2O_3. In Studies in surface science and catalysis (Vol. 127, pp. 161-168). *Elsevier*.

108. Cattaneo, R., Shido, T., & Prins, R. (1999). The relationship between the structure of $NiMo/SiO_2$ catalyst precursors prepared in the presence of chelating ligands and the hydrodesulfurization activity of the final sulfided catalysts. *Journal of Catalysis*, 185(1), 199-212.

109. Cattaneo, R., Weber, T., Shido, T., & Prins, R. (2000). A quick EXAFS study of the sulfidation of $NiMo/SiO_2$ hydrotreating catalysts prepared with chelating ligands. Journal of Catalysis, 191(1), 225-236.

110. Stanislaus, A., & Cooper, B. H. (1994). Aromatic hydrogenation catalysis: a review. Catalysis Reviews—*Science and Engineering*, 36(1), 75-123.

111. Frisch, M. J., Trucks, G. W., Schlegel, H. B., Scuseria, G. E., Robb, M. A., Cheeseman, J. R., Scalmani, G., Barone, V., Petersson, G. A., Nakatsuji, H., Li, X., Caricato, M., Marenich, A. V., Bloino, J., Janesko, B. G., Gomperts, R., Mennucci, B., Hratchian, H. P., Ortiz, J. V., Izmaylov, A. F., Sonnenberg, J. L., Williams-Young, D., Ding, F., Lipparini, F., Egidi, F., Goings, J., Peng, B., Petrone, A., Henderson, T., Ranasinghe, D., Zakrzewski, V. G., Gao, J., Rega, N., Zheng, G., Liang, W., Hada, M., Ehara, M., Toyota, K., Fukuda, R., Hasegawa, J., Ishida, M., Nakajima, T., Honda, Y., Kitao, O., Nakai, H., Vreven, T., Throssell, K., Montgomery, J. A., Jr., J. E. Peralta, F. Ogliaro, M. J. Bearpark, J. J. Heyd, E. N. Brothers, K. N. Kudin, V. N. Staroverov, T. A. Keith, R. Kobayashi, J. Normand, K. Raghavachari, A. P. Rendell, J. C. Burant, S. S. Iyengar, J. Tomasi, M. Cossi, J. M. Millam, M. Klene, C. Adamo, R. Cammi, J. W. Ochterski, R. L. Martin, K. Morokuma, O. Farkas, J. B. Foresman, and D. J. (2016). Gaussian 16, Revision C.01. *Fox, Gaussian, Inc., Wallingford CT*.

112. Becke, A. D. (1993). Density-functional thermochemistry. III. The role of exact exchange. *J. Chem. Phys*, 98, 5648–5652.

113. Saravanan, S., & Balachandran, V. (2014). Quantum chemical studies, natural bond orbital analysis and thermodynamic function of 2,5-dichlorophenylisocyanate, Spectrochim. *Acta - Part A Mol. Biomol. Spectrosc*, 120, 351–364.

114. P. Politzer and F. Abu-Awwad. (1998). A comparative analysis of Hartree-Fock and Kohn-Sham orbital energies, *Theor. Chem. Acc*., 99, 83–87.

115. Mulliken, R. S. (1934). A new electroaffinity scale; Together with data on valence states and on valence ionization potentials and electron affinities. *J. Chem. Phys*, 2, 782–793.

116. Hoffmann, R. (1988). Solids and Surfaces: A Chemist's View of Bonding in Extended Structures, VCH Publishers, *New York*.

117. Parr, R. G., Szentpály, L. V., & Liu, S. (1999). Electrophilicity index. *J. Am. Chem. Soc*, 121, 1922–1924.

118. Padmanabhan, J., Parthasarathi, R., Subramanian, V., & Chattaraj, P. K. (2007). Electrophilicity-based charge transfer descriptor. *J. Phys. Chem. A*, 111, 1358–1361.

119. Tian, H., Roberts, C.A., & Wachs, I.E. (2010). Molecular structural determination of molybdena in different environments: aqueous solutions, bulk mixed oxides, and supported MoO_3 catalysts. *J.Phys. Chem. C*. 114, 14110–14120.

120. Weber, R. (1995). Effect of local structure on the UV-Visible absorption edges of molybdenum oxide clusters and supported molybdenum oxides. *J. Catal*, 151, 470–474,

121. Ashley, J.H., Mitchell, P.C.H. (1968). Cobalt–molybdenum–alumina hydrodesulphurization catalysts. Part I. A spectroscopic and magnetic study of the fresh catalyst and model compounds, *J. Chem. Soc. A*, 2821–2827.

122. van de Water, L.G.A., Bezemer, G.L., Bergwerff, J.A., Versluijs-Helder, M., Weckhuysen, B.M., de Jong, K.P. (2006). Spatially resolved UV–vis microspectroscopy on the preparation of alumina-supported Co Fischer-Tropsch catalysts: linking activity to Co distribution and speciation. *J. Catal*, 242, 287–298.

123. Ataloglou, T., Bourikas, K., Vakros, J., Kordulis, C., Lycourghiotis, A. (2005). Kinetics of adsorption of the cobalt ions on the electrolytic solution/ -alumina interface. *J. Phys. Chem. B*, 109, 4599–4607.

124. Jeziorowski, H., Knözinger, H. (1979). Raman and ultraviolet spectroscopic characterization of molybdena on alumina catalysts. *J. Phys. Chem*, 83, 1166–1173.

125. Liu, Z., Chen, Y. (1998). Spectroscopic studies on tetragonal ZrO_2-supported MoO_3 and $NiOMoO_3$ systems. *J. Catal*, 177, 314–324.

126. Fournier, M., Louis, C., Che, M., Chaquin, P., Masure, D. (1989). Polyoxometallates as models for oxide catalysts. Part I. An UV-visible reflectance study of polyoxomolybdates: influence of polyhedra arrangement on the electronic transitions and comparison with supported molybdenum catalysts. *J. Catal*, 119, 400–414.

127. Rinaldi, N., Al-Dalama, K., Kubota, T., Okamoto, Y. (2009). Preparation of Co–Mo/B_2O_3/Al_2O_3 catalysts for hydrodesulfurization: effect of citric acid addition. *Appl. Catal. A Gen*, 360, 130–136.

128. van Haandel, L., Bremmer, G. M., Hensen, E. J. M., & Weber, T. (2017). The effect of organic additives and phosphoric acid on sulfidation and activity of (Co) Mo/Al_2O_3 hydrodesulfurization catalysts. *Journal of Catalysis*, 351, 95-106.

129. Qiu, Z., Hua, Z., Li, Y., Wang, M., Huang, D., Tian, C., & Li, E. (2018). Acetone sensing properties and mechanism of Rh-Loaded WO_3 nanosheets. *Frontiers in chemistry*, 6, 385.

130. Masud, J., Van Nguyen, T., Singh, N., McFarland, E., Ikenberry, M., Hohn, K., & Hwang, B. J. (2015). A Rh_xS_y/C catalyst for the hydrogen oxidation and hydrogen evolution reactions in HBr. *Journal of the Electrochemical Society*, 162(4), F455.

131. Jin, C., Xia, W., Nagaiah, T. C., Guo, J., Chen, X., Bron, M., & Muhler, M. (2009). On the role of the thermal treatment of sulfided Rh/CNT catalysts applied in the oxygen reduction reaction. *Electrochimica acta*, 54(28), 7186-7193.

132. Hayes, J. R., Bowker, R. H., Gaudette, A. F., Smith, M. C., Moak, C. E., Nam, C. Y., & Bussell, M. E. (2010). Hydrodesulfurization properties of rhodium phosphide: Comparison with rhodium metal and sulfide catalysts. *Journal of Catalysis*, 276(2), 249-258.

133. Marot, L., Mathys, D., De Temmerman, G., & Oelhafen, P. (2008). Characterization of sub-stoichiometric rhodium oxide deposited by magnetron sputtering. *Surface science*, 602(21), 3375-3380.

134. Kim, N. H., Choi, S. J., Kim, S. J., Cho, H. J., Jang, J. S., Koo, W. T., ... & Kim, I. D. (2016). Highly sensitive and selective acetone sensing performance of WO_3 nanofibers functionalized by Rh_2O_3 nanoparticles. *Sensors and Actuators B: Chemical*, 224, 185-192.

135. Yang, H. C., Lee, M. W., Hwang, H. S., Moon, J. K., & Chung, D. Y. (2014). Study of cerium-promoted rhodium alumina catalyst as a steam reforming catalyst for treatment of spent solvents. *Journal of Rare Earths*, 32(9), 831-836.

136. Karachi, N., Hosseini, M., Parsaee, Z., & Razavi, R. (2018). Novel high performance reduced graphene oxide based nanocatalyst decorated with Rh_2O_3/Rh-NPs for CO_2 photoreduction. *Journal of Photochemistry and Photobiology A: Chemistry*, 364, 344-354.

137. Shi, R., Yuan, X., Liu, A., Xu, M., & Zhao, Z. (2018). Determination of bisphenol a in beverages by an electrochemical sensor based on Rh_2O_3/reduced graphene oxide composites. *Applied Sciences*, 8(12), 2535.

138. Cesano, F., Bertarione, S., Piovano, A., Agostini, G., Rahman, M. M., Groppo, E., & Zecchina, A. (2011). Model oxide supported MoS_2 HDS catalysts: structure and surface properties. *Catalysis Science & Technology*, 1(1), 123-136.

139. Ehsan, M. A., Adam, A., Rehman, A., Hakeem, A. S., Isab, A. A., & Qamar, M. (2021). Morphologically controlled rapid fabrication of rhodium sulfide (Rh_2S_3) thin films for superior and robust hydrogen evolution reaction. *Sustainable Energy & Fuels*, 5(2), 459-468.

140. Ziegelbauer, J. M., Gatewood, D., Gulla, A. F., Guinel, M. J. F., Ernst, F., Ramaker, D. E., & Mukerjee, S. (2009). Fundamental investigation of oxygen reduction reaction on rhodium sulfide-based chalcogenides. *The Journal of Physical Chemistry C*, 113(17), 6955-6968.

141. Sosibo, N. M., & Revaprasadu, N. (2008). Synthesis and characterization of rhodium sulfide nanoparticles and thin films. *Materials Science and Engineering: B*, 150(2), 111-115.

142. Albiter, M. A., Huirache-Acuna, R., Paraguay-Delgado, F., Rico, J. L., & Alonso-Nunez, G. (2006). Synthesis of MoS_2 nanorods and their catalytic test in the HDS of dibenzothiophene. *Nanotechnology*, 17(14), 3473.

143. Pakhare, D., Wu, H., Narendra, S., Abdelsayed, V., Haynes, D., Shekhawat, D., & Spivey, J. (2013). Characterization and activity study of the Rh-substituted pyrochlores for CO_2 (dry) reforming of CH_4. *Applied Petrochemical Research*, 3(3), 117-129.

144. Escobar, J., Barrera, M. C., De los Reyes, J. A., Toledo, J. A., Santes, V., & Colín, J. A. (2008). Effect of chelating ligands on Ni-Mo impregnation over wide-pore ZrO_2-TiO_2. *Journal of molecular catalysis A: Chemical*, 278 (1-2), 33-40.